Study of transfer reaction properties with stable and unstable heavy ion beams

Čolović, Petra

University of Zagreb

FACULTY OD SCIENCE

Petra Čolović

Study of transfer reaction properties with stable and unstable heavy ion beams

DOCTORAL DISSERTATION

Zagreb, 2020

University of Zagreb

FACULTY OF SCIENCE

Petra Čolović

Study of transfer reaction properties with stable and unstable heavy ion beams

DOCTORAL DISSERTATION

Supervisor: Dr. sc. Suzana Szilner

Zagreb, 2020

Sveučilište u Zagrebu

PRIRODOSLOVNO-MATEMATIČKI FAKULTET

Petra Čolović

Istraživavanje svojstava reakcija prijenosa nukleona upotrebom stabilnih i nestabilnih ionskih snopova

DOKTORSKI RAD

Mentor: Dr. sc. Suzana Szilner

Zagreb, 2020

Supervisor

Dr. Suzana Szilner obtained B. Sc. and M. Sc. thesis at University of Zagreb, and the PhD thesis in double-supervised theses by University L. Pasteur in Strasbourg and University of Zagreb. She was postdoctoral fellow at Laboratori Nazionali di Legnaro. She was employed at Ruđer Bošković Institute, Zagreb, as research associate in 2003. She is the senior scientist since 2014 and the head of the Nuclear physics laboratory since 2016. Dr. Szilner was the principal investigator in several Croatian Science Foundation or Ministry of Science and Education projects. She participated, as collaborator, or as the member of the Project Management Board or as the work-package leader in several European projects (within FP7 and HORIZON2020). She is included in the activities of the Croatian scientific centers of excellence for Advanced Materials and Sensors.

Dr. Szilner participated in the different management and organizational activities at her home institution (member of the Board of governors, member of Scientific Council). She also participated in the organizational and scientific activities at EU (Scientific Steering Committee of the European Nuclear Science and Applications Research within ENSAR2 project, the Long Range Plan of the Nuclear Physics European Collaboration Committee). She was co-chair of several international conferences, and started the successful serii of Nuclear Structure and Dynamics conferences.

Dr. Szilner participated to the more than 70 nuclear physics experiments at different accelerator facilities in Europe, where she was a spokesperson of more than 15 experimental research projects. These research activities, according to Web of Science Core Collection, resulted in 205 publications, 4022 citations, h-index = 39, with several letters and one high cited topical review.

University of Zagreb
Faculty of Science
Department of Physics

Doctoral Dissertation

Study of transfer reaction properties with stable and unstable heavy ion beams

Petra Čolović
Institut Ruđer Bošković, Zagreb

The main subject of this thesis is to show that transfer reactions with the neutron-rich unstable beams and the heavy targets could be very adequate for the production of the neutron-rich heavy nuclei. To that purpose, the measurement of ^{94}Rb+^{208}Pb transfer reaction has been performed at the energy of about 30% above the Coulomb barrier, provided by the radioactive ion beam facility of CERN (HIE-ISOLDE). The high-resolution and high-efficiency experimental set-up consisted of a large γ-array MINIBALL, coupled to the CD fragment detector of wide angular range. From the measured particle-γ and particle-γ-γ coincidences, the characteristic γ transitions were attributed to ^{207}Pb, ^{208}Pb, ^{209}Pb and ^{210}Pb, and their binary partners, the isotopes of Rb. Based on the attributed γ transitions, the total cross sections in Pb isotopes were successfully constructed. In particular, in channels populated by transfer of neutrons from ^{94}Rb beam to ^{208}Pb target, the cross section of 138(8) mb was evaluated in ^{209}Pb, and 41(7) mb in ^{210}Pb. These significant values quantify the production of the moderately neutron-rich heavy nuclei for the first time in the transfer reaction induced by an unstable beam. The obtained results were fairly reproduced with the semi-classical model GRAZING, thus encouraging the use of the presented approach for the population of the neutron-rich heavy nuclei. This thesis strongly suggests that the presently available experimental techniques and radioactive ion beam intensities are very suitable to extend the reaction mechanism and the nuclear structure studies farther from the valley of stability.

(182 pages, 165 references, 103 figures, 16 tables, original in English)

Keywords: transfer reactions, neutron-rich heavy nuclei, γ-spectroscopy, total cross section

Supervisor: Dr. sc. Suzana Szilner, Ruđer Bošković Institute, Zagreb

Reviewers:
1. Prof. dr. sc. Matko Milin, University of Zagreb
2. Dr. sc. Suzana Szilner, Ruđer Bošković Institute, Zagreb
3. Prof. dr. sc. Tamara Nikšić, University of Zagreb
4. Dr. sc. Zdravko Siketić, Ruđer Bošković Institute, Zagreb
5. Prof. dr. sc. Nils Paar, University of Zagreb

Thesis accepted: 2020

Sveučilište u Zagrebu
Prirodoslovno-matematički fakultet
Fizički odsjek

Doktorski rad

Istraživavanje svojstava reakcija prijenosa nukleona upotrebom stabilnih i nestabilnih ionskih snopova

Petra Čolović
Institut Ruđer Bošković, Zagreb

Primarni zadatak ove disertacije je pokazati da su reakcije prijenosa nukleona s neutronski bogatim snopovima i teškim metama vrlo pogodne za proizvodnju neutronski bogatih teških jezgara. S tim ciljem, izvršeno je mjerenje reakcije ^{94}Rb+^{208}Pb s energijom snopa otprilike 30% iznad kulonske barijere, dobivenom pri postrojenju za radioaktivne snopove u CERN-u (HIE-ISOLDE). Eksperimentalni postav visoke rezolucije i efikasnosti sastojao se od složenog γ-spektrometra MINIBALL, vezanog s čestičnim detektorom širokog kutnog raspona, naziva CD. Mjerenje koncidencije između γ zraka i čestica omogućilo je pridjeljivanje karakterističnih γ prijelaza izotopima olova, ^{207}Pb, ^{208}Pb, ^{209}Pb i ^{210}Pb, i njihovim binarnim partnerima, izotpima rubidija. Na temelju pridjeljenih γ prijelaza, uspješno su konstruirani ukupni udarni presjeci u izotopima olova. Posebice, u kanalima prijenosa neutrona od snopa ^{94}Rb ka meti ^{208}Pb, udarni presjek u ^{209}Pb iznosio je 138(8) mb, i 41(7) mb u ^{210}Pb. Ove značajne vrijednosti udarnih presjeka po prvi puta opisuju proizvodnju umjereno neutronski bogatih teških jezgara u reakciji prijenosa nukleona uz upotrebu nestabilnog snopa. Dobiveni rezultati su dobro opisani računom GRAZING, te potiću daljnju upotrebu predstavljenog eksperimentalnog pristupa za proizvodnju teških jezgara bogatih neutronima. Disertacija jasno demonstrira da je korštenjem trenutno dostupnih eksperimentalnih tehnika i intenziteta radioaktivnih snopova moguće proširiti daljnja istraživanja nuklearne strukture i mehanizma reakcije značajno dalje od doline stabilnosti.

(182 stranice, 165 literaturnih navoda, 103 slike, 16 tablica, izvornik na engleskom jeziku)

Ključne riječi: reakcije prijenosa, neutronski bogate teške jezgre, spektroskopija gama-zračenja, ukupni udarni presjek

Mentor: Dr. sc. Suzana Szilner, Ruđer Bošković Institute, Zagreb

Povjerenstvo za obranu:

1. Prof. dr. sc. Matko Milin, Sveučilište u Zagrebu
2. Dr. sc. Suzana Szilner, Institut Ruđer Bošković, Zagreb
3. Prof. dr. sc. Tamara Nikšić, Sveučilište u Zagrebu
4. Dr. sc. Zdravko Siketić, Institut Ruđer Bošković, Zagreb
5. Prof. dr. sc. Nils Paar, Sveučilište u Zagrebu

Rad prihvaćen: 2020

our work should equip
the next generation of women
to outdo us in every field
this is the legacy we'll leave behind
progress - rupi kaur

Prošireni sažetak

Trenutno postoji rastući interes za proučavanje mehanizama reakcije koji pogoduju stvaranju teških jezgara bogatih neutronima. Posebno zanimljivo je područje jezgara u blizini olova jer se nalazi u okolini neutronske ljuske $N = 126$, vrlo važne u nukleosintezi teških elemenata. Glavni cilj ovog rada je pokazati da su reakcije prijenosa nukleona s neutronski bogatim snopovima (daleko od doline stabilnosti) i teškim metama vrlo pogodne za proizvodnju neutronski bogatih teških jezgara u blizini olova. S tom namjerom, izvršeno je mjerenje reakcije prijenosa nukleona ^{94}Rb+^{208}Pb s eksperimentalnim postavom visoke razlučivosti i efikasnosti.

Neutronski bogat nestabilan snop ^{94}Rb proizveden je na energiji oko 30% iznad kulonske barijere, koristeći nedavno nadograđeni akcelerator pri HIE-ISOLDE postrojenju u CERN-u. Eksperimentalni postav sastojao se od složenog γ-spektrometra MINIBALL, vezanog s čestičnim detektorom širokog kutnog raspona, naziva CD, i dvije mete olova ^{208}Pb različite debljine (1 i 13 mg/cm^2). Postav je omogućio uspješno mjerenje kutne raspodjele čestica, i raspada kratkoživućih i dugoživućih pobuđenih stanja. Konstrukcija koncidencije između γ prijelaza i čestica bila je nužna za doplerovu korekciju γ-zračenja izračenog u gibanju, i oduzimanje složene pozadine od β-raspada. Na temelju pročavanja karakterističnih γ prijelaza i koincidencija čestica i γ prijelaza (čestica-γ-γ), opažena je zastupljenost izotopa olova ^{207}Pb, ^{208}Pb, ^{209}Pb i ^{210}Pb, i njihovih binarnih partnera, izotopa rubidija.

Glavni rezultati rada su udarni presjeci u izotopima olova, koji su se pokazali značajnima u kanalima ^{209}Pb i ^{210}Pb. Time je po prvi puta kvantitativno opisana proizvodnja umjereno neutronski bogatih teških jezgara u reakcijama prijenosa nukleona uz korištenje nestabilnog snopa. Dobiveni udarni presjeci su dobro opisani računom GRAZING, što potiće daljnju upotrebu predstavljenog eksperimentalnog pristupa za proizvodnju teških jezgara bogatih neutronima. Eksperiment ^{94}Rb+^{208}Pb se može smatrati prvim korakom u planiranju budućih eksperimentalnih kampanja. Paralelno s daljnjim napredetkom tehnika radioaktivnih snopova, koje će u sljedećim godinama omogućiti i jače intenzitete snopova, reakcije prijenosa mnogo nukleona mogle bi se koristiti za proizvodnju neutronski bogatih jezgara dalje od doline stabilnosti.

Dodatno poglavlje ovog rada posvećeno je istraživanju svojstava magnetskog spektrometra PRISMA u mjerenju reakcije prijenosa nukleona ^{206}Pb+^{118}Sn. Veliki prostorni kut i širok energijski raspon spektrometra omogućili su istovremeno proučavanje masene rezolucije fragmenata nalik kositru (Sn), te fisijskih fragmenata. Potonji su produkti fisije inducirane prijenosom nukleona, i zamjećeni su u blizini atomskog broja $Z \sim 40$. Pokazano je da je masena rezolucija prigodna za proučavanje vjerojatnosti preživljavanja teških (neutronski bogatih) fragmenata proizvedenih u reakcijama prijenosa, kao i (eksperimentalno inače vrlo zahtjevnih) svojstava fisije.

Da bi se bolje proučila svojstva reakcije ^{94}Rb+^{208}Pb, posvećena je posebna pažnja karakteru pobuđenih stanja. Zamjećeno je snažno pobuđenje stanja kolektivnog karaktera u ^{208}Pb, posebice stanja 3^- i pridjeljenog (dobro poznatog) $E3$ prijelaza, ^{208}Pb: $3^- \rightarrow 0^+$. Stanja u ^{210}Pb razmatrana su u kontekstu dvočestičnih konfiguracija. U ^{207}Pb i ^{209}Pb, snažno su opažena stanja jednočestičnog karaktera. Također, opaženi su i snažni γ prijelazi mogućeg $E3$ karaktera, ^{207}Pb: $(19/2^-) \rightarrow 13/2^+$ i ^{209}Pb: $(21/2^+) \rightarrow 15/2^-$. Stanja $19/2^-$ i $21/2^+$ se mogu objasniti kao stanja najvišeg mogućeg spina multipleta dobivenog vezanjem šupljine, odnosno čestice, i oktupolnog pobuđenja. Stanja takvog karaktera, popraćena zastupljenošću stanja visokog spina, zamjećena su u prijašnjim reakcijama prijenosa mnogo nukleona i srednje teškim izotopima (u blizini zatvorenih ljuski), poput izotopa kalcija, argona i cirkonija. U pojedinim radovima, korištenjem modela ljusaka i računa vezanja čestičnih i oktupolnih modova, ukazuje se na značajnu ulogu 3^- stanja u strukturi jezgara u blizini olova. Ta uloga će biti daljnje istražena usporedbom ^{94}Rb+^{208}Pb reakcije s prikladnim modelima.

Contents

1. Introduction . . . 1

1.1. Motivation of the present study . . . 1

1.2. Selected studies with the stable beams . . . 3

1.2.1. Heavy-partner cross sections . . . 4

1.2.2. Studies in the $Z \sim 82$ and $N \sim 126$ region . . . 6

1.3. Multinucleon transfer reactions . . . 8

1.3.1. Main characteristics of transfer reactions . . . 10

1.3.2. Theoretical approach to transfer reactions . . . 14

1.3.3. The ^{40}Ar,^{90}Zr+^{208}Pb experiments . . . 22

2. The ^{94}Rb+^{208}Pb experiment at HIE-ISOLDE facility . . . 25

2.1. Techniques for the RIB production . . . 25

2.2. The HIE-ISOLDE facility . . . 26

2.2.1. Radioactive ion beam production . . . 27

2.2.2. Post-acceleration . . . 27

2.3. The MINIBALL station . . . 28

2.3.1. The γ-spectrometer MINIBALL . . . 29

2.3.2. The CD detector . . . 30

2.4. The ^{94}Rb+^{208}Pb experiment . . . 32

2.4.1. The intensity of the ^{94}Rb beam and the radiation safety issue . . . 33

3. Data analysis . . . 35

3.1. Calibration of MINIBALL . . . 35

3.2. Calibration of CD . . . 37

3.2.1. Position calibration . . . 37

3.2.2. Energy calibration . . . 39

3.2.3. Effects of multiplicity in CD 41
3.3. Fragment-γ coincidences 43
3.3.1. Background subtraction 46
3.4. Fragment-γ-γ coincidences 47
3.5. Doppler correction 50
3.6. Background radiation 52
3.6.1. The β-decay 52
3.6.2. Other background sources 53

4. Experimental results 57
4.1. Wilczyński plots 57
4.2. Angular distributions 61
4.2.1. Angular distribution calculations 63
4.3. Gamma-spectra 65
4.3.1. "Thin" target γ spectra 65
4.3.2. "Thick" target γ spectra 69
4.4. Excited states in $^{92-95}$Rb 71
4.4.1. Review of previous studies 71
4.4.2. ^{94}Rb 73
4.4.3. ^{92}Rb 76
4.4.4. ^{93}Rb 78
4.4.5. ^{95}Rb 79
4.5. The proton transfer channel 79

5. Excited states in $^{207-210}$Pb 81
5.1. ^{208}Pb 83
5.2. ^{210}Pb 87
5.2.1. ^{208}Pb+^{208}Pb experimental results 88
5.2.2. Half-lives of 6^+, 8^+ isomers 89
5.2.3. ^{94}Rb+^{208}Pb experimental results 89
5.3. ^{207}Pb 94
5.4. ^{209}Pb 99
5.5. Review and discussion 105

6. Cross section in the Pb isotopes . . . 111
6.1. Experimental cross section . . . 111
6.2. Total cross section . . . 114
6.3. Discussion . . . 115
6.4. Towards the neutron-rich heavy nuclei . . . 117

7. Outlook: the ^{206}Pb+^{118}Sn experiment . . . 121
7.1. Introduction . . . 122
7.2. The ^{206}Pb+^{118}Sn experiment . . . 125
7.3. Experimental set-up and data analysis . . . 128
7.4. Experimental results: mass distributions . . . 136
7.5. Perspectives . . . 140

Conclusion . . . 143

A. Appendix . . . 145
A.1. "Thick" target Wilczyński plot . . . 145
A.2. The γ spectra of $^{207-210}$Pb . . . 146

Bibliography . . . 149

List of Figures . . . 163

List of Tables . . . 175

Biography . . . 177

1

Introduction

The study of reaction mechanisms which favour the production of heavy and neutron-rich nuclei has been receiving a special attention in recent times. One of the promising mechanisms is the transfer of many nucleons at energies close to the Coulomb barrier. It is predicted that, with the use of neutron-rich projectile and heavy target, multinucleon transfer reactions might be a very suitable approach to populate the heavy and neutron rich regions of the nuclear chart.

This Chapter aims to introduce the latest and the most relevant experimental and theoretical advances concerning the production of the neutron-rich heavy nuclei. Particular attention is given to the valuable findings from the multinucleon transfer reaction measurements employing the stable beams, and the description of this mechanism.

1.1 Motivation of the present study

It is known that further from the valley of stability towards the neutron drip line there are a large number of neutron-rich isotopes of heavy and superheavy elements which are still unknown [1, 2]. Indeed, a glance at the up-to-date chart of nuclides reveals that the majority of all the known isotopes above the nuclear charge $Z = 60$ are still neutron-poor. While the neutron-rich regions from Sn ($Z\sim$50) down to Ni ($Z\sim$28) and calcium ($Z\sim$20) can be reached with several different reaction mechanisms, the neutron-rich nuclei above Pb ($Z\sim$82) are much more difficult to produce. At the same time, the production of these heavy neutron-rich nuclei (further from the stability) is very important for exploring their structure and decay properties and for understanding the r-process in nuclear astrophysics.

One of the promising ways to reach this heavy neutron-rich region of the nuclear chart is the transfer of many nucleons at energies close to the Coulomb barrier. Multinucleon transfer (MNT) is a mechanism of binary character, traditionally employed in the nuclear structure and reaction dynamics studies [3–9]. Recently, the total cross sections of different transfer channels were compared for several reactions employing the same ^{208}Pb target and projectiles going from neutron-poor to neutron-rich: ^{40}Ca, ^{58}Ni, and ^{40}Ar [10–12]. Only the neutron-rich (stable) ^{40}Ar beam allowed to access also the transfer channels which involved the proton pick-up and the neutron stripping[1]. For the heavier partner of the reaction, this processes could in principle lead to the neutron-rich regions in vicinity of ^{208}Pb. Experimental data were compared with the semi-classical model GRAZING, particularly well-suited for a description of nucleon transfer.

The same model predicts that by using the (very) neutron-rich unstable beams, the proton pick-up and neutron stripping channels become the dominant ones [13]. Other reactions models, envisaging different mechanisms for the production of heavy neutron-rich nuclei [8, 9, 14], reach the similar conclusions. However, it is also predicted that the primary cross sections in the neutron-rich sectors may be significantly influenced by the secondary processes, like for example the neutron evaporation or fission. How to successfully transfer neutrons to the heavy nuclei, while minimizing the influence of the secondary processes, is still an open question.

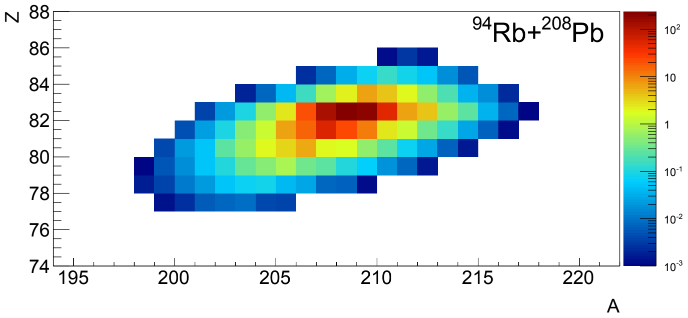

Figure 1.1: The ^{94}Rb+^{208}Pb reaction cross section distribution [mb] calculated by GRAZING for the ^{94}Rb beam energy of 6.2 MeV·A.

To explore the favourable experimental conditions for the population of the heavy neutron-rich nuclei by the MNT, we performed the measurement of ^{94}Rb+^{208}Pb reaction at energy $E_{\mathrm{LAB}} = 6.2$ MeV·A, close to the Coulomb barrier. The recently upgraded radioactive-ion beam facility HIE-ISOLDE of CERN provided the relatively intense neutron-rich beam ^{94}Rb ($N/Z = 1.54$). This beam was chosen to have a sufficient

---

[1] The direction of the transfer is commonly defined from the lighter partners viewpoint, as for instance, the term "proton pick-up" is used here to describe the transfer of protons from the target to the projectile.

statistics in certain transfer channels, taking into account the predicted cross section distribution, obtained by the GRAZING code and plotted in Fig. 1.1. As expected, the largest calculated cross sections are in the neutron transfer channels, with sizable cross sections in ^{209}Pb and ^{210}Pb, in particular. These cross sections were already corrected for the neutron evaporation. Even after considering the possible effect of the secondary process, the large primary cross sections with unstable beams predict that the MNT mechanism is a suitable tool for the production of the heavy neutron-rich nuclei around ^{208}Pb, which is what we tend to explore.

1.2 Selected studies with the stable beams

The production of neutron-rich heavy nuclei with stable beams has always been a very challenging task. Their direct identification is rather difficult, due to the large nuclear charge and mass numbers involved. At the moment growing interest in the neutron-rich heavy nuclei is closely connected to the recent experimental advances.

Multinucleon transfer reactions at bombarding energies of 5-10 MeV·A have proven to be a very successful approach in studies of the path leading to the population of moderately neutron-rich and heavy nuclei (see Subs. 1.2.1). In experiments using thin targets, at least one reaction partner is identified in a detector or a magnetic spectrometer. Magnetic spectrometers, such as PRISMA in Legnaro National Laboratories (LNL)[2], are traditionally employed for the heavy-ion reaction mechanism studies [15]. By coupling the spectrometer and the γ-array, one can also attribute the γ transitions to the particular fragment [16–19], as it will be explained in more details in Subs. 1.3.3. In experiments using thick targets, all the reaction products are stopped in the target, which is suitable for the isomer and prompt γ-ray spectroscopy [20] with large γ arrays (as for instance GAMMASPHERE [21]).

Another experimental approach is a fragmentation of projectile, very often ^{238}U, at the relativistic energies [22, 23]. Fragmentation techniques take advantage of the long-lived high-spin states populated in the reaction. Identified and selected inside the magnetic separator, fragments are stopped in the sufficiently thick target. The imperative are high-resolution and high-efficiency separators, such as the Fragment Separator (FRS [24])

---

[2] PRISMA is presented in Subs. 7.3 and refs. therein.

in GSI. This technique is successfully applied in the γ-ray spectroscopy studies (see Subs. 1.2.2), although limited to the isomers and β decays.

1.2.1 Heavy-partner cross sections

The advent of the large acceptance magnetic spectrometers has made it possible to directly identify the multinucleon transfer reaction products up to the masses of $A \sim$100-130. For example, the ions entering PRISMA are identified in Z, A and the charge state q via an event-by-event reconstruction of the trajectory inside the magnetic elements. Large solid angle (80 msr) and momentum acceptance ($\pm$10%) ensure the high-detection efficiency and sufficient sensitivity even for the weaker transfer channels.

A high-resolution measurement of the production of neutron-rich isotopes of $N = 126$ (and larger) was recently performed at GANIL [25]. The measurement used ^{136}Xe beam ($N/Z = 1.51$) onto a ^{198}Pt target at $E_{\mathrm{LAB}} = 7.98$ MeV·A. The Xe-like fragments were measured inside the magnetic spectrometer VAMOS++ [26, 27]. The γ rays associated with both the Xe-like and Pt-like fragments were measured by the γ-array EXOGAM [28]. The production of the Pt-like ions around the $N = 126$ shell closure was obtained from the complex iterative procedure. This procedure used the γ rays of the Pt-like fragments as well as the energies and the angles of the Xe-like fragments. Their main result is plotted in Fig. 1.2, in comparison with the result obtained from the fragmentation. This fragmentation experiment was measured at GSI, with 1 GeV·A ^{208}Pb beam onto a Be target [29]. Looking at the figure one observes that, for example, the cross sections from the ^{136}Xe+^{198}Pt experiment are large in the neutron-rich nuclei with Z$\leq$78.

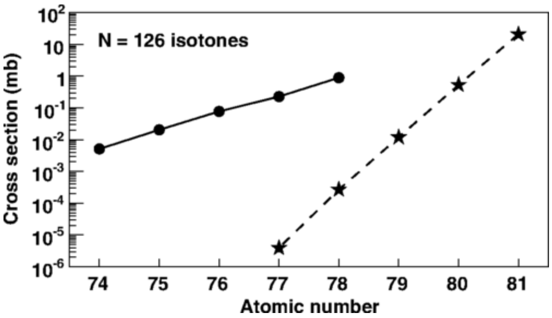

Figure 1.2: Experimentally deduced cross sections for the production of the $N = 126$ isotones as a function of Z. The circles are from MNT [25], while the stars are from fragmentation reactions [29].

To understand and quantify the production process for the heavy partner of the reaction, a simultaneous detection of both the light and the heavy fragment was performed in the ^{197}Au+^{130}Te experiment [6, 30]. The inverse kinematic of this experiment provided sufficient energies and forward-focused angular distributions for the successful detection of the fragments. The Te-like fragments were detected inside the PRISMA spectrometer, and the Au-like fragments inside the NOSE detector. NOSE [31] was specifically built for the coincident heavy partner detection, and consisted of multi-wire parallel-plate avalanche counter and Bragg ionization chamber.

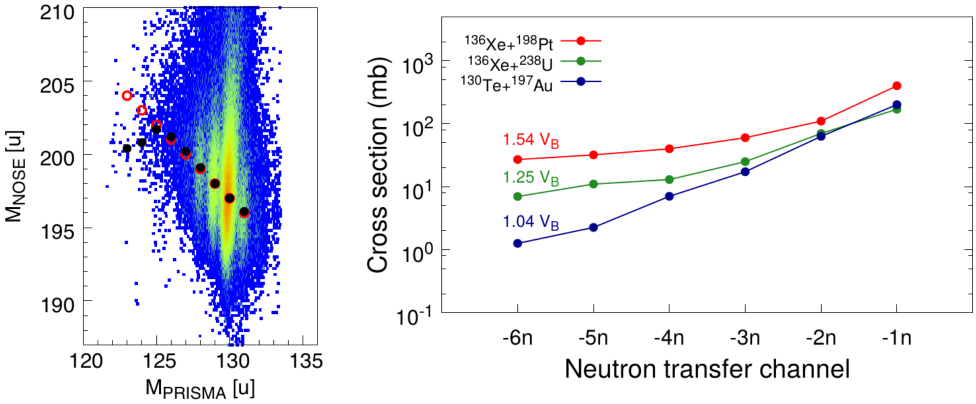

Figure 1.3: Left: Mass-mass correlation matrix of Te isotopes detected in PRISMA and the heavy partner detected in coincident NOSE detector. From Ref. [6]. Right: experimental total cross sections for neutron stripping channels and different reactions; ^{197}Au+^{130}Te [6], ^{136}Xe+ ^{198}Pt [25], and ^{136}Xe+^{238}U [32] mesaured at the indicated energies (given relatively to the barrier V_{B}). The lines are to guide the eye. From Ref. [30].

With this set-up it was possible to select true binary events and uniquely associate the Au-like fragments in NOSE detector with the Te-like ones in PRISMA. The obtained mass-mass correlation matrix for the neutron transfer channels is plotted in the left panel of Fig. 1.3. Notice that the yields measured in neutron-stripping channels correspond to the population of the neutron-rich Au isotopes. Due to the high-resolution of the mass identification for the light fragment and coincidence with the PRISMA spectrometer, the mass distributions of the Au-like events separate in well-defined bands. To discuss their behaviour, the centroids of the projections of each band were labeled with black circles. One observes how they slightly bend towards the lower masses, with respect to those expected for the corresponding primary neutron transfer channels and labeled with red circles. This indicates that the primary fragments, acquiring significant excitation energy, undergo secondary processes which clearly influence the final yield in the neutron-rich isotopes. In MNT large amount of energy is exchanged between the projectile and the target. Part of it is being dissipated by the evaporation of neutrons.

The effect of the evaporation depends strongly on the bombarding energy and the projectile and target combinations. This is illustrated in the right panel of Fig. 1.3, presenting the experimental total cross sections for neutron stripping channels from several reactions. These are ^{197}Au+^{130}Te [6], ^{136}Xe+^{198}Pt [25], and the ^{136}Xe+^{238}U [32] reaction, at energies $E_{\mathrm{LAB}} = 5.4$, 7.98, 7.35 MeV·A, respectively. One can see that the cross sections for the ^{197}Au+^{130}Te system drop off quite regularly, while those of the other two systems tend to flatten out after the transfer of few neutrons. The different behaviour is likely due to the larger energy losses, in turn leading to the larger effect of neutron evaporation in the ^{136}Xe+^{198}Pt, ^{238}U systems. Indeed the bombarding energy in the ^{197}Au+^{130}Te case is much closer to the Coulomb barrier (V_{B} label in the figure). This results in the lower transfer cross sections but, at the same time, the lower contribution of secondary processes. If this is true also for the heavy partner, the choice of bombarding energy seems to be quite important for the production of the neutron-rich heavy nuclei with high survival probability.

1.2.2 Studies in the $Z \sim 82$ and $N \sim 126$ region

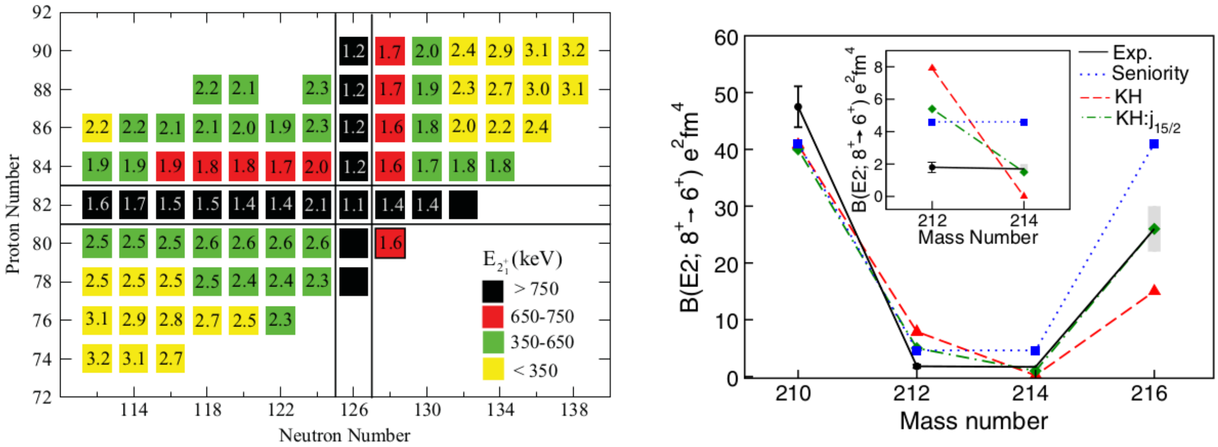

Figure 1.4: Left: Systematics of the $E_{ex}(2^+)$ energies and $E_{ex}(4^+)/E_{ex}(2^+)$ energy ratios for even-even nuclei around ^{208}Pb. From Ref. [33]. Right: Measured $B(E2)$ values for the isomeric states (black line), compared with the shell-model calculations in the neutron space beyond ^{208}Pb. For more details see Ref. [34].

An extensive γ-ray spectroscopy studies of ^{209}Pb and ^{210}Pb were recently obtained in the MNT reactions with stable beams [35, 36]. The ^{209,210}Pb were populated by the stable ^{136}Xe and ^{208}Pb beams (at $E_{\mathrm{LAB}} \approx$ 6-7 MeV·A), and a ^{208}Pb target of thickness sufficient to stop them. The identification of the isotopes and the newly observed states were achieved by measuring the multifold γ-γ coincidences with large γ arrays. These results are also of great importance for our work, and we will use them as a reference in Chap. 5, devoted to the study of excited states in the isotopes of lead.

In the meantime, the experiments employing the fragmentation of ^{238}U and highly-efficient large γ arrays enriched the spectroscopic data in the $Z \sim 82$ and $N \sim 126$ region. For example, in the work of Ref. [33] the excitation energy ratio $E_{ex}(4^+/2^+)$ in ^{210}Hg was extracted and compared with the other. This comparison is shown in the left panel of Fig. 1.4, illustrating the necessity to extend the studies in the direction south-east from the magic numbers $Z = 82$, $N = 126$.

The known region of the neutron-rich isotopes of lead is extended up to ^{216}Pb nowadays, thanks to the recent experiment employing the FRS-RISING setup at GSI [34]. The FRS separator was set-up for the $^{212-216}$Pb, and in these isotopes the population of $\nu g_{9/2}$ seniority isomers was observed. The extracted $B(E2 : 8^+ \rightarrow 6^+)$ reduced transition probabilities are shown in the right panel of Fig. 1.4. Results are compared to the shell-model calculations which use the Kuo-Herling interaction [37, 38] in the neutron space beyond ^{208}Pb. Without going into details, one observes the quantitative discrepancies of model and data for more neutron-rich isotopes, $^{212-216}$Pb. One notices that the commonly used interactions which successfully reproduce many other data sets need improvements (in this case considering the treatment of many-body terms in particular) when approaching the heavy neutron-rich nuclei.

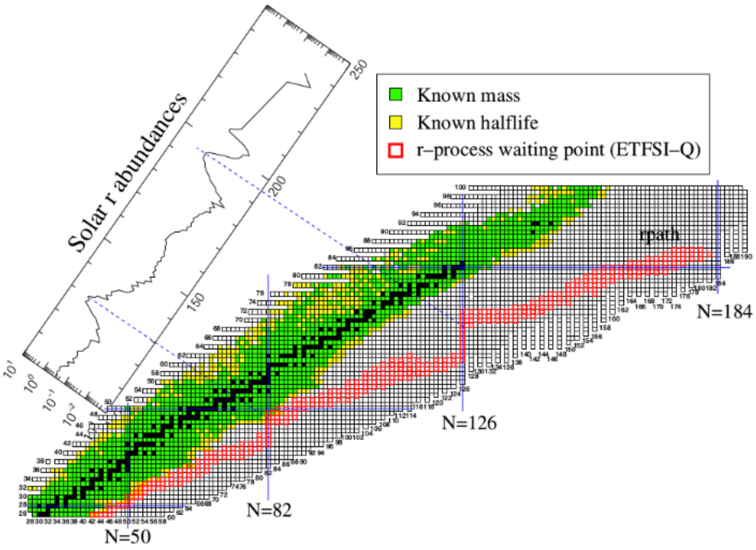

Figure 1.5: Illustration of r-process paths (red squares) and the observed r-process abundances (inset). Blue solid lines indicate proton and neutron magic numbers. From Ref. [39].

The neutron-rich heavy region in the vicinity of $N = 126$ is essential for the understanding of r-process [39, 40], which is thought to be responsible for the creation of about half of the nuclei in nature beyond Fe. The recent observation of a neutron-star merger GW170817 [41] (a possible location for the r-process) placed the question of the nucleosynthesis of heavy elements in the focus of the nuclear physics community. The r-process paths are illustrated in the chart of nuclides in Fig. 1.5, and one can notice that masses and half lives of neutron-rich nuclei (in theory produced in r-process) are generally unknown. The crossing of the r-process path with the neutron magic numbers is observed as the maxima at $A \simeq 130$ and 195 in the abundance distribution shown in the inset.

Discovering the unknown regions of the chart of nuclides remains of fundamental importance. New information will help to elucidate the properties of nuclei with an extreme N/Z ratio, infer the evolution of the (effective) nucleon-nucleon interaction in the presence of large neutron excess, and to answer the questions of the limits of nuclear existence [42].

1.3 Multinucleon transfer reactions

Examples of the multinucleon transfer experimental cross sections are plotted in Fig. 1.6. These cross sections were obtained using the ^{58}Ni, ^{40}Ca and ^{40}Ar beams and the ^{208}Pb target [10–12], at the energies in the vicinity of the Coulomb barrier. The most intense Z and N in each matrix represent the inclusive elastic plus the inelastic channel. One notices differences between these three distributions. How the cross section is distributed depends strongly on the characteristics of the light reaction partner. In general, the transfer processes are governed by the nuclear form factors and optimum Q-value considerations (both disscused in Sec. 1.3.2). Due to the characteristic behaviour of the binding energy through the nuclear chart, the lighter partner of the reaction governs transfer processes.

Typically, the use of the lighter stable projectiles and heavy targets results in the population of only proton stripping and neutron pick-up channels. This corresponds to the Z-N distributions as obtained with the neutron-poor ^{58}Ni ($N/Z = 1.07$), and ^{40}Ca ($N/Z = 1$) beams, and leads to the population of the moderately neutron-rich projectile-like nuclei. We illustrated the direction of such population pattern with green arrows in the chart of nuclides in Fig. 1.7. One observes that for target-like nuclei, this leads

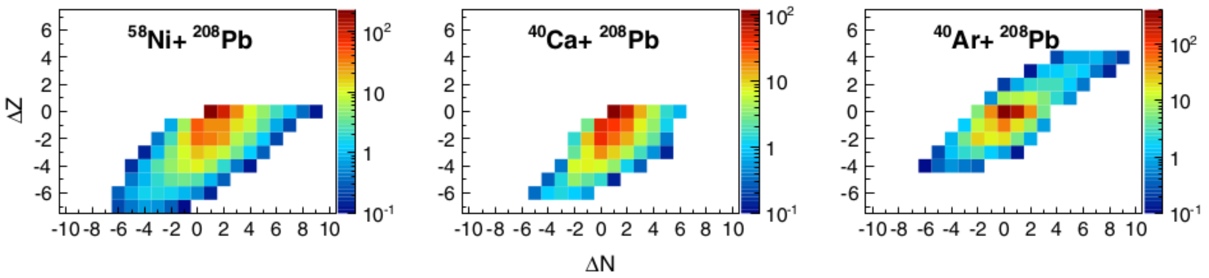

Figure 1.6: Angle and energy integrated total cross section for ^{58}Ni, ^{40}Ca and ^{40}Ar on the ^{208}Pb target, at energies E_{LAB} = 6, 6.2, and 6.4 MeV·A, respectively. The cross section values of the elastic (+inelastic) channel, with ΔN and ΔZ = 0, are scaled down by a factor 100 to better display the behavior of the transfer channels. From Ref. [12].

towards the neutron-poor region, left from the valley of stability.

On the other hand, using the more neutron-rich, yet still stable projectile, ^{40}Ar (N/Z = 1.22), it becomes evident that the proton pick-up and neutron stripping channels have opened up. This leads to the population of the target-like nuclei right from the valley of stability (pink arrows in Fig. 1.7), towards the neutron-rich heavy nuclei.

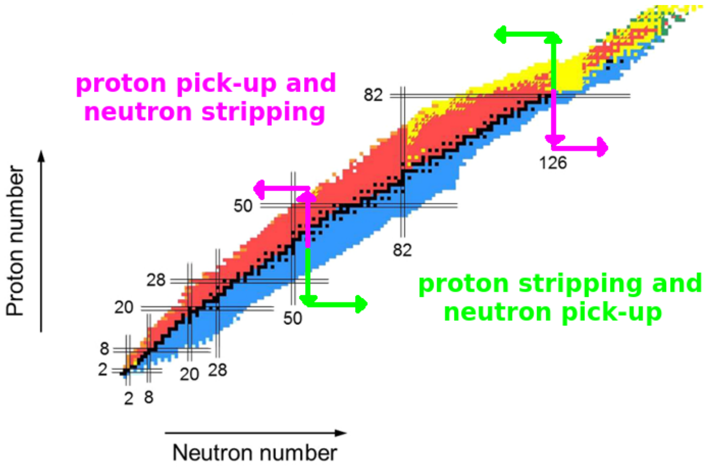

Figure 1.7: Chart of nuclides. Proton stripping and neutron pick-up are the dominant channels in reactions involving stable projectiles, populating the chart in direction indicated with green arrows. With neutron-rich projectiles, neutron stripping and proton pick-up channels open up, populating the chart in direction indicated with pink arrows.

Looking at the ^{40}Ar+^{208}Pb case in particular, it is evident that the proton pick-up channels still have lower cross sections than the stripping ones, although the distribution tends to be rather symmetric. A definite dominance of the proton pick-up and neutron stripping channels in the distribution of the transfer flux is predicted to occur with the use of the projectiles further away from the stability [13]. In Fig. 1.8 the contours of cross section calculated by the semi-classical model GRAZING for Xe+^{208}Pb reactions at $E_{\mathrm{CM}} = 700$ MeV are presented. Going from the neutron poor ($A = 118$), towards the neutron-rich ($A = 154$)[3] isotopes, proton pick-up and neutron stripping paths become the favoured ones. This behaviour is predicted for many more combinations of medium-heavy and heavy targets.

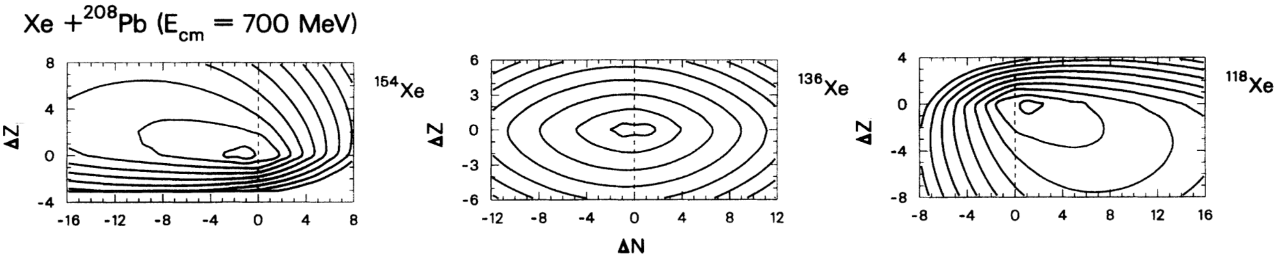

Figure 1.8: Contours of Xe+^{208}Pb ($E_{CM} = 700$ MeV) cross sections as a function of ΔN and ΔZ of projectile, calculated by the model GRAZING. Isotope of Xe is indicated in the spectra. From Ref. [13].

GRAZING model will be explained in details in Subs. 1.3.2. One can mention that other models have been recently employed to calculate multinucleon transfer cross sections, based on Langevin-type dynamical equations of motion [8, 43] and on a fully microscopic framework of the time-dependent Hartree-Fock theory [9, 44, 45]. These models reach similar conclusions for the production of heavy neutron-rich nuclei.

1.3.1 Main characteristics of transfer reactions

The evaporation processes (particularly discussed in a context of Fig. 1.3), which influence the production of neutron-rich heavy nuclei, are closely associated with the large energy losses. One can learn about the particular aspects of reaction mechanism, responsible for the production of the specific primary and secondary fragments, from the behaviour of the Total Kinetic Energy Loss (TKEL) distribution. In Fig. 1.9 we plotted mass distributions and TKEL spectra measured in the ^{90}Zr+^{208}Pb reaction [46, 47] with a magnetic spectrometer PRISMA. From this figure, one can follow the evolution of the TKEL spectra with respect to the number of transferred nucleons. The TKEL spectrum associated to ^{90}Zr corresponds to the elastic and inelastic scattering, and is located in a relatively narrow range around $Q = 0$. For instance, as the number of transferred protons

---

[3] ^{154}Xe beam is extremely neutron-rich and far from being available.

grow, both the centroids of the distributions shift and their tails increase towards the larger energy losses. In the single proton transfer channel, in particular, one can also notice the difference between the $(-1p+1n)$ and the $(-1p-1n)$ TKEL spectrum. This can be understood from the optimum Q-value considerations that favour the population of $(-1p+1n)$ channel, which is therefore mainly directly populated, unlike the $(-1p-1n)$. Especially with the increasing number of transferred protons, the spectra becomes Gaussian-like.

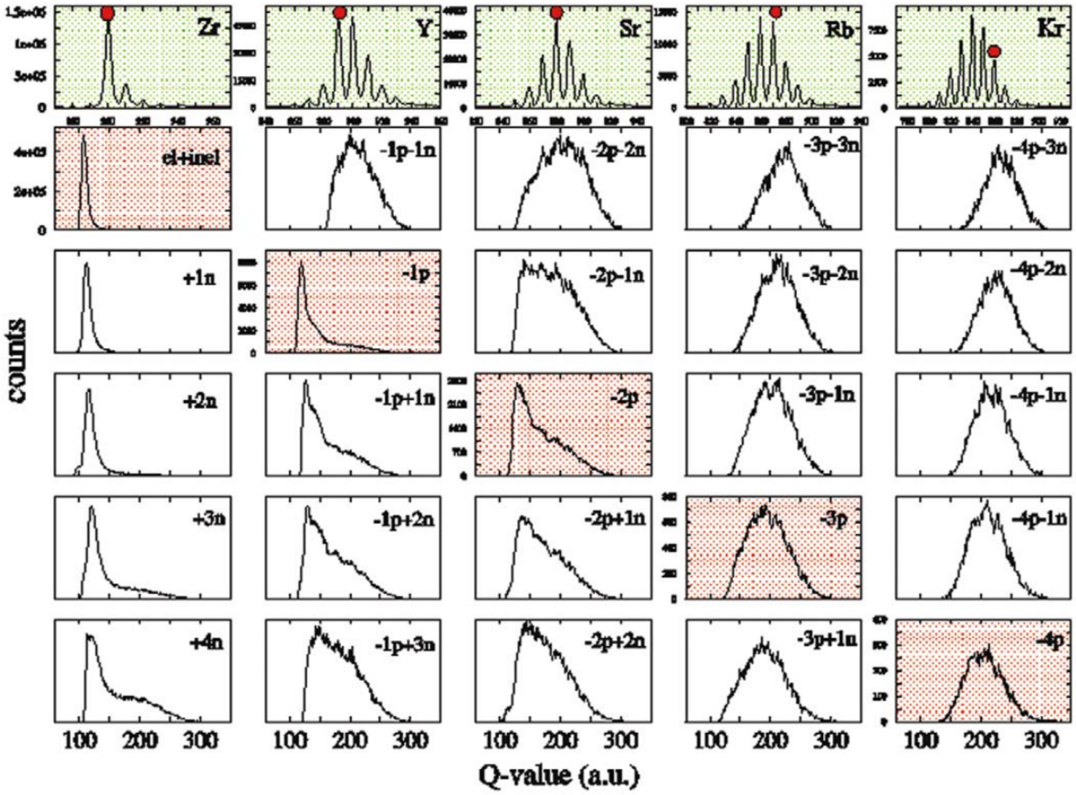

Figure 1.9: The ^{90}Zr+^{208}Pb (E_{LAB} = 6.2 MeV·A) Total Kinetic Energy Loss spectra for the indicated MNT channels. The mass distributions associated with the different nuclear charges are shown in the top row (yellow-coloured), with the labels pointing to the pure proton transfer channels (red-coloured TKEL). The centroid of the elastic + inelastic channel corresponds to Q = 0, shifted by 100 MeV. The scale of the Q-value axis is 1 MeV/channel. From Ref. [48].

One of the possible use of the TKEL information in fragment-γ coincidence measurement is the separation of the elastic from the inelastic scattering, or the selection of the particular excitation energy region. In this same ^{90}Zr+^{208}Pb experiment [46–48], PRISMA was coupled to the large γ-array CLARA [49]. TKEL distributions of ^{90}Zr are again presented (the left panel of Fig. 1.10), but this time with the specific gates on the fragment-γ coincidence. Distributions were extracted without coincidence with γ rays (dotted histograms), and with at least one γ-ray in coincidence (full histograms). The normalization was performed in the large TKEL (tail) region. Subtracting those two, one obtains the contribution of pure elastic scattering (blue histograms). Elastic scattering distribution is narrow and focused around TKEL ∼0 MeV. Employing the large angular acceptance of PRISMA, the angular distribution of elastic scattering was constructed, and compared to Rutherford. The results are shown in the right panel of the same figure. The experimental distribution and the GRAZING calculated one agree well. In particular, the absorption region (at large θ_{LAB}) is very well reproduced.

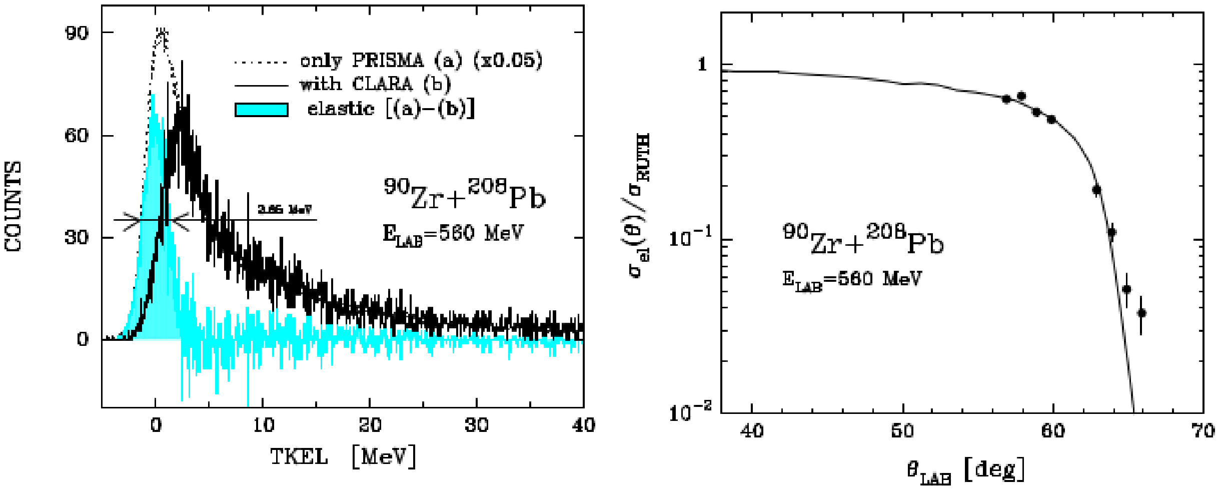

Figure 1.10: Experimental results from ^{90}Zr+^{208}Pb reaction (E_{LAB} = 6.2 MeV·A), obtained with PRISMA coupled to CLARA. Left: total kinetic energy loss distributions (TKEL) for ^{90}Zr. Distributions were extracted without coincidence with γ rays (dotted line), and with at least one γ-ray in coincidence (full line), and by subtracting those two (blue line). Right: experimental (points) and GRAZING calculated (curve) differential cross section for elastic over Rutherford scattering. From Ref. [46].

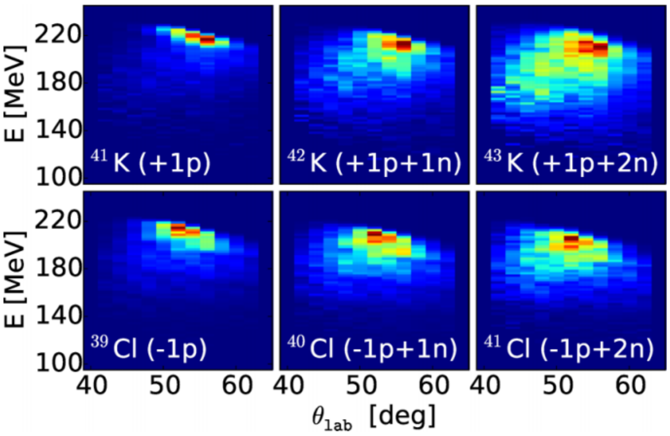

Figure 1.11: Wilczyński plots, kinetic energy E in the laboratory system vs. θ_{LAB}, for selected channels in the ^{40}Ar+^{208}Pb reaction (at E_{LAB} = 6.4 MeV·A). From Ref. [12].

From the measured energies and scattering angles one can construct an $E - \theta_{\mathrm{LAB}}$

matrix, also known as a Wilczyński plot [50], which is a good illustration of the energy loss behaviour. Figure 1.11 represents Wilczyński plots of few nucleon transfer channels in ^{40}Ar+^{208}Pb [12] experiment. For one-nucleon transfer channels the main strength is in a narrow region close to the largest kinetic energy (and smallest TKEL). For transfers of more nucleons, one sees a widening of the kinetic energy distributions towards the larger TKEL, here especially at more forward angles.

The characteristics of the reaction mechanism can be studied from the extraction of differential cross sections. In Fig. 1.12 we show the Q-value integrated angular distributions from the ^{64}Ni+^{238}U experiment [51], and for the indicated transfer channels. For few nucleon transfers one observes the bell-shaped distributions peaked at the grazing angle, a signature of direct processes. At the more backward angle the cross section decreases due to the effect of absorption. At the more forward angles the angular distribution may increase, due to the onset of deep-inelastic processes. One notices that as the number of transferred nucleons increases the distributions become broader.

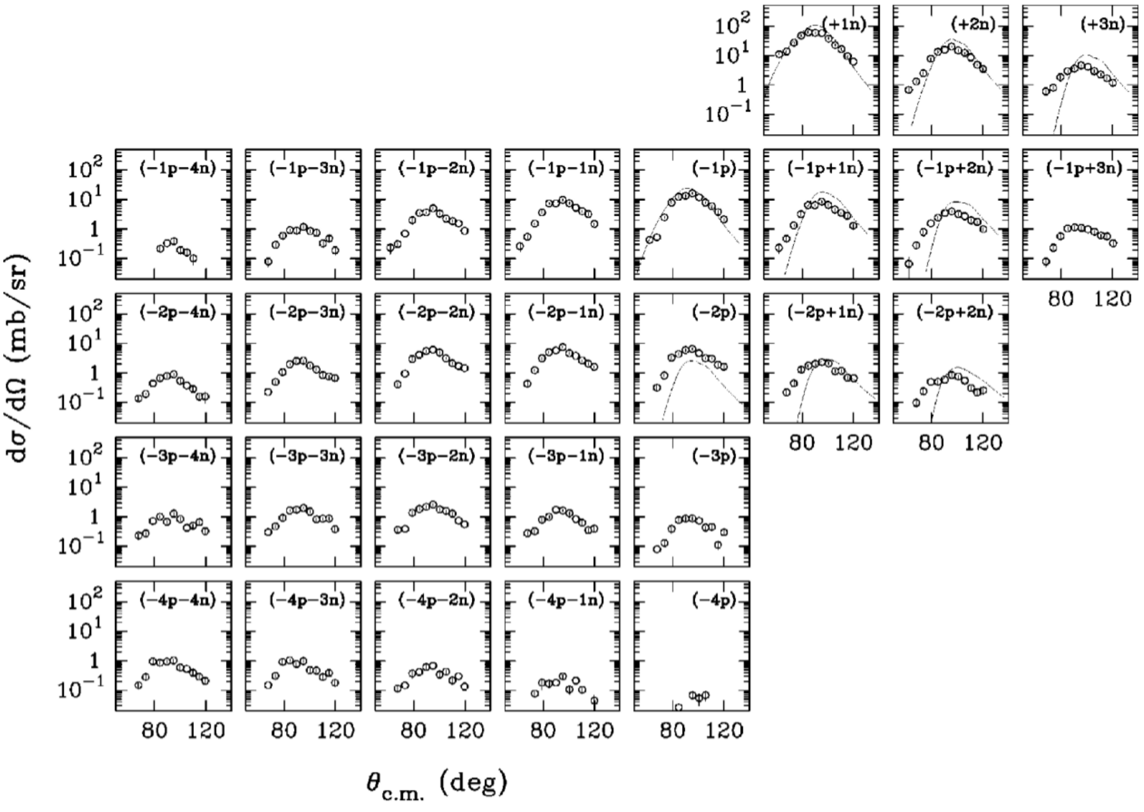

Figure 1.12: The ^{64}Ni+^{238}U experimental (points) and calculated (lines) Q-value integrated angular distributions for the indicated transfer channels. Lines are GRAZING calculations. From Ref. [51].

Through the examples presented above, we've shown how the multinucleon transfer reaction mechanism evolves from the quasielastic towards the deep-inelastic processes. Such evolution is accompanied by the increasing number of transferred nucleons, the tails towards the large energy losses in TKEL distributions, the widening of the angular distributions (and disappearance of the characteristic bell shapes), and so on. These phenomena are also correlated with the increasing strength of the competitive secondary processes (neutron evaporation and fission), which obviously influence the final yields in the multinucleon transfer reactions.

When two heavy ions collide at the energy above the Coulomb barrier various outcomes are possible, as schematically illustrated in Fig. 1.13 (and with respect to the impact parameter).

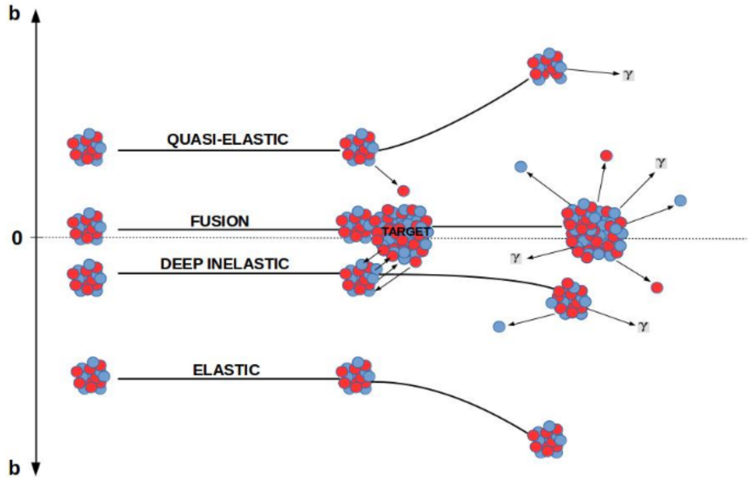

Figure 1.13: Illustration of the heavy-ion reactions (in vicinity of the Coulomb barrier), considering the impact parameter b.

1.3.2 Theoretical approach to transfer reactions

Let us consider a binary reaction a+A → c+C → b+B, where the $\alpha = (a,\, A)$ is the entrance, $\gamma = (c,\, C)$ intermediate, and $\beta = (b,\, B)$ exit channel mass partition. The effective interaction potential U_{eff} of two colliding nuclei in a head-on collision ($l = 0$) consists of Coulomb repulsion and a short range nuclear attractive potential. At interaction radius r one has for the Coulomb part

$$U^{C}_{aA}(r) = \frac{Z_a Z_A e^2}{r}. \tag{1.1}$$

For the nuclear part, one can use the Akyüz-Winther parametrization that describes very well the elastic scattering for the many different projectile and target combinations. It follows

$$U_{aA}^{N}(r) = \frac{-V_0}{1+e^{(r-R_a-R_A)/a}} \tag{1.2}$$

where the V_0 is potential depth, a diffusion parameter and $R_i = (1.2A_i^{1/3} - 0.09)$ nuclear radii. The U_{eff} potential ($l = 0$) is presented in Fig. 1.14 for the several projectiles (^{16}O,...^{208}Pb) and ^{208}Pb target. In the case of the ^{40}Ca+^{208}Pb system the height E_{B} of the Coulomb barrier is labeled as well (at corresponding r_{B}). One observes that the height of the Coulomb barrier increases with the Z_aZ_A product, while at the same time the potential pocket gets smaller. For the very large Z_aZ_A the maximum attractive force cannot compensate for the strong Coulomb repulsion and the Coulomb barrier vanishes.

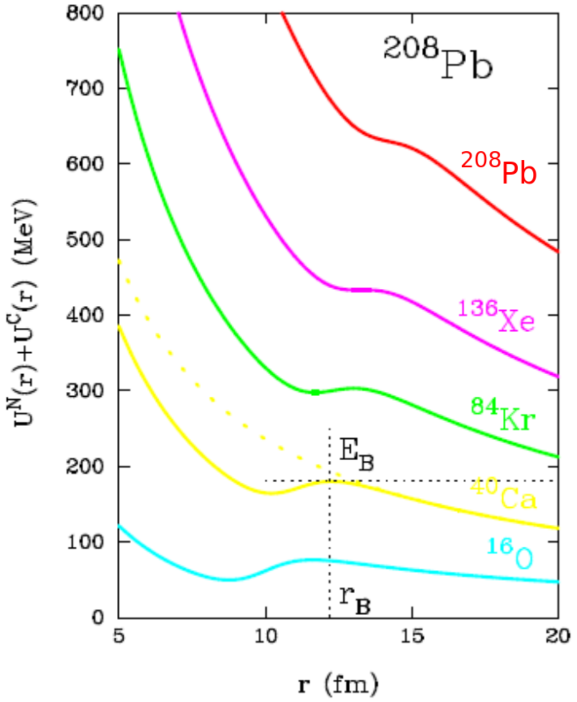

Figure 1.14: Effective interaction potential (Coulomb and nuclear) in a head-on collision ($l = 0$). Stable projectiles, as given in the inset, have a common ^{208}Pb target. The height of nominal Coulomb barrier E_{B} at r_{B} is labeled for the ^{40}Ca+^{208}Pb system.

The angular momentum dependence of the effective interaction U_{eff} is included with the centrifugal potential

$$U_{aA}^{l}(l,r) = \frac{\hbar^2 \ell(\ell+1)}{2m_{aA}r^2} \tag{1.3}$$

where the m_{aA} is reduced mass. One can distinguish the two regions, one dominated by the Coulomb repulsion and the other by the nuclear interaction defining the grazing angular momentum momentum l_g and radius r_g as

$$U_{eff}(l,r) = E_{\mathrm{CM}} \tag{1.4}$$

$$\frac{d}{dr}U_{eff}(l,r) = 0 \tag{1.5}$$

where the E_{CM} is system energy in the centre of mass. The angular momentum in vicinity of l_g mostly contributes to the quasielastic scattering. In experiments, the quasielastic yields are observed at grazing angle. Increasing the angular momentum l, barrier also increases and for some critical value l_c, vanishes.

Form factors and optimum Q-value

The coupled channel formalism is at the basis of the description of any direct reaction process [52]. A method to treat the coupled equations is obtained by generalizing the semi-classical theory of Coulomb excitation in order to include the nuclear interaction [3, 53]. In this approximation the relative motion is treated classically [4] while inelastic excitations and transfers are treated in a microscopic way.

The coupled-channel formalism introduces the total wavefunction ansatz (expansion in terms of ψ_β channel wavefunctions)

$$\Psi(t) = \sum_\beta c_\beta(t)\psi_\beta e^{\frac{-i\left(E_\beta t+\delta_\beta(t)\right)}{\hbar}} \tag{1.6}$$

where the coefficients $c_\beta(t)$ define the amplitude to be in channel β, and δ_β time-dependent phase. The evolution of the process is obtained by solving the time-dependent Schrödinger equation, leading to the system of coupled equations

$$\frac{\mathrm{d}}{\mathrm{d}t}c_\beta(t) = \frac{\mathrm{i}}{h}\sum_\gamma \left\langle \omega_\beta \left| (V_\gamma - U_\gamma) \right| \psi_\gamma \right\rangle c_\gamma(t)\mathrm{e}^{-\mathrm{i}\left[\left(E_\gamma - E_\beta\right)t - \left(\delta_\gamma(t) - \delta_\beta(t)\right)\right]/\hbar} \tag{1.7}$$

where U is the nuclear potential and V is the coupling interaction. It is solved using the conditions that at $t = -\infty$ system is in its entrance channel α, i.e. $c_\beta(-\infty) = \delta_{\alpha\beta}$. The ω_β wavefunctions derive from the introduction of dual-base, in order to overcome the non-orthogonallity of ψ_β.

---

[4] Since in direct reactions the wavelength associated to the relative motion is considered much smaller than the interaction region.

The matrix elements of Eq. 1.7 are non-local functions of the center-of-mass coordinates of the two channels, $\vec{r} = \frac{1}{2}\left(\vec{r}_\beta + \vec{r}_\gamma\right)$. The non-locality translates into a dependence on the momentum transfer, $\vec{\kappa}$, or so-called recoil effect. These elements are called form factors

$$\left\langle \omega_\beta \left| (V_\gamma - U_\gamma) \right| \psi_\gamma \right\rangle = f_{\beta\gamma}(\vec{\kappa}, \vec{r}) \tag{1.8}$$

and reflect the nuclear structure properties of the ions in collision. The transversal component of the $\vec{\kappa}$ dependence may be taken into account through a phase factor

$$f_{\beta\gamma}(\vec{\kappa}, \vec{r}) \sim \mathrm{e}^{\mathrm{i}\sigma_{\beta\gamma} t} f_{\beta\gamma}(0, \vec{r}) \tag{1.9}$$

where

$$\sigma_{\beta\gamma} \sim \frac{1}{\hbar} \frac{m_d}{m_b + m_B} \dot{r}(t) \left(R_B m_c - R_b m_C \right) \tag{1.10}$$

contains the mass of the transferred particle m_d, and the radial velocity $\dot{r}(t)$.

At large distances, for the particle transfer form factor one can use the following asymptotic behaviour

$$f_{\beta\gamma}(r) \sim \frac{1}{\kappa_{a_1'} r} e^{-\kappa_{a_1'} r} \tag{1.11}$$

governed by the coefficient $\kappa_{a_1'}$ that contains the binding energy of the single-particle state a_1' entering in the transition. For single-particle states close to the Fermi energy the decay length of the one particle transfer form factor is of the order of 1.2 fm, thus at large distances the transfer form factor prevails over the nuclear component of the inelastic form factor. In the case of inelastic excitation, one can express the radial part of the form factor using the macroscopic approximation. Such form factor is the r-derivative of the average nuclear potential of entrance and exit channels

$$f_\lambda = \beta_\lambda \frac{\partial U(r)}{\partial r}, \tag{1.12}$$

which reflects the collectivity of the state via β_λ deformation parameter[5]. Those are deduced from the experimental reduced transition probabilities, $B(E\lambda)$.

One is interested in estimating the magnitude of a given transfer process, and for this is not necessary to solve explicitly a full system of coupled equations but it suffices to use its first-order Born approximation. For a given impact parameter (incoming partial wave

---

[5] λ is here transferred angular momentum

l) the probability for the transition $\alpha \to \beta$ is obtained from

$$P_{\beta\alpha}(\ell) = \left| \frac{\mathrm{i}}{\hbar} \int_{-\infty}^{+\infty} \mathrm{d}t \mathrm{e}^{\mathrm{i}\sigma_{\beta\alpha} t} f_{\beta\alpha}(0, \vec{r}) \mathrm{e}^{\mathrm{i}\left[\left(E_\beta - E_\alpha\right) + \left(\delta_\beta - \delta_\alpha\right) \right] t/\hbar} \right|^2 . \tag{1.13}$$

In the approximation considering the transition as a direct process in which the two nuclei barely overlap one has

$$P_{\beta\alpha} = \sqrt{\frac{1}{16\pi\hbar^2 |\ddot{r}_0| \kappa_{a_1'}}} \left| f_{\beta\alpha}(0, r_0) \right|^2 g\left(Q_{\beta\alpha}\right). \tag{1.14}$$

This $P_{\beta\alpha}$ depends on the radial coordinate, r_0, which is the turning point for the grazing partial wave l_g, known as distance of closest approach. It follows that the $\ddot{r}_0$ is the radial acceleration (at r_0). A rough estimation of the total cross section for a particular transfer channel can be obtained by simply performing a Q-value integration of the transition probability. Transition probability is proportional to the square of the transfer form factor and the adiabatic cut-off function

$$g(Q) = exp\left(-\frac{\left(Q - Q_{opt}\right)^2}{\hbar^2 r_0 \kappa'_{a_1'}} \right) \tag{1.15}$$

which depends on the optimum Q-value of the reaction. The optimum Q-value for the charged particle transfer is both system and energy dependent

$$Q_{opt} = \left(\frac{Z_d}{Z_A} - \frac{Z_d}{Z_b} \right) E_B + \left(\frac{m_d}{m_b} - \frac{m_d}{m_A} \right) (E - E_B) + \frac{m_d \ddot{r}_0}{m_a + m_A} \left(R_A m_b - R_a M_B \right) \tag{1.16}$$

where d labels the transferred particle, and E_B the Coulomb barrier. The latter expression holds in the approximation that the trajectories of the colliding nuclei match smoothly, which means the r_0 remains unchanged before and after transfer process. This is generally true when the number of nucleons transferred is limited to few.

The adiabatic cut-off function $g(Q)$ defines the actual value of the transition probability with maximum at optimum Q-value. As an example, we show in Fig. 1.15 the $g(Q)$ for different transfer channels of the ^{58}Ni+^{208}Pb reaction at 330 MeV. From the behaviour of the $g(Q)$ one can see that in general Q_{opt} ~0 for the neutron transfer channels, while the for the proton transfer channels one has the behaviour as described in Eq. 1.16. The superimposed red lines represent the available states, therefore the overlap between the lines and the $g(Q)$ are open transfer channels. For this particular choice of system and

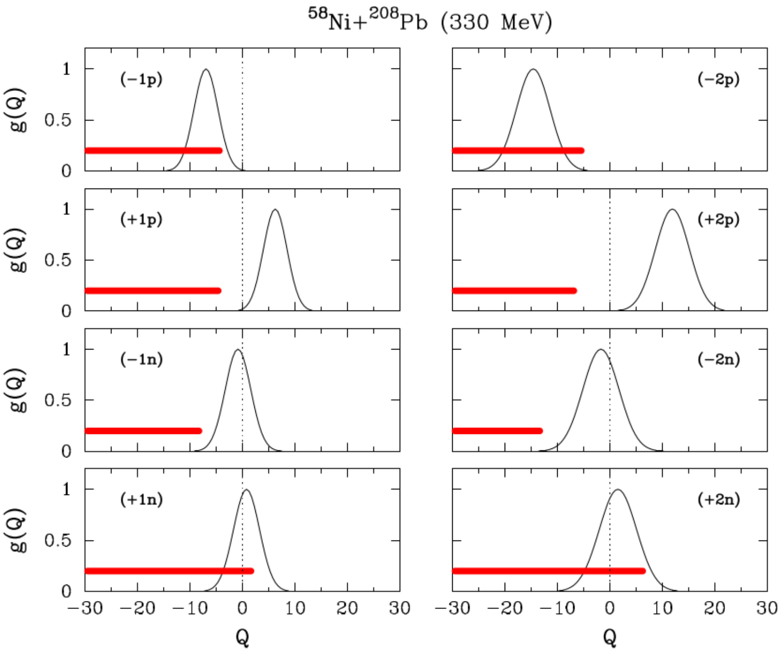

Figure 1.15: Adiabatic cut-off functions for one- and two-neutron and proton transfer channels for the ^{58}Ni+^{208}Pb reaction at 330 MeV. Q value is in MeV. The horizontal lines represent the location of all possible transitions (see text for details). From Ref. [3].

the bombarding energy we see that only the neutron pick-up and proton stripping channels are open. As one could expect, the total cross section obtained in the ^{58}Ni+^{208}Pb experiment (see Fig. 1.16) follows these optimum Q-value considerations.

In general, in transfer processes involving stable projectiles, only proton stripping and neutron pick-up are likely to occur. The reason for this lies in characteristics of reaction Q-values, which balance is mostly controlled by the lighter partner. Since the contours of binding energies in the $N-Z$ plane in the vicinity of the light stable nuclei are roughly symmetric around $N = Z$, it is clear that a cut for a given element (constant Z) yields a steeper energy gain toward the lighter isotopes than toward the heavier, thus favouring the acquisition of neutrons [13]. Using the neutron-rich projectiles (far away from the valley of stability), this population pattern shall eventually turn around, thus favouring the proton pick-up and neutron stripping channels, a direction towards the neutron-rich target-like nuclei.

The GRAZING code

The code GRAZING [54] is based on the semiclassical model of Winther [55, 56], and suited for the description of inelastic scattering, nucleon transfer in grazing collision of heavy ions, fusion and fusion barrier distribution. GRAZING describes quite well few nucleon transfer processes with relatively small kinetic energy losses. In fact, it can predict how the total reaction cross section is shared between the different channels. The model is capable of including also the effect of evaporation, by taking into account the average excitation energies of the binary products. GRAZING has successfully reproduced a wealth of the experimental data, and has found a great application in the both experimental results interpretation and the planning of the experiments.

At the basis of GRAZING is the concept of the elementary modes of excitation and the classical treatment of the relative motion of the two interacting nuclei. The interaction for relative motion is described with Coulomb and nuclear potential, such as the one of Fig. 1.14. Since the wavelength of the centre of mass motion is small compared with the interaction range, the classical trajectories are a valid approach which simplifies the calculations. Nuclei are represented as an ensemble of independent particles that can vibrate around their spherical equilibrium shapes and can exchange nucleons. The exchange of many nucleons proceeds via a multi-step mechanism of single nucleon transfer. The excitation of surface modes is treated with the inelastic form factors and the nucleon transfer with the transfer form factors, as previously stated in formula 1.12 and 1.11, respectively. Different states that participate in the transfer process are not taken explicitly, but described with average single-particle level densities.

Under the assumption that the transfer probability for each transfer channel is small, which is generally true with the heavy ions, GRAZING introduces the probability distribution (rather than obtaining it explicitly within the coupled-channel formalism). Each transition probability is then extracted from the distribution (characteristic function) following classical trajectories constructed in a self-consistent way to be compatible with the different quantities defining the final states.

In Fig. 1.16 we show the comparison of the GRAZING calculated and the experimental total cross sections, for the ^{58}Ni,^{40}Ca,^{40}Ar+^{208}Pb systems. Total (or inclusive) cross sections were obtained by integrating over the whole angular and energy range of a dedicated PISOLO (in the case of ^{58}Ni, ^{40}Ca) and PRISMA (^{40}Ar) spectrometer. We remind that these cross sections were already shown in Z-N panels of Fig. 1.6. A good agreement of the model and experiment is particularly achieved for few nucleon transfers, as it has been shown in many other heavy-ion collisions close to the Coulomb barrier [3].

As more nucleons are transferred, a disagreement of the model and experiment arises, most likely due to the deep-inelastic component which is not fully taken into account. In fact, GRAZING provides only an estimation of the flux that overcomes the Coulomb barrier but is not able to completely follow the evolution of the reaction mechanism toward a more complex regime (eventually leading to the formation of a di-nuclear system or of a compound nucleus). Another feature which cannot be accounted for in the GRAZING calculations are pair transfer modes. For example, it was shown that their addition, which is possible within the CWKB semi-classical calculations, produces a better overall agreement with data in the case of ^{58}Ni+^{208}Pb system (as shown in Fig. 20. of Ref [3]).

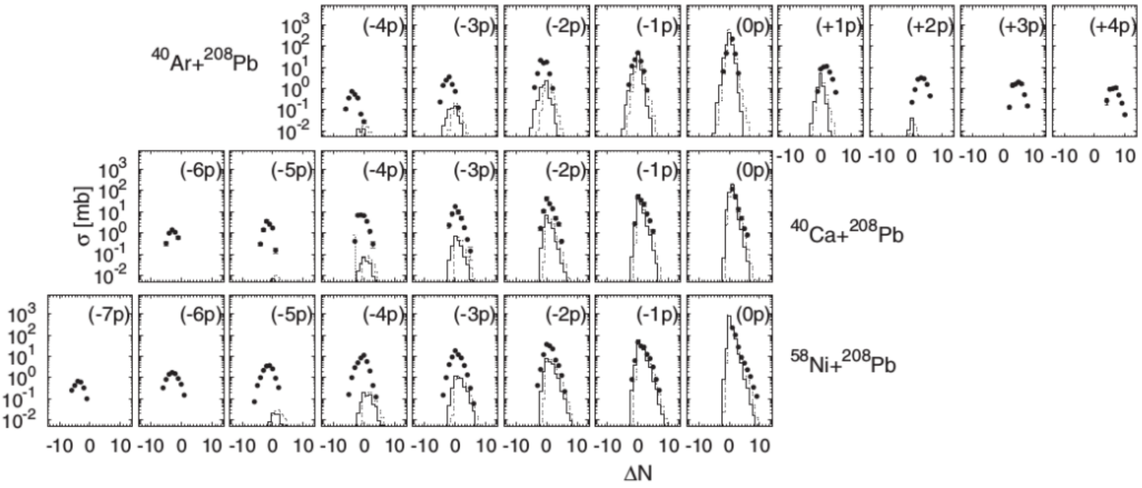

Figure 1.16: Total experimental cross section (points) for the ^{58}Ni, ^{40}Ca, ^{40}Ar+^{208}Pb reactions, compared to the GRAZING calculations not including (dashed) and including (solid line) neutron evaporation.

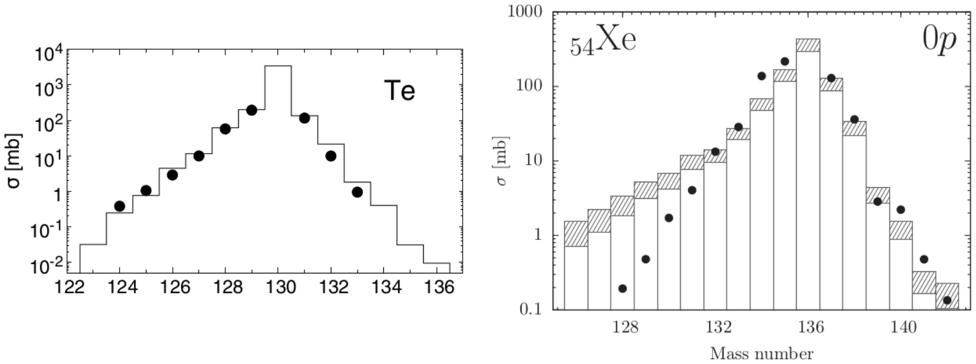

Figure 1.17: Total experimental cross sections in pure neutron-transfer channels obtained with magnetic spectrometer PRISMA. Left: ^{197}Au+^{130}Te experiment (circles) and GRAZING calculations (lines) [6]. Right: ^{136}Xe+^{238}U experiment (lines) and GRAZING (circles) [32].

The experimental yields in neutron-transfer channels for more heavy systems of ^{197}Au+ ^{130}Te (left panel) and ^{136}Xe+^{238}U (right) measured with PRISMA are shown in Fig. 1.17.

One arrives to the similar conclusion, that the channels involving few-neutron transfers are here quite well reproduced in the both pick-up and stripping directions.

1.3.3 The ^{40}Ar,^{90}Zr+^{208}Pb experiments

Multinucleon transfer reactions are widely employed in the spectroscopic studies. Many successful studies are carried out by using the new-generation magnetic spectrometers coupled to the large γ arrays, and measuring the particle-γ coincidences. In such measurements, as in the ones presented in the works of Refs. [16–18, 57–61], the light (medium-heavy) partner is identified inside the spectrometer, and the attribution of the corresponding γ transitions is unambiguously defined. This allows for studies of nuclei moderately far from stability whose structure is poorly or not known at all. At the same time, the heavy (undetected) partner can be identified and studied on the basis of the known (characteristic) γ transitions [19, 62, 63].

The ^{40}Ar+^{208}Pb and ^{90}Zr+^{208}Pb experiments, measured by the PRISMA magnetic spectrometer coupled to the CLARA γ-array [49], provided a rather comprehensive spectroscopic studies of Ar and Zr isotopes [47, 64–66]. Reactions ^{40}Ar+^{208}Pb [12, 67] and ^{90}Zr+^{208}Pb [46, 47] were performed at the energies in the vicinity of the Coulomb barrier, at $E_{\text{LAB}} = 6.4$ MeV·A and $E_{\text{LAB}} = 6.2$ MeV·A, respectively. The projectile-like fragments were identified in PRISMA, and the populated transfer channels were reported earlier in the text. Thus, the obtained mass spectra from the ^{90}Zr+^{208}Pb were plotted in the top-row panel of Fig. 1.9, and the total cross sections from ^{40}Ar+^{208}Pb in the right panel of Fig. 1.6. Employing the highly modular and efficient γ-array CLARA enabled to attribute the γ transitions in coincidence. Their Doppler correction was constructed from the velocity vector, which was measured for the projectile-like fragment and calculated for the target-like one (assuming the binary character of the reaction). Therefore the Doppler corrected γ-ray spectra were attributed to both the projectile-like and the target-like fragments. Generally, in the target-like γ spectra some γ rays arising from the neutron evaporation processes are also observed. The γ spectra of the Pb isotopes deserve a particular attention in this work, so we show them in Appendices A.3 and A.2.

In both experiments, the selectivity of the reaction mechanism towards the specific states was observed. In particular, in $^{89-94}$Zr most of the excited states were of yrast character, and the excitations up to $E_{ex} \approx 7.5$ MeV were observed. In $^{38-43}$Ar isotopes one observed generally the yrast states as well, up to $E_{ex} \approx 4.5$ MeV. In both reactions transfer strength in even-odd isotopes (^{89,91,93}Zr, ^{39,41,43}Ar) was distributed dominantly in the states of single-particle character. Besides, in these isotopes strong excitations of the states which were interpreted with the valence neutron coupled to the vibration quanta were present.

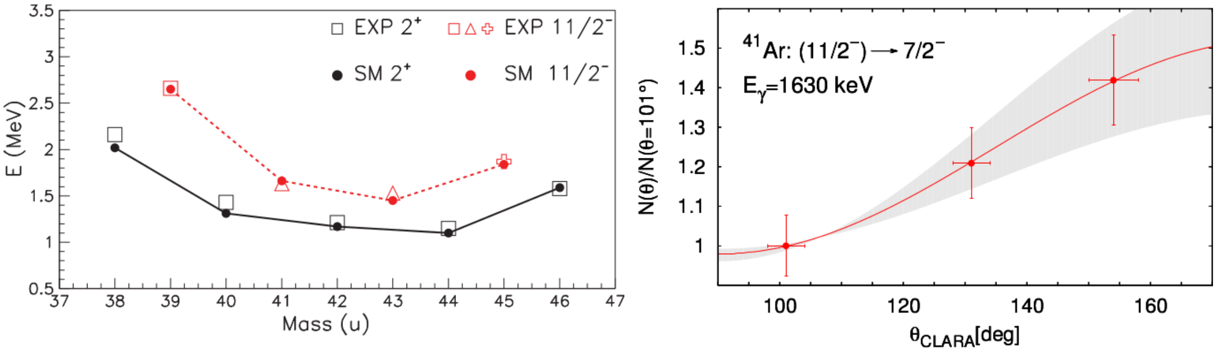

Figure 1.18: Left: energies of the 2^+ and $11/2^-$ states of $N = 20$-28 argon isotopes. The experimental data are compared with shell-model (full circles). From Ref [64]. Right: Angular distribution of the $E_\gamma = 1630$ keV, $11/2^- \rightarrow 7/2^-$, in ^{41}Ar. The result demonstrates the $E2$ character of the transition. From Ref. [65].

In particular, in the ^{40}Ar+^{208}Pb experiment the $11/2^-$ in ^{41,43}Ar was strongly populated. The ground states of ^{41,43}Ar can be described with the unpaired neutron in the first accessible orbit outside the $N = 20$ shell, $f_{7/2}$. Its coupling to the 2^+ state in the neighbouring even-even isotopes ^{40,42}Ar might populate the multiplet of $J^\pi = 11/2^-$, $9/2^-$, $7/2^-$, $5/2^-$, $3/2^-$ states. The preference towards the stretched configuration ($11/2^-$) populates the high-spin states. A phenomenon of the population of states of high spin (and excitation energy) is closely connected with the character of the mechanism, which, at the energies close to the Coulomb barrier tends to maximize the transferred angular momentum [3, 53, 66, 67]. It was observed that the large angular momentum transfer becomes even more pronounced with the increasing number of transferred nucleons.

In the left panel of Fig. 1.18 one can see the comparison of the measured and the shell-model calculated energies of 2^+ and $11/2^-$ states in ^{38,46}Ar ($N = 20$–28). The excitation energies point to the similar evolution of the collectivity, in the even-even and the even-odd isotopes. In the right panel of the same figure we presented the angular distribution of the $11/2^-$ transition towards the $7/2^-$ ground state in ^{41}Ar. Distribution was obtained thanks to the modularity of CLARA array. This distribution demonstrates the $E2$ character of the transition. It was found that it is also quite similar to the angular distribution of the $2^+ \rightarrow 0^+$ $E2$ transition in ^{40}Ar. With these examples, we wanted to illustrate that the properties of the particle-phonon states are expected to be largely determined by the properties of the corresponding phonon states.

In both experiments, newly observed (unknown) γ rays were successfully attributed to the argon and zirconium isotopes. We have shown how the high-degree of alignment can be reached in such experiments, thus enabling to directly measure the angular distributions, and also polarizations, which depend on the multipolarity and the electromagnetic character of the transition. From their measurement, J^π of the state involved (if unknown) can be deduced. We've seen that the whole chain of isotopes can be studied in the same experiment, and relying on the selective nature of the mechanism, the conclusions on the poorly known isotopes (i.e. more neutron-rich) in the chain can be deduced from the comparison to the better known ones.

We will come back to the ^{40}Ar,^{90}Zr+^{208}Pb studies in Chap. 5, dedicated to the spectroscopy of Pb isotopes. These Ar and Zr experiments used the different stable beams at similar energies and the "same" ^{208}Pb target, thus providing a great opportunity to make a comparison with the Rb experiment.

2

The ^{94}Rb+^{208}Pb experiment at HIE-ISOLDE facility

The measurement of transfer reaction with an unstable beam was performed at the recently upgraded High Intensity and Energy (HIE) ISOLDE facility in CERN. The facility is one of the few accelerator centres worldwide which employ Isotope Separation On-line (ISOL) technique for the Radioactive Ion Beams (RIB) production. The neutron-rich ^{94}Rb beam was delivered at 6.2 MeV·A onto the ^{208}Pb target at the high-resolution and high-efficiency MINIBALL station. In this Chapter, the RIB production techniques, focusing on the ISOL at HIE-ISOLDE, and the experimental set-up properties, will be outlined.

2.1 Techniques for the RIB production

The ISOL technique employs the primary proton beam to induce fission, spallation or fragmentation of a thick and heavy primary target. The reaction products are stopped in the target, thermally extracted, ionized, selected and reaccelerated. Produced RIB is transported to the experimental station, or the secondary target chamber and the experimental set-up dedicated to the reaction studies.

Post-acceleration provides the moderate energy RIBs of excellent optical quality. The technique is strongly dependent on the atomic properties and, due to the multi-step production processes, limited to the nuclei with lifetimes of the order of miliseconds. ISOL is nowadays employed in the accelerator facilities of GANIL, TRIUMF, and ISOLDE at CERN. Until very recently the achieved energies of the RIBs were 3 MeV·A. In the heavy-ion collisions at this energies one could perform the Coulomb excitation experiments and study a very few excited states, in general. Opening up the multinucleon transfer channels requires the energies in the vicinity or above the Coulomb barrier for heavy-ion systems, which is of the order of ∼5-10 MeV·A.

Such energies became achievable thanks to the ISOLDE facility upgrade. The upgrade provided the opportunity to measure the multinucleon transfer reaction with the use of ^{94}Rb beam onto a ^{208}Pb target. The achieved ^{94}Rb beam energy was 6.2 MeV·A, and the intensity $\sim 3 \cdot 10^6$ pps. The HIE-ISOLDE facility is nowadays well-suited to provide such high-energy RIBs using the ISOL method. In the following years, the 5-15 MeV·A RIBs are expected within the SPES project of INFN-LNL.

Isotope Separation In Flight is the other RIB production technique, complementary to ISOL. In flight technique is based on the fragmentation of the stable primary ion beam, and fragment separation inside the multi-stage magnetic separator [68]. Following the separation, RIB is stopped at the experimental station. Typical energies of the primary beams (such as ^{238}U) range from hundreds of MeV to few GeV per nucleon. The fragments thus preserve the high velocity, which allows to study even the nuclei with lifetimes shorter than 1 µs. However, the short-lived states of produced RIB cannot be measured directly, since they have to be populated by the higher in energy isomeric state. Since no reacceleration is needed, the production is independent of the atomic properties, on the contrary to the ISOL technique. On the other hand, the selection of the fragmentation product requires large angular and momentum acceptance separators with the extraordinary transmission efficiency and selectivity.

The technique is currently implemented in GANIL, NSCL, RIKEN and GSI. An exemplary case of the state-of-art separator is BigRips in RIKEN [69] with superconducting magnets, which can select the species of the production cross sections lower than 1 pb. Increased primary ion beam intensities and the separation efficiency is expected in near future from the FAIR project at GSI.

2.2 The HIE-ISOLDE facility

ISOLDE pioneered the RIB production, delivering the first beam in 1967, and is the oldest accelerator complex still in operation at CERN. Nowadays, it is capable of producing up to the 1300 RIBs of more than 70 elements. Very recently, in 2018, the facility was upgraded with the major aim to reach the 10 MeV·A for $A/q = 4$. This was obtained with the installation of additional superconducting cryomodules to the existing linac, and called HIE-ISOLDE [70, 71].

2.2.1 Radioactive ion beam production

The primary pulsed proton beam of 1.4 GeV and maximum current of 2 µA is produced by the Proton Synchrotron Booster, a pre-accelerator of the Large Hadron Collider. The most frequently used RIB production target is the uranium carbide ($\mathrm{UC_x}$). One usually exploits the proton-to-neutron converter target system configuration to optimize the production of the neutron-rich fission fragments [72]. Large target thickness (39 g/cm^2) stops the reaction products, which, exposed to the 2200°C, thermally diffuse out of it through a transfer line coupled to the ion source.

ISOLDE implements three types of ion sources, namely electron plasma, laser and surface ion source. The latest is particularly effective in ionisation of the isotopes with a low ionisation potential, retaining high selectivity. For example, the ionisation potential of Rb is only 4.12 eV, which makes it easy to strip an electron using the heated metal (W) surface [73]. Singly-charged ions are extracted with the anode at the ion source, and injected in the General Purpose Separator (GPS) with energies of 30-60 keV.

The GPS contains a system of multiple electrostatic quadrupoles and the analysing magnet with a bending radius of 1.5 m and a bending angle of 70°, with the mass resolving power of $A/\Delta A \sim 1000$. The peculiarity of the GPS is the switchyard after the magnet which allows the selection (based on electrostatic deflection) of the three ion beams within the mass range of ±15% from the central mass. The other separator (not employed in this experiment) is the High Resolution Separator [74] (HRS) with $A/\Delta A \sim 5000$.

2.2.2 Post-acceleration

The mass-separated ions of positive charge state (q =+1) enter the REXTRAP[6], a large-acceptance gas-filled (Ne, Ar) Penning trap. In order to maximize the transmission efficiency, the trap accumulates, bunches and deaccelerates the secondary beam. A transversal emittance of the ions is adjusted for the efficient charge breeding in the following stage, REXEBIS. Charge multiplication in the REX Electron Beam Ion Source is achieved by using the electron gun. High-density electron beam (∼100 A/cm^2) produces the ions with $2.5 \leq A/q \leq 4.5$, which suits the linac requirements.

---

[6] REX is abbreviation for the Radioactive ion beam Experiment.

Following the extraction from REXEBIS the RIB undergoes manipulation in the electrostatic deflector and the magnetic dipole. This selects proper A/q, free of contaminations, minimizing the energy spread of ions. The contaminations are mostly due to the buffer (trapping) noble gases from the precedent phase.

REXLINAC is a room-temperature linear accelerator [70], capable of accelerating RIBs up to 3 MeV·A. The success of the REXLINAC experimental campaigns (see for example Ref. [75]) encouraged the imminent RIB energy upgrade. By the time of our experiment in 2017, ISOLDE was upgraded with the three cryomodules housing superconducting high-β cavities to the REXLINAC. The HIE-ISOLDE accelerating structure is inherited from the LHC ring, and the acceleration efficiency is optimized for the ions of $v/c = 10\%$. As presented in Fig. 2.1, the upgrade will be finished after the installation of three more cryomodules.

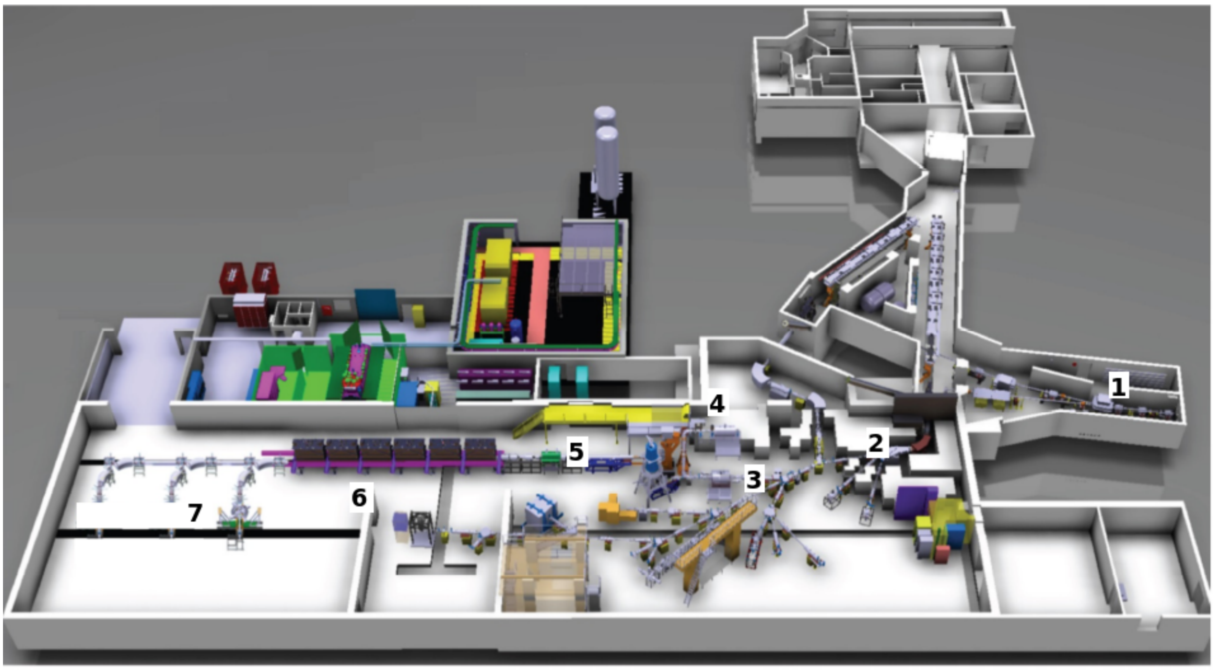

Figure 2.1: Schematical illustration of the HIE-ISOLDE experimental hall. 1) Proton beamline, 2) General Purpose Separator, 3) REXTRAP, 4) REXEBIS 5) REXLINAC, 6) HIE-ISOLDE, 7) MINIBALL station. The final upgrade involves the installation of six superconducting cryomodules.

2.3 The MINIBALL station

Experiments employing RIBs are generally challenging in a sense that they must compesate for the lower beam intensities while dealing with a very complex background coming from the radioactive decay. A dedicated high-resolution and high-efficiency γ-spectrometer MINIBALL meets the requirements at HIE-ISOLDE. The MINIBALL experimental campaign started in 2001 and carried out numerous successful Coulomb excitation and transfer reaction studies [71]. Such studies benefited from the high-quality Doppler correction of the emitted γ rays (even at the relativistic velocities).

2.3.1 The γ-spectrometer MINIBALL

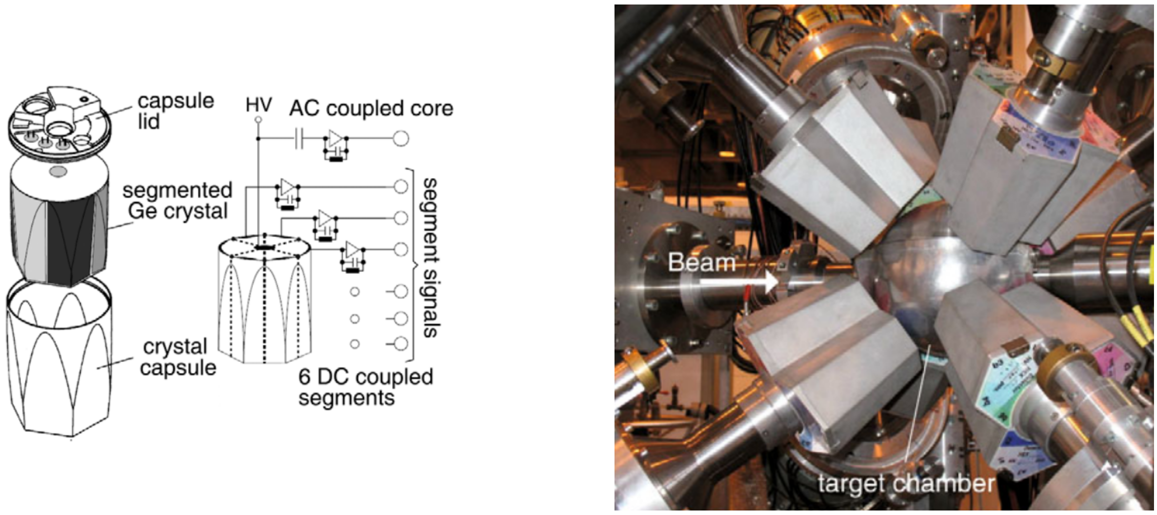

Figure 2.2: Left: the single HPGe capsule assembly and dedicated scheme of the detector's redaout. Right: the photograph of the γ-spectrometer MINIBALL and the spherical target chamber configuration [76].

MINIBALL consists of 24 high-purity germanium crystals (HPGe), individually encapsulated in Al sealed housing, as shown in the left panel of Fig. 2.2. Each HPGe crystal is a cylinder (78 mm length, 70 mm diameter), with a hexagonally tapered front end. The charge collection is obtained via central positive HV core electrode, and the six-fold segmented outer electrode. In total, the 144 signals from the segments are provided, and the 24 core signals, which actually match the sum of the segments signals. The signals are processed with the digital electronics, adapted to high counting-rates, using the 4-channels Digital Gamma Finder modules manufactured by XIA. A specifically designed CAMAC module provides the 40 MHz clocking signal for the DGF units, i.e. the 25 ns timestamps.

Compared to the stable beam experiments, the RIB intensities are generally lower, and the transfer yields consequently smaller. Therefore, the high detection efficiency is imperative. HPGe crystals are embedded in 8 triple-cluster cryostats and mounted on movable arms around the spherical target chamber. Each cluster is placed at an average distance of 10 cm from the target in compact configuration as shown in the right panel of Fig. 2.2. The angle between the beamline and each detector is ∼45° and ∼135°, considering forward and backward directions, respectively. In this configuration, about 60% of the solid angle is covered. In general, the absolute photopeak efficiency of 7.8% and the resolution of 2.3 keV at $E_\gamma = 1.33$ MeV of ^{60}Co source is achieved. In the ^{94}Rb+^{208}Pb experiment, the 23 crystals (of 24 in total) were used in the measurement. The absolute efficiency of the MINIBALL for the whole E_γ range is deduced in Sec. 3.1.

Even at such close-to-target distances, the earlier described read-out segmentation enables to retain the high position sensitivity. The γ-ray position is extracted using the concept of the main interaction. In the case of more interactions (like in the Compton scattering), this means that the position is constructed from the electrode with largest energy deposition.

The high-energy γ rays often deposit the energy in adjacent crystals within the cluster. Such interactions require the add-back procedure, which constructs the full E_γ from the partial E_γ depositions. The full E_γ is constructed by summing the energy of the crystal cores within the 100 ns coincident gate. The position of the γ-ray interaction after the add-back is connected to the crystal with largest partial E_γ deposition.

In the near future the MINIBALL spectrometer will be upgraded with the anti-Compton BGO[7] suppression shields. These shields will provide cleaner γ-ray spectra, and therefore higher peak-to background ratio.

2.3.2 The CD detector

The configuration of Compact Disk (CD) particle detector [77] was specifically designed to suit the MINIBALL spherical target chamber. It consists of four individual Double-Sided Silicon Strip detectors (DSSSD quadrants) which provide the energy and position, thus allowing the Doppler correction of the γ-ray emitted in flight. The CD detector type was exploited in numerous experimental campaigns at ISOLDE (see for example Ref. [78]).

The CD detector measured the beam-like fragments, and also (partially) the target-like fragments in coincidence. It was placed 21 mm downstream of the target with respect to the incoming beam, to cover the region in the vicinity of the grazing angle. The geometry

---

[7] Bismuth Germanate scintillator

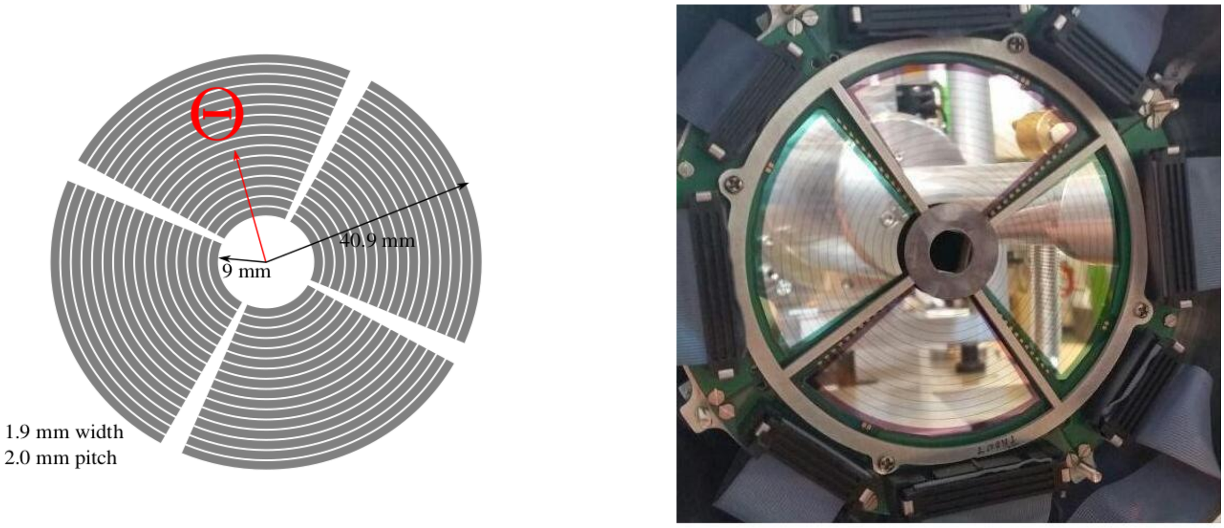

Figure 2.3: Left: schematic view of the front side of the Compact Disk double-sided silicon strip detectors. Right: the photograph of the installed detector. The photograph also shows the tantalum protection ring shielding the innermost strips.

and the photograph of the front side of the detector are shown in Fig. 2.3. Each DSSSD quadrant is divided into 16 circular strips (i.e. rings) of 1.9 mm width each. The position of ring (in target reference frame) is associated with the specific θ_{LAB}. The backside of the quadrant consists of 24 radial strips, perpendicular to the front strips. They were electronically paired to 12 strips in our setup, which resulted in the total number of the 768 pixels for the particle detection. These pixels define the position sensitivity. The energy of the ions is constructed from the charge collected by the ring. The full energy deposition for the heavy ions was ensured with the quadrant thicknesses of the 136, 480, 138, and 480 µm. The dead-layer thicknesses are expected to be below 1 µm, considering both the implantation and the aluminium metalization caused layers.

In this configuration, each quadrant covers the 81.6° in polar angle. Therefore the polar resolution, after the pairing of the backside strips, was $\Delta\phi = 6.8°$. Rings span the $\theta_{\mathrm{LAB}} = 23°$-$63°$ range overall. This means that the position sensitivity in θ_{LAB} varies from 2° to 5° when going from the outermost to the innermost rings, respectively. In the right panel of Fig. 2.3 one sees that the first two innermost rings were protected with the tantalum shield. This was done to avoid the possible detector damage from the scattered beam. Those first rings were not used in the data analysis, thus one can consider the active area of the CD detector is $\theta_{\mathrm{LAB}} = [32°, 63°]$. Also, one of the rings at central position $\theta_{\mathrm{LAB}} = 49°$ was not working properly, therefore reducing the efficiency at this angle by 25%, with respect to the other θ_{LAB}.

The CD read-out is obtained using the traditional analog electronics, and timestamped using the same 40 MHz clock as the DGF modules.

2.4 The ^{94}Rb+^{208}Pb experiment

The multinucleon transfer reaction with ^{94}Rb beam was used to populate the nuclei around the doubly-magic ^{208}Pb. The γ-spectrometer MINIBALL, coupled to the CD detector, allowed to measure the fragment angular distribution and the prompt and delayed γ-decay of the excited states. The isotopes were identified from their characteristic γ rays, and the level schemes built through γ-γ coincidences.

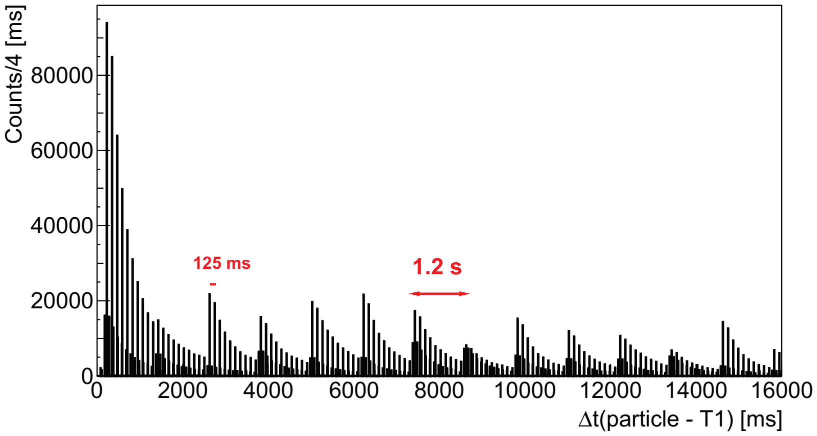

Figure 2.4: Timing structure of the RIB. X-axis represents the time difference between the particle detected in the CD detector and the proton impinging on the UC$_x$ target ($T1$). Only the [0,16] s time range is presented.

The average pulsed proton beam current of 0.35 µA, provided by the PSB, was impinging at the 1.2×n (n $\in$ [1,42]) cycles onto the UC$_x$ target. The extracted reaction products were ionized ($q = +1$) using the surface ion source and mass-separated ($A = 94$) in the GPS separator. Such ions underwent trapping and further ionization in REXTRAP and REXEBIS. For ^{94}Rb ions one obtained the $q = 23^+$ charge prevalence, i.e. $A/q = 4$. The timestamp of the ^{94}Rb beam is described in the Fig. 2.4 with respect to the proton arrival onto the production target (a $T1$ flag). Two dominant timing structures are present, one is emerging from the frequency of the PSB, and the other one from the RIB post-acceleration (bunching) properties. The frequency of the beam spills at the secondary target station was 125 ms, with a width of 1.6 ms for each spill. From the same figure, one might notice the offset of the first beam spill of $\sim$ 230 ms overall. This offset describes the time needed for the first bunch preparation, i.e. the time between the production reaction at the UC$_\mathrm{x}$ target station and the injection in REXLINAC. The intensity of the produced RIB was insufficient for the reading from the Faraday cup, which is typically used for the stable beam focusing. Therefore, in order to maximize the accelerator transmission, a mix of $A/q = 4$ isotopes, ^{20}Ne, ^{16}O, ^{12}C, ^{4}He, was focused onto a ^{107}Ag target.

The REXEBIS timestamp was used to signalize the arrival of the RIB to the REXLINAC (and to the MINBALL data acquisition system). By employing the REXLINAC and the HIE-ISOLDE acceleration system, the achieved velocity of the ^{94}Rb ions was $\beta = 11\%$, corresponding to the energy $E_\mathrm{LAB} = 583$ MeV (with uncertainty of 1.5%). The beam also contained the (unavoidable) 10% ^{94}Sr isobaric contamination.

Ions were impinging onto the ^{208}Pb target of two different thicknesses, 1 mg/cm^2 and 13 mg/cm^2. Throughout this work, we will often refer to these targets as "thin" and "thick", for convenience. The "thin" target was used to extract quantitative information relevant for the reaction mechanism, like the angular distributions. The thickness of the "thick" target was carefully chosen in order to stop the Pb-like ions. The RIB was passing throughout targets to the shielded beam-dump at the end of the beam-line. The 11% of the total beam time was devoted for the "thin" target measurement, and the rest for the "thick" target measurement.

During the "thin" target measurement the acquisition was so-called "triggerless", in the sense that all the γ rays and particles were recorded. In the "thick" target measurement the particles outside the 4 µs particle-γ coincident gate were downscaled by a factor of 16. Downscaling helped to reduce the elastic scattering induced dead-time in the CD detector electronics. The length of the data acquisition window was set to 1.6 ms, to suit the beam spill width.

The data acquisition system, used for the readout and the event building, and the basic framework for the data analysis, are provided and maintained by the MINIBALL group. The details on the data presorting and the analysis will be given in Chap. 3.

2.4.1 The intensity of the ^{94}Rb beam and the radiation safety issue

The production yield of the ^{94}Rb beam at HIE-ISOLDE is 1.8×10^8 per 1 µC of the proton beam. Taking into account the maximum current of 2 µC/s, very high intensities of the

RIB can be reached. However, at the beginning of the ^{94}Rb+^{208}Pb experiment, the HIE-ISOLDE radiation safety rules were not adapted to the amount of radiation produced in the experimental hall. The dose was reaching the 140 µS/h, and for the personnel in the hall this would mean the exposure to the annual dose limit in just six days. In the accepted experimental proposal the required proton beam current was 1.5 µA. Due to the radiation safety rules, the current was drastically reduced to the values of 0.1-0.7 µA, and the 0.35 µA on average. Consequently, the ^{94}Rb current on the target was $\sim 3\times 10^{6}$ pps in average, which is $\sim 5\times 10^{-1}$ ppA only.

After the experiment, the HIE-ISOLDE scientific coordinators re-defined the radiation safety rules, in order to perform the high energy and intensity RIB experiments in the near future. Furthermore, this is the first step which has to be done in order to benefit from the proton beam intensity upgrade, expected by the end of the CERN Long Shutdown in 2021. With this upgrade, the proton current should increase up to 6.7 µA (i.e. by a factor three). The production target and the ion source will be further optimized to work at these new conditions. ISOLDE community currently works on the laser ion source and the HRS improvements, to reduce the (isobaric) beam contaminants to a minimum.

3

Data analysis

In this Chapter, we will present the most important aspects of data analysis. The analysis is based on the MINIBALL data acquisition software [79], adapted to the multinucleon transfer reaction experiment. Software is written within the ROOT data analysis framework [80], in the C++ programming language. A large part of the analysis was the implementation of new software subroutines, which were required, for example, to construct the cross section.

The first step in data analysis is calibration. After the calibration of the γ-spectrometer MINIBALL and the CD detector was performed, we extracted the fragment-γ and fragment-γ-γ coincidences. When using the neutron-rich beam in particular, the fragment-γ coincidences help to reduce the number of γ rays connected to the radioactive decay. More importantly, the fragment-γ coincidences allow to properly attribute the γ transitions to the short-lived state or the isomer and to perform a Doppler correction (in case of the γ rays emitted in flight).

3.1 Calibration of MINIBALL

The energy calibration of the γ-spectrometer was performed using the standard calibration sources ^{152}Eu and ^{133}Ba, with typical γ rays in the 0.08-1.4 MeV energy range [81]. The first-order polynomials were used to calibrate energy signals provided by the segments and cores of MINIBALL. We remind that the cores are essentially summed segment's signals (see Subs. 2.3.1). Figure 3.1 shows the energy calibrated γ-spectrum for ^{152}Eu and ^{133}Ba. This spectrum was obtained by summing over all cores of MINIBALL, and by applying the add-back procedure.

The same calibration sources were used for the MINIBALL absolute efficiency calibra-

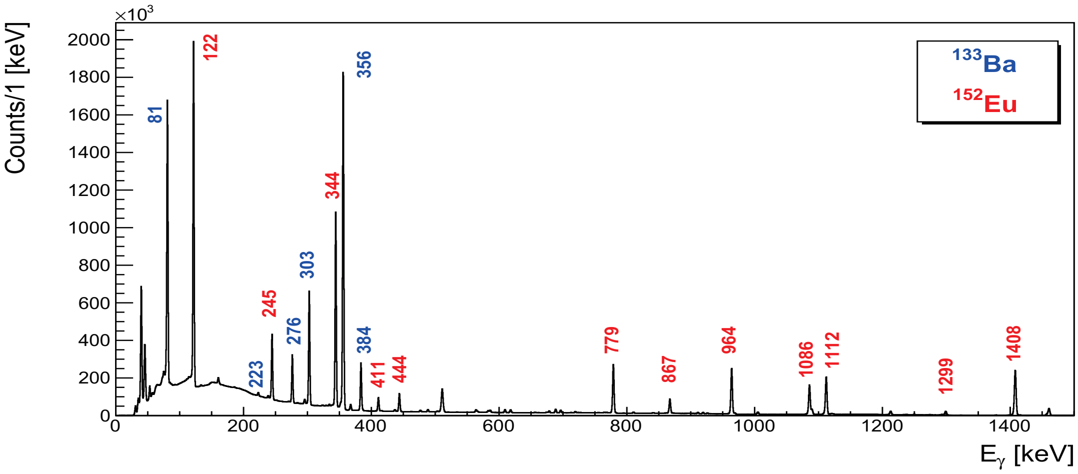

Figure 3.1: The ^{152}Eu (red) and ^{133}Ba (blue) γ rays measured with MINIBALL.

tion. At the time of calibration, the activity of the sources was 7.08 kBq (^{152}Eu) and 5.78 kBq (^{133}Ba). To improve the efficiency calibration at higher E_γ, we have also used the ^{66}Ga source. It covers the energy range up to 4.8 MeV with well known relative intensities. The short lived ^{66}Ga ($\tau_{1/2}$ = 9.5 h), produced by ISOLDE for calibration purposes, was implanted at the target position of MINIBALL. The information about this procedure and full ^{66}Ga decay spectrum can be found in Ref. [82]. Using the ^{152}Eu, ^{133}Ba sources, and selected high-energy γ rays of ^{66}Ga, the function $\epsilon(E_\gamma)$ was obtained and presented in Fig. 3.2. It describes the sharp increase of the efficiency at the low energies, and the exponential-like decrease towards the higher. This function will be used to correct the measured γ-ray intensities.

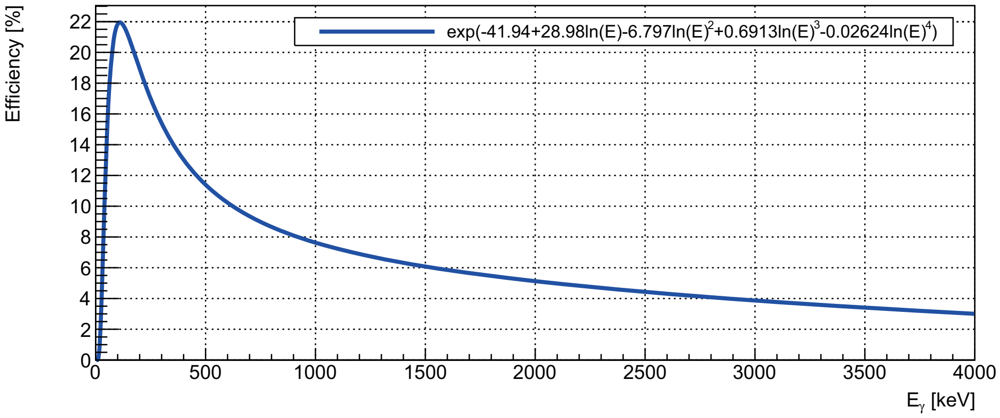

Figure 3.2: The absolute efficiency of MINIBALL as a function of the γ-ray energy, $\epsilon(E_\gamma) = exp(-41.94 + 28.98ln(E) - 6.797ln(E)^2 + 0.6913ln(E)^3 - 0.02624ln(E)^4)$

In conclusion, the energy resolution and the absolute efficiency of MINIBALL in the experiment were 3.2 keV and 6.3% at $E_\gamma = 1408$ keV, respectively. The resolution of γ rays emitted in flight is lower, and depends on the Doppler correction. We obtained the 18 keV resolution for $E_\gamma = 1567$ keV in ^{209}Pb ($v/c \approx 3\%$).

3.2 Calibration of CD

3.2.1 Position calibration

Knowing the absolute position of the CD detector pixel very precisely is of great importance for Doppler correction. The detailed geometry of the detector was given in Subs. 2.3.2. To associate each pixel to the coordinates in the target (laboratory) reference frame two variables are required. These are the corresponding distance between the CD detector centre and the target along the beam-axis ($d_{\rm CD}$), and the polar offset of the reference strip ($\phi_{\rm LAB}$). The set-up values were $d_{\rm CD} = 21$ mm and $\phi_{\rm LAB} = 14°$.

More precise definition of $d_{\rm CD}$ and $\phi_{\rm LAB}$ was constructed from the best E_γ resolution after the Doppler correction. For details on the Doppler correction, see Subs. 3.5. Using the 1 mg/cm^2 target, the γ-ray spectrum in coincidence with the fragments in CD detector was constructed. The Doppler correction for the light and heavy binary fragments was performed by varying the combinations of $d_{\rm CD}$ and $\phi_{\rm LAB}$, in the vicinity of set-up ones.

To illustrate this method, we show the $d_{\rm CD}$-E_γ matrices at $\phi_{\rm LAB} = 14°$ in Fig 3.3. In the matrix Doppler corrected for the light fragments (left panel), the strongest γ rays in the selected energy range are 324 keV and 405 keV, attributed to ^{93}Rb and ^{94}Rb, respectively. In the matrix Doppler corrected for the heavy fragments (right), the strongest γ-ray is 2615 keV of ^{208}Pb. The best energy resolution obtained was $\sim$1.5% at $E_\gamma = 324$, 405 keV, and $\sim$1% at E_γ=2615 keV. It was produced for $d_{\rm CD} = 20.8$ mm and $\phi_{\rm LAB} = 14°$, and these values were used to construct the pixel position. The choice of these particular $d_{\rm CD}$ and $\phi_{\rm LAB}$ is maybe better understood from the spectrum plotted in Fig. 3.4.

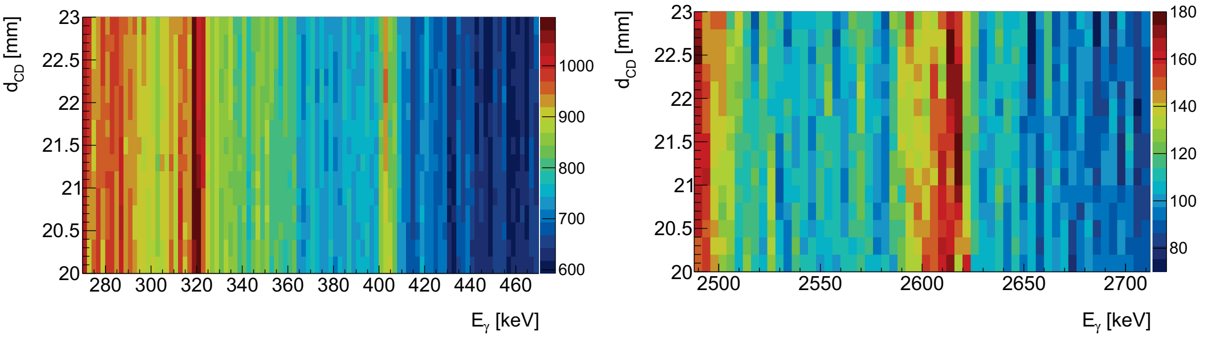

Figure 3.3: The d_{CD} vs. E_γ matrix in the selected energy ranges, obtained with the use of 1 mg/cm^2 target. Left: Doppler corrected for light fragment. Right: Doppler corrected for heavy fragment. Notice the difference in the binning.

To cross-check the position calibration, we constructed the θ_{CM} of two elastically scattered particles. Elastic scattering event was obtained by requiring the absence of the γ-ray in coincidence. Figure 3.4 illustrates the θ_{CM} at $\phi_{\mathrm{LAB}} = 14°$, for the three different values of d_{CD}. Each distribution of θ_{CM} is Gaussian-like, with an exponential tail towards the lower values. This tail is associated with the inelastic scattering and the undetected γ rays. One notices that the distributions have a maximum close to 180°. The maximum of the $d_{\mathrm{CD}} = 20.8$ mm distribution, which was selected in the construction of the detectors geometry as described earlier, is slightly below the 180°. Having in mind that the elastically scattered ions experience some energy losses in dead-layer materials, and the presence of the exponential tail (and the reasons behind it), the obtained result supports our d_{CD} and ϕ_{LAB} selection.

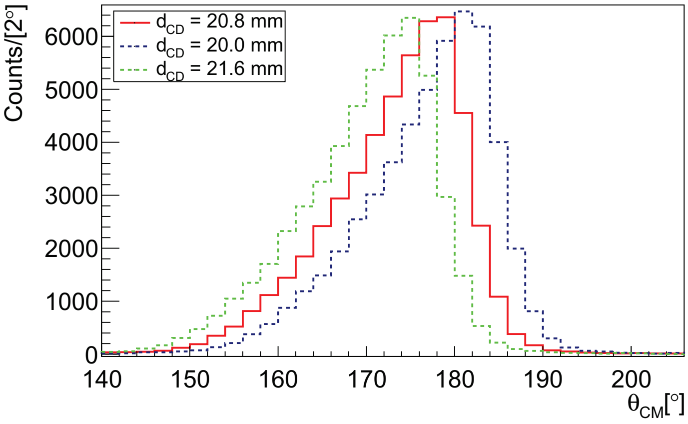

Figure 3.4: The θ_{CM} of two fragments detected without a γ-ray in coincidence, at $\phi_{\mathrm{LAB}} = 14°$ and selected d_{CD} (see text).

3.2.2 Energy calibration

Since the kinetic energy of Rb-like fragments is rather high, the energy calibration is performed from the elastic scattering. The MINIBALL collaboration software [83] implements the CD detector geometry and provides the elastic scattering calculations taking into account the energy losses in the target. We used the calibration obtained in the ^{72}Se, ^{16}O, ^{12}C+^{196}Pt reaction at E_{LAB} = 4.4 MeV·A, as a starting point. This reaction was measured during the preceding experiment, which used the same set-up. Elastic scattering of ^{72}Se, ^{16}O and ^{12}C was observed in the whole θ_{LAB} range of CD, and thus the corresponding calibration functions could have been extracted for all rings.

We remind that in our experiment, the ^{20}Ne, ^{16}O, ^{12}C, ^{4}He "coctail" beam was used during the preparation runs. The beam was impinging at E_{LAB} = 6.2 MeV·A onto a ^{107}Ag target (1.9 mg/cm^2 thickness). The accumulated statistics enabled to observe the peaks which correspond to the elastic scattering of ^{20}Ne, ^{16}O and ^{12}C in the angular range of θ_{LAB}=[32°, 54°]. The resulting energy spectra obtained from the single ring at θ_{LAB} = 41° (central position) of each of four quadrants are shown in Fig. 3.5. The elastically scattered ^{20}Ne, ^{16}O, ^{12}C were stopped in the CD detector, thus they deposited their total kinetic energy. In the quadrants of 0.1 mm thickness, ^{4}He deposited only the part of its total energy.

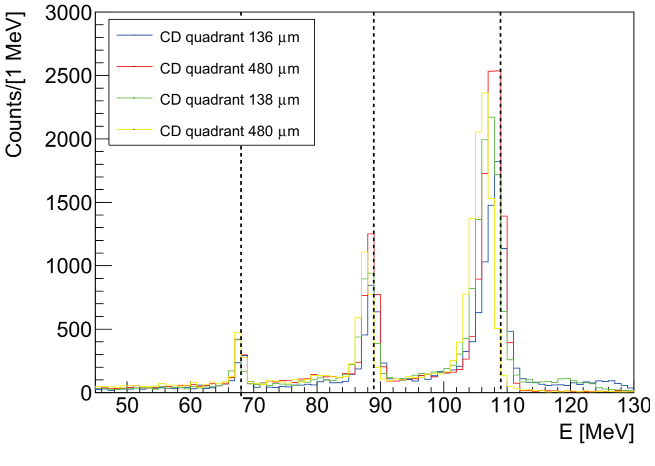

Figure 3.5: Energy spectra of the individual ring at θ_{LAB} = 41°, for each of four CD quadrants. Spectra are obtained from the measurement of ^{20}Ne^{16}O^{12}C^{4}He+^{107}Ag reaction at E_{LAB} = 6.2 MeV·A using the MINIBALL group calibration coefficients. Dotted lines are the energies calculated for the elastic scattering, $E(^{20}\mathrm{Ne})$ = 109 MeV, $E(^{16}\mathrm{O})$ = 89 MeV and $E(^{12}\mathrm{C})$ = 69 MeV.

To illustrate the quality of energy calibration we plotted in Fig. 3.5 also the lines which represent the calculated energies of the elastic scattering of ^{20}Ne, ^{16}O and ^{12}C, at $E(^{20}\mathrm{Ne}) = 109$ MeV, $E(^{16}\mathrm{O}) = 89$ MeV and $E(^{12}\mathrm{C}) = 69$ MeV, respectively. The calculated energies agree well with the experimental ones. The experimental energies are still slightly shifted towards the lower energy values, particularly for ^{20}Ne, which can be understood in terms of the energy losses ($\sim$MeV) in detectors dead layers. This effect was not included in the calculations, since the dead layer precise thickness is not well defined. Another feature of this spectra are small misalignments in measured E of different rings (at the same θ_{LAB}). As the total energy spectra will be constructed by summing over the four quadrants, in order to maximize the energy resolution it was necessary to realign different quadrants.

This procedure was performed by using the ^{94}Rb+^{208}Pb reaction measured with the 1 mg/cm^2 target. The elastically scattered ^{94}Rb ions (i.e. the most energetic ions in the reaction) were observed within the $\theta_{\mathrm{LAB}} = [32°, 56°]$. In Fig. 3.6 we plotted the spectra measured with the rings at $\theta_{\mathrm{LAB}} = 41°$, 47°, 51° and 55°, for the each ring and quadrant individually. To maximize the energy resolution (which is visible from the spectra), those spectra were re-aligned to the calculated values. Calculated energies for the elastic scattering of ^{94}Rb (dotted lines) were obtained from the ^{94}Rb+^{208}Pb kinematics at $E_{\mathrm{LAB}} = 583$ MeV. Using those points, as well as the zero energy point, the realignment of the rings spanning the $\theta_{\mathrm{LAB}} = [32°, 56°]$ range was performed.

The elastic scattering calculations are plotted in the $E - \theta$ matrix representation in the left panel of Fig. 3.7. Events at higher energies correspond to ^{94}Rb, and the other to ^{208}Pb. Matrix illustrates the angular span of each CD ring, and the ±15 MeV uncertainty in energy which was applied to rougly imitate the measurement.

The right panel of Fig. 3.7 shows the measured, calibrated and aligned $E - \theta$ matrix. This matrix was obtained by summing over all the rings of the CD detector. We remind that the region below the $\theta_{\mathrm{LAB}} = 32°$ is shadowed by a protection ring, as visible from the figure. The full black circles represent the 10 calculated points, which were used to align the rings as explained above. Since the CD was set for the measurement of the Rb (and Rb-like) ions, it was only partialy covering the binary partner, as obvious from this experimental matrix.

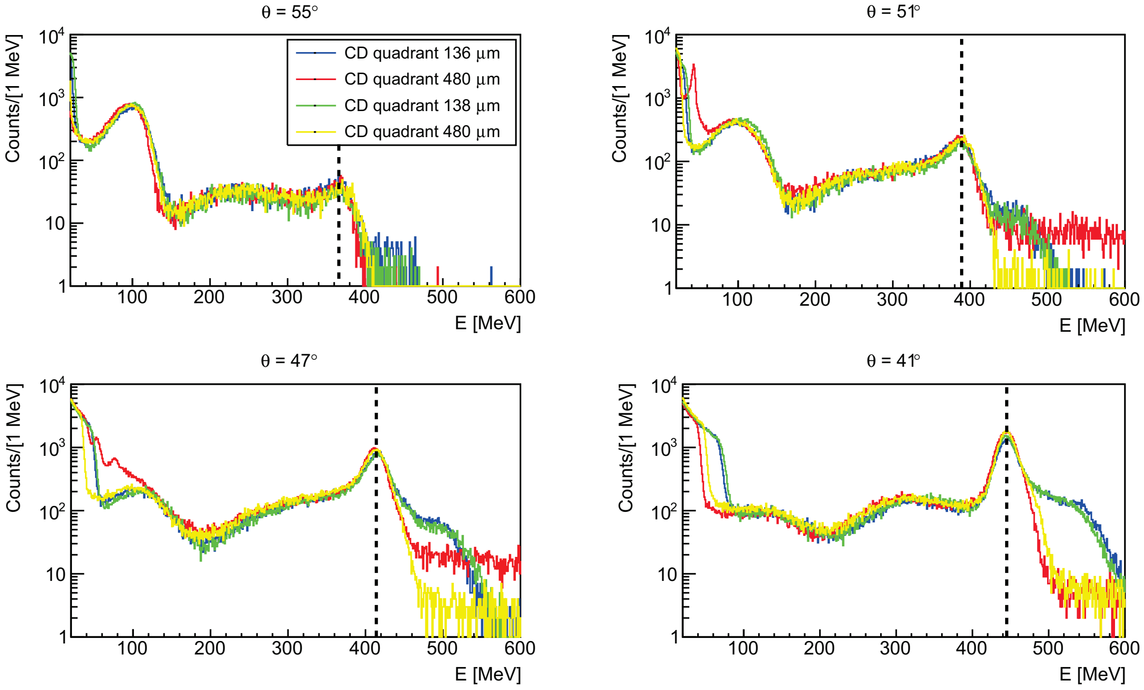

Figure 3.6: The measured energy spectrum at the given θ_{LAB} (center of the ring) of each CD detector quadrant. Different quadrants are indicated with different colors. Lines are plotted at $E(\theta_{\mathrm{LAB}} = 41^\circ) = 445$ MeV, $E(47^\circ) = 414$ MeV, $E(51^\circ) = 388$ MeV, $E(55^\circ) = 366$ MeV (see text).

3.2.3 Effects of multiplicity in CD

In Subs. 2.3.2 we introduced the CD position sensitivity, determinted with the number of pixels (768) for the particle detection. In an ideal case, the fragment induces a signal in the particular ring and strip, and the pixel can be unambiguously identified. This is an exemplary case of the valid event in the data analysis. The event is not valid if the pixel cannot be constructed, i.e. ring or strip information is missing.

If only one fragment impinges at particular quadrant during the data acquisition window width, it is what we consider a single multiplicity event. The multiplicity is quite important, since the unambiguous pixel definition is a prerequisite for the Doppler correction. Sometimes the fragment deposits its energy in neighbouring rings and/or strips. In such case, the energy is deposited in two rings and one strip, or vice versa, thus the energy of the adjacent rings (or strips) should be summed up. The resulting energy is then associated to the ring or strip with larger energy deposition. This procedure allows to fully reconstruct the energy of the fragments, and the conservation of the single multiplicity in the quadrant.

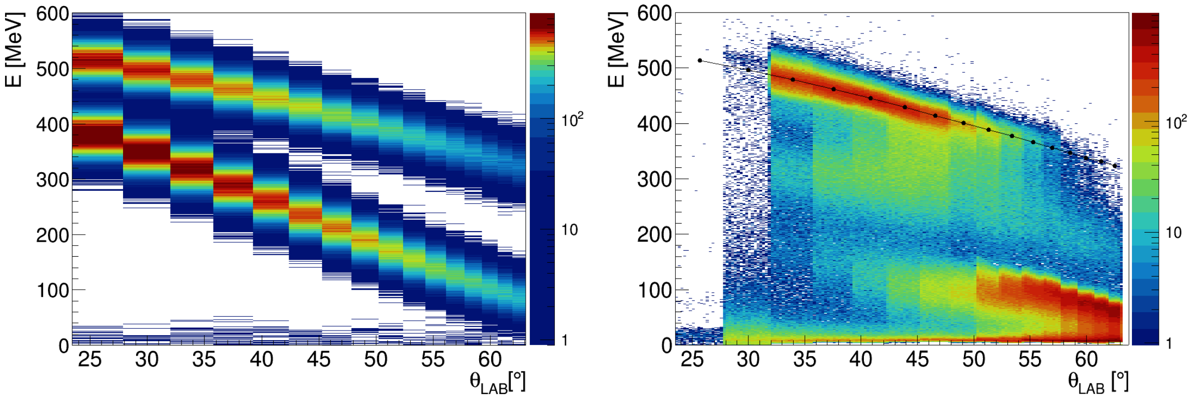

Figure 3.7: Left: the calculated kinematics of ^{94}Rb and ^{208}Pb at $E_{\mathrm{LAB}} = 6.2$ MeV·A in $E-\theta$ matrix representation. Right: the measured $E-\theta$ matrix of all particles. Black line connects the calibration points (full black circles).

The single multiplicity gate is then safe to apply. It rejects the cases in which there are two or more fragments in the same quadrant. The spectra of the $\theta_{\mathrm{LAB}} = 41^{\circ}$ ring from two different quadrants, 0.1 and 0.4 mm thickness, are presented in the left and right panel in Fig. 3.8, respectively. The high energy Gaussian-like peak around 475 MeV is associated to the Rb-like fragments. Without the multiplicity gate (blue lines), in the spectrum obtained with the 0.1 mm quadrant, one observes the high energy tail.

Such phenomena were already observed in previous measurements with the CD detector, as for example in the ^{132}Sn+^{206}Pb experiment [82, 84], where four 138 μm DSSSDs in the CD configuration were used. The origin of the high energy tail was then explained through the capacitive coupling of the neighbouring segments or charge sharing induced by the beam-like ions impinging on the detector. Larger the charge sharing, the charge cloud becomes more spread over a larger area, which results in the detection of more charge carriers. This might explain the larger energy losses. More localized charge cloud on the other hand would imply more charge trapping (lower E losses).

After applying the single multiplicity gate (see the red lines in Fig. 3.8), the tail in the detector of 0.1 mm thickness disappears. In the spectrum obtained with the 0.4 mm thick quadrant, the tail is less pronounced. We assume this is due to the higher bias which was applied to the thicker quadrants, thus lowering the charge sharing. Also, in this way the depletion region is wider, and the capacity and the capacitive coupling therefore are obviously less significant.

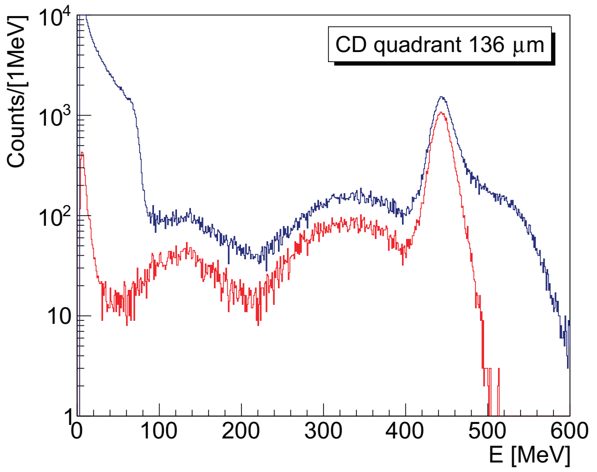

Figure 3.8: The measured energy spectra of the ring at $\theta_{\mathrm{LAB}} = 41°$, before (blue line), and after the single multiplicity gate (red). Left: spectrum obtained with the 136 μm quadrant thickness. Right: spectrum obtained with the 480 μm quadrant thickness.

3.3 Fragment-γ coincidences

The study of properties of ^{94}Rb+^{208}Pb reaction mechanism is based on the fragment-γ coincidences. The experiment is using a β-decaying beam, which produces complex and strong background in the γ-ray spectra. Such background can be very successfully minimized by using the fragment-γ timing difference. The fragment-γ coincidences largely reduce the number of the observed γ transitions connected to the β-decay. They enable to attribute properly the reaction associated γ transitions to the short-lived state or the isomer. Moreover, the fragments in coincidence with a specific γ-ray can be used in the construction of the angular distributions.

The measured matrices of E_γ vs. the time difference (Δt) between the fragment and γ can be seen in Fig. 3.9. In total, $5.6{\times}10^6$ coincidences were collected during the "thin", and $4.5{\times}10^7$ during the "thick" target measurement. In the case of "thin" target, the coincidences are generated either by the Rb-like or the Pb-like products impinging onto a CD. In the case of the "thick" target, due to the 13 mg/cm^2 target thickness, the Pb-like fragments are stopped and mostly the Rb-like fragments are detected. The "thin" and "thick" target matrices are qualitatively similar, being the majority of the γ rays detected within the ~200 ns time window following the fragment detection. In the "thick" target matrix, the more pronounced accumulation of the background is visible on the right side of the Δt peak (a shadow-like structure). This is due to the much larger velocity spread

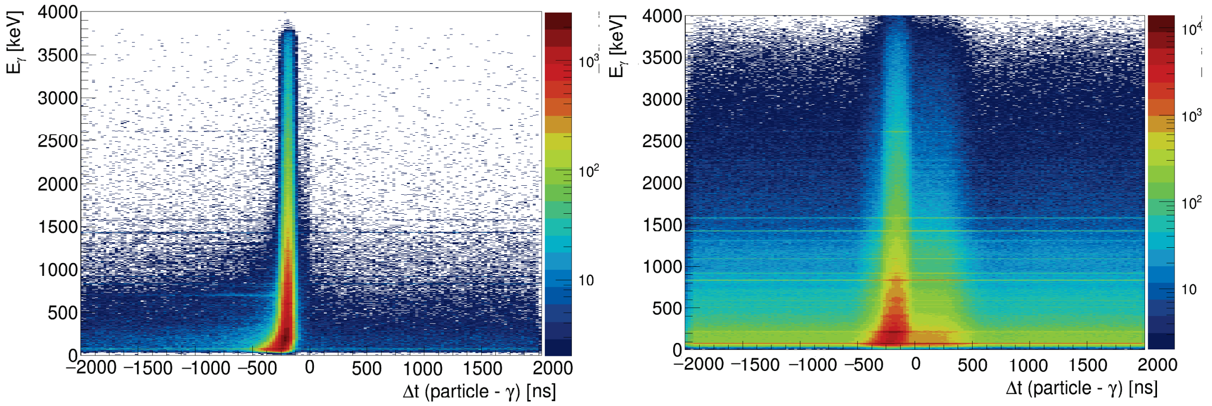

Figure 3.9: Gamma energy (E_γ) vs. the time difference between the fragment and γ (Δt) obtained with the use of 1 mg/cm^2 target (left), and of 13 mg/cm^2 target (right). The small offset from 0 ns is hardware related.

in the measurement with "thick", than in the "thin" target.

One might notice the Δt bending at lower E_γ. Both the particle and the γ-ray modules use the leading edge triggering method to derive a timing logic signal. This method is amplitude dependent, which causes lower energy signals to appear slower ("walk effect"). This "walk effect" was corrected with a dedicated calibration function. More detailed explanation of the walk correction procedure can be found, for instance, in Ref. [85]. As an example, the corrected E_γ-Δt matrix obtained with the use of "thick" target is plotted in Fig 3.10 (left panel). Similar results were obtained in the case of "thin" target.

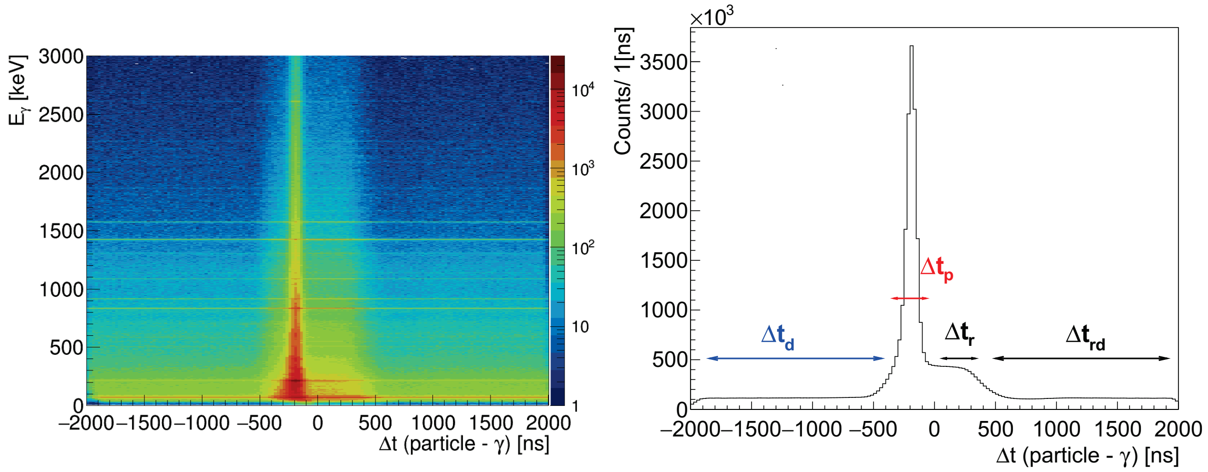

Figure 3.10: Left: γ-ray energy vs. the time difference between the fragment and γ, obtained with the use of 13 mg/cm^2 target and the walk correction. Right: the projection onto the x-axis. Labels are for delayed (Δt_d), prompt (Δt_p) and random (Δt_r, $\Delta t_{r,d}$) timing windows.

In the same figure (right panel) we also show the matrix projection onto a Δt axis, with exact timing windows (gates) as used in the analysis. The prompt timing window was defined as Δt_p = -[275,75] ns. Besides the prompt γ rays from the ^{94}Rb+^{208}Pb reaction, this window contains also the unwanted (background) γ rays. Those origin mostly from the decay of ^{94}Rb beam (and ^{94}Sr beam contamination). The random coincidences, in general, also contribute to the background. To gate on the random coincidences, we defined the Δt_r = [0,200] ns random timing window. It was used to evaluate and subtract the random background.

The delayed timing window was set to Δt_d = -[2000,275] ns. It was used to study the γ rays following the decay of the isomers with half-life of the order of ~[10-1000] ns. Similarly to the prompt γ case, to better understand the effect of the background, we defined the random delayed timing window, and set it to Δt_{rd} = [500,2000] ns. The width and the position of each Δt gate was carefully optimized in order to maximize the intensity of the selected γ rays associated to ^{209}Pb and ^{210}Pb, with respect to the intensity of the γ rays connected with the β-decay.

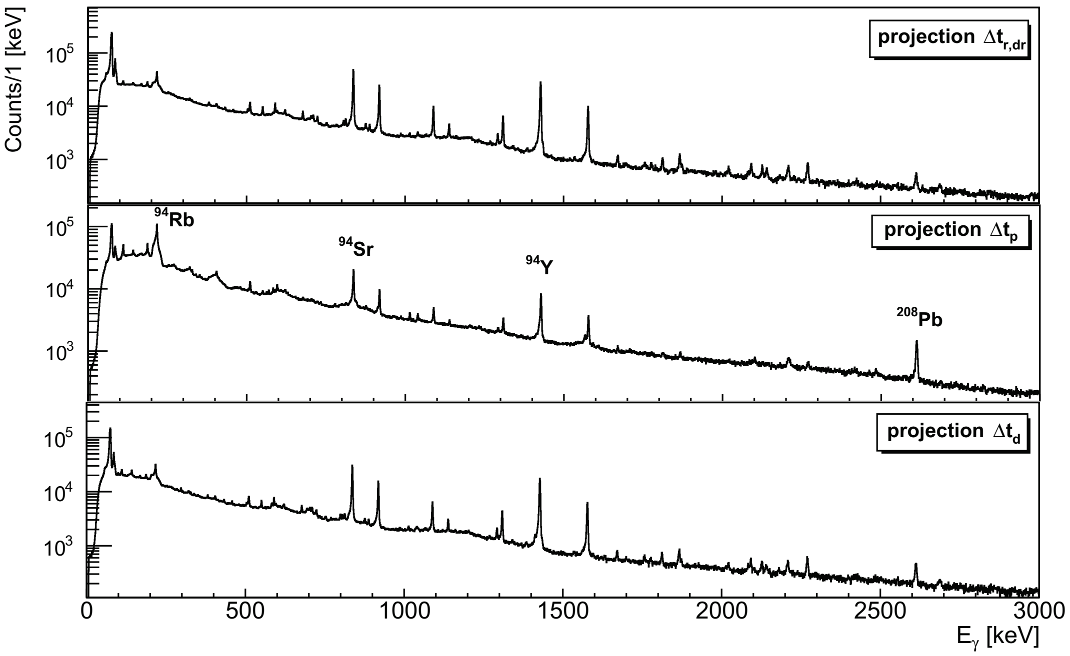

Figure 3.11: Projections of the E_γ-Δt matrix onto the E_γ axis, for the indicated Δt timing gates. Obtained with the use of 13 mg/cm^2 target.

To better illustrate the selection of different timing gates, we show in Fig. 3.11 the γ spectra for the prompt and delayed events, as well as for the region on the right side of the prompt peak. The strongest γ rays in the Δt_p-gated γ-spectrum are associated to

^{94}Rb, ^{94}Sr, ^{94}Y and ^{208}Pb. Moving outside of the prompt window, one can notice the relative change of intensity between the reaction associated (^{94}Rb+^{208}Pb) γ rays and the background (^{94}Sr, ^{94}Y) γ rays. Increase in the intensity of the β-decay associated γ lines is clearly visible in both the $\Delta t_{r,rd}$ and the Δt_d gated spectra. The background, which in majority can be attributed to the ^{94}Rb and ^{94}Sr decay, is quite complex. In the following text, we will focus on the background subtraction procedure. For more detailed study of the background composition see Subs. 3.6.

3.3.1 Background subtraction

An example of the background subtraction procedure is illustrated in Fig. 3.12, with the "thick" target γ spectra and for different timing gates.

The strongest γ transitions in a selected energy region (1.2-1.7 MeV) were labeled. In the γ-spectrum obtained with the Δt_r gate (bottom panel) one can clearly see that the strongest γ rays are the background associated γ transitions of E_γ = 1428 keV (^{94}Y) and E_γ = 1578 keV (^{94}Sr). In the Δt_p-gated γ-spectrum (central panel), these γ rays are still the strongest ones, together with the γ transitions attributed to the one neutron transfer channel, ^{209}Pb. The E_γ = 1567 keV ($5/2^+ \rightarrow 9/2^+$) of ^{209}Pb is clearly observed, while the E_γ = 1423 keV ($15/2^- \rightarrow 9/2^+$) of ^{209}Pb appears only as a tail of the 1428 keV γ-peak.

Subtracting the Δt_r-gated γ-spectrum from the Δt_p-gated γ-spectrum, one obtains the γ-spectrum plotted in the top panel of the same figure, which illustrates well the importance of the background subtraction in the such type of experiments. It is evident that the background subtraction largely enhances the peak-to-total ratio of 1423 and 1567 keV γ rays of ^{209}Pb. Moreover, their relative intensities become significantly stronger with respect to 1428 keV and 1578 keV γ rays. One must keep in mind that the subtraction, although improving the sensitivity to the reaction associated γ rays, may influence the shape and the intensity of γ-peak. Therefore, a careful analysis is necessary when extracting the intensity of the γ-ray which is close in energy to the background associated γ-ray, as is the case of E_γ = 1423 keV.

The above described procedure was applied for both the "thick" and the "thin" target data, using the identical $\Delta t_{r,p}$ gates. For the analysis of the longer lived states, we applied the same procedure with the delayed gates (see Fig. 3.10). In short, this means that we subtracted the appropiately scaled Δt_{rd}-gated γ-spectrum from the Δt_d-gated

γ-spectrum, obtaining the result which will be shown later.

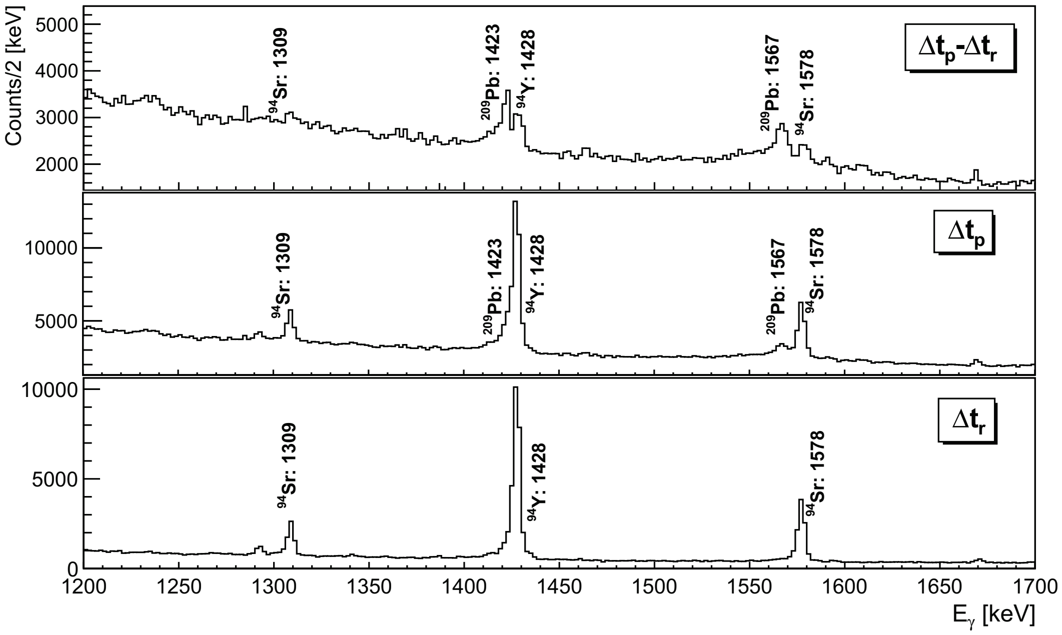

Figure 3.12: Gamma spectra in coincidence with fragment, obtained by the use of "thick" target. Timing gates are indicated in the inset.

3.4 Fragment-γ-γ coincidences

Only for the measurement which used the "thick" (13 mg/cm^2) target collected statistics allowed to study also the γ-γ coincidence, to some extent. The measured time difference of the two γ rays is plotted in the left panel of Fig. 3.13. A γ-γ coincidence gate, $\Delta t_{\gamma\gamma}$, is labeled and was set to [-100,100] ns.

The γ-γ matrix obtained using the $\Delta t_{\gamma\gamma}$ gate is shown in the right panel (of the same figure). This matrix is dominated by the β-decay associated γ rays, to be discussed in Sec. 3.6. To enhance the ^{94}Rb+^{208}Pb reaction associated γ-γ coincidences, we constructed a fragment-γ-γ coincidence. The fragment-γ-γ coincidence is used for the level scheme construction and the identification of newly observed transitions.

At first, the γ-γ matrix in coincidence with fragments was constructed. This coincidence was achieved by applying the Δt_p =-[275,75] ns gate for the fragment and the γ-ray. Then, the $\Delta t_{\gamma\gamma}$ gate was applied for the time difference of the two γ rays. From now on, we will frequently show this matrix, calling it simply the "γ-γ matrix", even if it

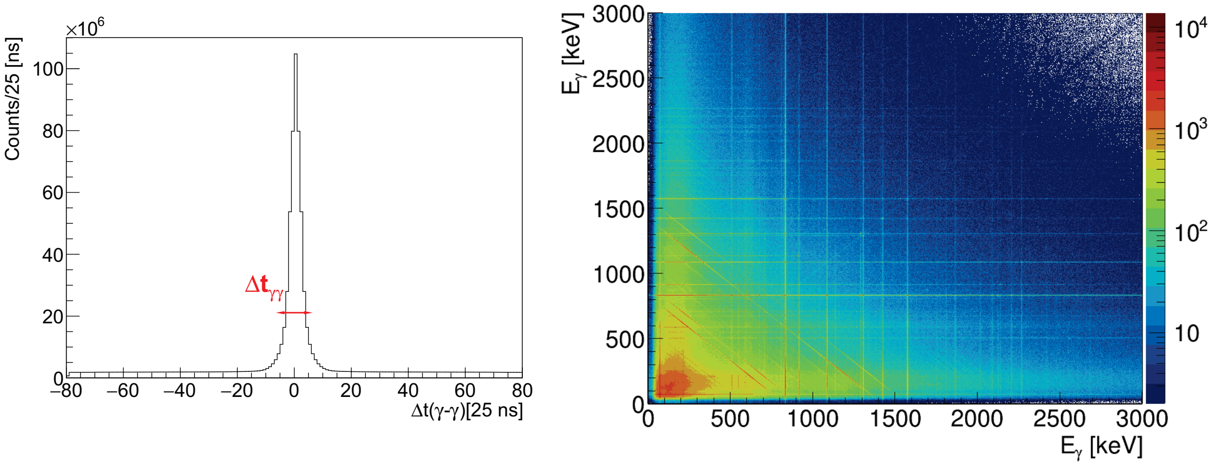

Figure 3.13: Left: the measured γ-γ time difference. Right: the γ-γ matrix obtained using the $\Delta t_{\gamma\gamma}$ gate. Strongest lines are associated with the β-decay.

assumes also the coincidence with the fragment.

To evaluate the background, a random γ-γ matrix is constructed from the same steps as illustrated above, but using the Δt_r = [0,200] ns gate. Background subtraction in the γ-γ matrix is then performed by subtracting the random γ-γ matrix. The γ-γ matrix, background subtracted, is plotted in Fig. 3.14. The same figure illustrates an example of E_γ gate, as it was used in the data analysis. The γ-gate is set to E_γ = [1563, 1571], to select a strong E_γ = 1567 keV ($5/2^+ \rightarrow 9/2^+$) γ-transition in ^{209}Pb. Projection of this gate is shown in the top panel of Fig. 3.15. In the 1567 keV gated spectrum, one observes a strong peak which corresponds to E_γ = 465 keV ($1/2^+ \rightarrow 5/2^+$) γ-transition in ^{209}Pb. One can also see the coincidences with the γ rays which do not belong to ^{209}Pb. To improve this, we subtracted the E_γ = 1567 keV gated and the background gated spectra, with the gates as illustrated in Fig. 3.15. The background gated γ-spectrum (middle panel) was scaled (to suit the E_γ gate width) and subtracted from the E_γ gated one (top panel). The result is shown in the bottom panel of the same figure. In this spectrum the background is significantly reduced, and the coincidence between the 465 keV and the 1567 keV γ rays is very clear.

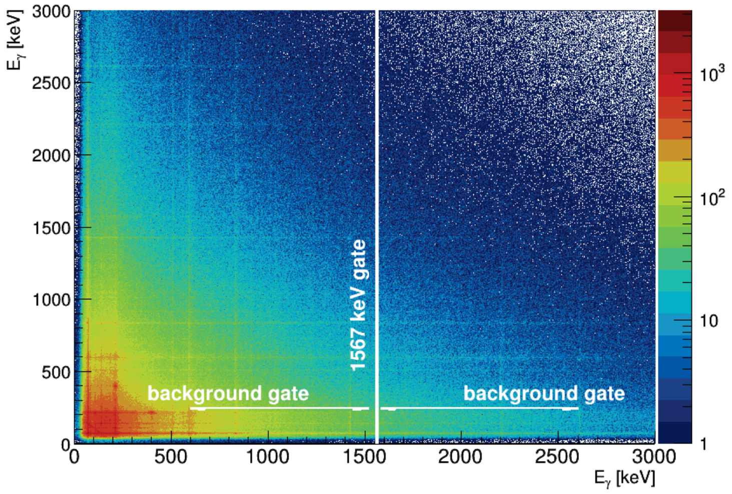

Figure 3.14: The background subtracted γ-γ matrix. Superimposed lines describe the width of the E_γ = 1567 keV gate, and the background gates (left and right) from it.

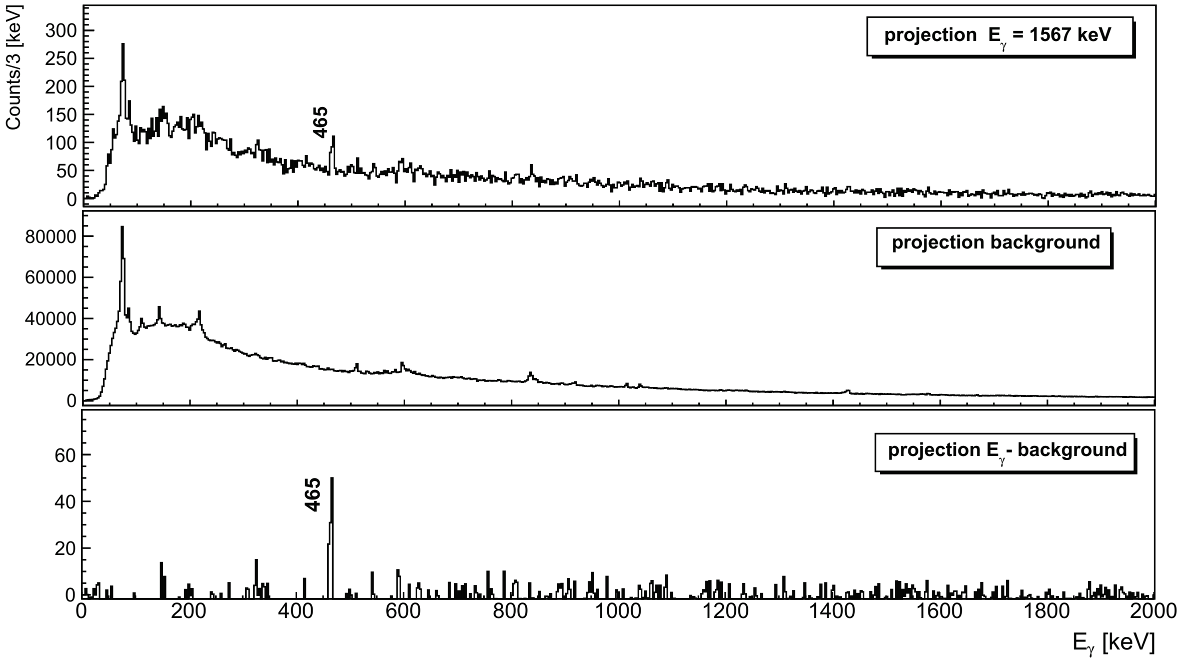

Figure 3.15: Projections of the γ-γ matrix. Top: gate on E_γ = 1567 keV. Middle: gate on the background. Bottom: gate on E_γ = 1567 keV, background subtracted.

In order to study the delayed γ transitions of the excited states, we constructed in the same manner the fragment-γ-γ delayed matrix. The matrix was built using the Δt_d =-[2000,275] ns gate for the fragment-γ coincidences, and the $\Delta t_{\gamma\gamma}$ gate for γ-γ. To evaluate the background in the delayed region, we selected the Δt_{rd}=[500,2000] ns events and created corresponding random delayed γ-γ matrix. The random delayed γ-γ matrix is scaled (to suit the Δt_d gate width), and subtracted from the delayed γ-γ matrix. In addition, the prompt-delayed γ-γ matrix was also built to study the prompt feeding to the isomers, and vice versa.

3.5 Doppler correction

A majority of the γ rays populated in reaction were associated with the prompt ($\tau \sim$ fs-ns) decay of states. Several, but rather strong γ rays were also associated to the delayed decay ($\tau \gtrsim 100$ ns) of the isomers in Pb. During the measurement with the "thin" (1 mg/cm^2) target, the prompt γ rays are emitted in-flight. As a consequence, E_γ are measured with an angle-dependent Doppler shift and the proper Doppler correction is of extreme importance. Relation of the measured (E'_γ) and the irradiated energy (E_γ) in is given by

$$E_\gamma = \gamma \left[1 - \beta \cos\left(\vartheta_\gamma\right)\right] E'_\gamma \tag{3.1}$$

where $\gamma = 1/\sqrt{1-\beta^2}, \beta = v_{\text{LAB}}/c$ and ϑ_γ is the angle between the γ-ray and the emitting fragment. The velocities of the Rb-like and Pb-like fragments in our reaction, close to the grazing angle, are $\beta \sim 10\%$ and $\beta \sim 3\%$, respectively.

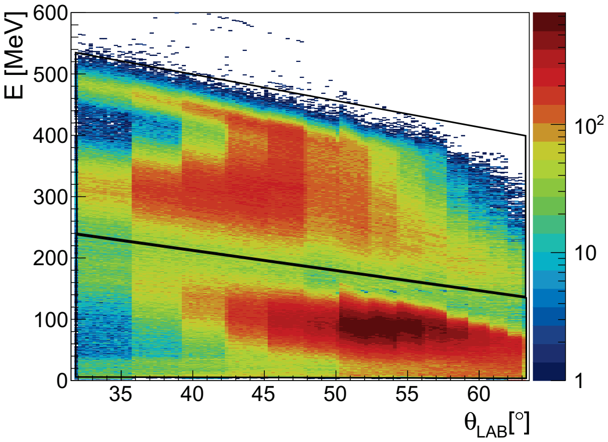

Figure 3.16: The measured $E-\theta$ matrix of fragments in coincidence with the γ-ray, background subtracted. The gates are as used in Doppler correction for the light (top), and the heavy binary fragment (bottom).

If the fragment and the γ ray were both detected, the angle ϑ_γ is extracted directly from the measurement. The position resolution is defined by the HPGe crystal segment and the CD detector pixel (see Subs. 2.3.1 and 2.3.2). The E_γ is then constructed from the measured ϑ_γ and extracted v_{LAB}.

The v_{LAB} determination is based on the fragment position in the $E-\theta$ matrix (see Fig. 3.16). Different gates for the light (top) and the heavy fragment (bottom) are depicted in the same figure. To properly select the fragments with the prompt γ-ray, the Δt_p gate was applied, and the background was subtracted using the Δt_r gate. Fragment velocity v_{LAB} is then determined by assuming the elastic scattering at measured θ_{LAB}, i.e. masses of $A = 94$ and $A = 208$ for light and heavy fragment, respectively. Energy losses in the target are taken into account.

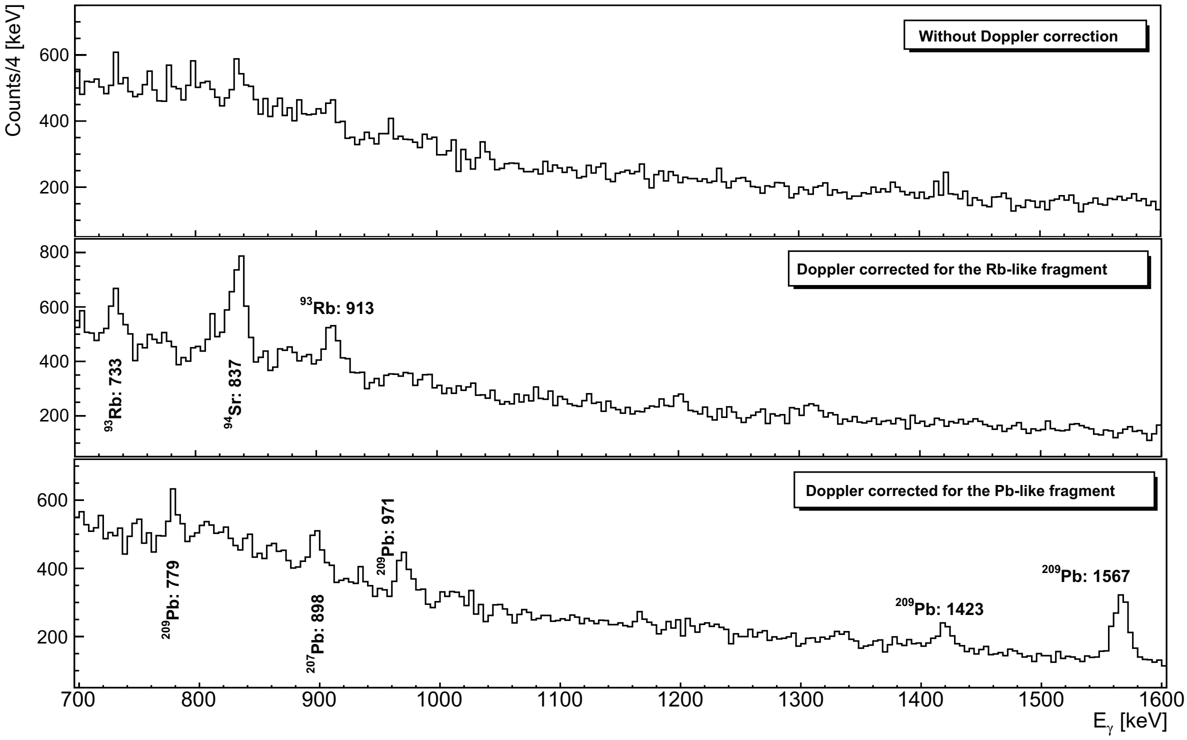

Figure 3.17: Background subtracted γ-spectrum in coincidence with Rb-like fragments. Top: non Doppler corrected. Middle: Doppler corrected for the Rb-like. Bottom: Doppler corrected for the Pb-like. Obtained with the use of 1 mg/cm^2 target.

Each measured E'_γ was also Doppler corrected for the undetected fragment. For instance, if the light fragment was detected, the correction is calculated for the heavy, and vice-versa. The Doppler correction of the undetected fragment was obtained by assuming a binary character of the reaction and imposing the energy and momentum conservation to calculate the velocity. Doppler corrected spectra are plotted in Fig. 3.17, in which the strongest γ rays are labeled as well. Gamma rays associated to the one neutron transfer channel, ^{94}Rb+^{208}Pb $\rightarrow$ ^{93}Rb+^{209}Pb, are $E_\gamma = 733$, 913 keV (^{93}Rb) and $E_\gamma = 779$, 971, 1423, 1567 keV (^{209}Pb). Without Doppler correction (see the top panel of Fig. 3.17) this channel is not clearly observed.

The Doppler correction procedure assigns the velocity to the β-decay emitters (at rest), hence, their γ rays become wrongly Doppler corrected. These β-decay associated γ peaks therefore strongly contribute to the background.

3.6 Background radiation

3.6.1 The β-decay

The strongest source of background is the radioactive ion beam decay. ^{94}Rb ($\tau_{1/2} = 2.7$ s) has two decay branches, as schematically described in Fig. 3.18. Dominant branch is the β^- decay (90% strenght), and the other branch is β^--delayed neutron emission (10% strenght). Since the GPS separator selects only the A/q ratio of primary reaction products, our beam contains 10% of ^{94}Sr contamination as well (see Subs. 2.2.1). ^{94}Sr ($\tau_{1/2} = 75$ s) decay by β^--decay.

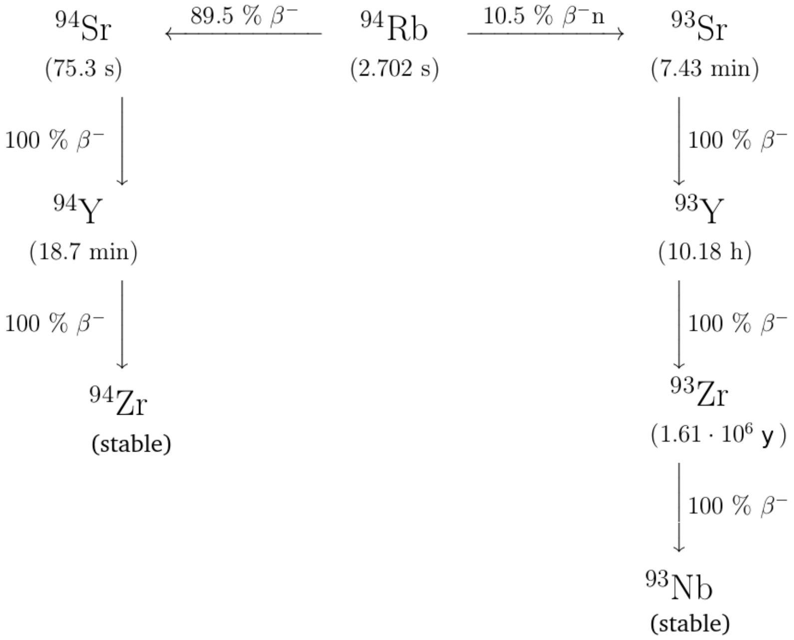

Figure 3.18: Decay scheme of ^{94}Rb beam [86]. Half-life ($\tau_{1/2}$) of each nuclide is given in parenthesis.

Consequently, the β-decay chain associated γ rays contribute to the complex background, which had to be carefully evaluated. This contribution is observed to be the strongest in the 0.8-1.6 MeV energy range. The fragment-γ-γ matrix in this energy range is plotted in Fig. 3.19. This matrix was obtained by gating on the Δt_d and the Δt_{rd} time windows for fragment and γ (see Subs. 3.4). Horizontal labels label the strongest γ rays: 837 keV (^{94}Sr), 919 keV (^{94}Zr), and 1428 keV (^{94}Y). Vertical lines label $E_\gamma = 1090$, 1309 and 1577 keV γ rays in coincidence with 837 keV in ^{94}Sr, and $E_\gamma = 1139$ keV in coincidence with 919 keV in ^{94}Zr .

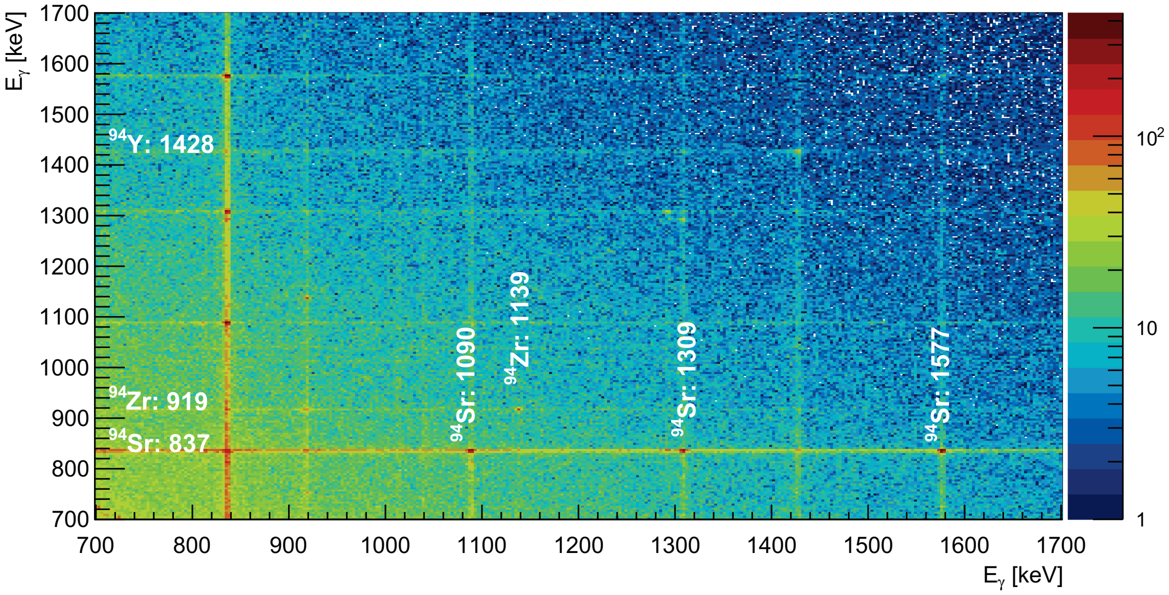

Figure 3.19: The γ-γ matrix obtained using the sum of the Δt_{rd} and Δt_d fragment-γ gate. Horizontal labels indicate the strongest β-decay associated γ rays, and vertical the γ rays in coincidence with the $E_\gamma = 837$ keV (^{94}Sr).

It is important to mention that the general background properties and the β-decay products were extensively studied within our experimental group. The results of these studies were presented in the master thesis of M. Crnac (University of Zagreb [86]) and the bachelor thesis of M. Bortolami (University of Padova [87]). More than 20 levels and γ transitions in ^{94}Zr were more firmly established and/or observed for the first time.

3.6.2 Other background sources

True coincidences with the beam contamination and the electron transitions of lead ($K_{\alpha,\beta}$), are also the sources of the γ-ray background. Thus, particularly strong γ peaks in the Δt_p gated spectrum can be found at 837 keV (^{94}Sr: $2^+ \rightarrow 0^+$) and at 75, 73 and 85 keV (Pb).

The another source of the background is the scattering on different materials in the experimental chamber. For example, aluminium is a building material of target chamber, target holder, and the HPGe crystals housing. Therefore, $E_\gamma = 1014$, 2120 keV of ^{27}Al were observed. The $E_\gamma = 595$ keV from the ^{74}Ge(n,$n^{'}\gamma$)^{74}Ge process is also strongly present. In Table 3.1 we listed the strongest background associated γ rays in Δt_p gated γ-spectrum, and their intensities. The intensities were also corrected for the efficiency of MINIBALL.

Table 3.1: The background associated γ rays in the Δt_p gated γ-spectrum. E_γ is from Ref. [88], and I_γ is the measured intensity. Obtained by the use of "thick" target.

E_γ[keV]	I_γ [a.u.]	Isotope
75	15 855 (55)	Pb
85	2 031 (52)	Pb
168	213 (49)	^{93}Y
382	96 (28)	^{94}Zr
511	846 (29)	e^+e^-
551	212 (33)	^{94}Zr
590	152 (29)	^{93}Y
595	397 (39)	Ge
678	194 (40)	^{94}Sr
837	4761 (44)	^{94}Sr
876	159 (36)	^{93}Y
919	1866 (31)	^{94}Zr
1015	317 (21)	^{27}Al
1040	306 (32)	^{93}Y
1089	782 (29)	^{94}Sr
1139	195 (33)	^{94}Zr
1293	181 (59)	^{94}Sr
1309	636 (28)	^{94}Sr
1385	85 (36)	^{93}Y
1427	3378 (52)	^{94}Y
1463	64 (25)	^{40}Ar
1577	1292 (34)	^{94}Sr
1670	163 (32)	^{94}Zr
1812	98 (34)	^{94}Sr
1867	109(27)	^{94}Sr
2093	31(8)	^{94}Sr
2143	32 (20)	^{94}Zr
2208	354 (83)	^{94}Sr, ^{27}Al
2270	147 (28)	^{94}Sr

4 Experimental results

4.1 Wilczyński plots

To learn about the behaviour of the ^{94}Rb+^{208}Pb reaction, we constructed the Wilczyński plots from the fragments energy and the scattering angle. The Wilczyński plots, or the E-θ matrices, were obtained with the use of "thin" (1 mg/cm^2) target. The wide angular coverage of the CD allowed to measure both the projectile-like and the target-like fragments simultaneously. Resulting matrices are plotted in Fig. 4.1.

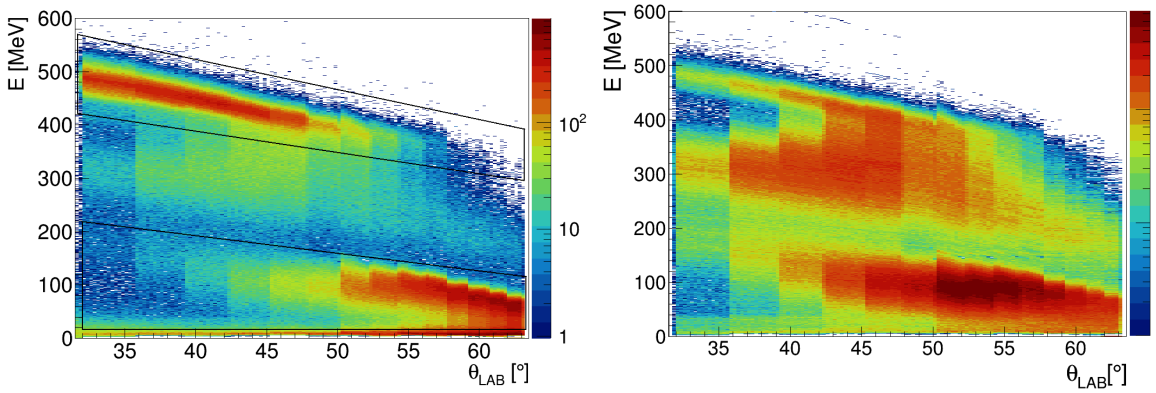

Figure 4.1: Wilczyński plots, i.e. the $E - \theta$ matrices, measured with the "thin" target. Left: all the fragments detected in the CD detector (for explanation of gates see the text). Right: the fragments in coincidence with the γ-ray in MINIBALL. Only the reaction γ rays were selected, defined by the Δt_p fragment-γ gate, and background subtracted by the Δt_r gate.

The left panel matrix was built from the fragments detected in the CD detector. One observes two separated distributions where the most intense events follow the kinematics of the elastically scattered fragments. To select them we used the gates as illustrated in the figure. Fragments whose $E - \theta$ are inside the top gate can be associated to ^{94}Rb and the Rb-like fragments. Fragments whose $E - \theta$ are inside the bottom gate can be associated to ^{208}Pb and the Pb-like fragments. For the sake of simplicity, in following text we will refer to these fragments as to the "Rb-like" and "Pb-like". The fragments between them (which are outside of the gates) will be referred to as "in-between".

The right panel matrix of Fig. 4.1 is the same Wilczyński plot as shown by the left panel, built by requiring that the fragments have at least one reaction-associated γ-ray in coincidence. Consequently, the intensity of the fragments associated to the pure elastic scattering were immediately reduced. On the contrary, the intensity of the fragments associated with the inelastic and transfer channels should become more pronounced. Indeed, the maximum of distributions of the Rb-like and the Pb-like fragments is now clearly around the grazing angles $\theta_{\mathrm{LAB}} = 50^\circ$ and 55°, respectively.

A closer look at the distribution of Rb-like fragments reveals that for the more forward angles the energy is spread in a relatively narrow range, following the kinematics of the Rutherford scattering. Going toward the larger angles, in the vicinity of the grazing angle, one notices the bending of the distribution towards the larger energy losses. The larger kinetic energy losses can be correlated with the more dissipative processes. In fact, in the region "in-between" one observes significant statistics after requiring the coincidence with γ rays. "In-between" fragments are distributed over rather wide E and θ ranges, and have higher γ ray multiplicity. It is expected that the corresponding Z and A of these fragments also have more broad distributions, due to the large energy losses and the possible contribution of non-binary reaction mechanism.

To better understand the underlying reaction mechanisms we have also studied the multiplicity of the γ rays in more details by looking at the regions of Rb-like, Pb-like and "in-between" separately, and with respect to the angle. The constructed γ-ray multiplicity distributions are plotted in Fig. 4.2 for a more forward (red histogram) and a more backward θ_{LAB} (blue). A more forward angular range involves the angles forward and near the grazing for the Rb-like fragments. According to the binary partner kinematics, a more backward angular range includes the angles larger than the grazing for the Rb-like fragments, and near the grazing for the Pb-like.

By looking at the γ-ray multiplicity distribution for the Rb-like fragments one can see that the low multiplicity of the γ rays dominates at the more forward angle (red histogram). For the larger angles (blue), which are also larger than the grazing angle, the number of events with higher multiplicity increases. A qualitatively similar behavior

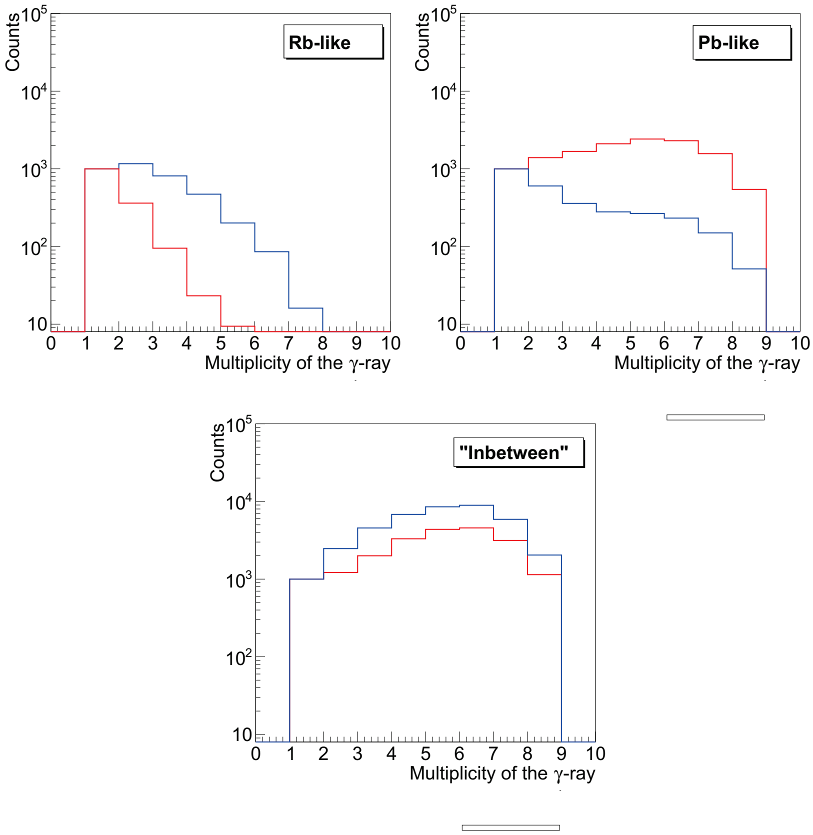

Figure 4.2: Gamma-ray multiplicity distribution in coincidence with the fragment which is given in the inset. The different θ_{LAB} regions are labeled with different colors, red corresponding to the θ_{LAB} = [41, 54]°, and blue to the θ_{LAB} = [54, 63]°.

is observed in the γ-ray multiplicity distribution for the Pb-like fragments (with respect to their kinematics). On the contrary, the distributions associated to the "in-between" fragments have maximum at large multiplicity (≈5-6) and do not show angular dependence. This indicates that the underlying processes might be significantly different than the grazing collisions and guided by a strong dissipation.

The $E - \theta$ behavior observed in the Wilczyński plots depends also on the product of the charge numbers of the projectile and the target, $Z_a Z_A$. For comparison with our system, in Fig. 4.3 we show an example of Wilczyński plots, measured for the different $Z_a Z_A$ [89]. When this product increases, the reaction evolves from an “orbiting-like” configuration (top panels), in which the two nuclei are in contact for quite a long time and rotate in a di-nuclear configuration exchanging many nucleons, towards an intermediate or "focusing" configuration. In “focusing” configuration (bottom left panel), the reaction products are scattered in a more limited angular range with a strong overlap of quasi-elastic and dissipative processes. Finally, in the “repulsive” configuration (bottom right panel) the Coulomb field is so high that the nuclei cannot come into close contact. The ^{94}Rb+^{208}Pb system, considering it's Z_aZ_A, is somewhere in-between these "orbiting" and "focusing" cases.

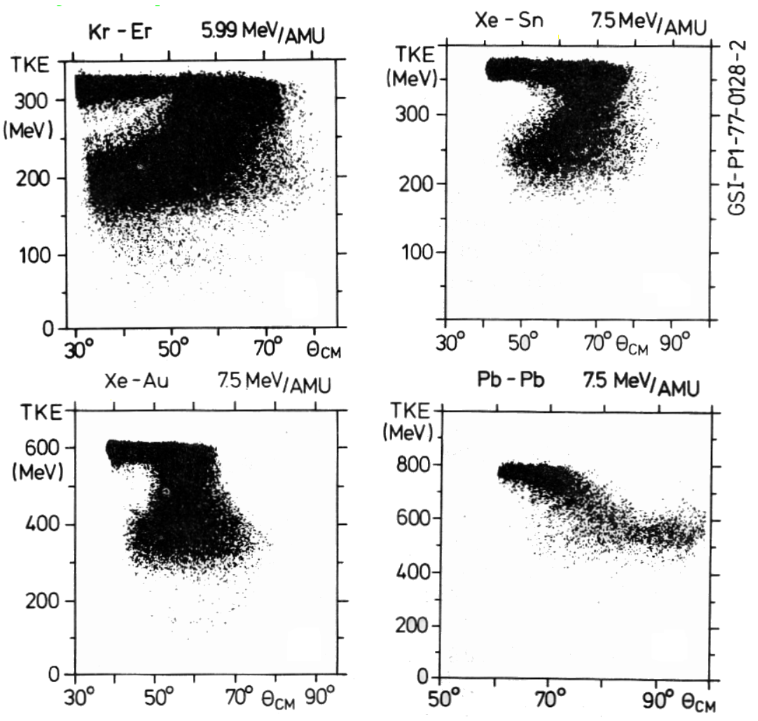

Figure 4.3: Wilczyński plots for different heavy-ion reactions at the indicated energies. From Ref. [89].

For completeness, the Wilczyński plot was constructed also by using the "thick" (13 mg/cm^2) target. As one expects, significantly larger energy losses than in the "thin" target case were observed. Nevertheless, one could recognize the two distributions which, in principle, correspond to the Rb-like and the Pb-like fragments. The resulting matrix is shown in Appendix in Fig. A.1.

At this point we want to briefly comment on the CD detector angular coverage. Looking at the Wilczyński plots of ^{94}Rb+^{208}Pb one could see that Rb-like fragments are scattered inside the whole CD detector angular range. At the same time the Pb-like are detected in a reduced angular range, as expected from the binary partner kinematics. In fact, the detector position was chosen to fully cover the Rb-like, which are also the most energetic reaction partners. In that selected position, also the high geometrical efficiency is being preserved.

4.2 Angular distributions

Large active area of the CD detector ($\theta_{\text{LAB}} = [32{,}63]^\circ$) offers the possibility to study the fragment angular distributions. At first, we had carefully investigated the CD modularity by constructing the angular distributions with different step in θ_{LAB}. The step of $\Delta\theta = 3.12^\circ$ was the best choice, as it is similar to the average angular width of the each ring.

A starting point in the analysis of the angular distributions is usually to extract and study the elastic scattering. For this aim, we selected only the fragments for which no γ-ray was detected. In this way, the Rb-like and the Pb-like fragments were selected (see the gates in Fig. 4.1) and their elastic angular distributions were studied. The obtained experimental points of $d\sigma/d\Omega$ [a.u.] in Fig. 4.4 were constructed from the relation

$$\frac{\Delta\sigma(\theta_i)}{\Delta\Omega} = \frac{N(\theta_i)}{2\pi sin(\theta_i)\Delta\theta} \tag{4.1}$$

where $N(\theta_i)$ is the number of counts, and θ_i is the geometrical center of each $\Delta\theta$. By definition, $N(\theta_i)$ is integrated over the $\Delta\phi = 2\pi$ and $\Delta\theta = 3.12^\circ$ angular ranges. Extracted $d\sigma/d\Omega$ values were normalized to the Rutherford differential cross section $d\sigma/d\Omega_R$. For the normalization point we used the value measured at the forward angle $\theta_{\text{LAB}} = 39^\circ$. In addition, θ_{LAB} of the Pb-like fragments were translated into the kinematically corresponding θ_{LAB} of the Rb-like, and plotted in the same figure. This allowed to compare the two distributions, obtained independently from each other. One can see that the distributions overlap.

Although the efficiency of MINIBALL is rather high (∼6%), some selected fragments might have an undetected γ-ray in coincidence. This means that, besides the pure elastic scattering, by imposing a condition that no γ-ray was detected in coincidence, the inelastic and transfer channels may contribute to the extracted angular distributions as well. Since we do not have Z and A identification, this is inevitable. For these reasons we refer to the extracted distribution using the term "quasi-elastic". Still, at the most forward scattering angles, where the elastic scattering is by far the most dominant process, the contribution of the other processes can be considered negligible.

To cross-check the elastic angular distributions, we have used different methods. For

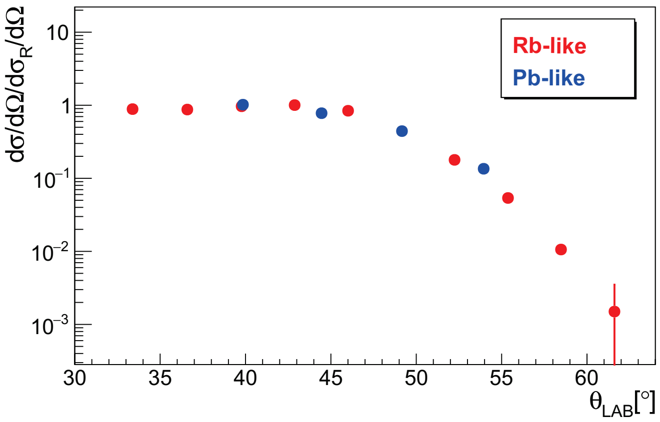

Figure 4.4: The quasi-elastic angular distribution of the Rb-like fragments (red) and the Pb-like fragments (blue), constructed without a γ-ray in coincidence. The error bars are statistical.

instance, we investigated how these distributions change when two fragments were detected in coincidence. We also tried to gate on the fragments in coincidence with the γ rays in delayed regions, or with the particular strong β-decay lines. All these methods resulted in similar angular distribution shapes. In conclusion, the method based on the fragments for which no γ-ray was observed in coincidence gave the statistically most significant results. This relatively simple requirement preserves statistics, differently from the application of more complex gates, or multiple coincidences.

To obtain the normalization factor for the total cross section we have used the Distorted Wave Born Approximation (see the next Subsection), and we also constructed the angular distributions of the excited states, in a manner similar as for the quasi-elastic distribution. A strongly excited state in ^{208}Pb, the 3^- was selected[8]. The angular distribution of 3^- was constructed from the fragments in coincidence with $3^- \rightarrow 0^+$ transition of $E_\gamma = 2615$ keV. The 3^- state is populated predominantly via a direct mechanism, and the only considerable population from above comes from the $5^- \rightarrow 3^-$ transition of E_γ $= 583$ keV. Thus, the $5^- \rightarrow 3^-$ angular distribution was also constructed and subtracted from the $3^- \rightarrow 0^+$ one. The final results are presented in Fig. 4.5. The error bars in Fig. 4.5 (and also in Fig. 4.4) are only statistical. In the construction of these angular distributions the background was subtracted using the fragments in coincidence with the γ-ray regions left and right from $E_\gamma = 583,\ 2615$ keV. These γ transitions can be also seen in the top γ-spectrum of Fig. 4.7.

---

[8] ^{208}Pb level scheme is presented in Sec. 5.1, Fig. 5.3

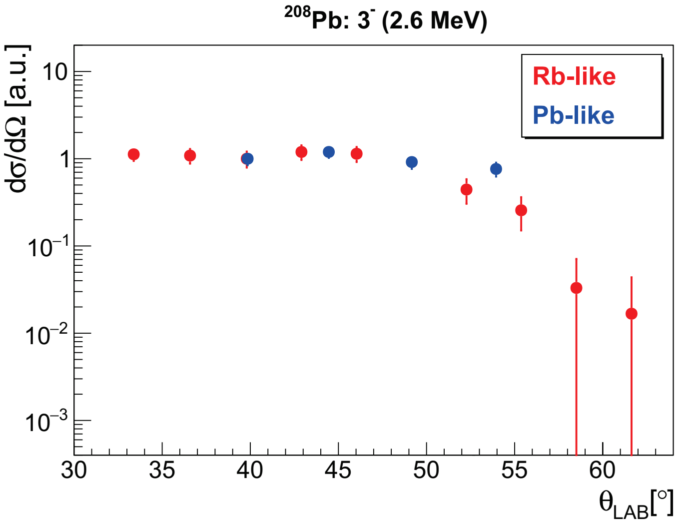

Figure 4.5: The angular distribution of the 3^- state in ^{208}Pb, from the Rb-like fragments (red) and the Pb-like fragments (blue). The error bars are statistical.

4.2.1 Angular distribution calculations

In Fig. 4.6 we presented the experimental angular distributions (points) alongside with the DWBA calculations (lines). The angular distributions of the inelastic excitations were in many cases successfully reproduced with DWBA, as for example in Refs. [5, 90]. Also, the comparison of the experimental and DWBA calculated distributions is often used to obtain the absolute normalization factor. The calculations were provided in collaboration with Prof. G. Pollarolo from the theoretical group of the University of Torino. They were obtained within the coupled channel approach, using the code PTOLEMY with the standard optical potential and tabulated values [91–93]. For the channels not accounted for explicitly in the coupling, the additional (microscopically calculated) imaginary part of the potential was used [94, 95].

The potential was checked first through the comparison with the quasi-elastic distribution. Data and theory are shown with red points and red line in the figure. As one could expect, at forward angles the quasi-elastic distribution agrees with the Rutherford scattering. The calculations describe well the extracted distribution, although the drop in the experimental distribution is not so steep as the calculated one. The largest differences are observed at the most backward angle where the inelastic and transfer contributions are also expected to be the largest ones.

To obtain the normalization factor, the distribution of the directly populated 3^- state in ^{208}Pb was normalized to the calculated $d\sigma/d\Omega$ [mb/sr]. Similarly to the quasi-elastic distribution, the 3^- distribution is rather flat at the most forward angles (black points). The DWBA distribution (black lines) shows some oscillations with the maximum at the grazing angle. It is obvious that due to the large step in θ_{LAB}, the data cannot reproduce the oscillations. The overall agreement of the calculated and experimental data we have presented supports the procedure adopted to extract the angular distributions.

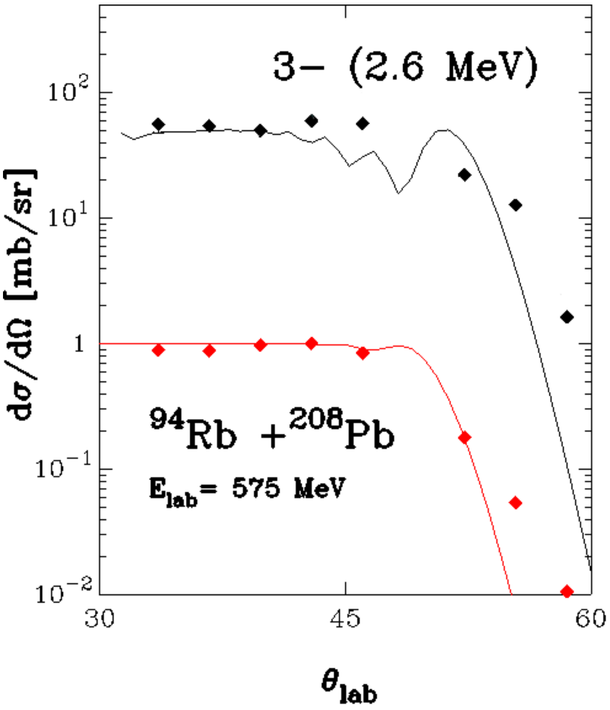

Figure 4.6: The experimental angular distributions (points) and the DWBA calculations (lines), performed at the beam energy at mid-target, $E_{\mathrm{LAB}} = 575$ MeV. Bottom data and calculations were also normalized to Rutherford.

A next step in the cross section evaluation was to perform the integration of the angular distribution of the 3^- state

$$\sigma = \sum_{i=33.56^\circ}^{61.64^\circ} 2\pi \frac{\Delta\sigma(\theta_i)}{\Delta\Omega} \sin(\theta_i)\,\Delta\theta \tag{4.2}$$

where the $\Delta\sigma/\Delta\Omega$ are the experimental points, and θ_i central angles within the [33.56, 61.64]° range. The interval between each θ_i is $\Delta\theta_{\mathrm{LAB}} = 3.12^\circ$. σ obtained in this way is 77.12 (6.9) mb, which corresponds to the 125(11) counts observed in the MINIBALL.

One then obtains the corresponding normalization factor N_σ

$$N_\sigma = 0.617\, mb \tag{4.3}$$

We will use this coefficient to deduce the cross sections of different transfer channels in Pb isotopes.

4.3 Gamma-spectra

To study the reaction cross section and the structure of the populated isotopes we used (mainly) the prompt and delayed γ spectra. The procedure to obtain these spectra was explained in details in Secs. 3.3, 3.4, 3.5.

4.3.1 "Thin" target γ spectra

For the total cross section studies, in particular, the "thin" target and the γ rays in coincidence with the Rb-like fragments were used. By employing the Rb-like fragment-γ coincidence gate we have successfully reduced the background. The resulting prompt γ-ray spectra, which were Doppler corrected for the Pb-like and Rb-like fragments, are plotted in Fig. 4.7. Also, the non Doppler corrected prompt and delayed γ-ray spectra are plotted in Fig. 4.8. In each spectrum only the strongest E_γ were labeled. One can easily see that the majority of the γ peaks were attributed to ^{94}Rb and ^{208}Pb, and to the following neutron transfer channels:

- $(-1n)$: ^{93}Rb $+^{209}$Pb
- $(+1n)$: ^{95}Rb $+^{207}$Pb
- $(-2n)$: ^{92}Rb $+^{210}$Pb.

In particular, in the spectrum Doppler corrected for the Pb-like fragments in Fig. 4.7, the strong γ transitions of 583 and 2615 keV are observed. They are attributed to ^{208}Pb, and, as we stated before, used for the construction of the 3^- state angular distribution. Most of the γ transitions attributed to transfer channels are observed in the E_γ = [500, 1700] keV range. The γ transitions at 779, 1423 and 1567 keV were attributed to ^{209}Pb, and the 570, 898, and 2485 keV to ^{207}Pb. The latter γ-peak is rather strong, and we assume it contains also the contribution of E_γ = 2491 keV, which is a single-particle transition in ^{209}Pb. Through the comparison with the "thick" target γ-spectrum (Fig. 4.9), where the resolution in E_γ allows to resolve these two γ-transitions, we could estimate that the contribution of E_γ = 2485 keV is stronger. The obtained relationship of intensities of E_γ = 2491 keV and E_γ = 2485 keV was used to estimate the relative contributions of these two transitions.

Then, E_γ = 528 keV and E_γ = 1234 keV, which are not labeled in the spectrum, are attributed to ^{210}Pb. The undesignated E_γ = 351 keV could be attributed to the $(+1p)$ channel, i.e. ^{95}Sr $+^{207}$Tl. In fact, the first excited states of both partners have very similar γ transitions towards the ground state, namely 351 keV (^{207}Tl) and 352 keV (^{95}Sr) (see Sec. 4.5). Most likely, we observe the overlap of the correctly and wrongly Doppler corrected γ-ray.

The low energy part of the spectrum (E_γ < 100 keV) is strongly dominated by the $K_{\alpha,\beta}$ electron transitions of lead. In addition, E_γ = 511 keV, which is essentially the γ-ray from e^-e^+ process, is also the γ-transition in ^{208}Pb. Below the 500 keV one observes a strong contribution of the Rb-like γ rays wrongly Doppler corrected for the Pb-like.

Similarly, in the spectrum Doppler corrected for the Rb-like fragments in Fig. 4.7 the strongest γ transitions were attributed to the beam and to the binary partners of ^{209}Pb, ^{207}Pb and ^{210}Pb. Many low energy γ rays were attributed to ^{94}Rb, the 111, 186, 217 and 405 keV. One also observes the strong 837 keV transition of ^{94}Sr, which is mainly coming from the beam impurity, and wrongly Doppler corrected β-decay. E_γ = 253, 267, 324, 733 and 913 keV were attributed to ^{93}Rb, and the E_γ = 142.0, 142.3 and 146 keV to ^{92}Rb. Due to the energy resolution, the latter are observed within the same γ peak, and labeled simply as an '142' γ-transition. For more details, see Sec. 4.4.3, where we discuss the ^{92}Rb γ-γ coincidences. At last, the structure of very neutron-rich ^{95}Rb is rather unknown. There is a possibility that some of the unattributed γ rays (labeled with '*' in the spectrum) could be from ^{95}Rb.

As expected, when the Doppler correction is not applied (see Fig. 4.8), the γ rays of both the Rb-like and the Pb-like fragments are observed together (along with the β-decay). Of the uttermost importance are E_γ = 97, 297, 800 keV, attributed to isomeric decays in ^{210}Pb. The half-lives of the isomers in ^{210}Pb are comparable to the width of the prompt gate, and this is why we had observed them in the prompt γ-spectrum as the stopped components. Indeed, the application of the delayed gate reduces the background (with respect to the situation one has with the prompt gate). In the delayed γ-spectrum, one can more clearly see the rather strong E_γ = 97, 297 and 800 keV, related to the decay of the isomeric states. The other γ transitions, attributed to ^{92,94,95}Rb, point to the population of other isomers.

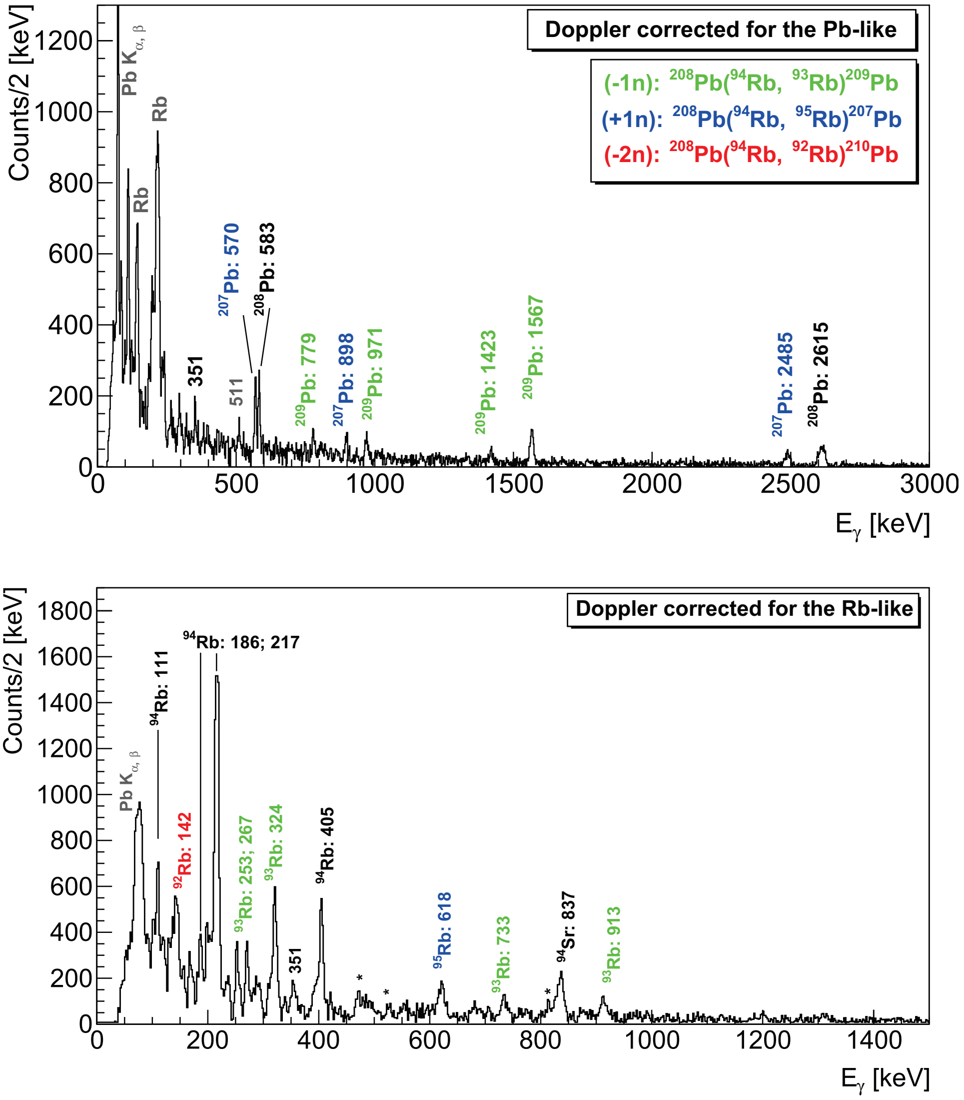

Figure 4.7: The prompt γ-ray spectra, obtained with the use of 1 mg/cm^2 target. The spectra were Doppler corrected for the Pb-like fragments (top), and for the Rb-like (bottom). The values of E_γ are as tabulated [88], except the $E_\gamma = 405$ keV (^{94}Rb) which is as in our work and Ref. [96]. Color code of the γ-transition describes the neutron transfer channel, as given in the inset. Only the relevant parts of the x-axis range are plotted. Labels '*' are for the unattributed γ rays.

In Tab. 4.1 we have summarized the intensities of the γ transitions attributed to Pb isotopes, I^1_γ. The values of I^1_γ are thus obtained by the use of "thin" target, and corrected for the efficiency of MINIBALL (Subs. 3.1). Only the main transitions used in the construction of the cross sections are listed. The selection of these transitions and the cross sections obtained are discussed in Chap. 6. Especially concerning the cross section extraction, for ^{208,207,209}Pb we have used the prompt and Doppler corrected γ-spectrum, and for ^{210}Pb the non Doppler corrected γ spectra. In the latter case both the prompt and the delayed components were taken into account.

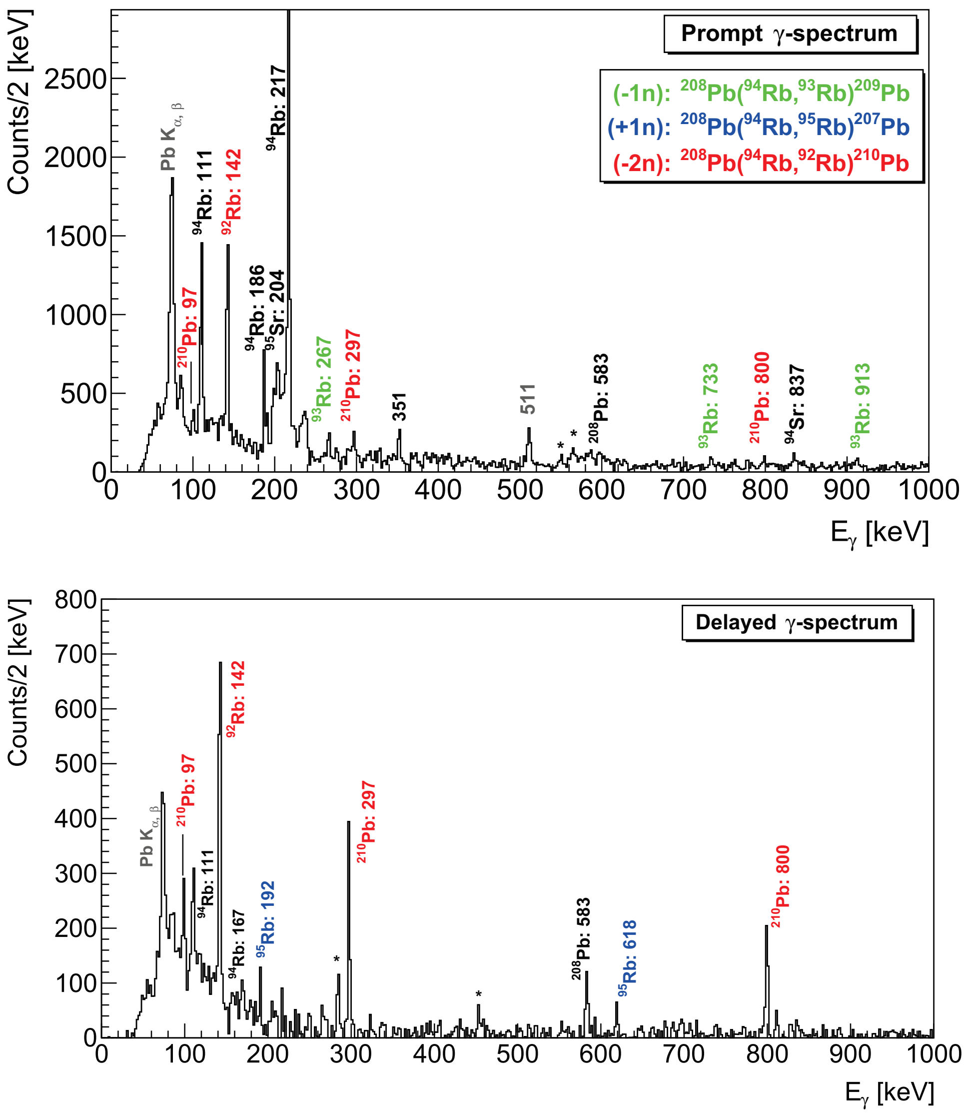

Figure 4.8: The 1 mg/cm^2 target γ-ray spectrum, prompt (top) and delayed (bottom). The values of E_γ are as in Ref. [88], except the $E_\gamma = 297$, 405 keV which are as in the our work and Refs. [97] and [96], respectively. Color code of the γ-transition describes the neutron transfer channel, as given in the inset. Only the relevant parts of the x-axis range are plotted. Labels '*' are for the unattributed γ rays.

Table 4.1: The measured intensity of E_γ attributed to the Pb isotopes, used in the ^{207,208,209,210}Pb cross section evaluation. Top part: I^1_γ from the prompt γ-spectrum Doppler corrected for the Pb-like, and the non-Doppler corrected for E_γ = 800 keV. Bottom part: I^1_γ from the delayed γ-spectrum. E_γ are as in Ref. [88], and I^1_γ is corrected for the efficiency of MINIBALL.

E_γ[keV]	I^1_γ [a.u.]	Isotope
Prompt		
570	73(11)	^{207}Pb
583	75(19)	^{208}Pb
779	39(13)	^{209}Pb
800	12(5)	^{210}Pb
898	36(16)	^{207}Pb
1423	21(7)	^{209}Pb
1567	124(18)	^{209}Pb
2485	82(12)	^{207}Pb
2491	13(2)	^{209}Pb
2615	207(13)	^{208}Pb
Delayed		
800	56(13)	^{210}Pb

4.3.2 "Thick" target γ spectra

For nuclear structure studies, mainly the γ spectra and the γ-γ coincidences from the measurement with "thick" target were analysed. We plotted the corresponding prompt and delayed γ spectra in Fig. 4.9 (top and bottom panels, respectively). In each spectrum only the strongest E_γ are labeled. These spectra were obtained from all fragments. Considering the "thick" target thickness (13 mg/cm^2), a character of detected fragments should mainly be the Rb-like. Also, the contribution of the fragments populated by the processes other than the transfer reactions is possible.

Similarly to the "thin" target case, the observed γ transitions are mainly attributed to ^{94}Rb and ^{208}Pb, and to the $(-1n)$, $(+1n)$, $(-2n)$ neutron transfer channels. As one could expect, all the γ transitions which are attributed to these channels and observed in the "thin" target spectra (Figs. 4.7, 4.8), are also observed in the "thick" target ones.

Moreover, the statistics collected during the measurement with the "thick" allowed to observe a larger number of γ transitions. A detailed analysis of the "thick" target γ spectra will be given in the following Section and Chap. 5, dedicated to the excited states in the isotopes of Rb and Pb, respectively.

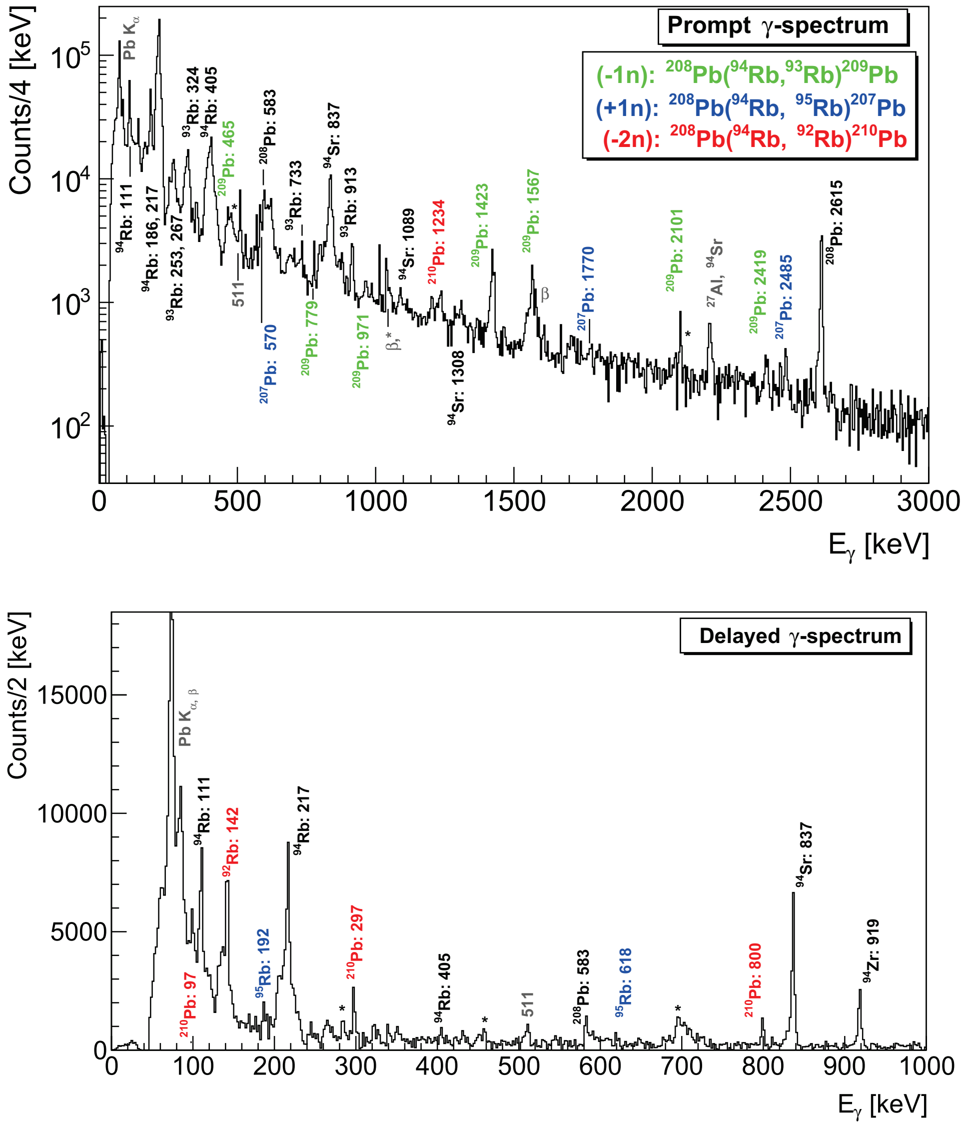

Figure 4.9: The "thick" (13 mg/cm^2) target γ-ray spectrum, prompt (top) and delayed (bottom). The values of E_γ are as in Ref. [88], except the E_γ = 297, 405 keV which are as in the our work and Refs. [97] and [96], respectively. Colour code of the γ-transition describes the neutron transfer channel, as given in the inset. Only the relevant parts of the x-axis range are plotted. Labels '*' are for the unattributed γ rays

4.4 Excited states in $^{92-95}$Rb

Rubidium isotopes populated in the reaction are the $^{207-210}$Pb binary partners, $^{92-95}$Rb. Obviously, these Rb isotopes are well away from the stability line ($N/Z \sim 1.5$). Thus, the evaluated spectroscopic information in $^{92-95}$Rb, which is reported in the Evaluated Nuclear Structure Data Files [88], was obtained mostly from fission and β-decay studies. Using this data as a reference, we have successfully attributed the observed γ transitions to $^{92-95}$Rb.

In this Section, the $^{92-95}$Rb level schemes will be presented. Level schemes were constructed by analysing the prompt γ-spectrum and the γ-γ matrix, both obtained with the use of "thick" (13 mg/cm^2) target. The prompt γ-spectrum is plotted in the top panel of Fig. 4.9. The intensity of the γ rays observed in this spectrum, I_γ^{13}, had to be corrected for the efficiency of MINIBALL (see Subs. 3.1).

The level scheme properties, the energy of the γ-transition (E_γ), and energies and spins of the associated initial (E_i, J_i^π) and final states (E_f, J_f^π) are mainly adopted from the evaluated data files [88]. The results of the same analysis for $^{207-210}$Pb will be discussed in more details in Chap. 5.

4.4.1 Review of previous studies

The β-decay studies were the first to explore the neutron-rich Rb isotopes. They paved the way to the ^{252}Cf, ^{248}Cm spontaneous fission techniques, which use the known γ rays to select the fission products. In the work of Ref. [98], employing the ^{252}Cf source and the GAMMASPHERE γ-array, the authors reported the new γ transitions in ^{91,92,93}Rb. These γ transitions were attributed to the newly observed states, which are inaccessible in the β-decay studies, such as $J^\pi = 7/2^-$ in ^{93}Rb. More specifically, the known $142(1^-) \xrightarrow{142} 0(0^-)$ keV γ-transition in ^{92}Rb and $217(4^-) \xrightarrow{217} 0(3^-)$ keV γ-transition in ^{94}Rb were used to attribute the new γ transitions to the complementary fragments, ^{155,156}Pm. The identification of the new γ transitions in ^{155,156}Pm helped to identify the unknown and strongly observed $E_\gamma = 913$ keV. From the comparison of the fission yields in neighbouring channels, the latter was uniquely attributed to the $913(7/2^-) \xrightarrow{913} 0(5/2^-)$ keV transition in ^{93}Rb. A rather rich level scheme up to 4 and 4.7 MeV was built for ^{92}Rb and ^{93}Rb, respectively.

The advent of thermal neutron-induced fission techniques has opened up the new possibilities. In the work of Refs. [96, 99, 100] a thermal neutron beam was provided by the Institut Laue-Langevin reactor, in Grenoble, and sent onto a thin ^{235}U target. The fragments of interest were stopped in the foil, surrounded by the 16 HPGe detectors, while complementary fragments were entering a mass separator. The cascade of 111, 169, 217, 339 and 648 keV γ transitions related to the decay of unknown isomer was observed [96]. The isomer was uniquely attributed to ^{94}Rb, from the mass distribution of the complementary fragment in coincidence. The mentioned γ transitions were used to gate on the ^{252}Cf, ^{248}Cm spontaneous fission γ spectra, to identify the prompt (feeding) γ rays. The two isomeric states were described as 1485(8^+) keV and 2075(10^+) keV, with half-lives of 18(1) and 107(16) ns, respectively. In this way, ^{94}Rb level scheme up to E_{ex} = 3944 keV and $J = 15$ was established. In addition, in the similar manner as for ^{94}Rb (using the mass distribution of a complementary fragment), the isomer at 284 keV ($\tau_{1/2}$ = 54(3) ns) was attributed to ^{92}Rb.

In ^{9}Be(^{238}U,X) experiment at E_{LAB} = 80 MeV·A [101, 102] ^{95}Rb was selected inside the fragment separator. Using the single HPGe detector, few states and γ rays could be observed, following a decay of E_{ex} = 835 keV isomer ($\tau_{1/2}$ < 500 ns). In the more recent work of Ref. [100] (also cited above), new properties were proposed for this same isomer. They proposed the similar excitation energy, E_{ex} = 810 keV, and the $\tau_{1/2}$ = 94(7) ns. However, up to date, ^{95}Rb level scheme remains rather unknown.

Probably the most interesting phenomena in Rb and nearby isotopes is the sudden transition from spherical to deformed nuclear shapes at N = 60 [103]. The mean square charge radii have been systematically measured in this region and presented in Fig. 4.10. The linear trend in the difference of the mean square charge radii ($\delta < r_C^2 >$) was observed in Mo isotopes, and in Kr isotopes up to $N = 60$. In the other isotopes presented in the figure one notices a drastic increase of $\delta < r_C^2 >$ at $N = 60$ (a shape transition). Among these isotopes, Rb lie the farthest from stability.

Only recently, the excited states of very short-lived ^{97}Rb ($N = 60$) and ^{99}Rb ($N = 62$) were reported for the first time. Radioactive ion beams of ^{93,95,97,99}Rb were produced by ISOLDE at E_{LAB} = 2.8 MeV·A. The level schemes presented in Fig. 4.11 [104] were obtained with the MINIBALL coupled to the CD. This allowed to fulfill the missing spectroscopic data in the more neutron-rich side of Rb chain. The authors have reported that the ground-state excitations show a marked distinction between single-particle-like structures below the $N = 60$, and rotational bands above.

At this point, we would like to mention that ^{93,95}Rb level schemes were also obtained in this same experiment. These results are yet unpublished, and were presented in conference talks and proceedings (as for example in Ref. [105]). Once these results are published, it would be interesting to make a comparison to their level schemes.

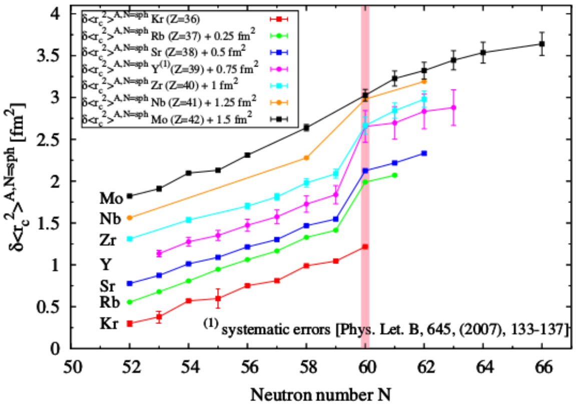

Figure 4.10: Difference in the mean square charge radii in the vicinity of $N = 60$ for Kr, Rb, Sr, Y, Zr, Nb, and Mb isotopes, given relative to their spherical form. Each isotonic chain is set apart by 0.25 fm^2 for clarity. From Ref. [106]

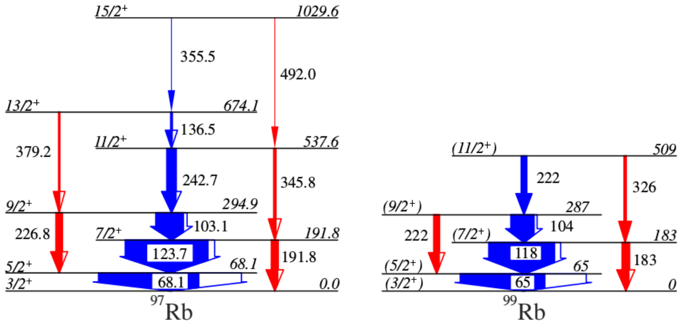

Figure 4.11: Level schemes of ^{97}Rb and ^{99}Rb. Pure $E2$ transitions are given with red arrows, while the mixed ($M1$, $E2$) with blue ones. From Ref. [104].

4.4.2 ^{94}Rb

In ^{94}Rb+^{208}Pb experiment, we observed the excitation of states up to $E_{ex} = 359$ keV in ^{94}Rb. The γ transitions attributed to ^{94}Rb dominate the low energy part of the prompt γ-ray spectra. Their intensities I_γ^{13}, obtained with the use of "thick" target, are summarized in Tab. 4.2. The I_γ^{13} were normalized to the intensity of $E_\gamma = 217$ keV, which is also the strongest transition in the prompt γ-spectrum (Fig. 4.9).

A projection of the γ-γ matrix at E_γ = 217 keV was constructed, and plotted in the top left panel of Fig. 4.12. Two strong transitions are observed in coincidence, E_γ = 111 and 405 keV, and their projections are shown in the same figure. Thus the 328(5^-) $\xrightarrow{111}$ 217(4^-) $\xrightarrow{217}$ 0(3^-) keV γ transitions were added in ^{94}Rb level scheme in Fig. 4.14.

Table 4.2: Gamma rays attributed to ^{94}Rb. The energy, spin, parity of levels, and the energy of γ transitions are as in [107], except for E_γ = 405 keV (see text). Relative intensities I_γ^{13} are normalized to the strongest γ-ray at E_γ = 217 keV.

E_γ[keV]	E_i[keV]	J_i^π	E_f[keV]	J_f^π	I_γ^{13}[%]
111	328	(5^-)	217	(4^-)	35(1)
167	359	(1,2,3)	191	-	3.1(0.4)
186	191	-	5	-	30(1)
217	217	(4^-)	0	3 ($^-$)	100(1)
219	224	-	5	-	-
355	359	(1,2,3)	5	-	1.3(0.1)
359	359	(1,2,3)	0	3 ($^-$)	0.8(0.1)
405	622	-	217	(4^-)	13(1)

According to our knowledge, E_γ = 405 keV of ^{94}Rb was observed in the work of Ref. [96]. Probably due to its relatively low intensity, the authors did not place it in the ^{94}Rb level scheme. In our case, the coincidence between the 217 keV and 405 keV is rather strong, and we added a 622$\xrightarrow{405}$217(4^-) $\xrightarrow{217}$0(3^-) keV transition in the level scheme. Thus, we have proposed a new state at E_{ex} = 622 keV.

The other strong branch is 359(1,2,3) $\xrightarrow{167}$ 191(4^-) $\xrightarrow{186}$ 5 keV (see Fig. 4.13). State of spins (1,2,3) has three decay branches of comparable strength, E_γ = 167, 355, 359 keV. All of them were observed. However, the intensities of these E_γ (the ones in Tab. 4.2) are not in agreement with the evaluated branching ratios, obtained from ^{94}Kr β-decay. No other experiment reports the observation of (1,2,3) state.

While E_γ = 167 and 359 keV are clearly observed in the "thick" target γ-spectrum,

$E_\gamma = 355$ keV is not. This is due to its vicinity to the strong 351 keV γ-ray. $E_\gamma = 355$ keV was inscribed as an dashed-arrow (tentative) γ-transition in ^{94}Rb level scheme.

At this point, we would like to mention that the Doppler broadening of the strongest $E_\gamma = 217$ keV is rather large. Thus, one couldn't make any firm conclusions about the observation of $E_\gamma = 219.5$ keV. The latter can be attributed to an 224→ 5 keV transition [107]. In our case, it is not present in the γ-γ coincidences, but we kept it in the level scheme and labeled it with dashed-arrow.

A glance at the "thick" target delayed γ-spectrum (Fig. 4.9) points to the isomers in ^{94}Rb. In that γ-spectrum, the $E_\gamma = 111$, and 217 keV attributed to ^{94}Rb are strongly observed.

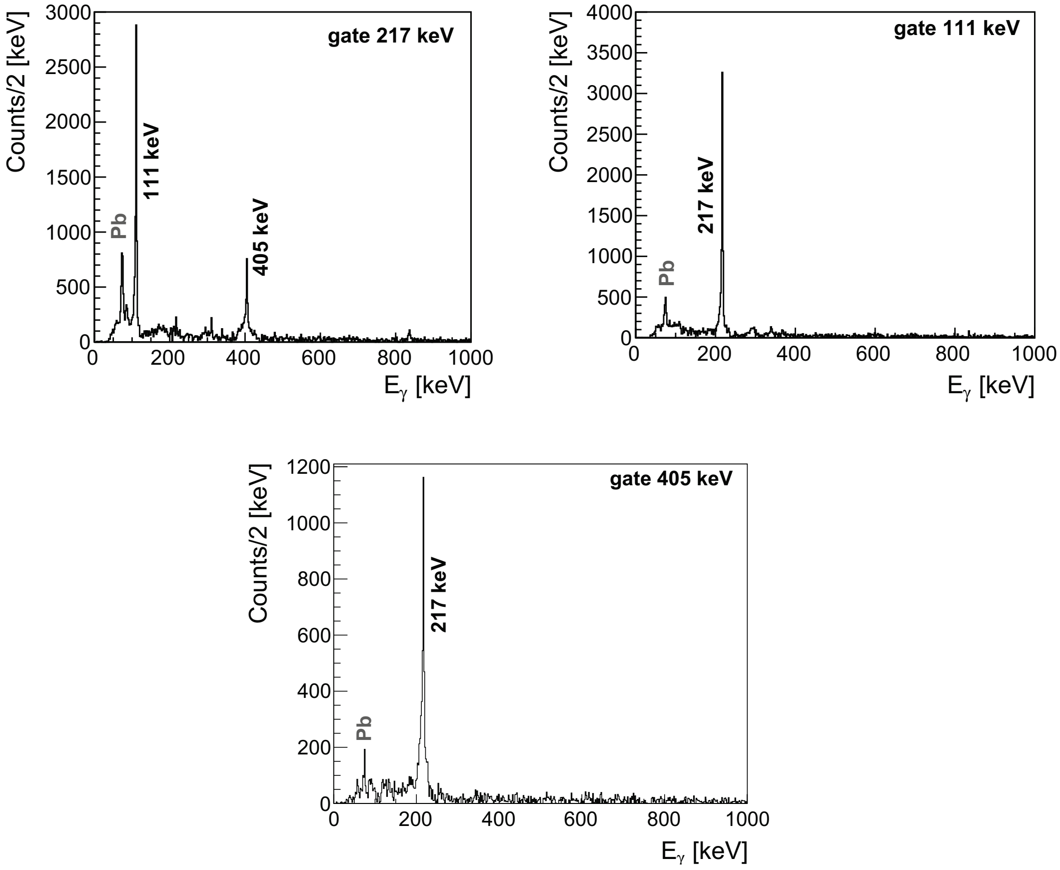

Figure 4.12: Projected γ-γ matrix, obtained with the 217 keV gate (top left), 111 keV gate (top right), and the 405 keV (bottom).

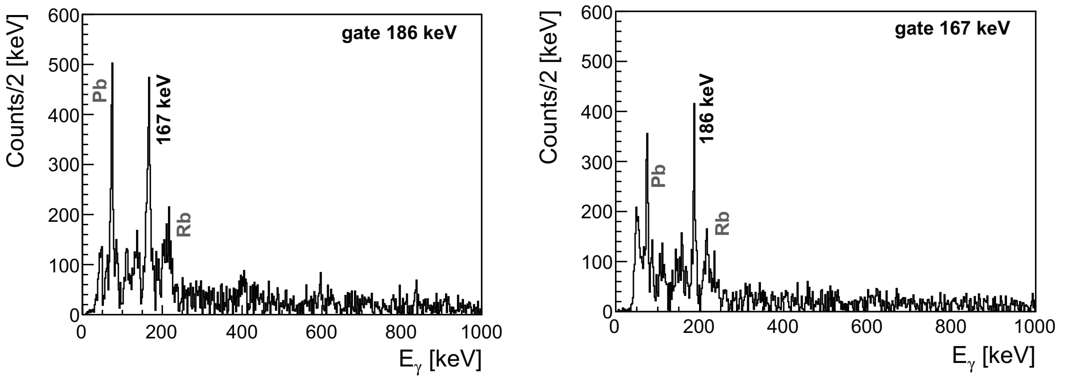

Figure 4.13: Projected γ-γ matrix, obtained with the 186 keV gate (left) and the 167 keV gate (right).

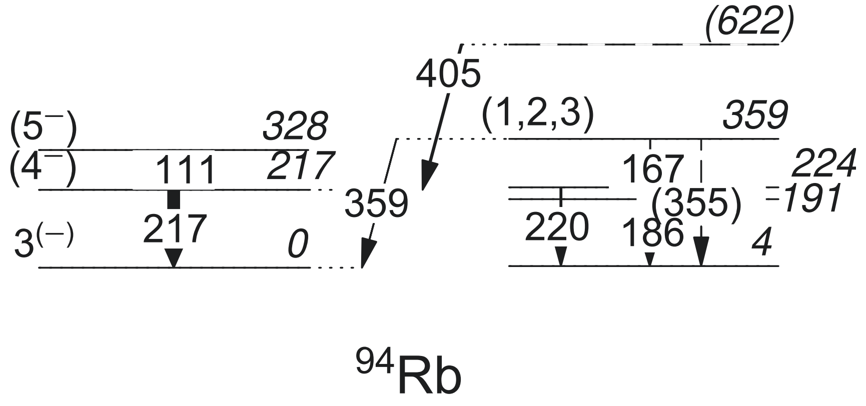

Figure 4.14: The experimental level scheme of ^{94}Rb. Relative γ-ray intensities are indicated by the width of the arrows. The energy, spin and parity of levels and the energy of γ transitions, if known, are as in Ref. [107]. $E_\gamma = 405$ keV was attributed to the state at $E_{ex} = 622$ keV in this work.

4.4.3 ^{92}Rb

We observed states up to $E_{ex} = 432$ keV in ^{92}Rb, from the attributed $E_\gamma = 142.3$, 142.0 and 146 keV. One notices that these E_γ, also presented in Tab. 4.3, are very similar. Thus, for the γ transitions of $284(3^-) \xrightarrow{142} 142(1^-)$ keV and $142(1^-) \xrightarrow{142} 0(0^-)$ keV, only the summed intensity I_γ^{13} could be extracted. The latter is much stronger than the I_γ^{13} attributed to $E_\gamma = 146$ keV.

A projection of the γ-γ matrix at $E_\gamma = 142$ keV is plotted in the left panel of Fig. 4.15. The inset of the γ-spectrum represents a closer look at the 0.14 MeV energy region. One observes that both the $E_\gamma = 142$ keV and $E_\gamma = 146$ keV are in coincidence with $E_\gamma = 142$ keV. $E_\gamma = 146$ keV was attributed to the $432(4^-) \xrightarrow{146} 142(1^-)$ keV transition, and added in ^{92}Rb level scheme in Fig. 4.16.

The evaluated half-life of the 1^- state is $\tau_{1/2} = 54(3)$ ns [99, 108]. This is why the $E_\gamma = 142$ keV, which was attributed to that state, is observed rather strongly also in the delayed γ-spectrum in Fig. 4.9.

Table 4.3: Gamma rays attributed to ^{92}Rb. The energy, spin, parity of levels, and the energy of γ transitions are as in Ref. [108]. Relative intensities I_γ^{13} are normalized to the strongest E_γ = 142 keV (see text).

E_γ[keV]	E_i[keV]	J_i^π	E_f[keV]	J_f^π	I_γ^{13}[%]
142.3	142	1^-	0	0^-	100(2)
142.0	284	3^-	142	1^-	100(2)
146	432	(4^-)	284	3^-	27(4)

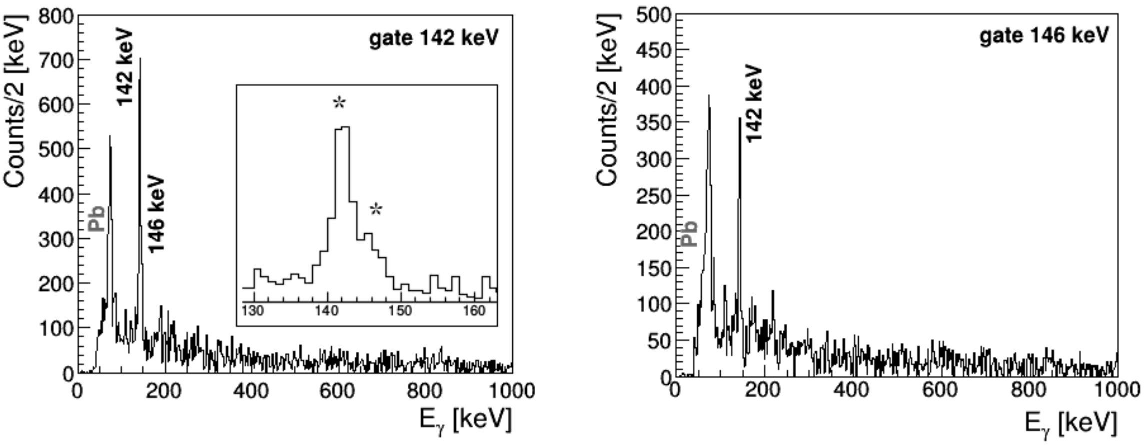

Figure 4.15: Projected γ-γ matrix, obtained with the 142 keV gate (left) and the 146 keV gate (right). The inset of the left panel spectrum shows the region in vicinity of E_γ = 142 and 146 keV, which are labeled with '*'.

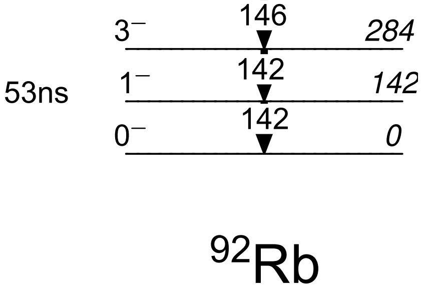

Figure 4.16: The experimental level scheme of ^{92}Rb. Relative γ-ray intensities are indicated by the width of the arrows. The energy, spin and parity of levels and the energy of γ transitions are as in Ref. [108].

4.4.4 ^{93}Rb

States in ^{93}Rb up to $E_{ex} = 913$ keV were observed. They are listed, together with the attributed γ transitions, in Tab. 4.4. As for the other isotopes, the measured I_γ^{13} were normalized to the strongest γ-transition, a 324 $(3/2^-, 5/2^-) \xrightarrow{324} 0$ $(5/2^-)$ keV transition. Data from the table are embedded in the ^{93}Rb level scheme in Fig. 4.17.

Table 4.4: Gamma rays attributed to ^{93}Rb. The energy, spin, parity of levels, and the energy of transitions are as in Ref. [109]. Relative intensities are normalized to the strongest $E_\gamma = 324$ keV.

E_γ[keV]	E_i[keV]	J_i^π	E_f[keV]	J_f^π	I_γ^{13}[%]
253	253	$3/2^-$, $5/2^-$	0	$5/2^-$	27(4)
	506	$1/2^-$, $3/2^-$	253	$3/2^-$,$5/2^-$	
267	267	$1/2^-$, $3/2^-$,$5/2^-$	0	$5/2^-$	44(4)
324	324	$3/2^-$, $5/2^-$	0	$5/2^-$	100(5)
733	733	$(7/2^-)$	0	$5/2^-$	36(3)
913	913	$7/2_2^-$	0	$5/2^-$	46(2)

In ^{93}Rb level scheme one notices $E_\gamma = 253$ keV, which can be attributed to both the decay of 506$(1/2^-, 3/2^-)$ keV state and 253$(3/2^-, 5/2^-)$ keV state. Both states (and their decays) were kept in the level scheme.

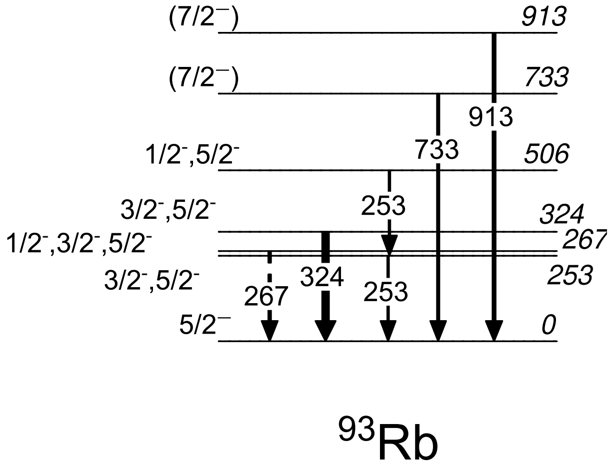

Figure 4.17: The experimental level scheme of ^{93}Rb. Relative γ-ray intensities are indicated by the width of the arrows. The energy, spin and parity of levels and the energy of γ transitions are as in Ref. [109].

4.4.5 ^{95}Rb

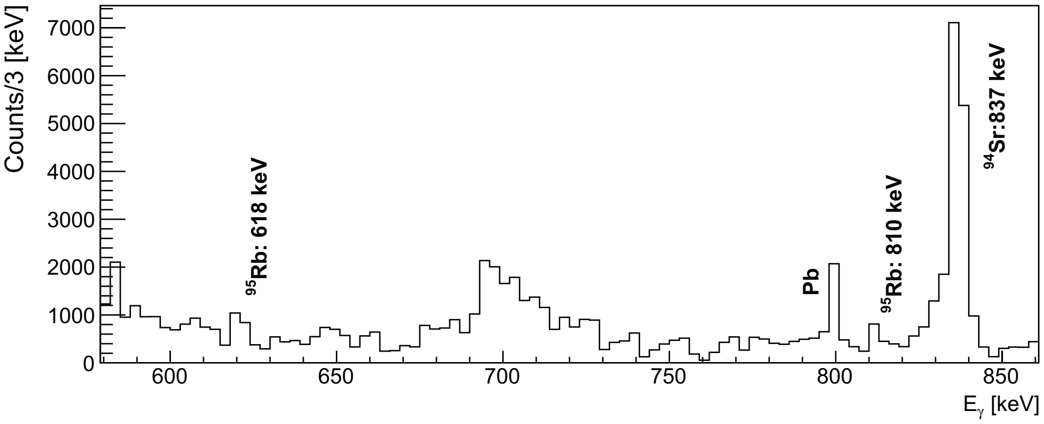

Figure 4.18: Delayed γ-ray spectrum in a selected energy range. The values of E_γ are as in Ref. [101]. Obtained with the use of "thick" target.

We would like to remind the reader that the evaluated spectroscopic information for ^{95}Rb [101, 102] is rather scarce. Data for ^{95}Rb were obtained from ^{9}Be(^{238}U,X) reaction, employing a fragment separator to select ^{95}Rb, and single HPGe detector. Thus, a few known γ transitions of ^{95}Rb follow the E_{ex} = 835 keV isomer decay. In the above cited work, an upper limit of it's lifetime was determined, $\tau_{1/2} < 500$ ns, while the other work of Ref. [100] has suggested $\tau_{1/2} = 94(7)$ ns.

In our experiment, E_γ = 192, 618, 810 keV were observed. We labeled some of them in the delayed γ-spectrum in Fig. 4.18. Besides these E_γ, one could also expect to observe the γ transition of $835\xrightarrow{835}0(5/2^-)$ keV [101, 102]. Due to strong E_γ = 837 keV of ^{94}Sr, we couldn't conclude on the presence of E_γ = 835 keV in ^{95}Rb.

All the γ transitions were summarized in Tab 4.5, with intensities I_γ^{13} and $\mathrm{I}_{\gamma,d}^{13}$, obtained in the prompt and delayed γ-spectrum, respectively. The presented table is of informative character.

4.5 The proton transfer channel

In addition to the neutron transfer channels, in which the accumulated statistics allowed for a detailed studies, we also observed the proton pick-up channel, ^{94}Rb+^{208}Pb $\rightarrow$ ^{95}Sr+^{207}Tl. Figure 4.19 shows the projection of the γ-γ matrix, obtained with the E_γ = 352 keV gate ($3/2^+ \rightarrow 1/2^+$) in ^{95}Sr. Coincidence with E_γ = 204 keV, the $7/2^+ \rightarrow 3/2^+$

Table 4.5: Gamma rays attributed to ^{95}Rb. The energy, spin, parity of levels, and the energy of γ transitions are as in Ref. [101]. Relative intensities I_{γ}^{13} are given in arbitrary units.

E_γ[keV]	E_i[keV]	J_i^π	E_f[keV]	J_f^π	I_γ^{13}[a.u.]	$I_{\gamma,d}^{13}$[a.u.]
192	192	-	0	$5/2^-$	180(15)	45(2)
618	810	-	192	-	373(17)	46(3)
810	810	-	0	$5/2^-$	60(30)	64(4)
835	835	-	0	$5/2^-$	-	-

transition in ^{95}Sr, is clearly observed. One also notices the $E_\gamma = 351$ keV ($3/2^+ \rightarrow 1/2^+$) attributed to the partner, ^{207}Tl. According to the Evaluated Nuclear Structure Database [110, 111], these $E_\gamma = 351$ and 352 keV are the γ transitions attributed to the first excited state in ^{95}Sr and ^{207}Tl, respectively, which are obviously very similar in energy. Due to the insufficient statistics, more detailed studies in this channel (cross section, level schemes) were not possible to be performed with the acceptable precision.

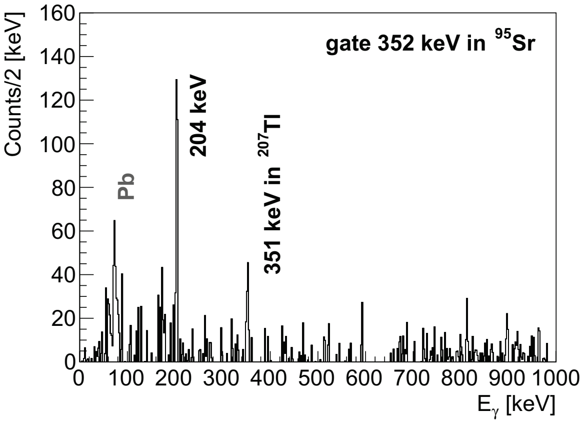

Figure 4.19: Projected γ-γ matrix, obtained with the 352 keV gate in ^{95}Sr (see text).

5

Excited states in $^{207-210}$Pb

The development of light ion beams alongside the particle spectroscopy techniques in the late '60s paved the way for more extensive studies of the isotopes of lead [112–114]. Such studies generally established the spin and parity (J^{π}) and the excitation energy (E_{ex}) of the first excited states. Particle spectroscopy provides an energy resolution typically of the order of few to tenths keV (for the light ions). One of the improvements in energy resolution came with the development of γ-ray spectroscopy techniques, nowadays widely exploited. The most recent γ-ray spectroscopy studies benefit from large and highly efficient, modular γ arrays, which allow the measurement of multifold γ coincidences. Mainly by employing heavy-ion beams (at energies above the Coulomb barrier) and ^{208}Pb thick targets, the level schemes of the isotopes of lead are nowadays established up to the rather high J^{π} and E_{ex} [88].

Measurement of the ^{94}Rb+^{208}Pb transfer reaction with the γ-spectrometer MINIBALL coupled to the CD detector allowed for γ-ray spectroscopy studies in the neutron transfer channels. The observed γ transitions were attributed to $^{207-210}$Pb and embedded in the level schemes.

The level schemes from this Chapter were constructed analysing the "thick" target γ spectra and γ-γ matrices. The properties of the ^{207}Pb, ^{208}Pb, ^{209}Pb level schemes were mainly adopted from the Evaluated Nuclear Structure Data Files [88]. This means that the energy (E_{γ}) of the γ-transition, and energies and spins of the associated initial (E_i , J_i^{π}) and final states (E_f , J_f^{π}) are as evaluated. Concerning the specific states in ^{207,209,210}Pb we adopted the values from the most recent (yet unevaluated) works and our work, to be discussed later on.

The result of the "thick" target γ spectra analysis is the intensity of the γ rays, the I_{γ}^{13}, which was always corrected for the efficiency of MINIBALL (Subs. 3.1). In some cases, when the populated states are known to have a complex decay pattern, with transitions of different intensities, we observed only the strongest decay branch. In cases when more γ transitions could be attributed to the same states, we will discuss their relative strength, and the agreement with the evaluated strength.

For the attribution of the strongest γ transitions, the γ-γ coincidence relationship could be established. For the other γ transitions, comparison with the evaluated and most recent spectroscopic studies was rather important. This is particularly true in the case of tentative γ transitions. When the γ-transition is characterized as tentative, this is usually due to the lower statistics (larger experimental errors), or the properties of the γ-peak (the centroid position and width). Particular attention is given to such γ transitions. In cases where it helps to elucidate the attribution of the tentative γ-transition, we will also refer to the "thin" target γ-spectrum.

In this Chapter, to learn about the reaction mechanism of the ^{94}Rb+^{208}Pb, the character of the states populated in $^{207-210}$Pb will be discussed. Through this discussion we will mainly recall the standard shell-model and previous studies. Thus, in the following subsections dedicated to $^{207-210}$Pb we will often give an insight into the level schemes as obtained in other relevant studies.

Since the γ-γ coincidences could be measured for the strongest transitions, we benefited from the ^{40}Ar+^{208}Pb [12, 64, 67] and ^{90}Zr+^{208}Pb [46, 47] measurements. In these experiments, described in Subs. 1.3.3, the light partner was identified in PRISMA, and the heavy one via characteristic γ rays in the γ-spectrometer CLARA (and in coincidence with the light partner). In this way one obtains the γ spectra attributed to the particular transfer channel, of which the γ spectra for $^{207-210}$Pb are presented in the Appendix. From the attributed γ transitions, we built the $^{207-210}$Pb level schemes, correcting their intensity for the efficiency of CLARA[9]. Extensive studies of the nuclear structure for the light partner can be found in our earlier works [47, 64, 65].

By comparing the ^{40}Ar,^{90}Zr+^{208}Pb and ^{94}Rb+^{208}Pb level schemes, we will illustrate the transfer reaction properties, when using the ^{208}Pb target and different beams at the similar energies (20-30% above the Coulomb barrier). ^{90}Zr is a stable, rather neutron-poor beam, while ^{40}Ar is the most neutron-rich stable argon beam. Lastly, ^{94}Rb is unstable, and obviously the most neutron-rich beam amongst these.

---

[9] For the efficiency of CLARA see for example Ref. [57]

5.1 ^{208}Pb

^{208}Pb is the heaviest doubly-magic nuclei, nowadays well known [36, 115]. For convenience, the shell-model orbitals in the vicinity of the proton $Z = 82$ and neutron $N = 126$ closed shells are schematically presented in Fig. 5.1.

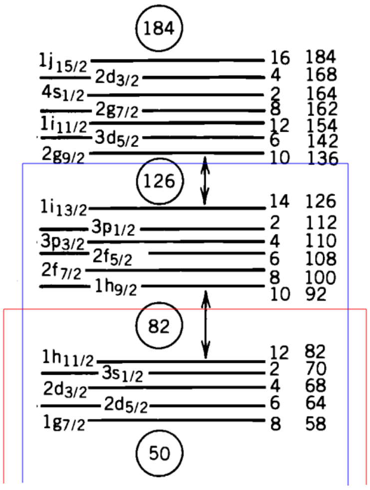

Figure 5.1: A relevant part of the ^{208}Pb shell-model orbitals. Numbers to the right of each orbital label its degeneracy. Blue and red frames indicate $N = 126$ and $Z = 82$ shells, respectively.

The first excited state 3^- at $E_{ex} = 2615$ keV is built up of numerous configurations, with many nucleons being promoted outside the closed shells. Altogether, they comprise the collective surface vibration. Thus the $3^- \to 0^+$ transition has a rather large $B(E3)$ = 34 W.u. [115]. As we will see, this octupole excitation will be of the great importance for understanding the character of strongly excited states in ^{207,209}Pb.

It is worth mentioning that, according to the vibrational phonon model [116], one expects double-octupole states at about twice the energy of the octupole excitation. The coupling of $3^- {\times} 3^-$ gives rise to multiplets of states, $J^\pi = 0^+$, 2^+, 4^+ and 6^+. States 0^+, 2^+ and 4^+ are indeed observed around $E_{ex} \sim 5.2$ MeV [117, 118], and their character discussed in terms of double-octupole excitations. Concerning the $J^\pi = 6^+$ member, there are indications [119, 120] that its double-octupole strength is rather fragmented, in the $E_{ex} = 4.4$ MeV and the other higher-energy states.

On the other hand, many states up to $E_{ex} = 7$ MeV have rather pure configurations [35, 119]. In the work of Ref. [121] two different reactions were used to populate different particle-hole states in ^{208}Pb. The ^{207}Pb$(d,p\gamma)^{208}$Pb reaction ($E_{\mathrm{LAB}} = 10$ MeV) populated exclusively the neutron particle-hole states, with the hole in the $3p_{1/2}$ orbital, as in the ground state of ^{207}Pb. Similarly, the ^{209}Bi$(t, \alpha\gamma)^{208}$Pb reaction ($E_{\mathrm{LAB}} = 11.5$ MeV) populated the proton particle-hole states, with the proton in the $1h_{9/2}$ orbital, as in the ground state of ^{209}Bi. Measuring the projectile-like particle-γ coincidence, the spectroscopic factors and the γ-transition branching ratios for $E_{ex} < 4.6$ MeV were extracted. This experimental data was used to empirically derive the shell-model wavefunctions (reported in Ref. [35]). In particular, in this energy region, shell-model single particle-single hole configurations are a valid description.

In the ^{94}Rb+^{208}Pb experiment, we observed the excitation of the states up to the $E_{ex} = 3947$ keV, among which yrast 2615 (3^-), 3198 (5^-) and 3475 (4^-) keV states. All the observed γ transitions were identified and their intensity (I_γ^{13}) obtained from the 13 mg/cm^2 target γ-spectrum. The results are summarized in the Tab. 5.1.

Table 5.1: Gamma transitions attributed to ^{208}Pb. The energy, spin and parity of levels, and the energy of γ transitions are as in Ref. [115]. Relative intensities I_γ^{13} are normalized to the strongest $E_\gamma = 2615$ keV.

E$_\gamma$[keV]	E$_i$[keV]	J$_i^\pi$	E$_f$[keV]	J$_f^\pi$	I$_\gamma^{13}$[%]
511	3708	5_2^-	3198	5^-	*39(2)*
583	3198	5^-	2615	3^-	22(1)
749	3947	4_3^-	3198	5^-	3(1)
861	3475	4^-	2615	3^-	2(1)
2615	2614	3^-	0	0^+	100(2)

The strongest γ-ray in the measurement is $E_\gamma = 2615$ keV, considering the heavy fragment γ rays. It was attributed to the $3^- \rightarrow 0^+$ transition. The projection of γ-γ matrix at $E_\gamma = 2615$ keV was constructed and plotted in the left panel of Fig. 5.2. One notices the strong coincidence with $E_\gamma = 583$ keV, the $3^- \rightarrow 5^-$ transition. The right panel of the same figure shows the 583 keV gated spectrum. This coincidence was placed in the ^{208}Pb level scheme in Fig. 5.3, together with the other γ transitions (listed in the Tab. 5.1). The width of the arrows in the level scheme corresponds to I_γ^{13}. All the attributed γ transitions are the strongest branch (100%) of the excited states. Other branches, when present, were not observed.

To the 5_2^- state we attributed a 511 keV ($5_2^- \rightarrow 5^-$) γ-transition, of a rather large

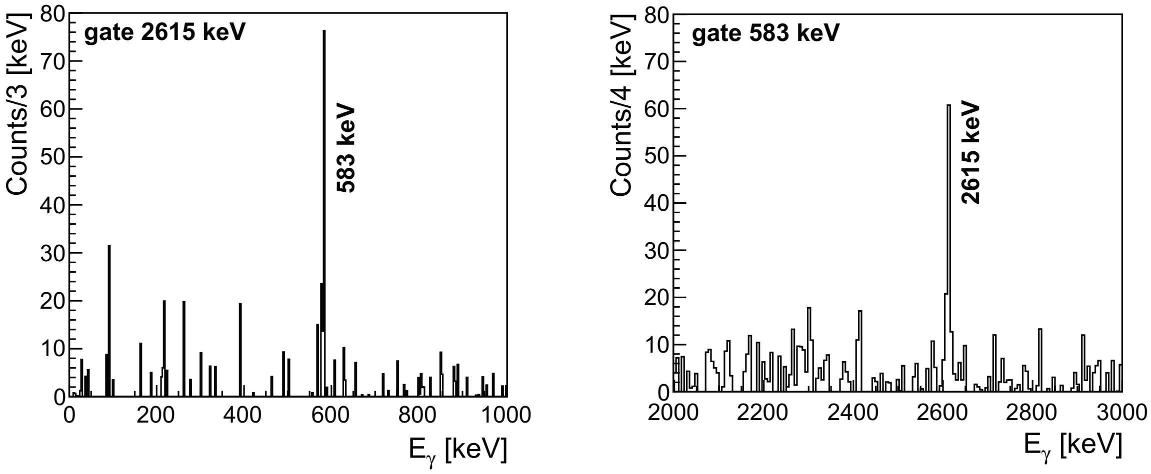

Figure 5.2: Projected γ-γ matrix, obtained with the 2615 keV gate (left) and the 583 keV gate (right). Notice the difference in the x-axis range.

$I_\gamma^{13} = 39\%$ (with respect to $I_\gamma^{13}(2615)$). The main contribution to $I_\gamma^{13}(511)$ comes from e^-e^+ annihilation. The background subtraction procedure can reduce, but not completely remove, the annihilation peak. Since $E_\gamma = 511$ keV is also observed in the "thin" target Doppler corrected γ-spectrum, with the 7% intensity of $E_\gamma = 2615$ keV, we assumed that its placement in the level scheme was consistent. Therefore, it is characterized as a tentative (dotted-arrow) γ-transition, with an arbitrary arrow width (I_γ^{13}) in the level scheme.

In summary, in the ^{94}Rb+^{208}Pb experiment states up to 4 MeV in ^{208}Pb were observed, with a strong excitation of the 3^- state. Latter will be of particular importance for the character of the states populated in ^{207,209}Pb. Besides the 3^- state, we had observed only the odd-parity states in ^{208}Pb, where the particle-hole configurations play a significant role.

The ^{208}Pb level scheme from ^{94}Rb+^{208}Pb is compared to the ^{40}Ar,^{90}Zr+^{208}Pb level schemes in Fig. 5.11. States of 2615 (3^-), 3198 (5^-), 3475 (4^-), 3709 (5_2^-), 4086 (2^+) and 4424 (6^+) keV were observed in both stable beam experiments. In particular, in the level scheme obtained with the ^{90}Zr beam one notices the positive-parity states at higher excitation energies. This level scheme is more detailed than the one from the ^{94}Rb beam experiment, due to the statistics accumulated during the ^{90}Zr+^{208}Pb measurement.

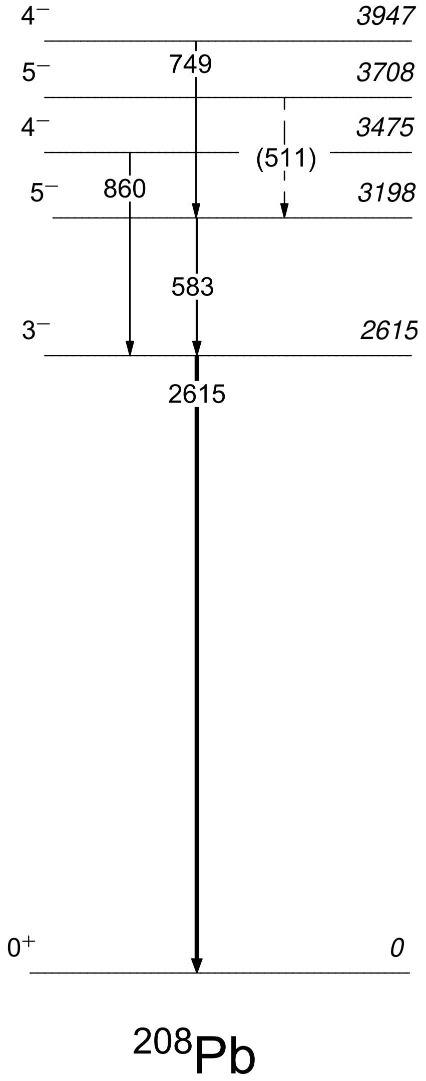

Figure 5.3: The experimental level scheme of ^{208}Pb. Relative γ-ray intensities are indicated by the width of the arrows. For tentative (dashed-arrow) γ transition intensity is arbitrary. The energy, spin and parity of levels, and the energy of γ transitions are as in Ref. [115].

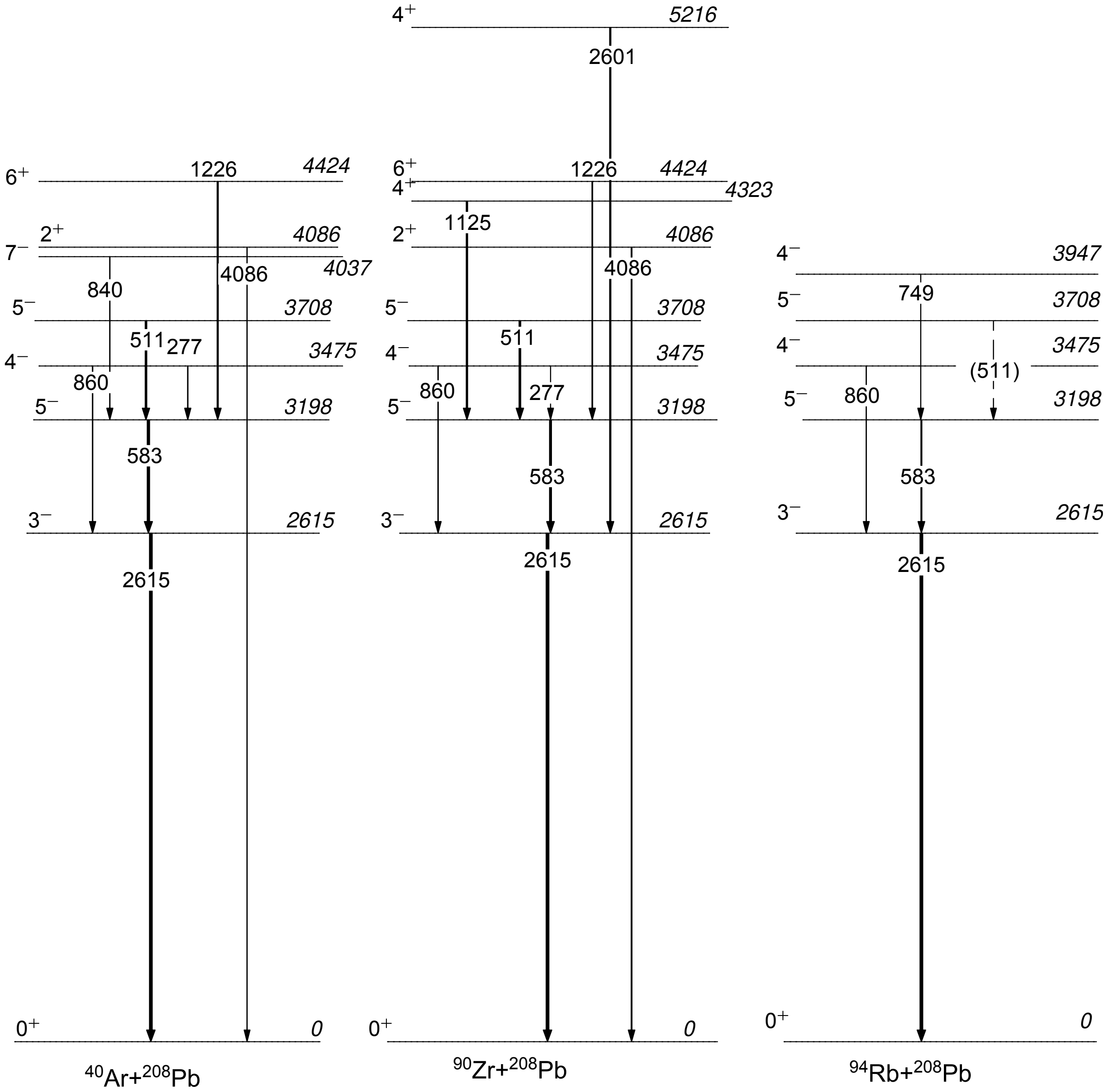

Figure 5.4: The experimental level scheme of ^{208}Pb from: ^{40}Ar+^{208}Pb (left), ^{90}Zr+^{208}Pb (middle), ^{94}Rb+^{208}Pb (right) experiments. Relative γ-ray intensities are indicated by the width of the arrows. For tentative (dashed-arrow) γ-transition intensity is arbitrary. The energy, spin and parity of levels, and the energy of γ transitions are as in Ref. [115].

5.2 ^{210}Pb

The nucleus ^{210}Pb has two neutrons outside ^{208}Pb closed shells. Thus, one can expect the structure of ^{210}Pb (close to the ground state) to be described with two-neutron configurations. Two neutrons in the first orbital outside the $N = 126$ shell would form a $\nu(g_{9/2})^2$ configuration and the multiplet: $J^\pi = 0^+, 2^+, 4^+, 6^+$ and 8^+. The promotion of one neutron to the higher orbital, in particular to $i_{11/2}$ or $j_{15/2}$, could populate the states of J^π up to 10^+ or 12^- respectively.

Studies using light-ion induced two-neutron transfer reactions, (t,p), $(t,p\gamma)$, (^{7}Li, $\alpha p\gamma$) and the ^{208}Pb target, helped to establish the E_{ex} and J^{π} of the first excited states [122], in particular of the 800 (2^{+}), 1098 (4^{+}), 1195 (6^{+}) and 1278 (8^{+}) keV states. Employing γ-ray spectroscopy with thick targets significantly enriched the ^{210}Pb level scheme. From the γ-γ coincidences observed in ^{136}Xe,^{208}Pb+^{208}Pb (at $E_{\rm LAB} \approx 6$ MeV·A) with EUROBALL, the relatively high-spin states of 1806 (10^{+}), 2512 (11^{-}), 3152 (13^{-}), 4133 (14^{+}) keV were added to the level scheme [123]. In the ^{238}U+ ^{208}Pb experiment [124] multifold γ-ray coincidences were measured with the γ-spectrometer GAMMASPHERE, which high efficiency (101 HPGe crystals) allowed to extend studies up to E_{ex} = 5.8 MeV (and undetermined J^{π}).

However, the evaluated E_{ex} [122] of all the states above 4^{+} still have rather large uncertainties (~5-10 keV). This is due to uncertainty in the γ-ray energy of the $8^{+} \rightarrow 6^{+}$ γ-transition: E_{γ} = 83(3) keV, and $6^{+} \rightarrow 4^{+}$: E_{γ} = 97(3) keV. States of 8^{+} and 6^{+} are isomers, having high internal conversion rates, in correlation with the low energy of the attributed γ rays. Another obstacle in the low energy region is the presence of $K_{\alpha,\beta}$ electronic transitions of lead. One sees how it could be very difficult to extract the energy and intensity of $8^{+} \rightarrow 6^{+} \rightarrow 4^{+}$ transitions with high precision.

5.2.1 ^{208}Pb+^{208}Pb experimental results

Excitation energies of significantly improved precision (~0.1 keV) were reported in the work of Broda et al. [97] published in 2018. The study exploits the prompt and delayed γ-ray spectroscopy in the ^{208}Pb+^{208}Pb measurement, at $E_{\rm LAB}$ = 6.9 MeV·A. The fragments were stopped in the thick target surrounded by the GAMMASPHERE. Two and higher-fold γ-ray coincidences were constructed, alongside the angular distributions for the strongest transitions.

The E_{γ} of the isomeric $8^{+} \rightarrow 6^{+}$ and $6^{+} \rightarrow 4^{+}$ transitions were reported, with E_{γ} = 80.2 keV and E_{γ} = 97.6 keV, respectively. These E_{γ} were obtained by using the combination of the prompt $2^{+} \xrightarrow{803} 0^{+}$ gate in the binary partner ^{206}Pb, and delayed $4^{+} \xrightarrow{298} 2^{+}$ gate in ^{210}Pb. The same γ transitions were observed from the $4^{+} \xrightarrow{298} 2^{+} \xrightarrow{800} 0^{+}$ delayed gates in ^{210}Pb as well. Also, from the comparison of measured intensities, the internal conversion coefficients (ICC) for the 8^{+} and 6^{+} isomers were extracted. ICC is defined as the ratio of the number of deexcitations via electron emission, over the number of deexcitations via γ-ray. Thus, the obtained ICCs were $ICC(8^+) = 18(4)$, and $ICC(6^+) = 6.9(5)$. Besides the 4^+ state with the reported $ICC(4^+) = 0.15$, no other states in ^{210}Pb are known to have considerable internal conversion rates.

A very rich level scheme was constructed up to 17$\hbar$ and 6 MeV, containing mainly yrast and near-yrast states. This was achieved also by comparing the identified E_γ and their coincidence relationships to the data of previously measured systems, namely the ^{48}Ca, ^{76}Ge,^{82}Se+^{208}Pb and ^{48}Ca,^{208}Pb+^{238}U [36]. In particular, in the ^{208}Pb+^{208}Pb experiment, strong γ transitions were attributed to 10^+ and 11^- states.

5.2.2 Half-lives of 6^+, 8^+ isomers

The first evidence for isomers in ^{210}Pb was observed in the ^{208}Pb(^{7}Li, $\alpha p\gamma$)^{210}Pb thick target experiment [125] ($E_{\mathrm{LAB}} = 33$ MeV). Half-lifes of the 8^+ and 6^+ states were measured with a few Ge(Li) detectors from the timing difference between the (pulsed) beam and the $4^+ \xrightarrow{298} 2^+ \xrightarrow{800} 0^+$ γ rays. Similar half-lifes were obtained in the ^{208}Pb($t,p\gamma$)^{210}Pb experiment [126] ($E_{\mathrm{LAB}} = 16$ MeV), which also used the beam and the γ timing distributions and the same γ rays. The evaluated half-lifes [122] $\tau_{1/2}(8^+) = 201(17)$ ns and $\tau_{1/2}(6^+) = 49(6)$ ns are from those experiments.

In the ^{208}Pb+^{208}Pb experiment [97], the reported $\tau_{1/2}(6^+) = 92(10)$ ns is nearly twice as long as the evaluated one. It was extracted from the $6^+ \xrightarrow{98} 4^+$ time distributions. For the 98 keV time distribution the γ ray gates which were used were the ones directly populating the 8^+ state (528, 641, 1234, and 1346 keV), and the 298 and 800 keV delayed γ rays. Also the separate time distribution was constructed from the same delayed γ rays, and the 864 keV γ-transition, which directly populates the 6^+ state: $(6^+, 7^+) \xrightarrow{864} 6^+$. Broda et al. [97] claim the difference in the extracted half-life in their and the light-ion beam experiments is due to this direct (and prompt) feeding component, which had not been observed nor precisely accounted for previously.

5.2.3 ^{94}Rb+^{208}Pb experimental results

In the ^{94}Rb+^{208}Pb experiment, states up to 3 MeV were observed. As for ^{208}Pb, the intensity of γ transitions was obtained from the "thick" (13 mg/cm^2) target measurement and the results summarized in Tab. 5.2. From the same table one notices the two different intensity notations, I_γ^{13} and $I_{\gamma d}^{13}$. I_γ^{13} was extracted with the Δt_p (prompt) gate of the fragment-γ coincidence, and $I^{13}_{\gamma d}$ with the Δt_d (delayed) gate. For the definition of the prompt and delayed gates see Sec. 3.3.

Table 5.2: Gamma transitions attributed to ^{210}Pb. The energy, spin and parity of levels, and the energy of γ transitions are as in Ref. [122]. Relative intensities, I^{13}_{γ} and $I^{13}_{\gamma d}$ correspond to the prompt and delayed fragment-γ coincidence, respectively. They were normalized to the strongest ^{210}Pb transition in the prompt region, $E_\gamma = 1234$ keV.

E_γ[keV]	E_i[keV]	J^π_i	E_f[keV]	J^π_f	I^{13}_γ[%]	$I^{13}_{\gamma d}$[%]
298	1097	4^+	800	2^+	28(3)	81(12)
528	1806	(10^+)	1278	8^+	98(6)	-
640	3152	(13^-)	2512	11^-	*21(3)*	-
800	800	2^+	0	0^+	35(5)	119(3)
1234	2512	(11^-)	1278	8^+	100(9)	-
1346	3152	(13^-)	1806	(10^+)	*12(4)*	-

In the prompt region, the strongest E_γ are 528 and 1234 keV, attributed to the $10^+ \rightarrow 8^+$ and $11^- \rightarrow 8^+$ transitions, respectively. They are embedded in the ^{210}Pb level scheme in Fig. 5.8, together with the other γ transitions from Tab. 5.2. States of 8^+ and 6^+ are isomers with $8^+ \rightarrow 6^+ \rightarrow 4^+ \rightarrow 2^+ \rightarrow 0^+$ decay, between which we strongly observe $4^+ \xrightarrow{298} 2^+ \xrightarrow{800} 0^+$.

Projections of the prompt and delayed γ-γ matrices at 298 and 800 keV were constructed, and plotted in Fig. 5.5 and Fig. 5.6 respectively. The coincidence relationship of these γ transitions is very clear, particularly in the delayed region. This is due to the random coincidences which have smaller contribution in the delayed region.

To study the $8^+ \rightarrow 6^+ \rightarrow 4^+$ transitions the sum of the γ-γ delayed matrix projections at $E_\gamma = 298$ and 800 keV was constructed. As illustrated in the projected spectrum in Fig. 5.7, these transitions are indeed observed at $E_\gamma = 80$ keV ($8^+ \rightarrow 6^+$) and $E_\gamma = 98$ keV ($6^+ \rightarrow 4^+$). The K_α and K_β electronic transitions are labeled at around 75 and 85 keV in the spectrum, respectively. These energies are particularly close to $E_\gamma = 80$ keV, and this is why background subtraction was not performed. Consequently the coincidence relationships are not very clear.

From the same projected spectrum, we had also extracted the ratio of intensities of the $E_\gamma = 80$, 98 keV, and obtained $I_\gamma(E_\gamma = 80 \text{ keV})/I_\gamma(E_\gamma = 98 \text{ keV}) = 0.27(0.09)$. This intensity ratio can be compared to the ratio of internal conversion coefficients extracted in the ^{208}Pb+^{208}Pb, which is $ICC(E_\gamma = 80 \text{ keV})/ICC(E_\gamma = 98 \text{ keV}) = 0.26(0.06)$. One notices the two ratios agree well and within the experimental error.

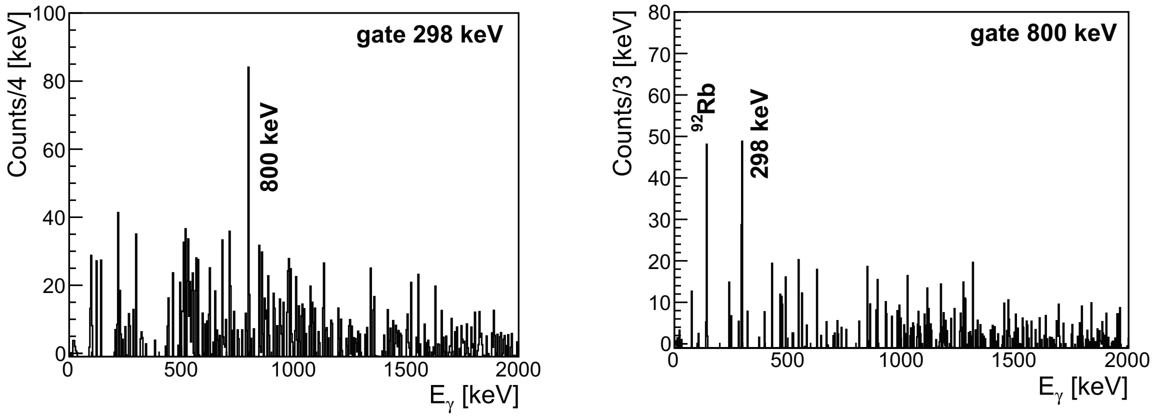

Figure 5.5: Projected γ-γ matrix, obtained with the 298 keV gate (left) and the 800 keV gate (right).

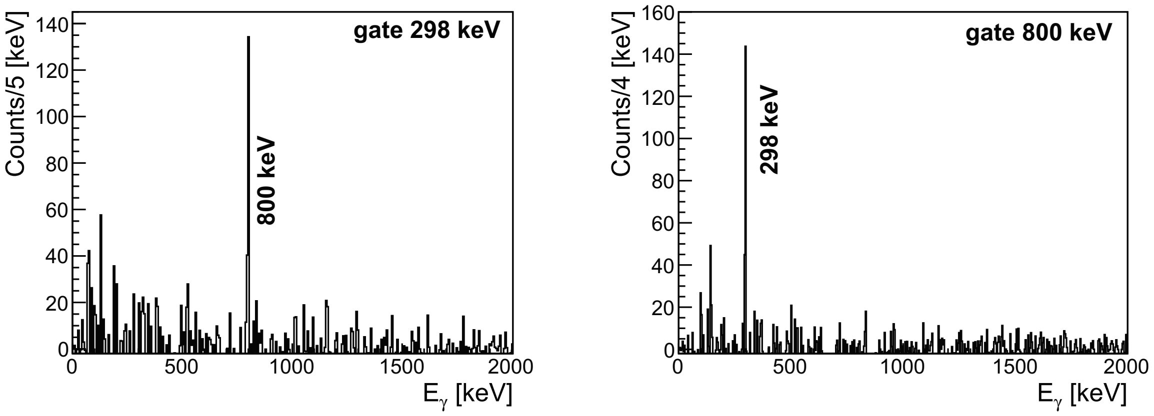

Figure 5.6: Projected γ-γ delayed matrix, obtained with the 298 keV gate (left) and the 800 keV gate (right).

In Tab. 5.3 we compared the E_γ and E_{ex} obtained from the ^{94}Rb+^{208}Pb experiment to the ones of previous studies. Between the previous studies, we chose the ^{208}Pb+^{208}Pb dataset [97] (labeled "PbPb"), and the Evaluated Nuclear Structure dataset [122] (labeled "ENS"). From this table one notices that the ^{94}Rb+^{208}Pb experimental data suggests the improved precision for the E_γ and E_{ex} up to $E_{ex} = 2508$ keV, when compared with the "ENS" (evaluated) data. The achieved precision in the ^{94}Rb+^{208}Pb experiment is similar to the one in ^{208}Pb+^{208}Pb. Moreover, the ^{94}Rb+^{208}Pb dataset agrees with the ^{208}Pb+^{208}Pb dataset within a $\sim$1 keV. In particular, both experiments suggest a $E_\gamma =$ 80 keV value for the $8^+ \rightarrow 6^+$ transition, previously evaluated as $E_\gamma = 83$ keV. This 3

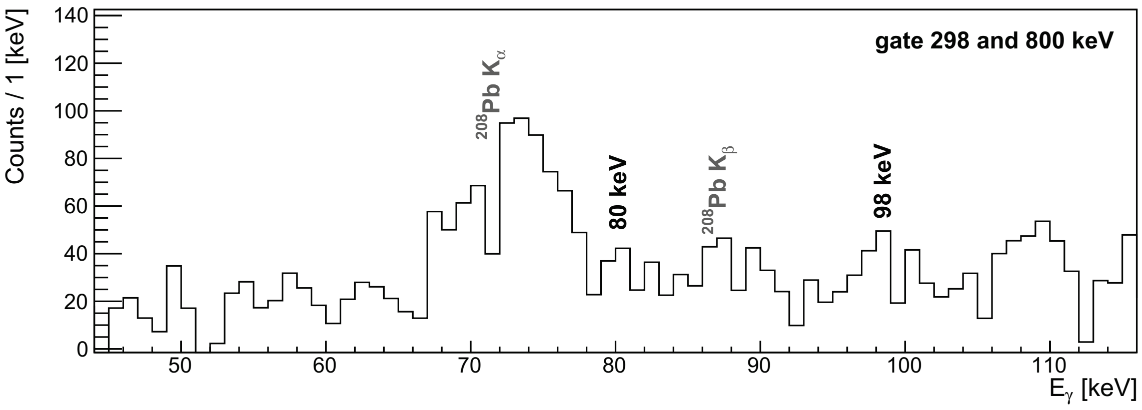

Figure 5.7: Projected γ-γ delayed matrix, obtained with the sum of the $E_\gamma = 298$ and 800 keV gate.

Table 5.3: The states and γ rays observed in ^{210}Pb. The energy E_γ^{RbPb} and the excitation energies E_{ex}^{RbPb} are as in this experiment. E_γ^{PbPb} and E_{ex}^{PbPb} are as in the ^{208}Pb+^{208}Pb experiment [97], and E_γ^{ENS} and E_{ex}^{ENS} are as in Ref. [122]. All the values are in keV, with error (if known) given in parenthesis.

E_{ex}^{RbPb}	E_{ex}^{PbPb}	E_{ex}^{ENS}	E_γ^{RbPb}	E_γ^{PbPb}	E_γ^{ENS}
799.8(1)	799.6	799.7(1)	799.8(1)	799.6(1)	799.7(1)
1097.28(8)	1097.0	1097.7(10)	297.48(7)	297.4(1)	298(1)
1194(1)	1194.6	1195(4)	97(1)	97.6	97(3)
1274(2)	1274.8	1278(5)	80(1)	80.2	83(3)
1803(2)	1802.9	1806(5)	529.41(9)	528.1(1)	528.0(2)
2508(2)	2508.4	2512(5)	1234.1(4)	1233.6(1)	1233.7(2)

keV difference in E_γ influences the excitation energies above the 8^+ state.

One might add a few comments about $E_\gamma = 640$, 1346 keV attributed to the 3152(13^-) keV state. The 13^- state has two decay branches, the $13^- \xrightarrow{1346} 10^+$, which is the 100% branch and $13^- \xrightarrow{640} 11^-$, which is 83%. However, the observed intensities in our case (as in Tab. 5.2), suggest that the 640-keV branch is stronger. This might be due to the observed $E_\gamma = 643$ keV, attributed to the $15/2^- \rightarrow 11/2^+$ transition in ^{209}Pb. Since we could not resolve the 640 keV from the 643 keV γ-transition, and also $E_\gamma = 1346$ keV is not observed very clearly, both are plotted as dotted-arrows in the ^{210}Pb level scheme.

In this paragraph we would like to comment on the character of the populated states. According to the most recent shell-model calculations (employed in the work of Broda et al. [97]), nearly pure $\nu(g_{9/2})^2$ configurations were found in 2^+, 4^+, 6^+ and 8^+ states.

Similarly, the strongly excited 10^+ was associated with pure $\nu(i_{11/2})^2$ configuration. On contrary, the strong ^{208}Pb octupole excitation becomes important in the description of the 11^- state, to which we attributed the strongest prompt γ-ray in ^{210}Pb. The same shell-model suggests that this state is mainly composed of $\nu(g_{9/2}j_{15/2})$ configuration, with contribution of $\nu(g_{9/2})^2 \times 3^-$.

In summary, the ^{210}Pb level scheme was constructed up to 3 MeV and $J^\pi = (13^-)$ from the ^{94}Rb+^{208}Pb reaction. The strong $10^+ \rightarrow 8^+$ and $11^+ \rightarrow 8^+$ γ transitions populate the 2^+-8^+ yrast states sequence. The clearly observed $4^+ \rightarrow 2^+ \rightarrow 0^+$ transitions were used to gate delayed γ-γ matrix, and to study the low-lying E_γ of the 8^+ and 6^+ isomeric decay. In this way, improved precision (of 1 keV) was proposed for the observed E_γ and E_{ex}, with respect to the evaluated level scheme.

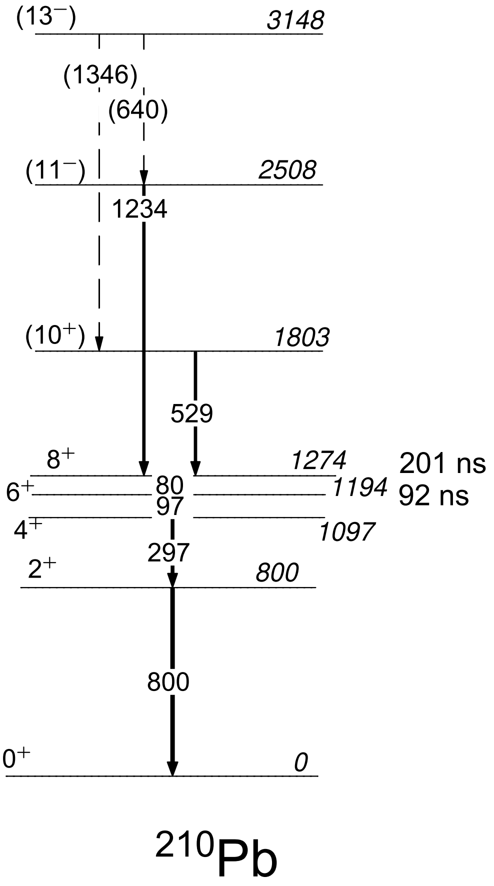

Figure 5.8: The experimental level scheme of ^{210}Pb. Relative γ-ray intensities are indicated by the width of the arrows. For tentative (dashed-arrow) γ transitions intensity is arbitrary. The energy, spin, parity of levels, and the energy of transitions are as in this work and Ref. [97].

The ^{210}Pb level scheme from ^{94}Rb+^{208}Pb is compared to the ^{40}Ar+^{208}Pb level scheme in Fig. 5.9. In the argon beam experiment states up to $E_{ex} = 3152$ keV were populated, 2^+, 4^+, 6^+, 8^+, 10^+, 11^- and 13^- states. One notices the two level schemes are rather similar, with the exception that the $8^+ \rightarrow 6^+ \rightarrow 4^+$ isomer decay could not be observed in the argon experiment. The Ar-like fragments were reaching the PRISMA focal plane with the ~200 ns time of flight, when the isomeric decay is still negligible, and outside the fragment-γ coincidence window. Also, the fact that we observed 13^- in the argon experiment suggests the tentative γ transitions in ^{94}Rb+^{208}Pb were correctly attributed to the 13^- state.

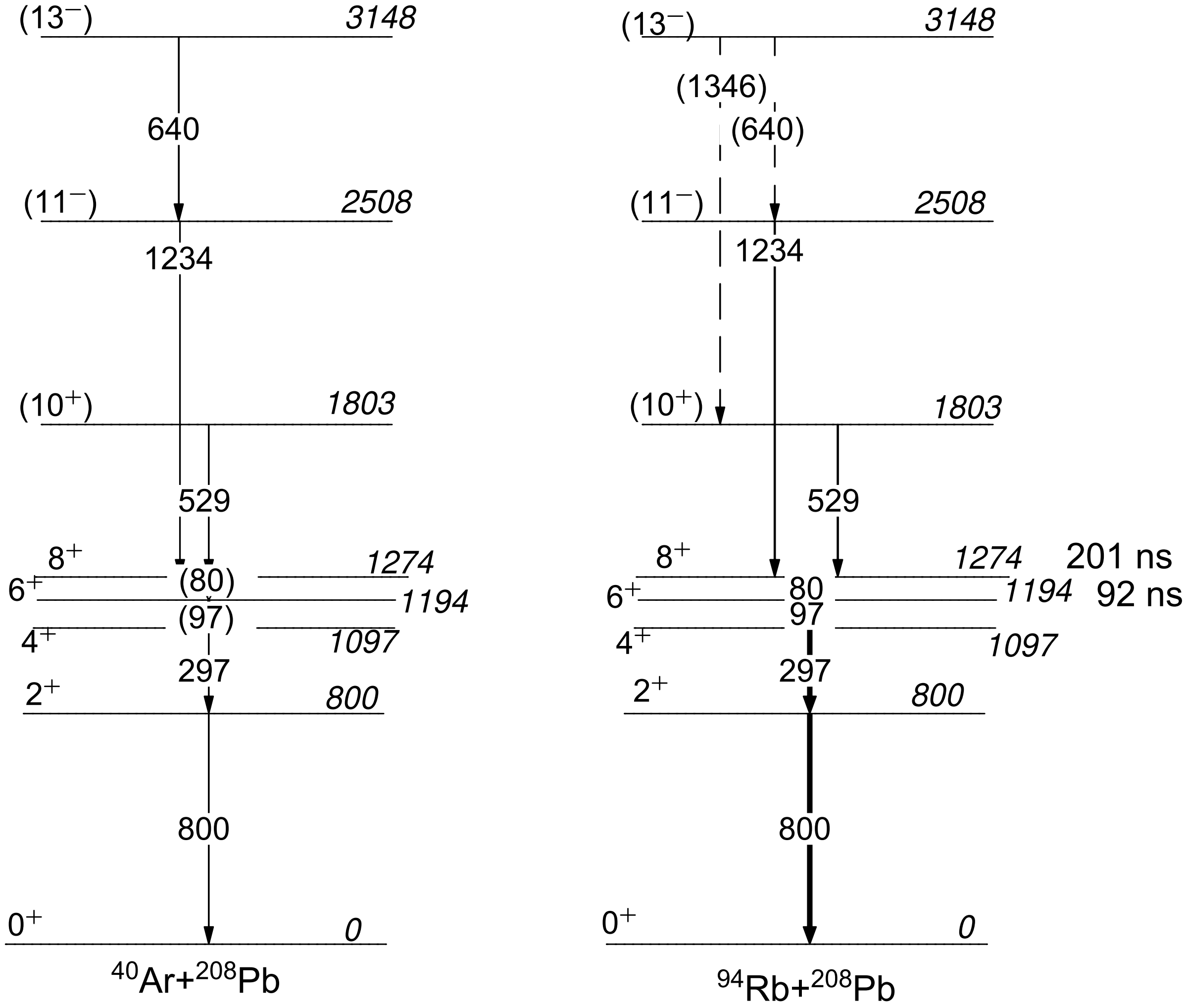

Figure 5.9: The experimental level scheme of ^{210}Pb from: ^{40}Ar+^{208}Pb (left) and ^{94}Rb+^{208}Pb (right). Relative γ-ray intensities are indicated by the width of the arrows. For tentative (dashed-arrow) γ transitions intensity is arbitrary. The energy, spin and parity of levels, and the energy of γ transitions are as in this work and Ref. [122].

5.3 ^{207}Pb

The ground state of ^{207}Pb is $1/2^-$. As ^{207}Pb has only one neutron less than the doubly-magic ^{208}Pb, its ground state can be described as a neutron hole in the $3p_{1/2}$ orbital. If the neutron from the same shell, or the $2f_{5/2}$, $3p_{3/2}$, $1i_{13/2}$, $2f_{7/2}$, $1h_{9/2}$ orbitals (see the Fig. 5.1), is promoted to the $3p_{1/2}$ hole, possible states are $5/2^-$, $3/2^-$, $13/2^+$, $7/2^-$ and $9/2^-$. It is expected that these states will have a dominant single-particle character. The spectroscopic factors for the one-neutron transfer from the ^{208}Pb ground state to states of ^{207}Pb were obtained from the light-ion induced reactions [127]. We selected the results from the (*p*,*d*) [128] and (*d*,*t*) [113] experiments, and plotted the spectroscopic factors $C^2S(2j+1)$ in Fig. 5.10. For example, for the $5/2^-$ state, one sees that the spectroscopic factors are ≈ 6, being very similar to the maximum value of $(2j+1) = 6$. This suggests the strong single-particle component in the $5/2^-$ state. Analogously, the same conclusion can be deduced in particular for the $1/2^-$ ground state and $3/2^-$ state.

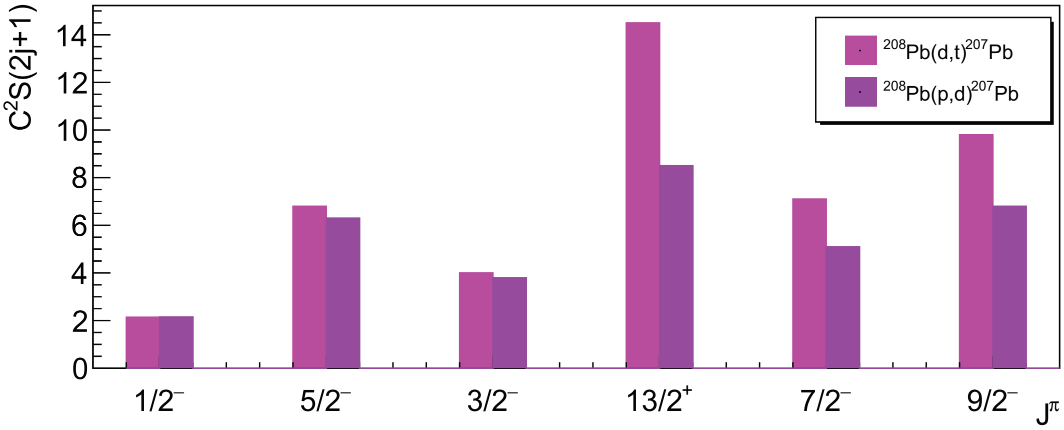

Figure 5.10: Spectroscopic factors for the states in ^{207}Pb, from the (*d*,*t*) reaction ($E_{\mathrm{LAB}} = 17$ MeV) [113], and (*p*,*d*) ($E_{\mathrm{LAB}} = 35$,41 and 65 MeV) [128].

Also, the heavy-ion induced neutron transfer reactions populate the states of single-particle character in ^{207}Pb. For example, by employing few HPGe detectors in the ^{32}S+^{208}Pb measurement ($E_{\mathrm{LAB}} = 5.8$ MeV·A), the γ transitions from the 570 ($5/2^-$), 898 ($3/2^-$) and 2340 ($7/2^-$) keV states were observed [129]. Very recently, ^{208}Pb+^{100}Mo experiment ($E_{\mathrm{LAB}} = 6.25$ MeV·A) was performed employing the AGATA γ-array coupled to a VAMOS++ magnetic spectrometer. By the means of the Recoil Distance Doppler shift technique they reported the lifetime of the $19/2^-$ state at 4118 keV [130], which will be discussed in more detail later on. Besides $19/2^-$, they observed strong excitations of $5/2^-$, $3/2^-$, $7/2^-$ states, and excitation of the 2662 ($7/2^+$) keV state.

In ^{94}Rb+^{208}Pb we observed the population of states up to 4 MeV excitation energy. The states with the expected single-particle character, 570 ($5/2^-$) and 898 ($3/2^-$) keV,

Table 5.4: Gamma transitions attributed to ^{207}Pb. The energy, spin and parity of levels, and the energy of γ transitions are as in Refs. [127, 131]. Relative intensities I_γ^{13} are normalized to the strongest transition, E_γ = 570 keV.

E_γ[keV]	E_i[keV]	J_i^π	E_f[keV]	J_f^π	I_γ^{13}[%]
570	570	$5/2^-$	0	$1/2^-$	100(3)
898	898	$3/2^-$	0	$1/2^-$	35(6)
1770	2340	$7/2^-$	570	$5/2^-$	14(2)
2093	2662	$7/2^+$	570	$5/2^-$	*17(2)*
2485	4118	$(19/2^-)$	1633	$13/2^+$	24(3)

are particularly strongly populated. The associated 570 and 898 keV γ transitions, which decay directly to the ground state, were labeled in "thick" and "thin" γ spectra (in Sec. 4.3). As for other Pb isotopes, the intensity of observed γ transitions was obtained from the "thick" (13 mg/cm^2) target γ-spectrum, and the results summarized in Tab. 5.4.

From the same table, one notices the relatively high-energy γ-transition at E_γ = 2485 keV, of I_γ^{13} = 24% (with respect to $I_\gamma^{13}(570)$). This brings us to the discussion on the origin of the 2485 keV γ-ray, which was firstly described in the γ-spectroscopy study of ^{64}Ni, ^{82}Se+^{208}Pb [132]. It was attributed to the 4118 keV state of tentative $(19/2^-)$ spin and parity, as a $(19/2^-)\xrightarrow{2485}13/2^+$ transition. However, the accepted evaluated J^π is $(15/2^-)$ [127], as deduced from ^{206}Pb(d,p)^{207}Pb. In a very recent experiment, which employed the highly modular γ-spectrometer GAMMASPHERE in the ^{208}Pb +^{208}Pb measurement [131], the angular distribution of the 2485 keV γ-ray showed anisotropy of the $E3$ transition, thus confirming the $19/2^-$ spin and parity of the 4118 keV state. These are the values we embedded in the ^{207}Pb level scheme in Fig. 5.11. In our experiment, the $(19/2^-) \rightarrow 13/2^+$ transition therefore describes the population of the $13/2^+$ isomer. The $13/2^+$ decay ($\tau_{1/2}$ = 0.806 s) could not be observed due to the shortness of the experimental acquisition window (4 μs). For a consistency, we plotted it in the level scheme with a dashed arrow.

Looking at the ^{207}Pb level scheme, one can notice that all of the states with the expected single-particle character were observed ($5/2^-$, $3/2^-$, $13/2^+$, $7/2^-$), except the $9/2^-$ state. The decay pattern of this state, at E_{ex} = 3415 keV, is rather complex and distributed over several transitions, among which two of them have high intensities. We assume that this might be the reason why we did not observe the $9/2^-$ state.

The $E_\gamma = 2093$ keV, attributed to the $7/2^+ \rightarrow 5/2^-$ dashed-arrow transition, is tentative. This is due to the presence of the other γ rays which make it more difficult for $7/2^+ \rightarrow 5/2^-$ to be clearly observed. For example, the 2093 keV γ-ray might be attributed to the strong transition in ^{94}Sr as well, and to the 2101 keV γ-ray of ^{209}Pb (the $(19/2^-) \rightarrow 15/2^-$ transition). For more details, see Tabs. 3.1 and 5.5.

Between the populated states, the spectroscopic factors from Fig. 5.10 indeed point to the dominant single-particle character for the $1/2^-$, $5/2^-$ and $3/2^-$ states. The structure of $13/2^+$ and $7/2^-$ is also based on the single-particle configurations, but for their description particle-octupole coupling becomes important as well. The importance of strong 3^- excitation in the structure of ^{207}Pb was discussed in the works of Refs. [130, 131, 133]. Using particle-octupole coupling model calculations, the authors in Ref. [133] proposed dominant single-particle configuration for the $13/2^+$ and $7/2^-$ states, with contributions from $\nu(f^{-1}_{7/2}) \times 3^-$ and $\nu(i^{-1}_{13/2}) \times 3^-$ coupling, respectively. In the structure of the 4118 $(19/2^-)$ keV state they stated the $\nu(i^{-1}_{13/2}) \times 3^-$ configuration exhausts the majority of the amplitude, and the rest of the strength was attributed to particle-double-octupole configuration, namely $\nu(f^{-1}_{7/2}) \times 3^- \times 3^-$. As we stated earlier, the authors in Ref. [131] measured the octupole transition of $19/2^- \rightarrow 13/2^+$, while in Ref. [130] a $19/2^-$ lifetime was reported. The large value of the reduced transition probability of 40(8) W.u. is similar to the one of the $3^- \rightarrow 0^+$ transition in ^{208}Pb, which is 34 W.u. [115] This supports the proposed spin and parity, and the discussed character of the $19/2^-$ state.

In summary, in the ^{94}Rb+^{208}Pb reaction the single-particle states in ^{207}Pb (states $5/2^-$ and $3/2^-$) are strongly populated. The $13/2^+$ isomer was observed, but due to its 0.806 s half-life, its decay was not. The population of the particle-octupole state $(19/2^-)$ provides the opportunity to study some very interesting aspects of the nuclear structure in the region, as are particle-double-octupole excitations.

The ^{207}Pb level scheme from ^{94}Rb+^{208}Pb is compared to the ^{40}Ar,^{90}Zr +^{208}Pb level schemes in Fig. 5.12. One notices these level schemes are rather similar. In both stable beam experiments there is a strong yield in the $5/2^-$, $3/2^-$ and $7/2^-$ states of the single-particle character. In addition, in the argon beam experiment we observed the population of 2662 $(7/2^+)$ keV, 2728 $(9/2^+)$ keV, and 4118 $(19/2^-)$ keV states. In the level scheme from the zirconium beam experiment one notices a non-yrast $9/2^+$ at $E_{ex} = 3414$ keV.

The 1633 ($13/2^+$) keV isomer was populated in both stable beam reactions from the $9/2^+$ → $13/2^+$ transition. Also, as in the case of ^{94}Rb+^{208}Pb, the $13/2^+$ isomeric decay was not observed. As we have already discussed concerning ^{210}Pb isomers (Subs. 5.2), this is due to the properties of the experimental set-up and the length of the fragment-γ coincidence window. For completeness, the $13/2^+$ → $5/2^-$ transition was added with a dashed arrow in the level scheme.

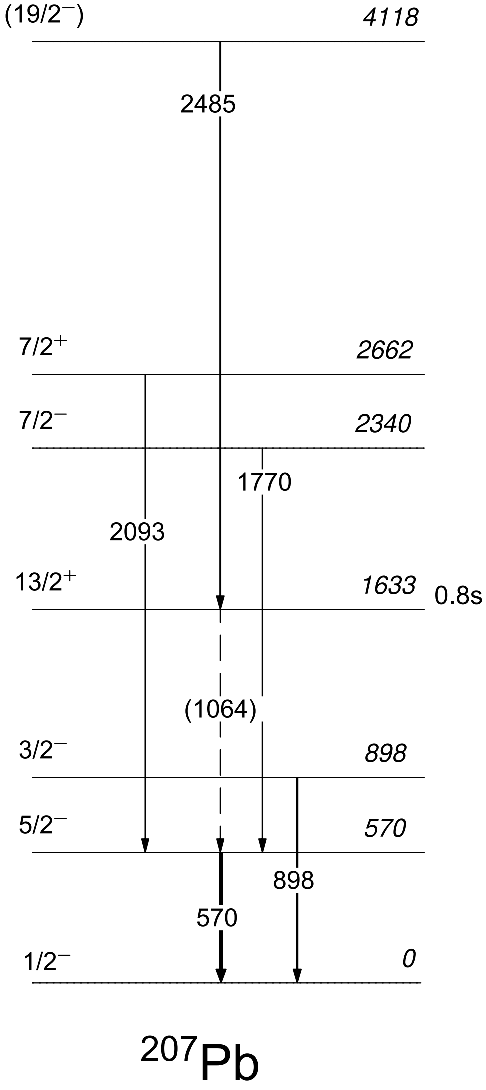

Figure 5.11: The experimental level scheme of ^{207}Pb. Relative γ-ray intensities are indicated by the width of the arrows. For tentative (dashed-arrow) γ transitions intensity is arbitrary. The energy, spin and parity of levels, and the energy of γ transitions are as in Refs. [127, 133]. Notice that the $13/2^+$'s half-life is $\tau_{1/2} = 0.8$ s.

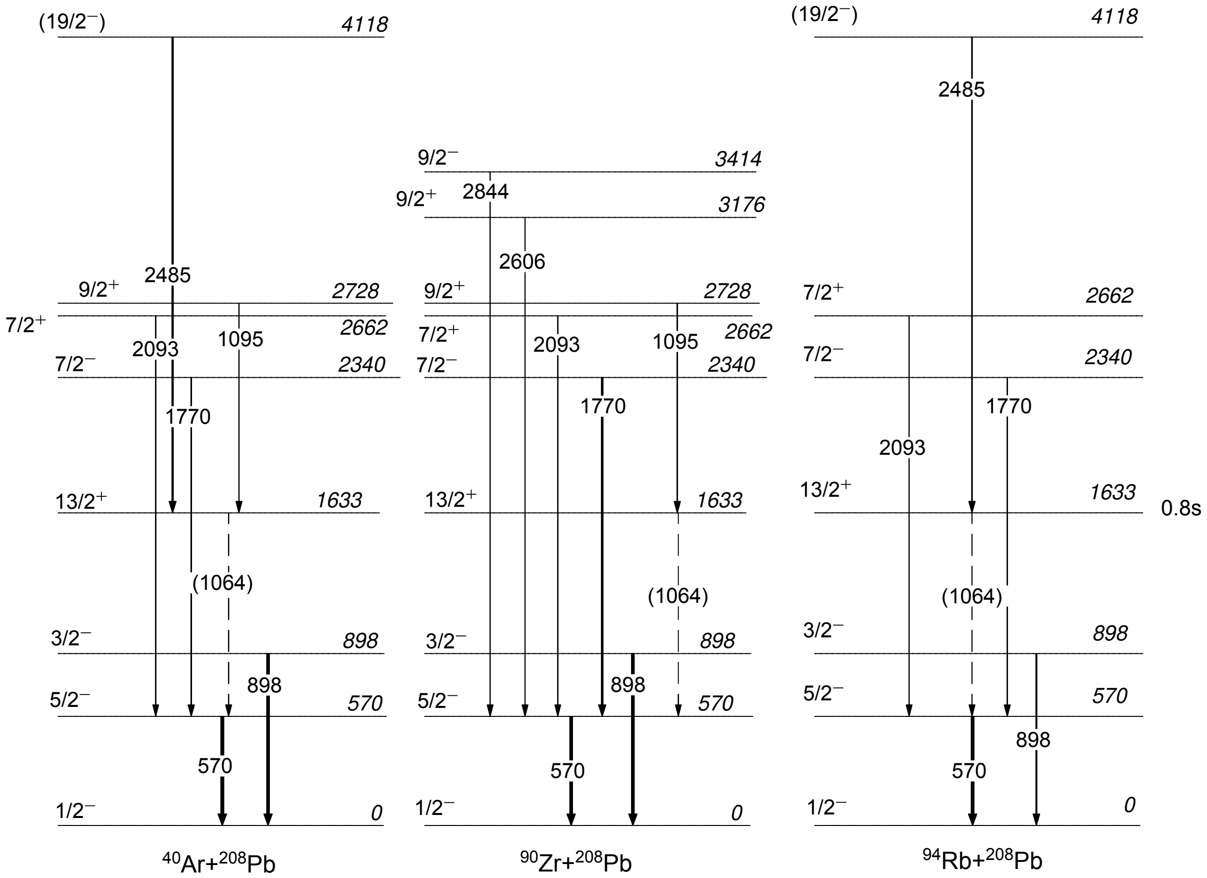

Figure 5.12: The experimental level schemes of ^{207}Pb from: ^{40}Ar+^{208}Pb (left), ^{90}Zr+^{208}Pb (middle) and ^{94}Rb+^{208}Pb (right) reactions. Relative γ-ray intensities are indicated by the width of the arrows. For tentative (dashed-arrow) γ transitions intensity is arbitrary. The energy, spin and parity of levels, and the energy of γ transitions are as in Ref. [127].

5.4 ^{209}Pb

The ground state of ^{209}Pb is $9/2^+$. As ^{209}Pb has only one neutron more than the doubly-magic ^{208}Pb, its ground state can be described as a neutron in the first orbital outside the $N = 126$ shell, $2g_{9/2}$ (see Fig. 5.1). If the $2g_{9/2}$ neutron moves to a higher orbital of the same shell, namely $1i_{11/2}$, $1j_{15/2}$, $3d_{5/2}$, $4s_{1/2}$, $2g_{7/2}$, and $3d_{3/2}$, the $11/2^+$, $15/2^-$, $5/2^+$, $1/2^+$, $7/2^+$ and $3/2^+$ states are possible, respectively. One expects the dominance of single-particle configuration in these states. The spectroscopic factors for the one-neutron transfer from the ^{208}Pb ground state to states of ^{209}Pb were obtained from light-ion induced reactions [134]. We selected ^{208}Pb(t,d)^{209}Pb and ^{208}Pb(d,p)^{209}Pb studies, and plotted their spectroscopic factors $C^2S(2j+1)$ in Fig. 5.13. For example, for the $5/2^+$ state, one sees that the spectroscopic factors are ≈ 6, being very similar to the maximum value of $(2j+1) = 6$. This suggests the strong single-particle component in the $5/2^+$ state. By looking at the same figure, a similar conclusion can be drawn for all the other states, besides $15/2^-$.

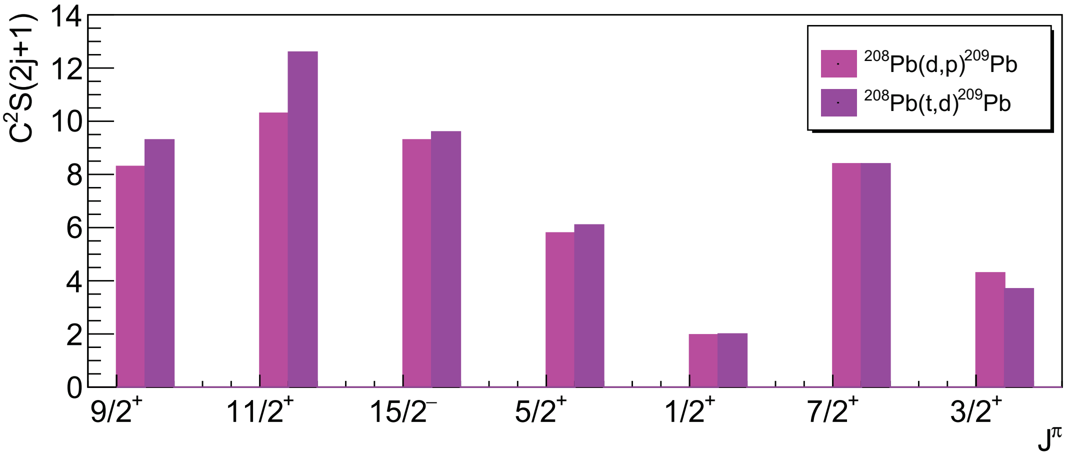

Figure 5.13: Spectroscopic factors for the states in ^{209}Pb, from the (d,p) reaction (E_{LAB} = 20 MeV) [135], and the (t,d) (E_{LAB} = 20 MeV) [112].

The discussed states were studied in ^{208}Pb(^{12}C,^{11}C)^{209}Pb and ^{208}Pb(^{16}O,^{15}O)^{209}Pb reactions (at E_{LAB} ~40-50 MeV·A) [136]. Using rather high beam energies, strong population of $9/2^+$, $11/2^+$, $15/2^-$ and $7/2^+$ states was observed. In the relatively recent ^{136}Xe,^{208}Pb+^{208}Pb γ-spectroscopy study [133, 137], at $E_{\mathrm{LAB}} \approx 6$ MeV·A, a detailed ^{209}Pb level scheme up to the 6 MeV (and the unknown J^{π}) was obtained. In particular, between the states of single-particle character, $11/2^+$, $15/2^-$, $5/2^+$ and $1/2^+$ were populated.

In ^{94}Rb+^{208}Pb, some of ^{209}Pb γ rays are between the strongest, considering the heavy-partner γ rays. This allowed for more detailed spectroscopic study. Its results are presented in Tab. 5.5. We observed clearly most of the states of single-particle character, as well as relatively high energy and high-spin states, such as $21/2^+$ and $23/2^+$ at ~4 MeV. Particularly strong are the 779 ($11/2^+$), 1423 ($15/2^-$), 1567 ($5/2^+$) and 2032 ($1/2^+$) keV states.

The intensity of these states enabled extraction of the associated γ-γ coincidences. A projection of the γ-γ matrix at E_γ = 1567 keV was constructed, and plotted in the left panel of Fig. 5.14. In this projected γ-spectrum one observes a strong 465 keV γ-transition. Its projection is plotted in the right panel of the same figure. We attributed these coincidences to $1/2^+ \xrightarrow{465} 5/2^+ \xrightarrow{1567} 9/2^+$ transitions, and, together with the other transitions as listed in Tab. 5.5, embedded them in the ^{209}Pb level scheme in Fig. 5.16.

Table 5.5: Gamma transitions attributed to ^{209}Pb. The energy, spin and parity of levels, and the energy of γ transitions are as in Ref. [134]. Relative intensities I_γ^{13} are normalized to the strongest transition in ^{209}Pb, E_γ = 1567 keV.

E_γ[keV]	E_i[keV]	J_i^π	E_f[keV]	J_f^π	I_γ^{13}[%]
465	2032	$1/2^+$	1567	$5/2^+$	41(4)
487	4329	$(23/2^+)$	3842	$(21/2^+)$	14(4)
644	1423	$15/2^-$	779	$11/2^+$	12(6)
779	779	$11/2^+$	0	$9/2^+$	67(5)
971	2538	$3/2^+$	1567	$5/2^+$	-
1423	1423	$15/2^-$	0	$9/2^+$	62(4)
1567	1567	$5/2^+$	0	$9/2^+$	100(5)
1624	3047	$(15/2_2)^-$	1423	$15/2^-$	7(3)
1669	3092	$(17/2^-)$	1423	$15/2^-$	21(2)
2101	3524	$(19/2^-)$	1423	$15/2^-$	32(3)
2419	3842	$(21/2^+)$	1423	$15/2^-$	12(2)
2491	2491	$7/2^+$	0	$9/2^+$	*2(1)*

We show the coincidence between the strong 1423 keV and 2419 keV γ transitions in Fig. 5.15. These E_γ were attributed to $(21/2^+) \xrightarrow{2419} 15/2^- \xrightarrow{1423} 9/2^+$ transitions. The $15/2^-$ has two evaluated branches [134], E_γ = 1423 keV being the strongest (100%). The other E_γ = 644 keV branch, the $15/2^- \xrightarrow{644} 11/2^+$ transition, has a branching ratio of 10%. We obtained nearly double branching ratio, evaluating the $I_\gamma^{13}(644)/I_\gamma^{13}(1423)$ of 18(9)%. This might be due to the contribution of the close in energy γ rays, E_γ = 640 keV in ^{210}Pb, and E_γ = 1427 keV in ^{94}Zr (from β-decay). The former has already been discussed in Subs. 5.2, and the latter is particularly strong background peak. Background subtraction might have influenced both the shape and intensity of the 1423 keV γ-peak, as illustrated in Fig. 3.12 in Chap. 3.

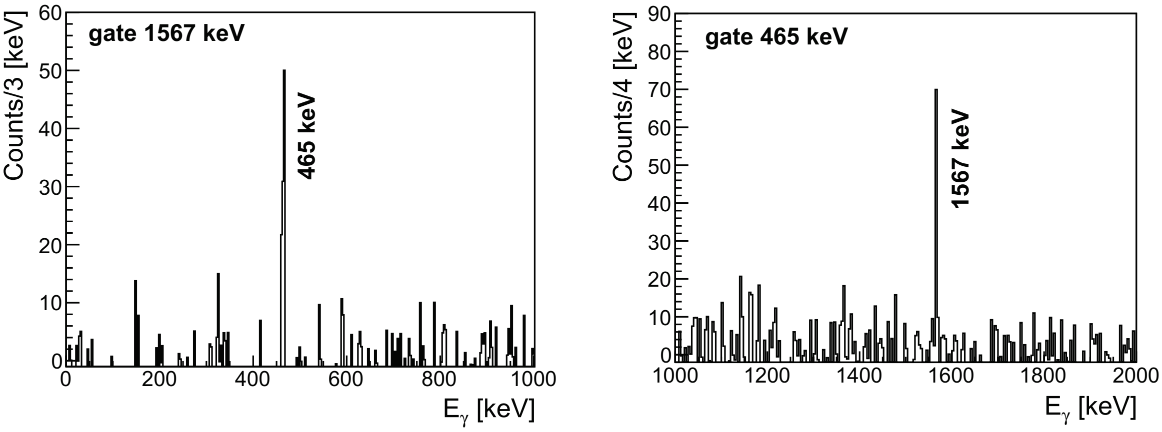

Figure 5.14: Projected γ-γ coincidence matrix in a selected energy range, obtained with the 1567 keV gate (left) and the 465 keV gate (right).

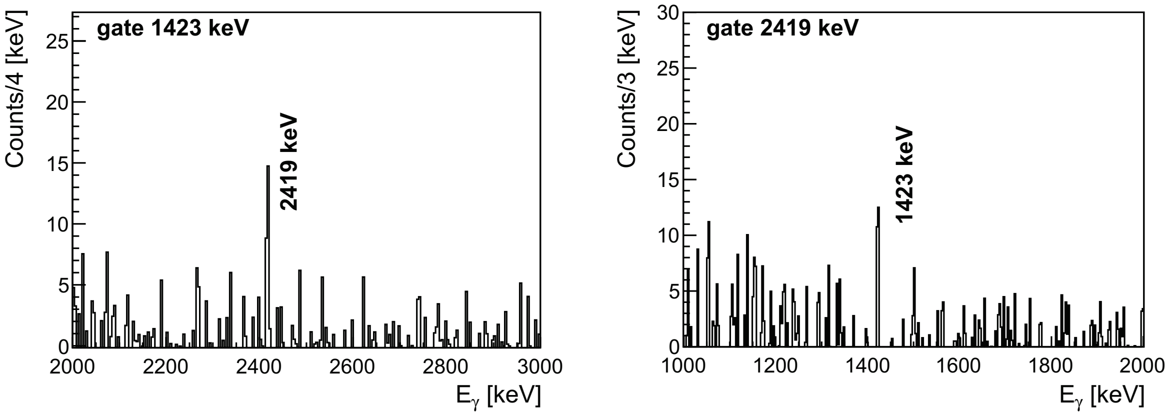

Figure 5.15: Projected γ-γ coincidence matrix in a selected energy range, obtained with the 1423 keV gate (left) and the 2419 keV gate (right).

The population of the 2491 $(7/2^+)$ keV and 2537 $(3/2^+)$ keV states, of possible single-particle character, is not clearly observed in our measurement. The γ-transition attributed to $7/2^+$, the $7/2^+ \xrightarrow{2491} 9/2^+$, is in the vicinity of $E_\gamma = 2485$ keV, a $(19/2^-) \to 13/2^+$ transition in ^{207}Pb. Thus, I_γ^{13} attributed to $E_\gamma = 2491$ keV (listed in Tab. 5.5) describes the strength of $7/2^+$ with great uncertainty. Therefore it was embedded with a dashed arrow in the ^{209}Pb level scheme in Fig. 5.16. Also, the 971 keV γ-ray, which can be attributed to the $3/2^+ \to 5/2^+$ transition, is not appropriately observed in the "thick" target γ-spectrum nor the γ-γ coincidences. We assume this is due to the $3/2^+$'s very short half-life, $\tau_{1/2} = 60$ fs. Since in the "thin" target (and Doppler corrected) γ-spectrum one observes $E_\gamma = 971$ keV clearly, we added it in the level scheme. For more details, see the top panel of Fig. 4.7.

Looking at the ^{209}Pb level scheme in Fig. 5.16 one notices few tentative transitions attributed to negative parity states. We would like to discuss the $(19/2^-)$ state, which has two decay branches, $(19/2^-) \xrightarrow{2101} (15/2^-)$ and $(19/2^-) \xrightarrow{432} (17/2^-)$. The observation of E_γ = 432 keV in the "thick" target γ-spectrum is hindered by the very strong E_γ = 405 keV, as illustrated in the "thick" target target γ-spectrum in the Fig. 4.9. This E_γ = 405 keV was attributed to ^{94}Rb, as it was discussed in Subs. 4.4.2. We remind that the velocity of ^{94}Rb is $\beta \sim 10\%$, thus the effect of Doppler broadening is rather large. However, after Doppler correction of the "thin" target spectrum one observes E_γ = 432 keV The evaluated ratio of E_γ = 432 keV and E_γ = 2101 keV intensities in the "thin" target, is $I_\gamma^1(2101)/I_\gamma^1(432) = 52\%$. Since this is in agreement with the evaluated branching ratio [134], both γ transitions were kept in the level scheme.

Between the populated states, the spectroscopic factors from Fig. 5.13 indeed point to the dominant single-particle character for $11/2^+$, $5/2^+$, $1/2^+$, $7/2^+$ and $3/2^+$ states. The spectroscopic factor of the 1423 $(15/2^-)$ keV state is $C^2S(2j+1) \sim 9$, or nearly half the value one would expect from the single-particle state ($C^2S(2j+1) = 16$). Also, the strength of the attributed $B(E3: 15/2^- \xrightarrow{1423} 9/2^+)$ transition is 26(4) W.u. [138]. In ^{136}Xe,^{208}Pb+^{208}Pb studies [133, 137], which exploited shell-model and particle-octupole coupling model calculations, the $15/2^-$ state was described as the $\nu(j^1_{15/2})$ single-particle configuration, with the rather important contribution of the $\nu(g^1_{9/2}) \times 3^-$ configuration. The same models predicted that the 3^- plays a significant role also in the structure of the 3047 $(15/2^-_2)$ and 3842 $(21/2^+)$ keV states. In fact, even the double-octupole configuration, $\nu(g^1_{9/2}) \times 3^- \times 3^-$, can be attributed to the $21/2^+$ state.

We emphasize that in ^{94}Rb+^{208}Pb the $21/2^+$ state is very clearly observed, from the $(21/2^+) \xrightarrow{2419} 15/2^- \xrightarrow{1423} 9/2^+$ γ-γ coincidence. On the contrary, the observation of E_γ = 1624 keV, which was attributed to the $15/2^-_2$ state, is not very clear. It is inscribed as a dashed-arrow transition in the ^{209}Pb level scheme in Fig. 5.16.

To summarize, in ^{94}Rb+^{208}Pb we observed strongly the states of single-particle character in ^{209}Pb: $11/2^+$, $5/2^+$ and $1/2^+$. We also observed the population of states which might contain a particle-octupole admixture, as $15/2^-$, or even particle-double-octupole admixture, as $21/2^+$. One might notice that states of similar character were populated in ^{207}Pb. The statistics of γ rays attributed to ^{209}Pb enabled more detailed spectroscopic study via γ-γ coincidences, however, some of the attributed γ transitions remain tentative.

Especially for some of these tentative γ transitions, we benefited from the comparison to the stable beam experiments, in particular ^{40}Ar+^{208}Pb. The simplified ^{209}Pb level scheme from ^{94}Rb+^{208}Pb is compared to the complete ^{40}Ar,^{90}Zr+^{208}Pb level schemes in Fig. 5.17. In the argon beam experiment the most states of single-particle character in ^{209}Pb were populated. In addition, γ transitions attributed to $15/2^-_2$ and $21/2^+$ were clearly observed. One notices the similarity between the ^{209}Pb level schemes from the argon and rubidium beam experiments, considering the excitation energies which were reached, and the populated states. This observed similarity speaks in a favour of attributing the tentative E_γ = 1624 keV, and E_γ = 2491 keV to the ^{209}Pb level scheme.

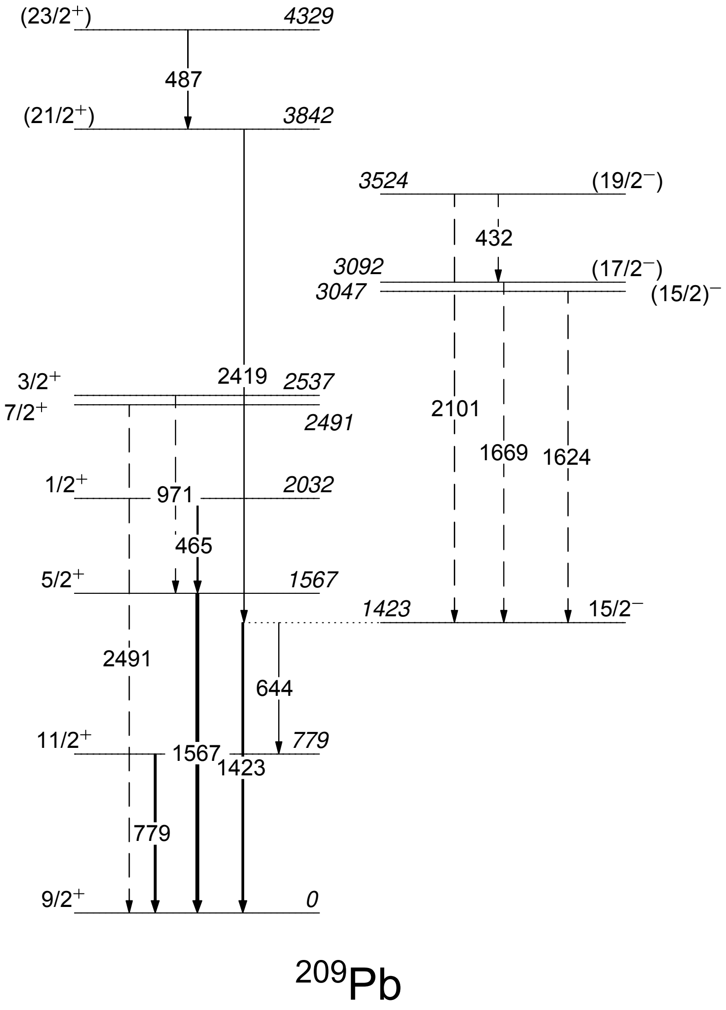

Figure 5.16: The experimental level scheme of ^{209}Pb. Relative γ-ray intensities are indicated by the width of the arrows. For tentative (dashed-arrow) γ transitions intensity is arbitrary. The energy, spin and parity of levels, and the energy of γ transitions are as in Ref. [134]

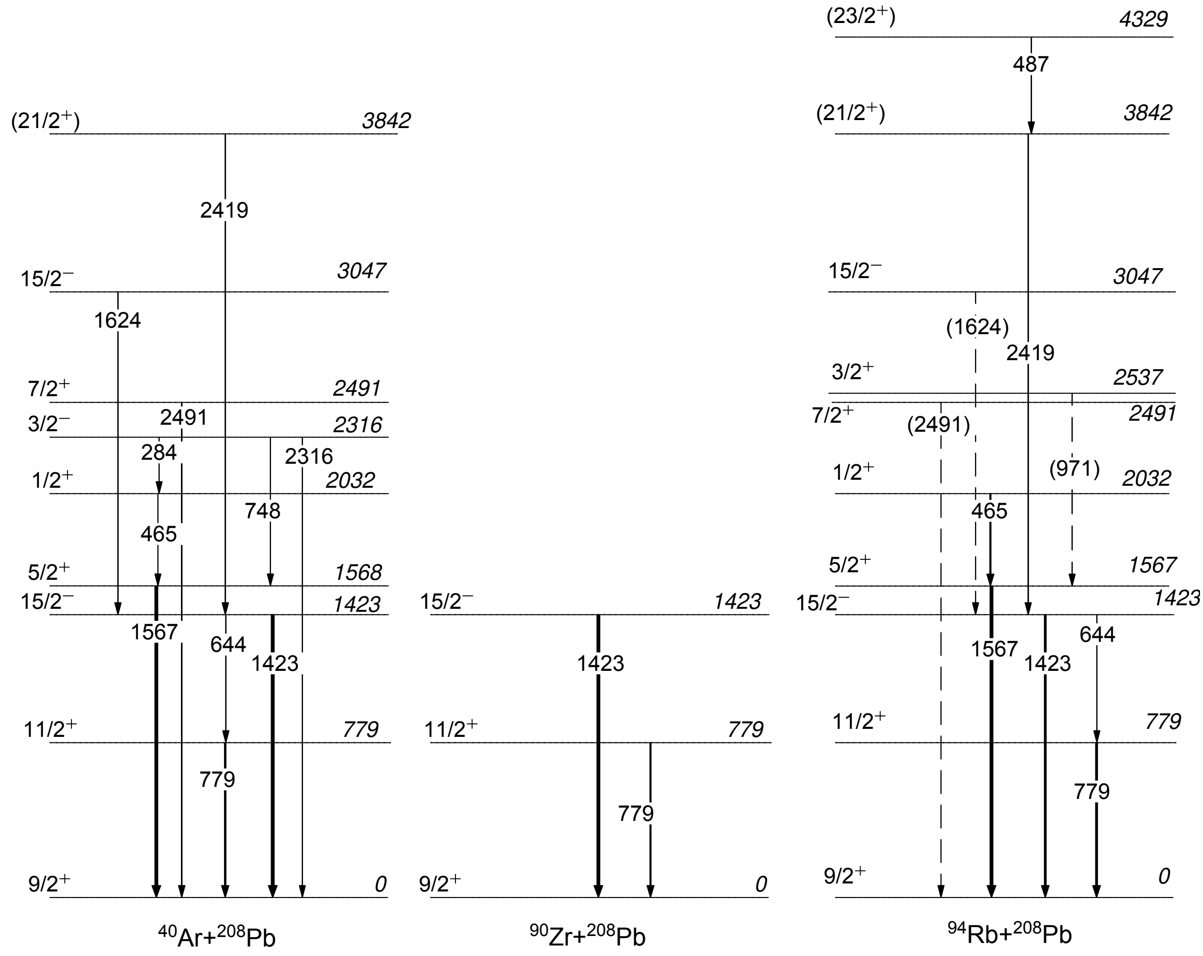

Figure 5.17: The experimental level scheme of ^{209}Pb from: ^{40}Ar+^{208}Pb (left), ^{90}Zr+^{208}Pb (middle), ^{94}Rb+^{208}Pb (right). Relative γ-ray intensities are indicated by the width of the arrows. For tentative (dashed-arrow) γ transitions intensity is arbitrary. The energy, spin and parity of levels, and the energy of transitions are as in Ref. [134].

5.5 Review and discussion

For convenience, the obtained $^{207-210}$Pb level schemes were plotted altogether in Fig. 5.18. From these level schemes one can see that the population of the states up to 4 MeV excitation energy was observed consistently in ^{207}Pb, ^{208}Pb and ^{209}Pb. Keeping in mind the statistics collected in ^{210}Pb is lower, states up to 3 MeV were observed. The populated states are mainly yrast, particularly in ^{207}Pb, ^{209}Pb and ^{210}Pb.

Between populated states, states of similar character were observed in ^{207}Pb and ^{209}Pb. For comparison, the normalized strengths in ^{207,209}Pb are plotted in Fig. 5.19. These strengths describe direct excitations, and were extracted from intensities I_{γ}^{13} (Tabs. 5.4 and 5.5) and the level schemes. Few lower strengths, mainly correlated to tentative (dashed-arrow) γ transitions could not be extracted with the acceptable accuracy and

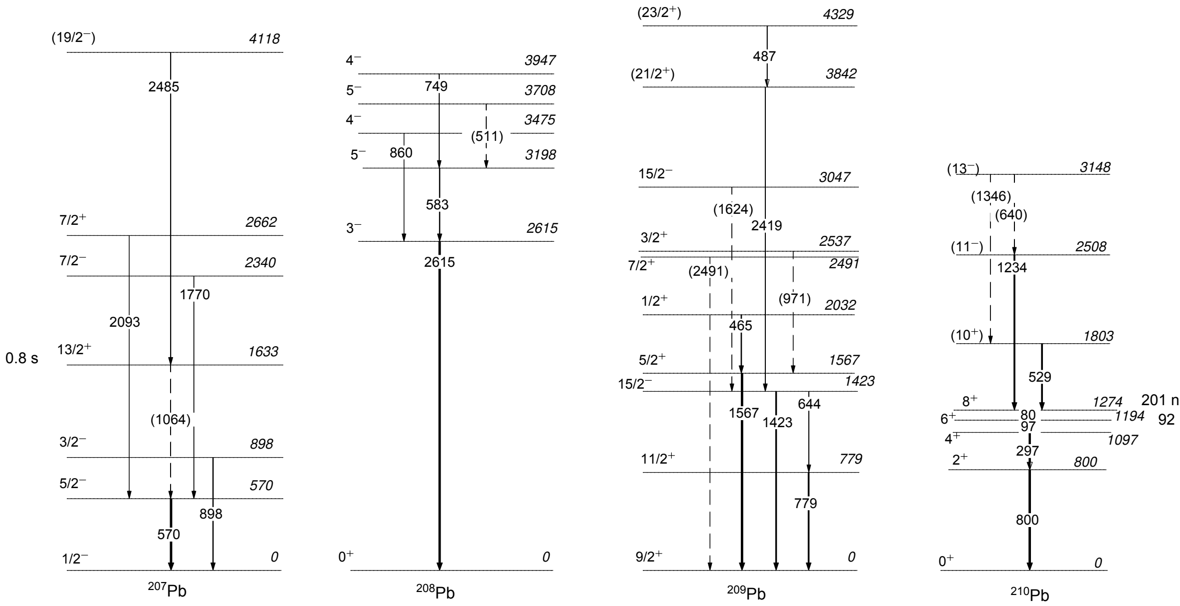

Figure 5.18: The experimental level schemes of ^{207,208,209,210}Pb. Relative γ-ray intensities are indicated by the width of the arrows. Only for tentative (dashed-arrow) γ transitions the intensity is arbitrary. The energy, spin and parity of levels, and the energy of γ transitions are as in our work and as in Ref. [88].

were omitted.

In the top panel of Fig. 5.19, one observes $5/2^-$, $3/2^-$, and $7/2^-$, which are the states of single-particle character in ^{207}Pb. Similarly, in the bottom panel, one notices $11/2^+$, $5/2^+$, $1/2^+$, which are in principle the states of single-particle character in ^{209}Pb. $15/2^-$ will be discussed later on. Then, higher-spin states around $E_{ex} = 4$ MeV are observed in both cases, $19/2^-$ in ^{207}Pb and $21/2^+$ and $23/2^+$ in ^{209}Pb. For the structure of $19/2^-$ and $21/2^+$ states in particular, the 3^- excitation in ^{208}Pb becomes rather important [130, 133, 137], as we have already pointed to (Subs. 5.3, 5.4).

In our experiment, the 3^- state and the attributed $3^- \xrightarrow{2615} 0^+$ transition of ^{208}Pb are strongly observed. Obviously, the latter is an $E3$ transition of reduced transition probability $B(E3) = 34.0(5)$ W.u. The other $E3$ transitions, also relatively strongly observed, were attributed to ^{207,209,210}Pb. These are

- ^{207}Pb: $19/2^- \xrightarrow{2485} 13/2^+$, $B(E3) = 40(8)$ W.u. [130]
- ^{209}Pb: $15/2^- \xrightarrow{1423} 9/2^+$, $B(E3) = 26(4)$ W.u. [138]
- ^{209}Pb: $21/2^+ \xrightarrow{2419} 15/2^-$
- ^{210}Pb: $(11^-) \xrightarrow{1234} 8^+$, $B(E3) = 21(2)$ W.u. [97]

which are, together with the $3^- \rightarrow 0^+$ transition, plotted in the level schemes in Fig. 5.20. From the experimental $B(E3)$ values given above (and obtained in the cited works) one

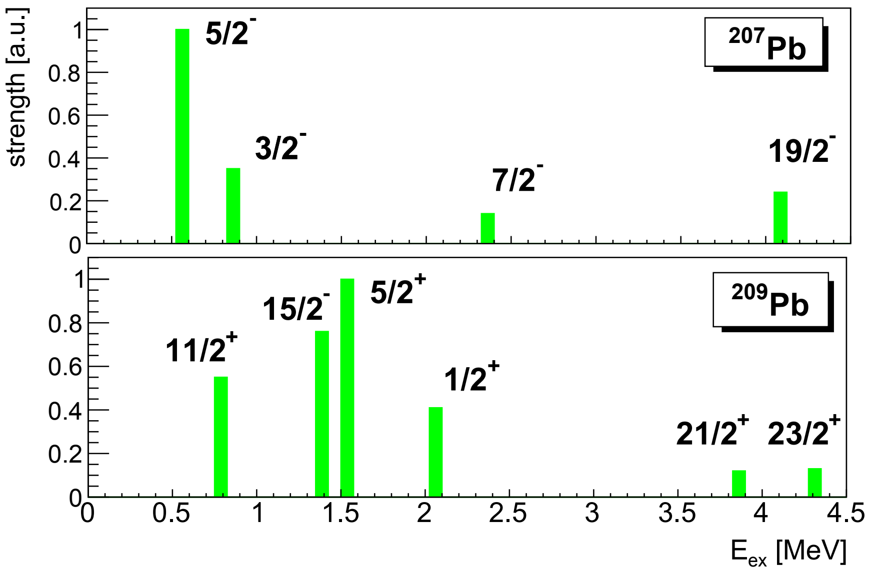

Figure 5.19: The experimental strengths of states, obtained from the measurement with the 13 mg/cm^2 target, for ^{207}Pb (top) and ^{209}Pb (bottom). Data was normalized to the largest strength in each isotope.

infers that the octupole-vibrations do indeed play a role in the character of the $19/2^-$ state in ^{207}Pb, $15/2^-$ in ^{209}Pb, and 11^- in ^{210}Pb. Possible configurations of these states are summarized in Tab. 5.6, of purely informative character. One can see that, for example, $J^\pi = 19/2^-$ is the stretched configuration of the attributed $\nu(i^{-1}_{13/2})\times\ 3^-$ and $\nu(f^{-1}_{7/2})\times\ 3^-\times\ 3^-$ multiplets. Similarly, the stretched coupling of octupole vibration is assumed to contribute to the structure of the other states listed in the table.

For the $21/2^+$ state in ^{209}Pb, the work of Ref. [133] predicts $B(E3 : 21/2^+ \xrightarrow{2419} 15/2^-)$ $= 50$ W.u. This $B(E3)$ was obtained on the basis of the particle-octupole vibration coupling calculations [139]. In these calculations, the $21/2^+$ state was described by $\nu(j^1_{15/2})\times\ 3^-$ and $\nu(g^1_{9/2})\times\ 3^-\times\ 3^-$ configurations, and $15/2^-$ by $\nu(g^1_{9/2})\times\ 3^-$ and $\nu(j^1_{15/2})$ configurations.

At this point, we would like to comment on the case of the $15/2^-$ state in ^{209}Pb (at E_{ex} = 1423 keV). Reflecting the contributions of both single-particle and the particle-octupole vibration excitations, its spectroscopic factor is $C^2S(2j+1) \approx 9$ (see Subs. 5.4 and Fig. 5.13). The missing $j_{15/2}$ spectroscopic strength is assumed to be distributed to higher E_{ex}, at about 3.5 MeV [135]. In the recent work of Ref. [34] (discussed in Subs. 1.2.2) it was shown that $j_{15/2}$ single-particle energy strongly influences the agreement between the experimental data and the calculations in the $^{212-216}$Pb. The measured

Table 5.6: The states involved in $E3$ transitions and observed in ^{207,209,210}Pb. Given configurations are purely descriptive.

Isotope	E^{ex}	J^{π}	Configuration
^{207}Pb	1633	$13/2^{+}$	$\nu(i^{-1}_{13/2})$, $\nu(f^{-1}_{7/2})\times$ 3^-
	4118	$(19/2^{-})$	$\nu(i^{-1}_{13/2})\times$ 3^-, $\nu(f^{-1}_{7/2})\times$ $3^-\times$ 3^-
^{209}Pb	1423	$15/2^{-}$	$\nu(j^{1}_{15/2})$, $\nu(g^{1}_{9/2})\times$ 3^-
	3842	$21/2^{+}$	$\nu(j^{1}_{15/2})\times$ 3^- $\nu(g^{1}_{9/2})\times$ $3^-\times$ 3^-
^{210}Pb	2508	11^{-}	$\nu(g^{1}_{9/2},j^{1}_{15/2})$, $\nu(g^{2}_{9/2})\times$ 3^-

$B(E2)$ for the $\nu g_{9/2}$ seniority isomers in $^{212-216}$Pb were compared to the shell-model calculations which use the Kuo-Herling interaction [37, 38] in the neutron space beyond ^{208}Pb. In particular, in the case of ^{212,214}Pb, a disagreement between the experimental and calculated $B(E2)$ was observed, as shown in the left panel of Fig. 1.4, Subs. 1.2.2. If one includes a 1 MeV shift of the single particle energy, as a reliable estimation of its actual value, disagreement decreases (but not completely). However, other problems arise, such as the tendency of the B(E2) of 4^+ state in ^{214}Pb to go to zero, making it a long-lived isomeric state not observed experimentally.

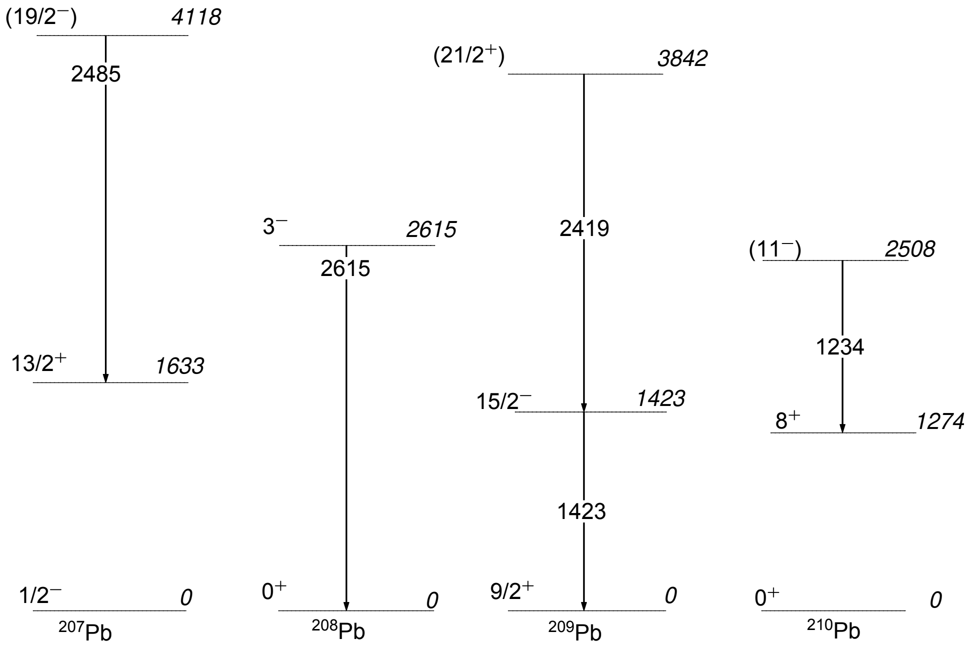

Figure 5.20: The experimental level schemes of ^{207,208,209,210}Pb. Only the selected γ transitions of an $E3$ character are plotted (see text).

From the excited states in Pb isotopes one could learn about the selective properties of the ^{94}Rb+^{208}Pb reaction mechanism. The selectivity is observed towards the yrast states prevalence, and particularly through the character of populated states. In even-even isotopes, we had the collective excitations, such as 3^- in ^{208}Pb, and the two-particle states in ^{210}Pb (see Subs 5.2). Then, in even-odd isotopes, ^{207,209}Pb, we had mainly single-particle and particle-octupole coupled states. Also, between these particle-octupole vibration states, only stretched configurations were observed. Thus, one could say that the high-spin states were populated selectively.

Our observations are in agreement with the main characteristics of the multinucleon transfer reaction mechanism which we presented in Subs. 1.3.1. The large angular momentum transfer (or the population of high-spin states) is characteristic at the energies close to the Coulomb barrier [3, 53, 66, 67]. The dominance of the single-particle and vibrational states, and states which can be explained from their coupling, were reported for several reactions with the stable beams (as in Refs. [47, 57, 64]). We must emphasize that our experiment provided the unique opportunity to extend the transfer reaction mechanism studies towards neutron-rich and unstable beams. We strongly believe that the degrees of freedom identified in this Chapter are also of great importance for understanding the path towards the more neutron-rich nuclei in lead region.

6 Cross section in the Pb isotopes

The ^{94}Rb+^{208}Pb reaction at energy close to the Coulomb barrier allowed to populate Pb isotopes moderately rich in neutrons. ^{207,208,209,210}Pb were identified from the attributed γ transitions, using the high-resolution γ-spectrometer MINIBALL and the CD fragment detector. In this Chapter, the total ^{207,208,209,210}Pb cross sections will be presented, alongside with the methods used to obtain it. Results will be discussed and compared to the semi-classical model GRAZING.

For the cross section measurement, we exploited the high efficiency of the experimental set-up and the use of ^{208}Pb target of two different thicknesses, 1 and 13 mg/cm^2. Using the 1 mg/cm^2 target, the Rb-like fragment-γ coincidence was studied, along with the angular distributions of strongly excited states. From the angular distribution of directly populated 3^- state in ^{208}Pb and the DWBA calculations, the cross section normalization factor was obtained. For more details, we refer to Subs. 4.2.1. Using the 13 mg/cm^2 thick target, the fragment-γ and the γ-γ coincidences were analyzed. The results of the analysis, ^{207,208,209,210}Pb level schemes, were presented and discussed in Chap. 5.

6.1 Experimental cross section

The cross section in ^{207,208,209,210}Pb was constructed on the basis of the attributed γ transitions. To illustrate which γ transitions essentially determine the cross sections, $^{207-210}$Pb level schemes are plotted altogether in Fig. 6.1. Level schemes were obtained by the use of "thin" target. Thus, the width of the γ-transition (the arrow width) corresponds to the intensity of γ-transition in coincidence with the Rb-like fragment, $I_\gamma^1(E_\gamma)$. I_γ^1 values were given in Tab. 4.1, of Subs. 4.3.1.

The cross sections of excited states σ_{ex} for both ^{207}Pb and ^{209}Pb were obtained by

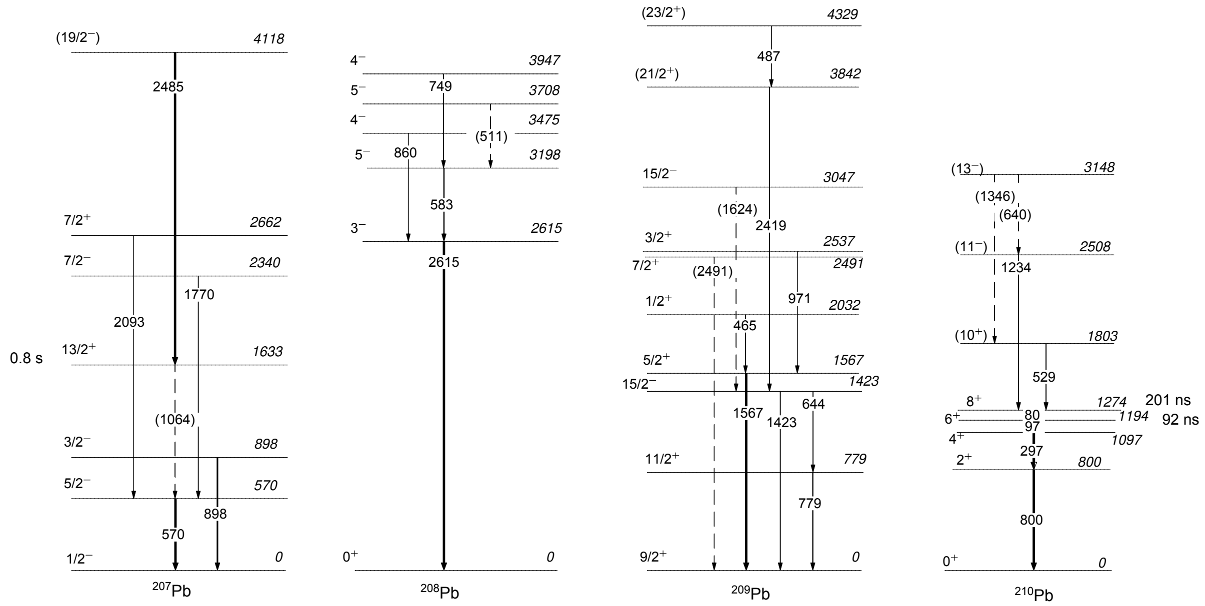

Figure 6.1: The experimental level schemes of ^{207,208,209,210}Pb. Relative γ-ray intensities are indicated by the width of the arrows. Only for tentative (dashed-arrow) γ transitions the intensity is arbitrary. The energy, spin and parity of levels, and the energy of γ transitions are as in our work and as in Ref [88]. Obtained with the use of "thin" target.

adding the intensities of all the γ-transitions which are not in a cascade. Thus, the $\sigma_{\text{ex}}(^{207}\text{Pb})$ was constructed as

$$\sigma_{\text{ex}}(^{207}\text{Pb})[mb] = [(I^1_\gamma(570) + I^1_\gamma(898) + I^1_\gamma(2485)] \cdot N_\sigma. \tag{6.1}$$

where the $N_\sigma = 0.617$ mb is the normalization factor (Eq. 4.3). In the same way, the cross section of excited states in ^{209}Pb was constructed from the intensities of $E_\gamma = 1567$, 1423, 779 keV, taking into account also the tentative (dashed-arrow) $E_\gamma = 2491$ keV.

One notices that the level schemes of ^{208}Pb and ^{210}Pb are rather simple, with all decays passing through the first excited state. To evaluate the $\sigma_{\text{ex}}(^{208}\text{Pb})$ we used the intensity of $E_\gamma = 2615$ keV, and to evaluate the $\sigma_{\text{ex}}(^{210}\text{Pb})$, the intensity of $E_\gamma = 800$ keV. To include also the isomer decay in $\sigma_{\text{ex}}(^{210}\text{Pb})$, the intensities from the prompt and delayed γ-spectrum were summed. This σ_{ex} cross sections are listed in Tab. 6.2, which will be discussed later.

The above presented method provides a lower limit for the cross sections as we are missing at least the ground state population. Thus, to obtain the total cross section, we had to make an estimation for the ground state cross section, $\sigma_{\text{g.s.}}$. For this estimation, we considered the main characteristics of the multinucleon transfer mechanism (Subs. 1.3.1)

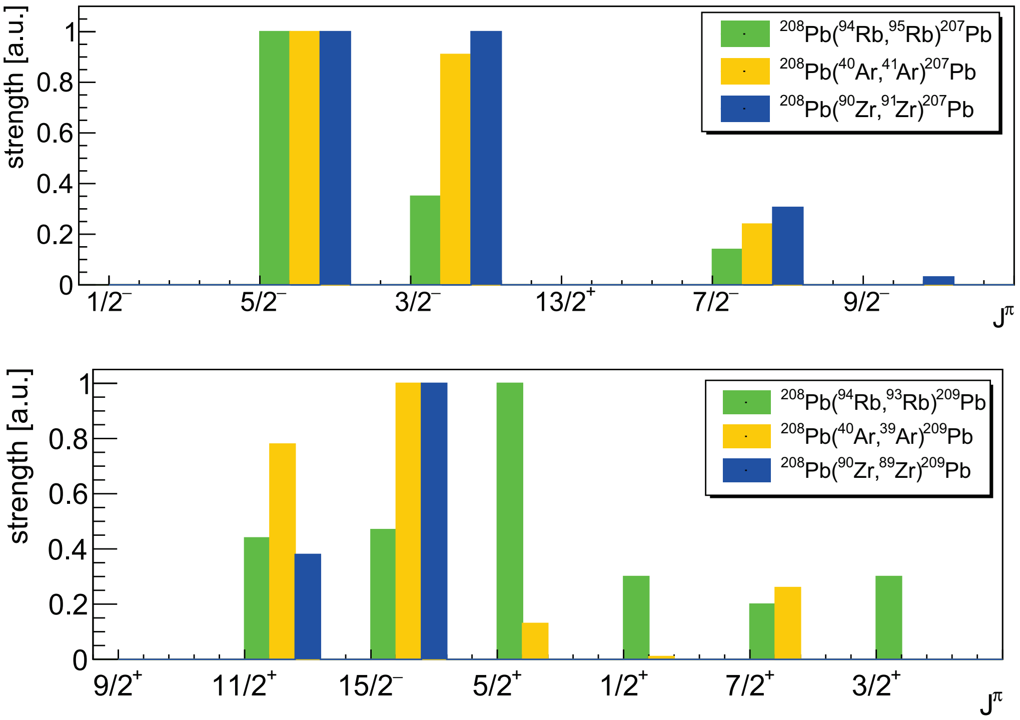

Figure 6.2: The ^{94}Rb,^{40}Ar,^{90}Zr+^{208}Pb experimental strengths of states of single-particle character, in ^{207}Pb (top) and ^{209}Pb (bottom). Data were normalized to the largest strengths. The ^{94}Rb+^{208}Pb strengths are from the measurement with the 1 mg/cm^2 target.

and the character of the excited states. A known property of the mechanism is that the optimum Q-value window[10] in the neutron transfer channels is close to 0 and has a width of a few MeV. This, for example, should manifest in the strengths of excited states. The strengths to be presented in the following text (I_{J^π}) were obtained from the experimental intensities of the γ transitions and the level schemes, to describe the direct excitation of the states.

The direct excitation strengths from the ^{40}Ar,^{90}Zr+^{208}Pb experiments (presented in Subs. 1.3.3, 5.3, 5.4 and Refs. therein) are plotted in Fig. 6.2. The presented experiments, besides that they obviously employ the same ^{208}Pb target, were measured at a similar bombarding energy range close to the Coulomb barrier. In both experiments (orange and blue histograms) the largest strengths are in the $5/2^-$ and $3/2^-$ states of ^{207}Pb, and the $11/2^+$ and $15/2^-$ states of ^{209}Pb. For convenience, the ^{94}Rb+^{208}Pb strengths were also added to the figure (green histograms).

In ^{207}Pb, the $1/2^-$ ground-state, and the $5/2^-$ and $3/2^-$ are the states of single-particle character. This is for example obvious from the spectroscopic factors in Fig. 5.10,

---

[10] Q_{opt} was given in the Eq. 1.16.

Chap. 5. These states are also similar in energy and the transferred angular momentum. Keeping in mind that the Q_{opt} ∼0 for the neutron-transfer channels, we assumed that the direct strength in the $1/2^-$ ground state ($I_{1/2^-}$) could be estimated as the average of direct strengths in the $5/2^-$ and $3/2^-$ states. In a similar manner, for the strength of the $9/2^+$ ground state in ^{209}Pb we adapted the strength of $11/2^+$ states. Strength values (I_{J^π}) are summarized in Tab. 6.1.

For the estimation of the ground-state cross section in ^{208}Pb and ^{210}Pb, we used the strength of the first excited state (i.e. their direct population), which are 3^- in ^{208}Pb and 2^+ in ^{210}Pb. This rather modest estimation was additionally supported exploiting the ^{40}Ar+^{208}Pb experiment, where one benefits from the very precise total cross section measurement. We remind that the projectile-like fragments were identified in Z, A, and charge state inside the PRISMA magnetic spectrometer, while the γ rays were measured by the CLARA γ-array. Thus, we inspected the cross sections measured with CLARA with the total absolute cross section measured with PRISMA. This method has determined the proportion of the ground states cross sections with respect to the total ones, and it suggested that the applied estimations were convenient [140].

Table 6.1: The I_{J^π} strengths of selected states (i.e. direct populations), used in the ^{94}Rb+^{208}Pb cross section estimation.

Isotope	$E_{ex}(J^\pi)$ [keV]	I_{J^π} [a.u.]
^{207}Pb	$570(5/2^-)$	60(10)
^{207}Pb	$898(3/2^-)$	36(16)
^{208}Pb	$2615(3^-)$	125(11)
^{209}Pb	$779(11/2^-)$	27(9)
^{210}Pb	$800(2^+)$	67(11)

This $\sigma_{\text{g.s.}}$ are summarized in Tab. 6.2.

6.2 Total cross section

The cross section of excited states σ_{ex} is plotted in Fig. 6.3 (blue points). One observes that σ_{ex} for ^{208}Pb, and for the one-neutron transfer channels, ^{207}Pb,^{209}Pb, are rather similar. After including the ground state cross section estimations ($\sigma_{\text{g.s.}}$), the total cross section σ_{tot} was obtained (red points). The total cross sections for $^{207-210}$Pb are therefore

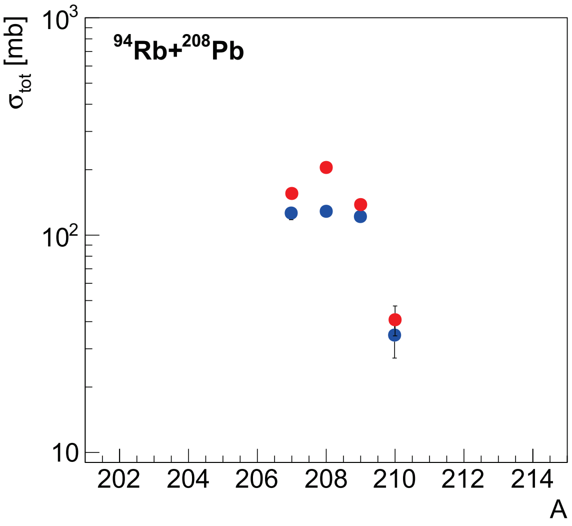

Figure 6.3: The experimental σ_{ex} (blue) and σ_{tot} (red) cross sections in $^{207-210}$Pb (see text).

equal to

$$\sigma_{\mathrm{tot}}(^{\mathrm{A}}\mathrm{Pb})[mb] = \sigma_{\mathrm{ex}}(^{\mathrm{A}}\mathrm{Pb}) + \sigma_{\mathrm{g.s.}}(^{\mathrm{A}}\mathrm{Pb}) \tag{6.2}$$

and listed in Tab. 6.2.

Table 6.2: The experimental σ_{ex}, $\sigma_{\mathrm{g.s.}}$, σ_{tot} cross sections in $^{207-210}$Pb (see text).

	^{207}Pb	^{208}Pb	^{209}Pb	^{210}Pb
σ_{ex} [mb]	126(8)	128(8)	121(6)	35(7)
$\sigma_{\mathrm{g.s.}}$ [mb]	30(7)	77(7)	17(6)	6(1)
σ_{tot} [mb]	156(10)	205(11)	138(8)	41(7)

The construction of cross sections profited from the excellent resolution of the experimental set-up, and the experimental set-up properties. More importantly, the measurement of delayed γ transitions, within the delayed fragment-γ coincidence, was essential to construct the cross section in ^{210}Pb. The isomers in ^{210}Pb level scheme (Fig. 6.1), were very clearly observed within the delayed gate (Δt_d), which allowed for the proper construction of $\sigma_{\mathrm{ex}}(^{210}\mathrm{Pb})$.

6.3 Discussion

The experimental σ_{tot} in $^{207-210}$Pb are plotted in Fig. 6.4, and compared to the GRAZING calculations. One notices that errors in σ_{tot} (green points) are asymmetrical, to describe

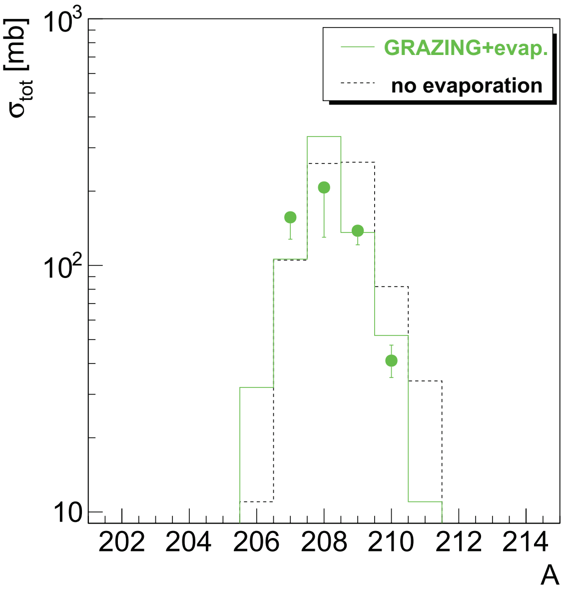

Figure 6.4: The experimental cross sections σ_{tot} in $^{207-210}$Pb (green points). The upper error bars are statistical, and the lower are set to σ_{tot}-$\sigma_{\text{g.s.}}$ at each A. Result is compared to the GRAZING code calculations including the effect of evaporation (green histogram), and neglecting it (black dotted histogram).

the corresponding σ_{ex} with lower bars. The model GRAZING (see Subs. 1.3.2 and refs. therein) includes also the effect of evaporation (green histograms), by taking into account the average excitation energies of the binary products.

One notices a rather fair agreement between the experimental data and the calculations. A sizeable cross sections are visible in the neutron-rich mass region. In particular, in the channel where one neutron is added to the target, ^{209}Pb, σ_{tot} is 138 mb. This value is particularly well reproduced by GRAZING. Then, in the channel where two neutrons are added to the target, ^{210}Pb, σ_{tot} is 41 mb, which is about 3 times lower than the σ_{tot} of ^{209}Pb. GRAZING predicts a slightly larger cross section in ^{210}Pb.

The comparison of the experimental results and the calculations depends strongly on the effect of evaporation. This is illustrated in Fig. 6.4, with the difference in the cross section calculated including the effect of evaporation (green histogram), and neglecting it (black dotted histogram). From these differences, one sees that the model predicts large effect of evaporation particularly in the neutron-rich sector. This effect is predicted to be larger as more neutrons are transferred (as for example in the cross section calculated for ^{211}Pb), which might be correlated to the higher excitation energies and the evolution of the mechanism towards the more complex regimes. As we had discussed earlier (especially

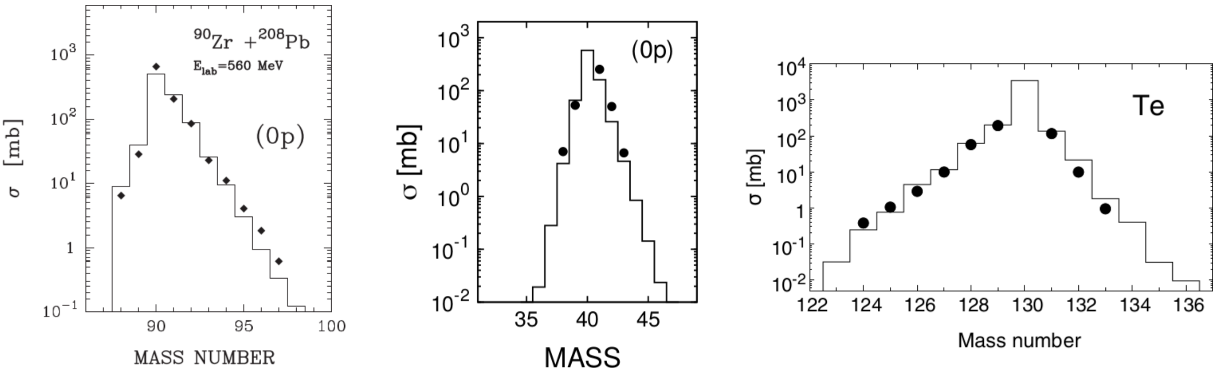

Figure 6.5: The experimental cross sections compared to the GRAZING calculations. Left: ^{90}Zr+^{208}Pb (E_{LAB} = 6.2 MeV·A) [46]. Middle: ^{40}Ar+^{208}Pb (E_{LAB} = 6.4 MeV·A) [67] Right: ^{197}Au+^{130}Te (E_{LAB} = 5.4 MeV·A) [6].

in the context of Fig. 1.3), the effect of evaporation depends strongly on the bombarding energy and on the projectile and target combination.

GRAZING has been so far successfully applied in the description of multinucleon transfer reactions as well as of fusion reactions. In particular, the model turned out to describe very well the experimental neutron transfer cross sections for a large amount of data sets taken in reactions with stable beams. Such examples are shown in Fig. 6.5, in which the presented cross sections for three different systems were obtained with the spectrometer PRISMA. These examples support the use of GRAZING, as good basis for the interpretation of the cross section obtained in $^{207-210}$Pb.

6.4 Towards the neutron-rich heavy nuclei

The evaluated total cross section in Pb isotopes leads us to the important conclusions. It shows that a considerable production of ^{209}Pb and ^{210}Pb can be achieved by transfer of neutrons from ^{94}Rb beam towards the ^{208}Pb target at the energy 30% above the Coulomb barrier. This successfully demonstrates that the heavy-ion transfer reaction induced by the neutron-rich unstable beam at energy close to the Coulomb barrier is a suitable mechanism for the population of the heavy nuclei moderately rich in neutrons. It also supports the choice of this particular neutron-rich beam, balancing between the neutron-richness and the intensity which can be provided by HIE-ISOLDE, and moderate bombarding energy.

The measured cross sections were appropriate for the γ-ray spectroscopy study. This study (presented in Chap. 5) have taught us that, in principle, the states of collective character were populated in the even-even Pb isotopes, ^{208}Pb and ^{210}Pb, and the states of single-particle character in even-odd, ^{207}Pb and ^{209}Pb. One observed a strong 3^- excitation in ^{208}Pb, which was important to understand the character of the populated states in neighboring ^{207,209}Pb, such as $19/2^-$ in ^{207}Pb and $21/2^+$ in ^{209}Pb. The structure of these relatively high-spin and higher in energy states, can be associated with the coupling of the octupole vibration to the $i^{-1}_{13/2}$ neutron hole and the $j^{1}_{15/2}$ neutron, respectively. A dominance of these particular configurations (in the total wavefunctions) is also predicted by the calculations [130, 131, 133, 137].

As seen from the population of yrast and high-spin states, large angular momentum transfers allowed to access a very interesting properties of nuclear structure (otherwise not achievable with the another reaction mechanism). For example, a particle-double-octupole vibrations are also predicted to contribute to the mentioned $19/2^-$ and $21/2^+$ states. Detailed particle-octupole vibration calculations are necessary to bring new information about these states, and to infer on their excitation in multinucleon transfer. Specifically in the case of $21/2^+$ in ^{209}Pb, the half-life and the character of the attributed γ transition are still unknown, yet of great interest.

The selectivity towards the particular elementary modes (collective and single-particle), and modes obtained from their coupling, accompanied by a maximization of the transferred angular momentum, has been repeatedly observed in the medium-mass nuclei populated by the multinucleon transfer reaction with stable beams [47, 57, 64, 65]. The ^{94}Rb+^{208}Pb study shows that the same degrees of freedom are rather important also when using the more neutron-rich and unstable beam, and along the path towards the more neutron-rich heavy nuclei.

As an example of the transfer cross section for channels where larger number of nucleons are involved, Fig. 6.6 represents the ^{94}Rb+^{208}Pb GRAZING calculated cross sections for the Hg isotopes. On the basis of GRAZING predictions, one supposes that the larger multinucleon transfer channels could have also been studied in the present experiment. For enough statistics in such channels (to perform a γ-spectroscopy study), an order of magnitude larger beam intensity had to be provided. Since these intensities are already achievable at HIE-ISOLDE and the other RIB facilities, GRAZING predictions will find their application in the future studies employing the multinucleon transfer reactions and the unstable heavy ion beams.

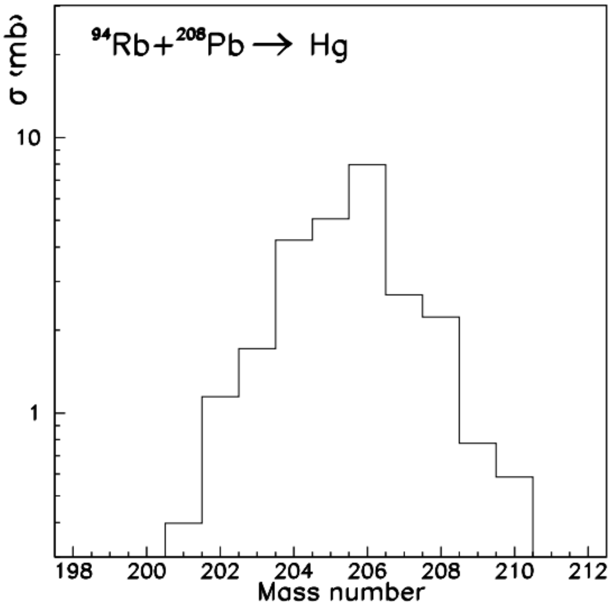

Figure 6.6: The ^{94}Rb+^{208}Pb GRAZING calculations (E_{LAB} = 583 MeV) for total cross sections of Hg isotopes.

In future studies, it will be of great importance to quantitatively evaluate the effect of the secondary processes, neutron evaporation and fission, which are expected to significantly affect the final yields in neutron-rich sector. Having this in mind, we also explored the performances of magnetic spectrometer PRISMA in the ^{206}Pb+^{118}Sn [141] reaction, where both the multinucleon transfer reaction products and fragments associated to the transfer-induced fission were observed. Our results, presented in the Outlook, demonstrate that PRISMA is suitable for the measurement of both kind of fragments. This can be exploited in future to quantitatively evaluate the survival probability of the heavy (neutron-rich) fragments produced in the multinucleon transfer reactions, and also to study the experimentally very demanding characteristics of fission processes.

At last, we would like to highlight the relevance of the ^{94}Rb+^{208}Pb experiment in context of the specific present (and forthcoming) experimental techniques and campaigns. The ^{94}Rb+^{208}Pb experiment highly encourages using the multinucleon transfer studies with heavy unstable beams, and their application in the γ-ray spectroscopy of the neutron-rich heavy nuclei. The presented physical case benefited from the heavy and high-energy beam provided by HIE-ISOLDE, thus fully exploiting a very recent upgrade of the facility. It was based on the particle-γ coincidence measurement with the MINIBALL γ-array coupled to the CD fragment detector. The experiment demonstrates a promising technique, especially in the context of the HIE-ISOLDE beam intensity upgrade (planned in the following years) which could open up a more neutron-rich sectors in the multinucleon transfer studies. Such physical cases will be also possible within the Selective Production of Exotic Species (SPES) project [142, 143], expected to bring the unstable beams to the Legnaro National Laboratories, and to start a new era of PRISMA and AGATA γ-array experimental campaigns.

7

Outlook: the ^{206}Pb+^{118}Sn experiment

Recently the accelerator facility of Legnaro National Laboratories provided for the first time the lead beam, the heaviest beam produced in this facility. This important achievement was motivated by the studies of the nucleon-nucleon pairing correlations probed in the presence of the high Coulomb field in the ^{206}Pb+^{118}Sn [141] reaction measured with the new-generation magnetic spectrometer PRISMA. The main goal of this measurement was to measure an excitation function at energies above and below the Coulomb barrier. Thus, the experiment was carried out at several bombarding energies (and angular settings). At the highest measured energy, 1200 MeV, and at the angle forward of the grazing angle we observed that besides the transfer reaction products close to the entrance channel mass partition, the fragments with different charge and energy distribution were also detected in PRISMA. These fragments are coming from the fission process, most likely the transfer-induced fission. We took the opportunity to analyze these fission fragments and to summarize the results of the analysis in this Outlook. Our main goals were to explore the capability of the PRISMA spectrometer in the identification in mass, charge and energy of these fragments and to pave the road for the future measurement in which the cross sections can be extracted. Such studies will be crucial in the quantitative evaluation of the survival probability of the heavy fragments produced in the multinucleon transfer reactions.

Since there is a lack of good quality data with the full isotopic (Z and A) identification of fission fragments, the potential of employing PRISMA in future measurement of the fission reaction mechanism (for the well selected cases) is very interesting. It would be also very important in view of the fact that the fission fragments can reach neutron-rich nuclei with the cross section sufficient to perform nuclear structure studies.

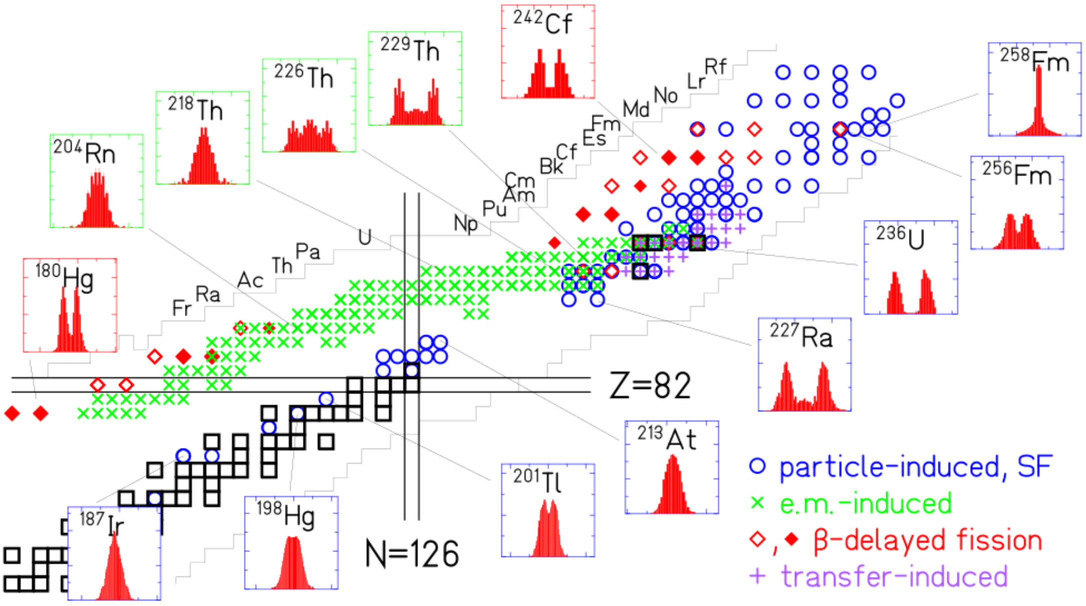

Figure 7.1: Overview of fissioning systems investigated until 2016 in low-energy fission studies taken from Ref. [144]. The multinucleon-transfer induced fission is labeled with purple crosses. Insets show the behaviour of the fission fragments mass distributions. For more details see Ref. [144] and refs. therein.

7.1 Introduction

Fission is a process in which the nucleus splits preferentially into two smaller fragments, accompanied by the release of a large amount of energy [144–147]. Formation of fission fragments is a subtle interplay of macroscopic and microscopic effects, such as shape-dependent surface and shell effects. This is particularly true for the low-energy fission at energy close to the barrier, where the single-particle shell structure of nucleons strongly influences the shape of the fissioning nucleus. Because of the complexity of the fission process, a large spread of the nuclear charges, masses and the different effects involved, the fission studies are very challenging.

The fission was studied by using the spontaneous fission, fission induced by thermal neutrons, fusion-fission, fission of radioactive beams, and transfer induced fission by using protons or light ions. Recently, also multinucleon transfer reactions have been used to study this challenging process. An overview of fissioning systems investigated in low-energy studies is presented in Fig. 7.1 [144]. This figure illustrates that the multinucleon transfer reactions have been already successfully used for the fission studies, especially in the actinide region. Systematic studies in actinide region have taught us that the centroid of the heavier fission fragment is at $A \sim 140$ and $Z = 52$ - 56, independently on the mass of

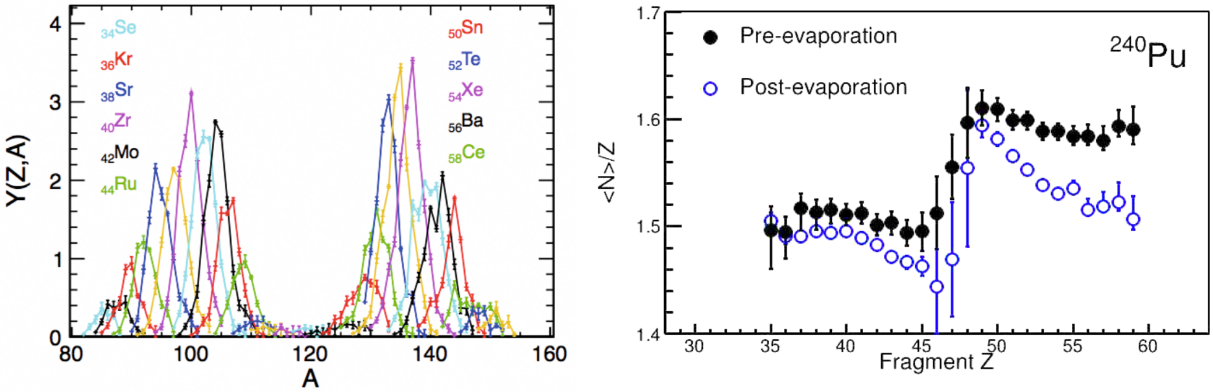

Figure 7.2: Selected experimental results from ^{238}U+^{12}C (at $E_{\mathrm{LAB}} = 6.1$ MeV·A). Left: fission mass distribution of ^{240}Pu. Right: neutron excess of pre-evaporation and post-evaporation fission fragments. For more details see text and Refs. [149, 150].

the fissioning nuclei. At the same time the mass distribution of the lighter fission fragment shifts towards lighter masses as the mass of the fissioning nuclei decreases (following the mass conservation). This behavior was explained by the fact that the fission depends on the shell structure of the heavy fragment, and is recently proposed to be also determined by the extra stability provided by octupole (pear-shaped) deformations [148]. While the almost constant mean Z numbers were observed in the heavy components of the fission fragment distributions for actinides, the weak variation of the Z number of the light peak was observed for the fission in the lead region. It was also noticed that when moving from the actinides to lighter fissioning systems, asymmetric fission gradually disappears, and symmetric fission takes over (see Fig. 7.1).

An important advance achieved recently was the full charge and mass identification of fission fragments, obtained in the ^{238}U+^{12}C [149, 150] multinucleon transfer reaction experiment measured with magnetic spectrometer in inverse kinematics. As an example of the achieved resolution the fission-fragment mass distribution for ^{240}Pu is presented in the left panel of Fig. 7.2. These data were obtained by VAMOS spectrometer [26] coupled to the annular particle detectors for the target-like fragment detection. One notices a two-peak structure, in which the centroid of the heavier fragment is around A∼140, while of the light is around A∼100. The $< N > /Z$ ratio or the average neutron excess of fission fragments of ^{240}Pu is plotted in the right panel of the same figure. Pre-evaporation data show that the light fragments are less neutron rich ($< N > /Z \sim 1.5$) and that the heavy fragments are more neutron rich ($< N > /Z \sim 1.6$) with respect to the fissioning nuclei (^{240}Pu, $N/Z = 1.55$). Obviously, the neutron evaporation has larger impact in the heavy fragment region.

For a better understanding of the fission mechanism a more complete systematic of low-energy fission is still needed. Legnaro National Laboratories, which provide the exceptional experimental apparatus such as magnetic spectrometer PRISMA have recently developed the heavy ion beams in the Pb region. Of particular interest is to investigate the Z and A distribution of the fission fragment, and the capability to detect such fragment with PRISMA. This is very important in view of the fact that the fission fragments can reach neutron-rich nuclei with the cross section sufficient to perform nuclear structure studies. On the other hand, it is important to study the survivial probability of the heavy fragments produced in the multinucleon transfer, in particular against fission.

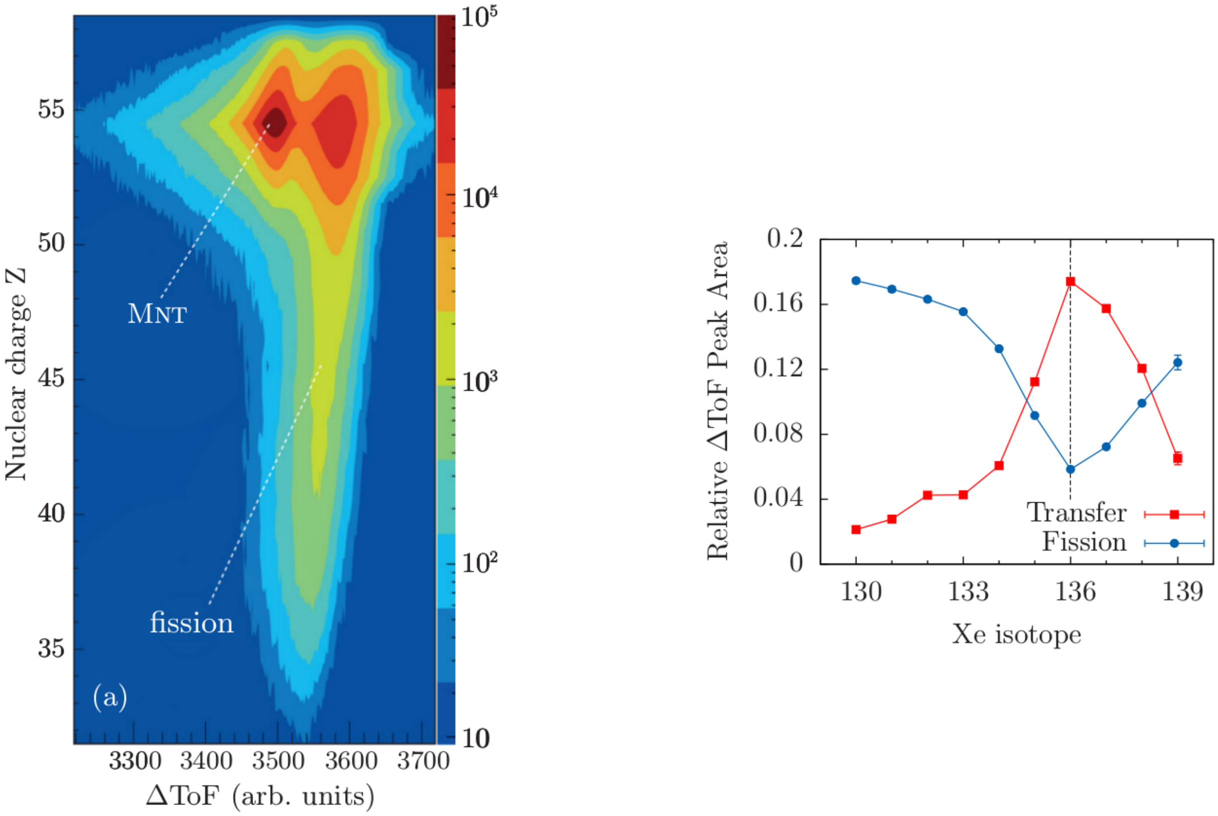

Figure 7.3: The experimental results from ^{136}Xe+^{238}U (at $E_{\text{LAB}} \sim 7.4$ MeV×A). Left: matrix of ΔTOF versus Z. Right: the relative contributions of MNT products and fission fragments. Lines are to guide eye. For more details see text and Ref. [32].

Short overview of selected PRISMA measurements. The ^{136}Xe+^{238}U multinucleon transfer reaction has been measured in particle-γ coincident experiment employing PRISMA coupled to the high-resolution Advanced Gamma Tracking Array (AGATA) and DANTE particle detector [32]. Beam-like reaction products were identified and selected with the PRISMA placed at the grazing angle $\theta_{\text{LAB}} \sim 50°$. The target-like reaction products were detected inside the DANTE array of microchannel plate detectors placed at the kinematically corresponding angle $\theta_{\mathrm{LAB}} \sim 56°$.

Matrix in Fig. 7.3 shows time-of-flight difference (ΔTOF) between the entrance detector of PRISMA and DANTE versus Z. The two different components separated in ΔTOF are visible. The distribution labeled "MNT" corresponds to the multinucleon transfer reaction products. In case of fission of the target-like nuclei, the fission fragment is also detected. Fission fragments, having different kinetic energies and velocities, are clearly separated and contained in the distribution labeled "fission". The distribution resembles the expected yield distribution from asymmetric fission of actinide nuclei around ^{238}U.

To illustrate the interplay of the two reaction mechanisms the relative contributions of multinucleon transfer reaction products and fission fragments are shown in the right panel of Fig. 7.3[11]. Transfer products have the maximum for nearly elastic and inelastic scattering, while the fission contribution increases in yield for more massive neutron transfers. This allowed for a systematic study of the structure of medium-heavy neutron-rich isotopes, such as Kr, studied up to ^{96}Kr (Z=36, N=50), as in the work of Ref. [151].

7.2 The ^{206}Pb+^{118}Sn experiment

The ^{206}Pb+^{118}Sn experiment was performed with the aim to study the reaction mechanism, and in particular the phenomena of pairing in nuclei [152–154]. Among a few possible ways to study pairing is the measurement of the transfer probability with respect to the distance of closest approach for single and multiple nucleon transfers. This technique has proven to be very successful in two pioneering experiments with PRISMA, ^{96}Zr+^{40}Ca [155] and ^{116}Sn+^{60}Ni [154, 156], which encouraged the ^{206}Pb+^{118}Sn experiment that combines more heavy target and projectile. The latter is also the heaviest (asymmetric) semi-magic system with closed proton shells and open neutron shells, very well Q-value matched for neutron transfers.

The experiment was set in inverse kinematics to provide the forward-focused target-like reaction products with high kinetic energies for a wide range of bombarding energies. PRISMA was positioned in grazing angular range for the target-like ions (Sn). Experi-

---

[11] One has to keep in mind that PRISMA was set-up to study the beam-like reaction products, so the transmission and Z identification of lower nuclear charges in the fission yield distribution was not optimal.

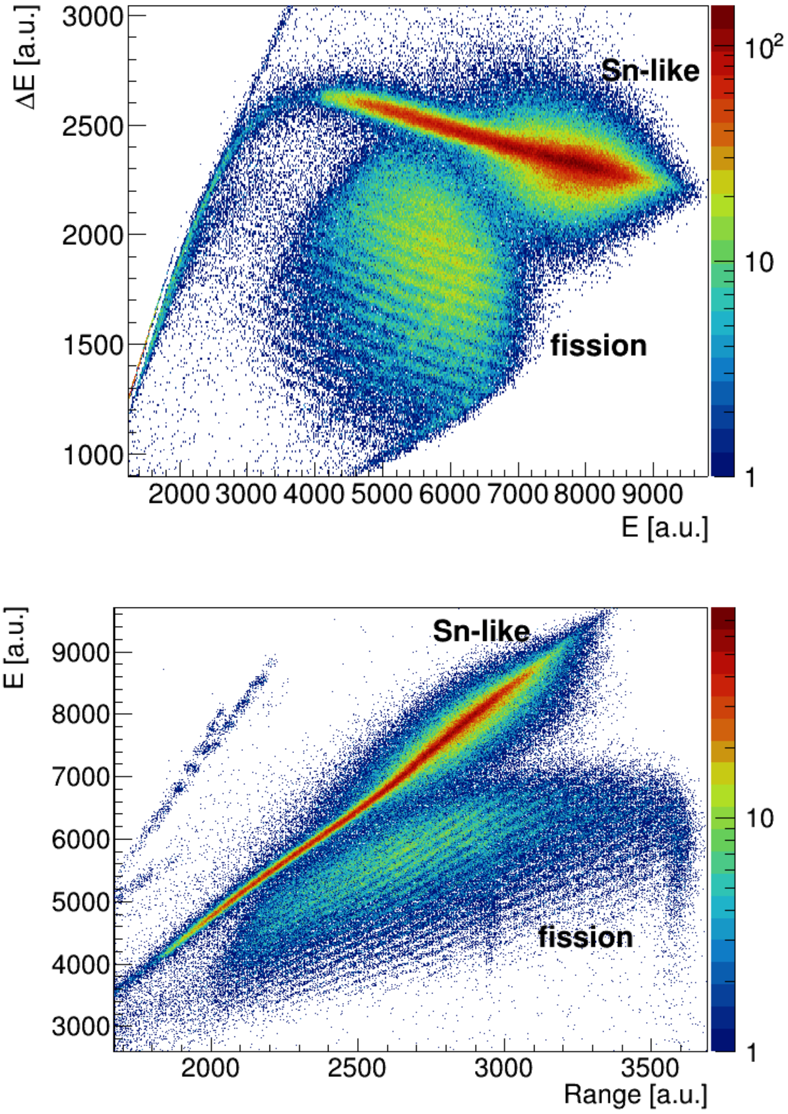

Figure 7.4: The ^{206}Pb+^{118}Sn experiment (at E_{LAB} = 5.8 MeV·A and $\theta_{\text{LAB}} = 25°$). Top: ΔE versus E matrix. Bottom: E versus *Range* matrix. Sn-like ions and fission fragments (around $Z \sim 40$) are labeled (see text).

mental set-up and data analysis details will be given in Sec. 7.3.

This work focuses on the measurement at highest energy, E_{LAB} = 1200 GeV (5.8 MeV·A) and angle $\theta_{\text{LAB}} = 25°$ (forward than grazing $\theta_{\text{gr}} = 32°$). The obtained matrices of the energy loss versus the total energy (ΔE - E) and the total energy versus the range (E - *Range*) are plotted in Fig. 7.4. In such matrices, used for Z identification, different Z can be discriminated and determined using Eq. 7.2. Notice that both the transfer reaction products and the fission fragments are observed (see the "Sn-like" and the "fission" label, respectively). The achieved Z resolution will be further discussed later in the context of Fig. 7.9.

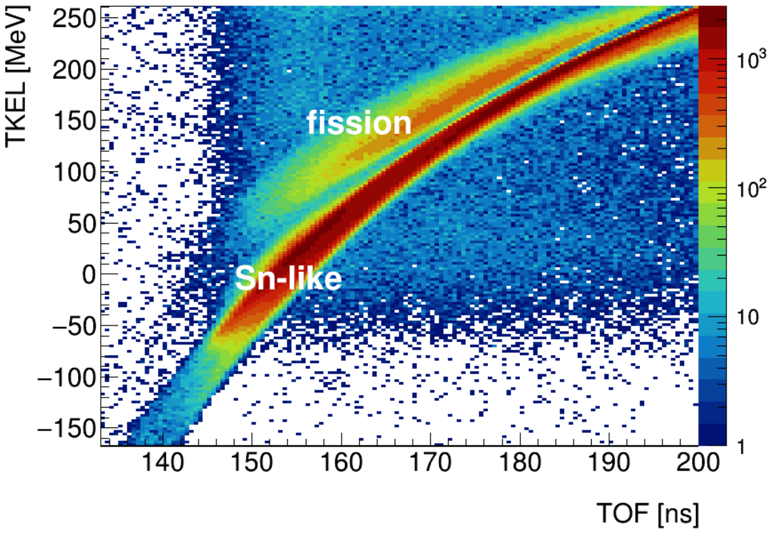

Figure 7.5: Matrix of TKEL versus TOF from the ^{206}Pb+^{118}Sn experiment (at $E_{\mathrm{LAB}} = 5.8$ MeV·A and $\theta_{\mathrm{LAB}} = 25°$). Sn-like ions and fission fragments are labeled.

Region labeled as "fission" is characterized by a rather large number of different isotopes, ranging from $Z = 45$ to $Z = 29$. These Z values point to the symmetric fission of the Pb-like nuclei. Since PRISMA was set to study the Sn-like ions they were stopped in the ionization chamber, while the faster fission fragements were not. This is visible as a punch-through effect in matrices in Fig. 7.4.

The total kinetic energy loss TKEL versus TOF is presented in Fig. 7.5. TKEL is constructed assuming a binary reaction, and is therefore wrongly calculated in the case of fission fragments. Despite this fact, a very good separation of the two different (labeled) regions is obtained. This figure also nicely illustrates the large energy acceptance of PRISMA.

The examples above clearly show the presence of fragments which differ from the transfer reaction fragments and which we charaterized as transfer-induced fission fragments. These fission fragments can be well discriminated from the multinucleon transfer reaction products. A large number of the fission fragments which was observed illustrates the extraordinary acceptance of PRISMA, ideal to exploit a diversity of fission processes. In this experiment the PRISMA was set up for the Sn-like ions and the extraction of the fission fragments cross section has not been achieved. Thus, the main aim of this work is to provide some information about the charge states and masses of fission fragments that are entering PRISMA.

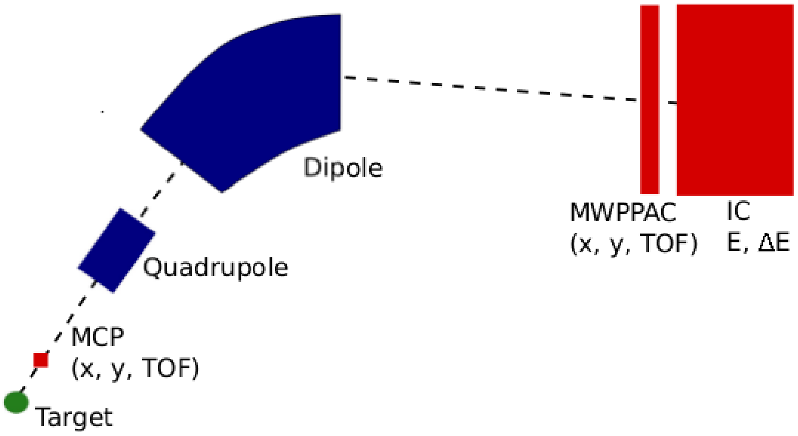

Figure 7.6: Schematic layout of the PRISMA spectrometer.

7.3 Experimental set-up and data analysis

The superconducting PIAVE-ALPI accelerator complex of LNL provided the ^{206}Pb beam at E_{LAB} = 1200 GeV (5.8 MeV·A) with average current of ∼ 2 pnA. The ^{118}Sn target of 100 μg/cm^2 thickness was sandwiched between 15 μg/cm^2 carbon layers (to reduce the sputtering effects on the target surface). PRISMA was set to $\theta_{\text{LAB}} = 25°$, for the detection of the Sn-like reaction products. The magnetic fields of PRISMA and the gas pressures of the focal plane detectors are listed in Tab. 7.1.

Table 7.1: The PRISMA settings for ^{206}Pb+^{118}Sn reaction measurement at E_{LAB} = 1200 MeV and $\theta_{\text{LAB}} = 25°$.

Dipole field	0.921 T
Quadrupole field	0.852 T
MWPPAC gas properties	C_4H_{10} at 6 mbar
IC gas properties	CF_4 at 34.5 mbar

PRISMA [46, 157, 158] is a large acceptance magnetic spectrometer, designed for the detection of medium-mass reaction products in heavy-ion reactions at energies close to the Coulomb barrier. Identification of Z, A, and charge state q is based on an event-by-event trajectory reconstruction inside the magnetic elements. PRISMA is composed of a quadrupole and a dipole magnet, and complex detectors system as illustrated in Fig. 7.6.

The entrance detector of PRISMA is a Micro Channel Plate detector (MCP). It provides the timing and position information in both x direction, which is defined along the dispersion (or horizontal) plane, and y direction, which is perpendicular to it. The detector exploits an electrostatic field for the acceleration of secondary electrons from a thin carbon foil onto the MCP assembly. It covers the whole solid angle of PRISMA, providing the position resolution of 1 mm, and the time resolution better than 350 ps.

The optical system of the spectrometer consists of a quadrupole singlet, used to focus the ions on the dispersion plane, and a dipole magnet, used to bend the trajectories of the ions depending on their ratio of momentum and charge state, p/q.

The focal plane detectors are the large-area gaseous ionisation detectors, which fully exploit the acceptance and dispersion of PRISMA. The array of Multiwire Parallel-Plate Avalanche Counters, or MWPPAC, provides the timing signal, and the x and y position with resolution around 1 and 2 mm, respectively. It is segmented in 10 independent sections. Each section is composed of the central cathode and two anode wired planes. The MWPPAC detector is followed by a multi-parametric transverse field Ionization Chamber array (IC), which measures the multiple ΔE signals. It is divided in 10 sections along the dispersion plane (same as MWPPAC) and in 4 sections in depth. The energy signals are provided by the 40 anode pads, a common Frisch grid and a common cathode. Additional side sections of IC are used as a veto for the highly bent trajectories, which are usually rejected during the data analysis (since their total energy cannot be constructed).

The main characteristics of PRISMA are summarized in Tab. 7.2, and the more detailed information can be found for example in Refs. [30, 67].

Table 7.2: Main characteristics of the PRISMA spectrometer.

Solid angle Ω	80 msr
$\Delta A/A$	1/250
$\Delta Z/Z$	1/60
$\Delta E/E$	1/1000
$\Delta p/p$	±10%
Maximum $B\rho$	1.2 Tm
$\Delta\theta_{\mathrm{LAB}}$	±6°
Rate capability	100 khZ

MCP position calibration. Figure 7.7 represents the ion position information ob-

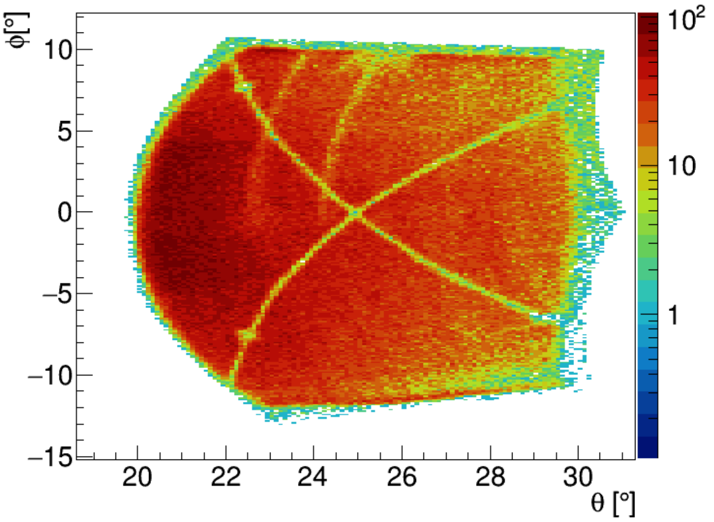

Figure 7.7: Matrix of the calibrated MCP detector in polar coordinates. The cross-shaped mask and the two probes for calibration purpose are visible.

tained with the entrance detector of PRISMA, MCP, by requiring a coincidence with the focal plane detector, MWPPAC. One immediately notices the lines which belong to the cross-shaped mask and the two probes inside the quadrupole magnet. They were used to calibrate the exact position of ions entering the spectrometer, x_{MCP} and y_{MCP}. To obtain the presented matrix, besides the position calibration, we applied a translation into the polar coordinates, θ_{LAB} and ϕ_{LAB}. Such representation more clearly illustrates the angles and angular acceptance of PRISMA.

MWPPAC position calibration. The x_{FP} is in principle constructed from the anode x-position information and calibrated by using the two short-circuited wires in the centre of each section.

TOF alignment. The ion time-of-flight (TOF) is measured as the time difference between the cathodes of the MWPPAC, which generate a starting signal, and the delayed timing signal of the MCP. The alignment of the TOF from different sections is a prerequisite to exploit the whole MWPPAC as a single detector. TOF measurement has a common offset, which had to be accounted for to obtain the total TOF. A total TOF of 155 ns for the elastic scattering of Sn ions was calculated from the ratio between the length of the central trajectory in PRISMA ($L \simeq$5.9 m) and the estimated velocity of the ions ($v \simeq$3.83 cm/ns).

Matrix of TOF versus the focal plane position x_{FP} is plotted in Fig. 7.8. One notices diagonal lines related to different ion mass-over-charge ratios that are reaching the focal

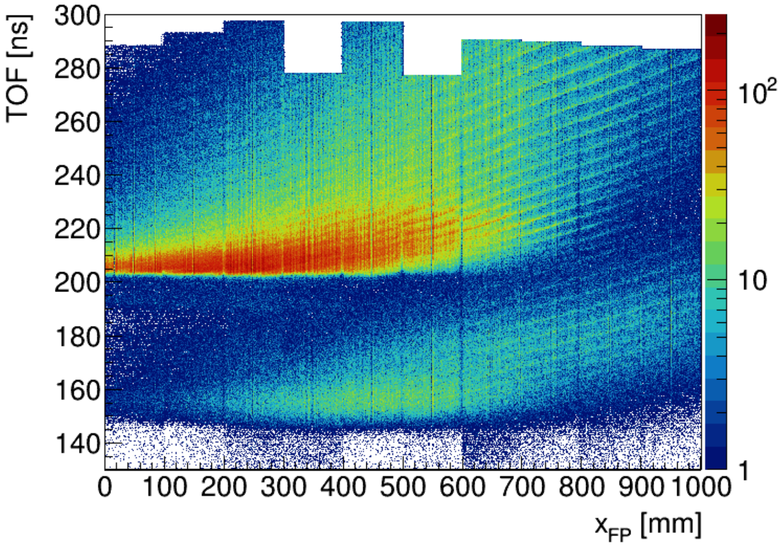

Figure 7.8: TOF versus calibrated x_{FP} position matrix, after the time alignment between the different sections. Two main structures correlated with the Pb-like ions (around TOF = 205 ns) and Sn-like ions (around TOF = 155 ns) are visible.

plane. The distribution of events around TOF = 155 ns corresponds to the Sn-like ions. At the present position of PRISMA the Pb-like ions were also entering the spectrometer, with TOF distributed around 205 ns.

A more precise determination of TOF offset is possible, for example, in the measurements which use PRISMA coupled to the γ-array. In such cases, one optimizes the Doppler correction of the well-known γ rays emitted in-flight (as for example in Refs. [67, 159, 160]).

IC calibration. IC provides 40 independent ΔE signals. A gain-matching of different signals is performed by using a charge integration device at the beginning of the experiment. Additional alignment of ΔE signals is performed to construct the total E.

Trajectory reconstruction. The ion parameters provided by PRISMA are entrance and focal plane positions, time of flight, energy loss and total energy. These parameters are used by an event-by-event trajectory reconstruction algorithm, which solves the equations of motion in the magnetic fields by assuming the straight trajectories outside the magnets of fixed length.

Ions entering the quadrupole magnet are focused vertically (y) and defocused horizontally (x) (with a hyperbolic motion). The dipole magnet bends the trajectories according to their magnetic rigidty (derived from the Lorentz law) [12]

$$B\rho = \frac{mv}{q}. \tag{7.1}$$

Obviously, the higher is the magnetic rigidity $B\rho$ (or higher momentum mv) the ions are less deflected. Result of the trajectory reconstruction is the curvature radius inside the dipole magnet ρ, path length L, total energy E (via TOF), and the mean path of ions in IC (*Range*). In following paragraphs we illustrate how to determine the ion Z, A, atomic charge state q, and velocity $\beta = v/c$.

Z **selection.** The ions of kinetic energy E, mass m, and nuclear charge Z entering an absorber experience the energy loss dE/dx. It can be described with relation

$$\frac{dE}{dx} \propto -\frac{mZ^2}{E} \ln\left(\frac{E}{m}\right) \tag{7.2}$$

derived from the Bethe-Bloch formula in a non-relativistic approximation. The ratio EdE/dx is only weakly dependent on E, and can be used to identify Z. The matrices of ΔE versus E and E versus *Range* were constructed and presented in top and bottom panels of Fig. 7.4, respectively. ΔE was constructed from the energy loss in the first sections of IC. Both matrices were obtained by applying the $TOF < 200$ ns gate to eliminate the Pb-like ions.

The most intense line in both matrices corresponds to the Sn ions (with the highest cross section of the ^{118}Sn elastically scattered). From the equation given above one expects that for a constant E, Z increases with energy loss, and decreases with range. Therefore, proton pick-up and stripping channels appear above and below the Sn line, respectively.

The Z distribution of proton transfer channels in this same measurement was studied in A. Utepov master thesis [161], obtained within our collaboration. By aligning the ΔE-E matrices obtained with different sections of IC, and then adding them altogether, one obtains the projection onto the ΔE axis as in Fig. 7.9. This spectrum illustrates the excellent Z resolution of PRISMA for the elements in vicinity of $Z = 50$, and that the proton transfer channels, from seven proton-stripping ($-7p$), and up to the six proton pick-up ($+6p$) have been reached. One notices that the proton-stripping are generally stronger then the proton pick-up.

---

[12] Assuming the radial component of the velocity is negliable.

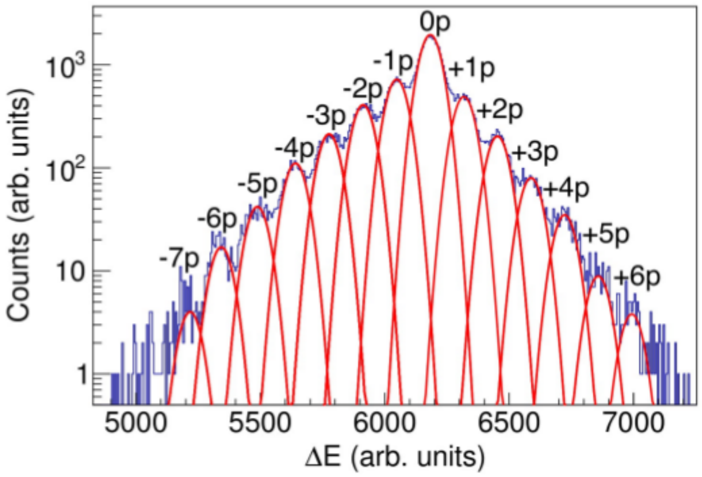

Figure 7.9: Mass-integrated Z distribution of proton transfer channels. The ΔE was constructed from the first two sections of IC. The multigaussian fits (red lines) describe the absolute yields for the indicated channels. From Ref. [161].

Atomic charge state q selection. Combining the expressions for magnetic rigidity $B\rho$ (Eq. 7.1) and the kinetic energy of an ion one comes to the relation

$$q = \frac{2}{B}\frac{E}{v\rho} \tag{7.3}$$

which is used for the atomic charge state separation. The individual atomic charge states can be separated in the two dimensional matrices of E versus $\rho\beta$. Such matrices are plotted in Fig. 7.10 for Sn ($Z = 50$) and Zr ($Z = 40$).

To properly attribute the charge state one uses the empirical charge state distribution calculations, such as one in Ref. [162]. The strength of the PRISMA magnetic fields was optimized to place the most probable charge state of ^{118}Sn ($Z = 50$, $E \sim 910$ MeV) in the central part of the focal plane. Having this in mind the most intense distribution in the Sn $\rho\beta$ - E matrix in Fig. 7.10 could be associated with the most probable charge state, $q = 40$. For a fixed $\rho\beta$, q increases with E.

By looking at the Zr $\rho\beta$-E matrix one notices that the obtained statistics and the resolution is sufficient for a charge state selection. Several charge states are clearly visible. However, since the PRISMA fields were set to select the most probable q for Sn ions, the charge state attribution in the case of fission fragments gets more complicated.

To better understand the charge state distributions of the fission fragments, we studied the Sn charge states in different energy regions. This should help to describe better the behaviour of the fission fragments inside spectrometer. In the ΔE-E matrix (top panel

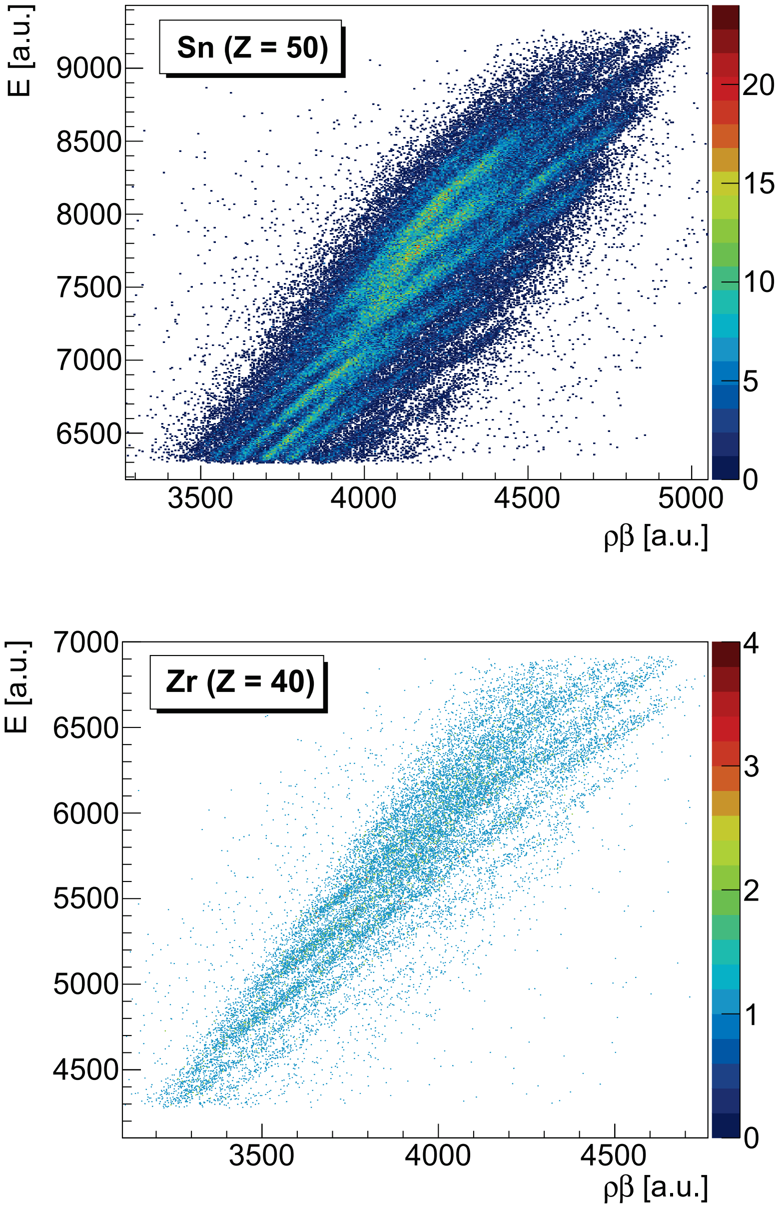

Figure 7.10: Sn (top) and Zr (bottom) $\rho\beta$ - E matrices used for charge state selection.

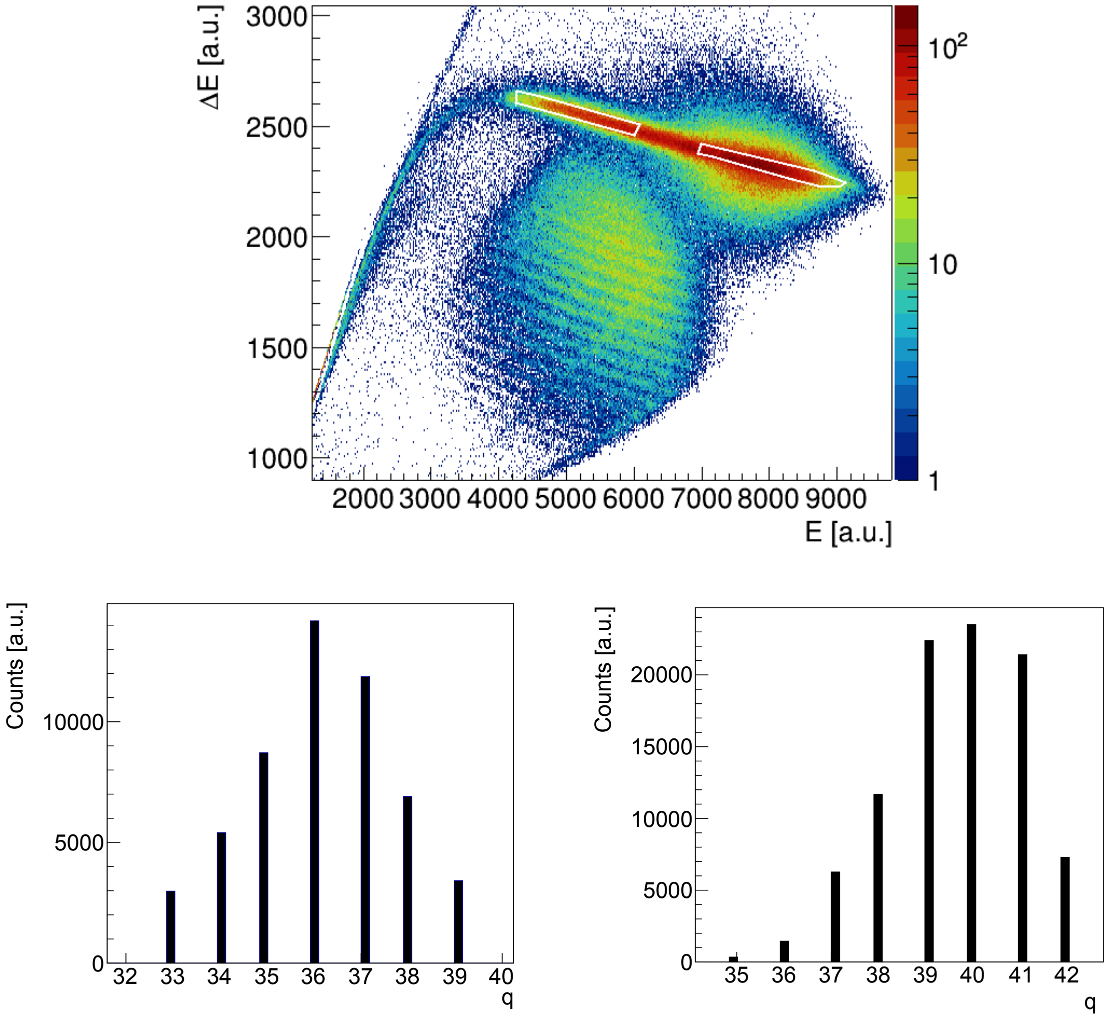

Figure 7.11: Top: ΔE versus E matrix. Gates illustrate two different ΔE-E regions. Bottom left: charge state distribution for the events inside the left ΔE-E gate (higher energy losses). Bottom right: charge state distribution for the events inside the right ΔE-E gate (lower energy losses).

of Fig. 7.11) two gates are inscribed with white polygons. While the high energy gate is characterized by the small energy losses, including also the elastic scattering, the lower energy gate is attributed to the large energy losses.

Charge state distributions from these two gates are plotted in left and right panel of Fig. 7.11. One notices that the charge state distribution shifts from $q \sim 40$ to $q \sim 36$ when going from small towards the larger energy losses. As the more probable interaction with detector matter is in connetion with the larger energy losses, this behaviour is what one should expect.

The A/q ratio and mass resolution. If one substitutes m with A, v with L/TOF, and includes relativistic equation for TOF[13] in Eq. 7.1 one obtains

$$\frac{A}{q} = B\rho \frac{TOF\sqrt{1-\beta^2}}{L}. \tag{7.4}$$

The matrix of A/q versus the x_{FP} position for Sn is presented in the top panel of Fig. 7.12. One observes the characteristic repetitive pattern of the different A/q, where the dominant elastic scattering ($A = 118$) is the most intense one. In principle, by performing the summation over the different charge states, one would obtain the total Sn mass distribution.

Besides this repetitive pattern one also observes curvatures due to the optical aberrations. They arise from the PRISMA optical properties not explicitly implemented in the trajectory reconstruction, such as the magnetic fields beyond the first-order approximation and fringe fields. Aberrations are generally more pronounced for heavier ions. Among the recent experiments with PRISMA, the aberration corrections successfully improved the mass resolution of Te [6, 30]. Corrections (explained in details in Ref. [30]) implement correction functions to straighten the A/q bands, and our result for Sn ions is plotted in the bottom panel of the same figure. The implementation of the aberration corrections for this measurement is still in progress and is part of J. Diklić PhD Thesis [163].

The mass distribution in terms of exact mass numbers in atomic mass units is obtained by the A/q calibration, being the calibration coefficients adapted to the Sn isotopes.

7.4 Experimental results: mass distributions

Sn-like ions. Following the mass reconstruction procedure as described above, we obtained the final Sn, Cd and Pd mass spectra plotted in Fig. 7.13. With the achieved mass resolution the different neutron transfer channels can be clearly distinguished.

The Sn mass spectrum is dominated by the elastic and inelastic channels. We observed the channels which correspond to the 7 neutron-stripping ($-7n$) and the 5 neutron pick-up ($+5n$). The ($+1n$) channel appears to be stronger than the ($-1n$). One might notice a rather large area of the peak around the $A = 121$, which is due to the repetition of the elastic channel, and can be reduced by improving the trajectory reconstruction [163].

In the Cd mass spectrum the $A = 117$ has the largest yield. With respect to the ^{118}Sn,

---

[13] $TOF = TOF\sqrt{1-\beta^2}$

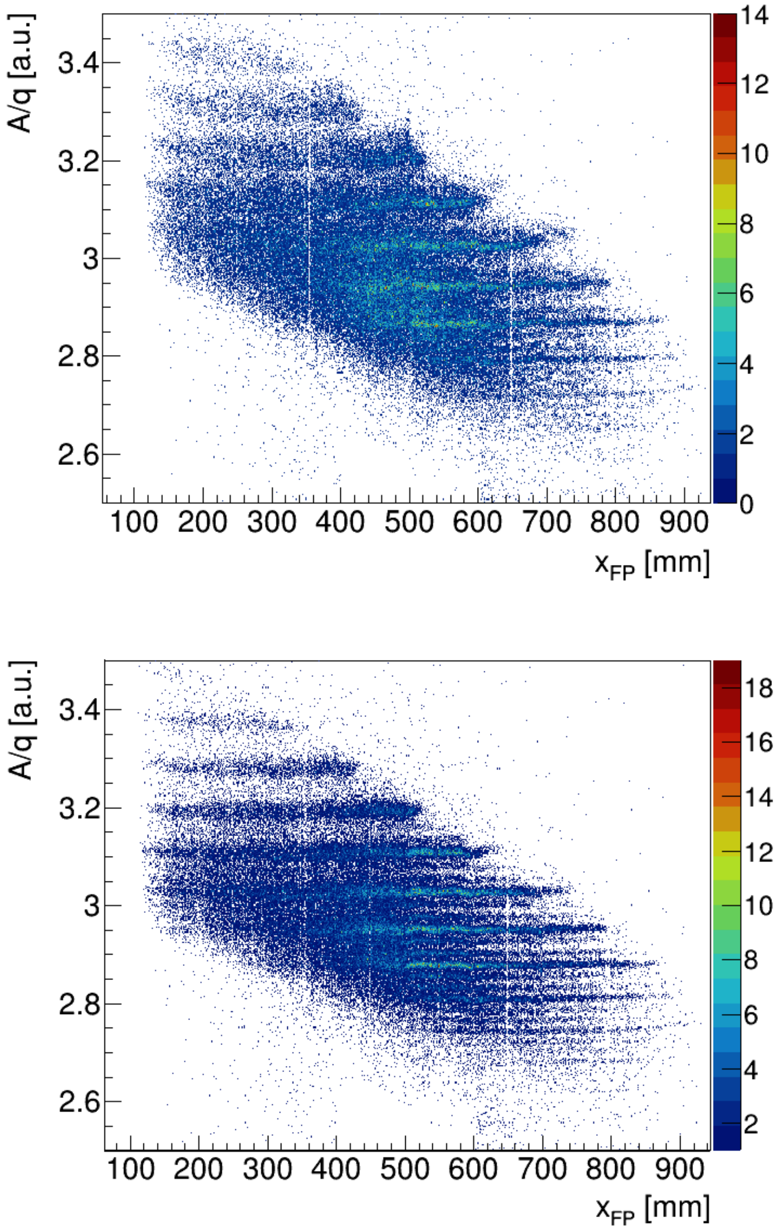

Figure 7.12: Matrix of A/q versus x_{FP} position for $Z = 50$. Top: before aberration corrections, botom: after aberration corrections (see text).

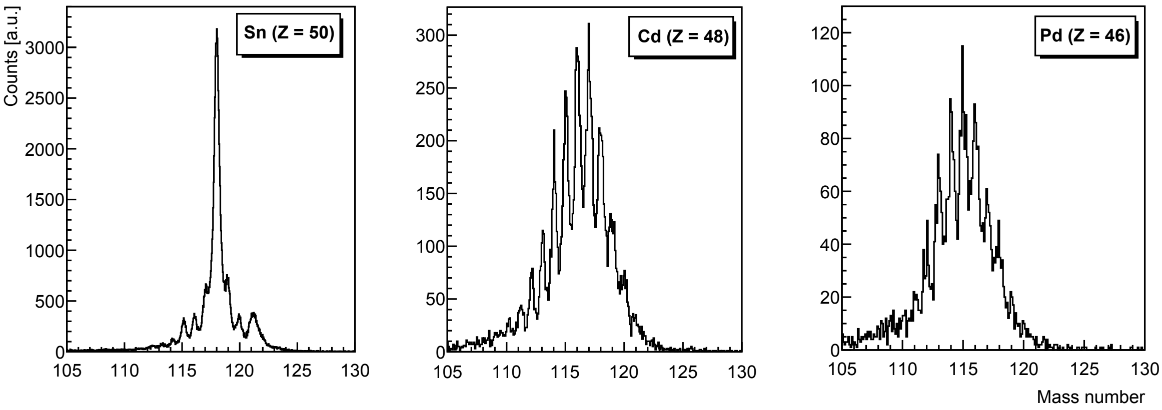

Figure 7.13: Mass spectra for Sn ($Z = 50$), Cd ($Z = 48$), Pd ($Z = 46$).

the channels from $(-2p-6n)$ to $(-2p+5n)$ are observed. In the Pd mass spectrum the largest yield is in $A = 115$, and the channels from $(-4p-4n)$ to $(-4p+5n)$ are observed. In both spectra the neutron stripping sector seems to be stronger than the neutron pick-up. One has to keep in mind that the yields in the neutron stripping channels are also expected to be more affected by neutron evaporation.

Looking at the mass distributions presented in Fig. 7.13, one can notice how the shape of the distribution is changing when going from the Sn isotopes with the pronounced elastic+inelastic channel, to the channels which involve the transfer of few protons. Such change of mass distributions is connected with the evolution of the reaction from the quasielastic to the deep-inelastic regime. To better understand this transition a more detailed analysis of the TKEL and angular distributions have to be performed. One expects the gradual widening of the angular distributions, which start to deviate from the expected bell shape centered at the grazing angle. Of course, when the large energy losses are present, the spectra may be modified to some extent by the acceptance of the spectrometer. Thus, for example, the TKEL spectra will change from the shape where the main strength is concentrated in a narrow band close to the largest kinetic energy for few nucleon transfer, to the more Gaussian-like shape for many nucleon transfers. This behaviour was studied in details in the ^{40}Ar+^{208}Pb reaction [12, 67]. For more details see for example, pg. 75 of Ref. [67], where the mass distributions of three dominant transfer channels in ^{40}Ar+^{208}Pb reaction were studied by gating on different (low and large) TKEL regions.

Fission fragments. Looking at the ΔE versus E matrix (Fig. 7.4), we see that the largest yields are in the region around $Z = 40$. Thus we decided to study into more details the Ru, Mo, and Zr isotopes i.e. $Z = 44$, 42, and 40, respectively. One of the key point in the extraction of the mass distribution is the correct attribution of the charge states. In order to better handle this attribution we follow the charge state selection from Sn-like ions towards the isotopes around $Z = 40$, taking into account only the energy region relatively far away from the elastic. This q distribution of Sn ions was represented in the right panel of Fig. 7.11. Since this q distribution is energy-dependent it was a good starting point for the further charge state assignment. Many different charge states attribution were systematically investigated for the selected fission fragments. One of the criteria for the correct attribution was that the masses reproduced after the trajectory reconstruction appear as close as possible to the integer numbers. To keep the possible systematic errors at minimum we decided to present the mass distribution for a selected charge state only. One of the possible sources of such errors can be attributed to the mass calibration performed at $Z = 50$, far away from the region studied here. In particular keeping in mind, as we have already stated, that the PRISMA was set for the elastically scattered ^{118}Sn, and not for the fission fragments which can be far away in the mass, charge and kinetic energy from the elastic scattering. Mass spectra obtained in this way are presented in Fig. 7.14, with Z and q given in the inset. In the case of Ru and Mo these are also the most favored charge states selected by PRISMA. In the case of Zr, there are few charge states with similar intensity (see the bottom panel of Fig. 7.10), and we decide to shown the one which provided the best mass reconstruction. The corresponding masses are distributed around $A = 101$ of Ru, $A = 93$ of Mo, and $A = 82$ of Zr. This indicate that in our case, PRISMA selects the stable and more neutron-poor fission fragments. If one considers the full charge state distribution, also of the higher charge states which are not preferentially selected with the present magnetic fields, more neutron-rich fission fragments were also produced in the reaction. In all these mass distributions one can easily separate different isotopes. The achieved mass resolution is very promising, and ensure that PRISMA is an excellent tool to study the transfer induced fission fragments.

As a next step, a dedicated measurement of the characteristics of fission fragments has to be performed, where one would scan the different magnetic fields for the better selection of the more neutron-rich fragments. To minimize the systematic errors in the charge state attribution, an additional kinematically coupled detector should be attached. For example, with the γ-detectors the identification of the specific isotope via characteristic γ

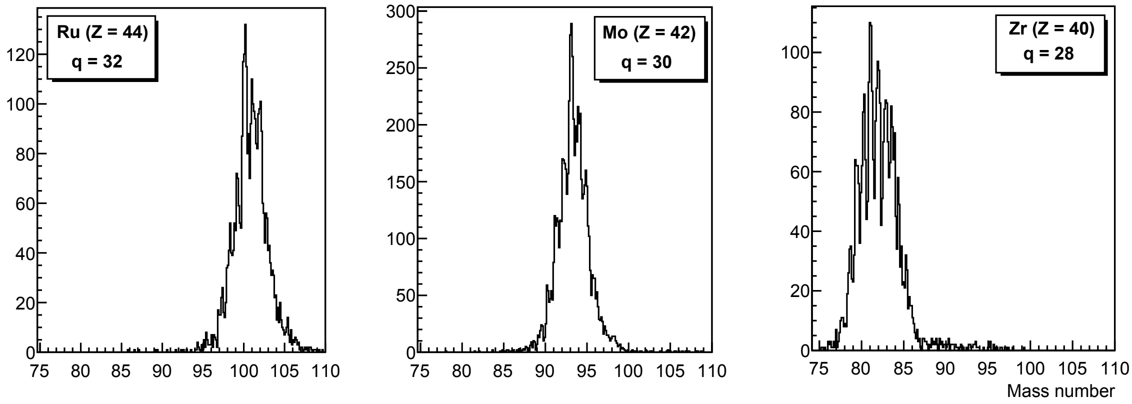

Figure 7.14: Mass spectra for selected Z and charge state q (both given in the inset).

transition can be performed. The measurement of the fission cross sections would profit from an additional particle detector for the full kinematical reconstruction of the event.

7.5 Perspectives

In this work, we presented selected results of the ^{206}Pb+^{118}Sn experiment, which was performed by using the heaviest beam of LNL facility and the extraordinary performances of PRISMA. Direct identification with good A and Z resolution is very challenging in the case of heavy (and rather slow) ions. The presented results proved that the ion identification (via event-by-event trajectory reconstruction) of the Sn-like ions in PRISMA can be successfully performed.

Taking the advantages of the inverse kinematics set-up, the measurement at E_{LAB} = 1200 MeV and PRISMA angle $\theta_{\mathrm{LAB}} = 25°$, illustrated the excellent resolution which was achieved for the Sn and the Sn-like ions. Currently ongoing analysis [163] of the measurements at lower energies (and other PRISMA angles) suggests that the principal goal of the experiment can be successfully reached. Once the ^{206}Pb+^{118}Sn study is completed, we will have a comparison between the experimental and theoretical probabilities for the odd and even neutron transfers, which will improve our understanding on the effect of neutron-neutron correlations in the presence of high Coulomb fields. This study will be also important for the comparison with the results of ^{54}Fe+^{92}Mo multinucleon transfer reaction, measured with PRISMA very recently and presented in Ref. [164].

In this same measurement (at E_{LAB} = 1200 MeV and $\theta_{\mathrm{LAB}} = 25°$) we observed nuclei which can be attributed to the transfer induced fission. We have shown in this work that the nuclear charge and mass resolution for both Sn-like and fission fragments is suitable for their studying, reflecting the unique performance of PRISMA. The observed Z distributions and obtained mass resolution of fission fragments is adapted for measuring the fission-fragment distributions in the future studies.

A start of the new experimental campaign at LNL, which employs PRISMA coupled to AGATA [165], is expected within the next year. Especially in the context of this campaign, it is of great importance to explore the production of the neutron-rich fission fragments, and the optimal experimental conditions to study the structure of these nuclei.

.

Conclusion

The ^{94}Rb+^{208}Pb reaction was measured at the energy about ∼30% above the Coulomb barrier, exploiting a very recent energy upgrade of HIE-ISOLDE radioactive-ion beam facility in CERN. The large γ-array MINIBALL was coupled to the CD particle detector positioned at the angles in the vicinity of grazing, thus allowing to perform a particle-γ and particle-γ-γ coincidence measurements. This made it possible to study the fragment angular distributions, and the prompt and delayed γ-decay of the excited states. Also, the background radiation, coming mainly from the unstable ^{94}Rb β-decay, was successfully reduced based on the particle-γ coincidence relationships. Transfer channels were identified from the attribution of the characteristic γ rays. An important part of this thesis provides a unique approach to the complex data analysis of the transfer reaction experiment with an unstable heavy-ion beam.

The transfer of neutrons populated ^{207}Pb, ^{208}Pb, ^{209}Pb and ^{210}Pb, and their associated binary partners. In $^{207-210}$Pb one generally observed the yrast states up to the moderately high energies. On the basis of the standard shell-model considerations and the previous studies, the states of collective character were recognized in ^{208}Pb, and the states of single-particle character in ^{207,209}Pb. The possible two-particle configurations were considered for the states in ^{210}Pb. In particular, the 3^- state of ^{208}Pb and the attributed $3^- \rightarrow 0^+$ transition were strongly observed. It is assumed that this 3^- state is rather relevant for the structure of the states in neighbouring Pb isotopes. Knowing that the transfer of nucleons at the energies close to the Coulomb barrier is accompanied by the large angular momentum transfer, the relatively high-spin states in ^{207}Pb, ^{209}Pb, and ^{210}Pb were discussed in terms of the stretched configurations of particle(s)/hole and 3^- state coupling. To better infer on the strength of particular modes of excitation in multinucleon transfer reactions, the presented results shall be discussed within the adequate theoretical model (such as particle octupole vibration coupling calculations). It would be of great importance to study in more details the structure of states involved in $21/2^+ \rightarrow 15/2^-$ transition in ^{209}Pb. This would mean, in particular, to measure the unknown half-life of the $21/2^+$ state and to infer on the puzzling case of the $j_{15/2}$ single-particle energy, which is known to strongly influence the agreement between the experimental data and the shell-model calculations in the Pb region.

The evaluated total cross section in Pb isotopes were significant in ^{209}Pb and ^{210}Pb, reached by transfer of neutrons from ^{94}Rb beam towards the ^{208}Pb target. Data showed a rather good agreement with the semi-classical theory incorporated in GRAZING calculations, which also takes into account the effect of neutron evaporation. This supports a predicted change in the population pattern of the light partner, where neutron stripping and proton pick-up channels open up, thus potentially leading towards the more neutron-rich heavy nuclei. Therefore the GRAZING calculations, so far successfully applied in the description of multinucleon transfer reactions (as well as of fusion reactions), are very suitable to be used for the further predictions of the cross sections in the neutron-rich heavy regions.

In the context of the production of neutron-rich nuclei it would be also of great interest to quantify the effect of the competitive processes, such as neutron evaporation and fission. Additionally, this thesis presented the ^{206}Pb+^{118}Sn experiment measured with magnetic spectrometer PRISMA. One simultaneously observed the Sn-like and fission fragments inside PRISMA, with the nuclear charge and mass resolution suitable for their studies. This demonstrated the potential of such experimental approach, to be exploited in studying the survival probability of the heavy (neutron-rich) fragments produced in the multinucleon transfer reactions, and also in the yet not sufficiently explored fission processes.

The experimental results contained in this thesis are very relevant for the future experimental campaigns, which could benefit from the further development of the radioactive-ion beams. The performances of the presently available experimental setups are very suitable to be exploited in the multinucleon transfer reactions with unstable beams, thus providing the opportunity to extend the reaction mechanism and the nuclear structure studies farther from the valley of stability.

A Appendix

A.1 "Thick" target Wilczyński plot

In this Appendix we present the Wilczyński plot, or the E-θ matrix, constructed from the measurement with the 13 mg/cm^2 target (Fig. A.1). Passing through the 13 mg/cm^2 target fragments experience large energy losses. Approximately the first 5 mg/cm^2 of the target thickness can be assumed the active part of the target (in which the projectile energy is still above the Coulomb barrier). This is causing a spread in the velocity of the projectile, and also makes the reaction mechanism more complex than it is in the case of 1 mg/cm^2 target.

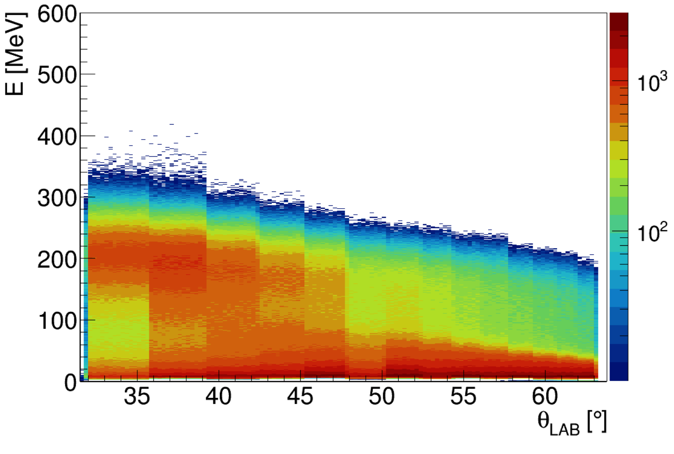

Figure A.1: Wilcziński plots, the $E-\theta$ matrix of all fragments. Obtained from the "thick" target measurement.

From the measurement with the 1 mg/cm^2 target we obtained the two nicely separated distributions (as in the left panel of Fig. 4.1), which we attributed to the Rb-like and Pb-like ions. In principle, in the case of 13 mg/cm^2 target Rb-like ions should be only decelerated in the target, while the Pb-like ions should be stopped. Thus one can associate the upper part of the presented matrix ($E > 100$ MeV) to the ^{94}Rb and the Rb-like fragments, with strong and inseparable contribution of the fragments associated with large energy losses and deep inelastic scattering. It is not excluded that products of such components contribute in the whole energy region. One can suppose that the lower part of the spectrum ($E < 100$ MeV) belongs to the Pb-like fragments in the same analogy as for the Rb-like fragments, under the assumption that some portion of the Pb-like fragments already escaped the target at small thicknesses.

A.2 The γ spectra of $^{207-210}$Pb

The Doppler corrected γ spectra of Pb isotopes was obtained in the ^{90}Zr+^{208}Pb and ^{40}Ar+^{208}Pb experiments, measured by the PRISMA magnetic spectrometer coupled to the CLARA γ-array. Detailed analysis of the γ spectra from Fig. A.2 was published in M. Varga Pajtler PhD thesis [66], and the analysis of the γ spectra from Fig. A.3 will be published in K. Gorički master thesis [140]. The obtained level schemes (corrected for the efficiency of CLARA) are presented in Chap. 5.

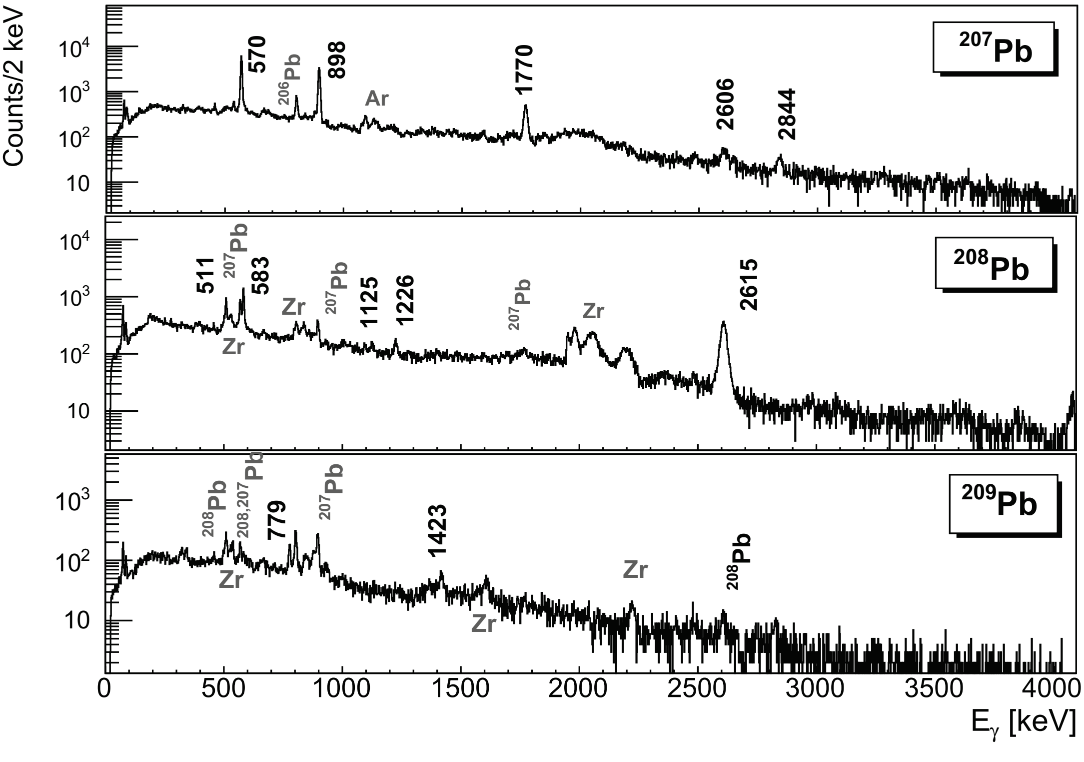

Figure A.2: The Doppler corrected γ spectra of $^{207-209}$Pb. From ^{90}Zr+^{208}Pb at $E_{\mathrm{LAB}} = 6.2$ MeV·A [46, 47, 66].

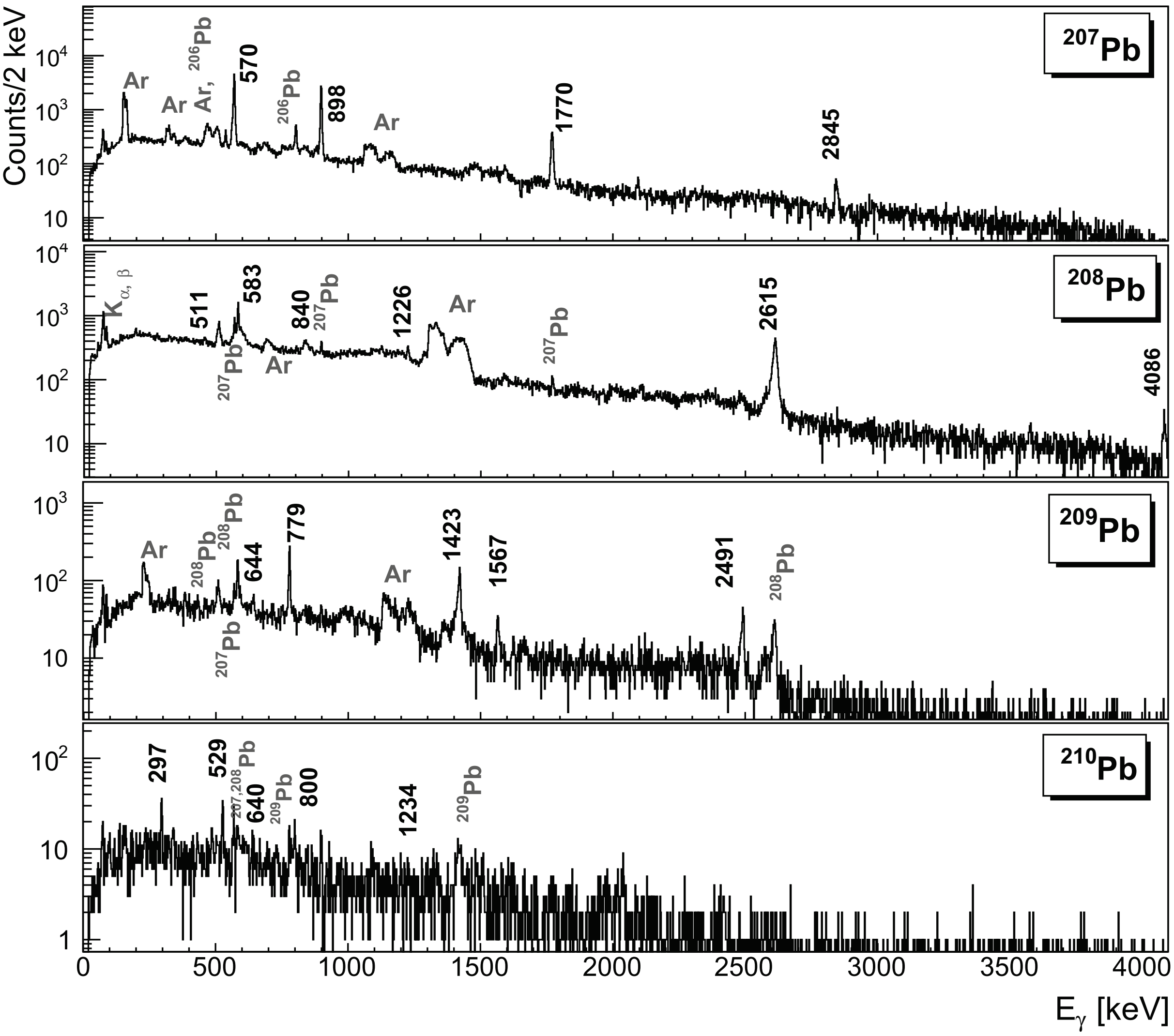

Figure A.3: The Doppler corrected γ spectra of $^{207-210}$Pb. From ^{40}Ar+^{208}Pb at $E_{\text{LAB}} = 6.4$ MeV·A [12, 67, 140].

Bibliography

[1] J. Erler et al. The limits of the nuclear landscape. *Nature*, 486:pg. 509–512, 2012.

[2] M. Thoennessen. *The discovery of isotopes.* Springer, 2016.

[3] L. Corradi, G. Pollarolo and S. Szilner. Multinucleon transfer processes in heavy-ion reactions. *Journal of Physics G: Nuclear and Particle Physics*, 36(11):113101, 2009.

[4] S. Szilner et al. Quasi-elastic reactions: an interplay of reaction dynamics and nuclear structure. *EPJ Web of Conferences*, 17:03005, 2011.

[5] D. Montanari et al. Elastic, inelastic, and one-nucleon transfer processes in ^{48}Ca+^{64}Ni. *Physical Review C*, 84:054613, 2011.

[6] F. Galtarossa et al. Mass correlation between light and heavy reaction products in multinucleon transfer ^{197}Au+^{130}Te collisions. *Physical Review C*, 97:054606, 2018.

[7] W. von Oertzen and A. Vitturi. Pairing correlations of nucleons and multi-nucleon transfer between heavy nuclei. *Reports on Progress in Physics*, 64:pg. 1247–1337, 2001.

[8] V. I. Zagrebaev and W. Greiner. Production of heavy trans-target nuclei in multinucleon transfer reactions. *Physical Review C*, 87:034608, 2013.

[9] K. Sekizawa and K. Yabana. Time-dependent Hartree-Fock calculations for multinucleon transfer processes in ^{40,48}Ca+^{124}Sn, and ^{58}Ni+ ^{208}Pb reactions. *Physical Review C*, 88: 014614, 2013.

[10] S. Szilner et al. Multinucleon transfer processes in ^{40}Ca+^{208}Pb. *Physical Review C*, 71: 044610, 2009.

[11] L. Corradi et al. Light and heavy transfer products in ^{58}Ni+^{208}Pb at the Coulomb barrier. *Physical Review C*, 66:024606, 2002.

[12] T. Mijatović et. al. Multinucleon transfer reactions in the ^{40}Ar+^{208}Pb system. *Physical Review C*, 94:064616, 2016.

[13] C. H. Dasso, G. Pollarolo, and A. Winther. Systematics of isotope production with radioactive beams. *Physical Review Letters*, 73:1907, 1994.

[14] L. Zhu et al. Theoretical study on production of heavy neutron-rich isotopes around the $N = 126$ shell closure in radioactive beam induced transfer reactions. *Physics Letters B*, 767:pg. 437–442, 2017.

[15] S. Szilner et al. Recent studies of heavy ion transfer reactions using large solid angle spectrometers. *EPJ Web of Conferences*, 223: 01064, 2019.

[16] S. Szilner et al. Structure of chlorine isotopes populated by heavy ion transfer reactions. *Physical Review C*, 87: 054322, 2013.

[17] J. J. Valiente-Dobon et al. Spectroscopy of neutron-rich $^{59-63}$Mn isotopes. *Physical Review C*, 78:024302, 2008.

[18] L. Kaya et al. Isomer spectroscopy in ^{133}Ba and high-spin structure of ^{134}Ba. *Physical Review C*, 100: 024323, 2019.

[19] P. R. John et al. Shape evolution in the neutron-rich osmium isotopes: Prompt γ-ray spectroscopy of ^{196}Os. *Physical Review C*, 90:021301, 2014.

[20] R. Broda. Spectroscopic studies with the use of deep-inelastic heavy-ion reactions. *Journal of Physics G: Nuclear and Particle Physics*, 32:R151, 2006.

[21] I-Y. Lee. The GAMMASPHERE. *Nuclear Physics A*, 520:pg. c641–c655, 1992.

[22] M. Pfutzner et al. New isotopes and isomers produced by the fragmentation of U at 1000 MeV/nucleon. *Physical Letters B*, 444:32, 1998.

[23] J. Kurcewicz et al. Discovery and cross-section measurement of neutron-rich isotopes in the element range from neodymium to platinum with the FRS. *Physics Letters B*, 717 (4-5):pg. 371–375, 2012.

[24] H. Geissel et al. The GSI projectile fragment separator (FRS): a versatile magnetic system for relativistic heavy ions. *Nuclear Instruments and Methods in Physics Research B*, 70 (1-4):pg. 286–297, 1992.

[25] Y. X. Watanabe et al. Pathway for the production of neutron-rich isotopes around the $N = 126$ shell closure. *Physical Review Letters*, 115:172503, 2015.

[26] H. Savajols et al. VAMOS: a VAriable MOde high acceptance spectrometer. *Nuclear Physics A*, 654:1027c–1032c, 1999.

[27] M. Rejmund et al. Performance of the improved larger acceptance spectrometer: VAMOS++. *Nuclear Instruments and Methods in Physics Research Section A*, 646(1):pg. 184–191, 2007.

[28] F.Azaieza et al. EXOGAM: a γ-ray spectrometer for radioactive beams. *Nuclear Physics A*, 654:1003c–1008c, 1999.

[29] T. Kurtukian-Nieto et al. Production cross sections of heavy neutron-rich nuclei approaching the nucleosynthesis r-process path around $A = 195$. *Physical Review C*, 89:024616, 2014.

[30] F. Galtarossa. *Multinucleon transfer in the* ^{197}Au+^{130}Te *reaction studied with a high-resolution kinematic coincidence.* PhD thesis, University of Ferrara, 2014.

[31] E. Fioretto et al. A gas detection system for fragment identification in low-energy heavy-ion collisions. *Nuclear Instruments and Methods in Physics Research section A*, 899:pg. 73–79, 2018.

[32] A. Vogt et al. Light and heavy transfer products in ^{136}Xe+^{238}U multinucleon transfer reactions. *Physical Review C*, 92:024619, 2015.

[33] N. Al-Dahan et al. Nuclear structure “southeast” of ^{208}Pb: Isomeric states in ^{208}Hg and ^{209}Tl. *Physical Review C*, 80:061302, 2009.

[34] A. Gottardo et al. New isomers in the full seniority scheme of neutron-rich lead isotopes: The role of effective three-body forces. *Physical Review Letters*, 109: 162502, 2012.

[35] M. Rejmund, M. Schramm, and K. H. Maier. Derivation of wave functions and matrix elements of the residual interaction in ^{208}Pb from experimental data. *Physical Review C*, 59:2520, 1999.

[36] R. Broda et al. Doubly magic ^{208}Pb: High-spin states, isomers, and E3 collectivity in the yrast decay. *Physical Review C*, 95:064308, 2017.

[37] E. Caurier et al. Full $0\hbar\omega$ shell model calculation of the binding energies of the $1f_{7/2}$ nuclei. *Physical Review C*, 59:2033, 1999.

[38] E. K. Warburton et al. Appraisal of the Kuo-Herling shell-model interaction and application to $A = 210$–212 nuclei. *Physical Review C*, 43:602, 2009.

[39] K. Langanke H. Grawe and G. Martinez-Pinedo. Nuclear structure and astrophysics. *Reports on Progress in Physics*, 70:1525, 2007.

[40] E. M. Burbidge et al. Synthesis of the elements in stars. *Reviews of modern physics*, 29:547, 1957.

[41] LIGO Scientific Collaboration and Virgo Collaboration. Multi-messenger observations of a binary neutron star merge. *The Astrophysical Journal Letters*, 848:59pp, 2017.

[42] W. Nazarewicz. Nuclear structure. *Nuclear Physics A*, 654:195c–214e, 1999.

[43] V. I. Zagrebaev and W. Greiner. Production of new heavy isotopes in low-energy multinucleon transfer reactions. *Physical Review Letters*, 101:122701, 2008.

[44] C. Simenel. Particle transfer reactions with the time-dependent Hartree-Fock theory using a particle number projection technique. *Physical Review Letters*, 105:192701, 2010.

[45] G. Scamps and D. Lacroix. Effect of pairing on one- and two-nucleon transfer below the Coulomb barrier: A time-dependent microscopic description. *Physical Review C*, 87:014605, 2013.

[46] S. Szilner et al. Multinucleon transfer reactions in closed-shell nuclei. *Physical Review C*, 76:024604, 2007.

[47] M. Varga Pajtler et. al. Selective properties of neutron transfer reactions in the ^{90}Zr+^{208}Pb system for the population of excited states in zirconium isotopes. *Nuclear Physics A*, 941:273, 2015.

[48] L. Corradi et al. Heavy ion transfer reactions: Status and perspectives. *Pramana - journal of physics*, 75:87, 2007.

[49] A. Gadea et al. The CLARA-PRISMA setup installed at LNL: first results. *Journal of Physics G: Nuclear and Particle Physics*, 31:S1443, 2005.

[50] J. Wilczyński. Nuclear molecules and nuclear friction. *Physics Letters B*, 47:448, 1973.

[51] L. Corradi et al. Multinucleon transfer processes in ^{64}Ni+^{238}U. *Physical Review C*, 59:261, 1999.

[52] G. R. Satchler. *Direct nuclear reactions.* Clarendon Press, 1983.

[53] R. A. Broglia and A. Winther. Heavy ion reactions. *Westview Press, USA*, 2004.

[54] G. Pollarolo. Personal pages. `http://personalpages.to.infn.it/~nanni/grazing/`.

[55] A. Winther. Grazing reactions in collisions between heavy nuclei. *Nuclear Physics A*, 572 (1):pg.191–235, 1994.

[56] A. Winther. Dissipation, polarization and fluctuation in grazing heavy-ion collisions and the boundary to the chaotic regime. *Nuclear Physics A*, 594 (2):pg.203–245, 1995.

[57] D. Montanari et al. Gamma spectroscopy of calcium nuclei around doubly magic ^{48}Ca using heavy-ion transfer reactions. *Physical Review C*, 85:044301, 2012.

[58] S. Lunardi et al. Spectroscopy of neutron-rich Fe isotopes populated in the ^{64}Ni+ ^{238}U reaction. *Physical Review C*, 76:034303, 2007.

[59] R. Chapman et al. First in-beam γ-ray study of the level structure of neutron-rich ^{39}S. *Physical Review C*, 94:024325, 2016.

[60] M. Rejmund et al. Shell evolution and the $N=34$ “magic number". *Physical Review C*, 76:021304, 2007.

[61] S. Bhattacharyya et al. Structure of neutron-rich Ar isotopes beyond $N = 28$. *Physical Review Letters*, 101:032501, 2008.

[62] P-A Soderstorm et al. Spectroscopy of neutron-rich ^{168,170}Dy: Yrast band evolution close to the N_pN_n valence maximum. *Physical Review C*, 81:034310, 2010.

[63] P. R. John et al. Spectroscopy of the neutron-rich actinide nucleus ^{240}U following multinucleon-transfer reactions. *Physical Review C*, 92:044319, 2015.

[64] S. Szilner et al. Interplay between single-particle and collective excitations in argon isotopes populated by transfer reactions. *Physical Review C*, 84:014325, 2011.

[65] P. Čolović et al. Stretched configuration of states as inferred from γ-ray angular distributions in ^{40}Ar+^{208}Pb neutron transfer reactions. *European Physical Journal A*, 53:166, 2017.

[66] M. Varga Pajtler. *Nucleon transfer reactions in the $^{90}Zr+^{208}Pb$ system.* PhD thesis, University of Zagreb, 2014.

[67] T. Mijatović. *Study of heavy-ion reactions with large solid angle magnetic spectrometers.* PhD thesis, University of Zagreb, 2015.

[68] Y. Blumenfeld, T. Nilsson and P. Van Duppen. Facilities and methods for radioactive ion beam production. *Physica Scripta*, T152:014023, 2013.

[69] H. Suzuki et al. Production cross section measurements of radioactive isotopes by BigRIPS separator at RIKEN RI Beam Factory. *Nuclear Instruments and Methods in Physics Research B*, 317:756, 2013.

[70] M. J. G. Borge and K. Riisager. Hie-isolde, the project and the physics opportunities. *European Physical Journal A*, 52:11, 2016.

[71] M. J. G. Borge and B. Jonson. Isolde past, present and future. *J. Physics G: Nuclear Part. Physics*, 44:044011, 2017.

[72] A. Gottberg et al. Experimental tests of an advanced proton-to-neutron converter at ISOLDE-CERN. *Nuclear Instruments and Methods in Physics Research B*, 336: 143–148, 2014.

[73] J. A. Lettry. Review of ion-source developments for radioactive ion-beam facilities. *Proceedings of the 1999 Particle Accelerator Conference*, 1:92, 1999.

[74] E. Kugler. The isolde facility. *Hyperfine Interact*, 129:1, 2000.

[75] L. P. Gaffney et al. Studies of pear-shaped nuclei using accelerated radioactive beams. *Nature*, 497:199, 2013.

[76] N. Warr et al. The Miniball spectrometer. *European Physical Journal A*, 49:40, 2013.

[77] A.N. Ostrowski et al. CD:A double sided silicon strip detector for radioactive nuclear beam experiments. *Nuclear Instruments and Methods in Physics Research Section A*, 480:448, 2002.

[78] J. Pakarinen et al. Collectivity in ^{196,198}Pb isotopes probed in Coulomb-excitation experiments at REX-ISOLDE. *Journal of Physics G: Nuclear and Particle Physics*, 44:064009, 2017.

[79] MINIBALL collaboration. Analysis code for MINIBALL experiments at ISOLDE. `https://github.com/Miniball/MiniballCoulexSort`.

[80] ROOT - A Data Analysis Framework. `https://root.cern.ch/drupal`.

[81] IAEA. *X-ray and gamma-ray standards for detector calibration.* IAEA, Vienna, Austria, 1991.

[82] D. Rosiak. *Coulomb excitation of doubly-magic ^{132}Sn at HIE-ISOLDE and development of escape-suppression shields for the MINIBALL spectrometer.* PhD thesis, University of Cologne, 2018.

[83] MINIBALL collaboration, L.P. Gaffney personal pages. Simulation of reaction kinematics for CD detector. `https://github.com/lpgaff`.

[84] D. Rosiak et al. Enhanced quadrupole and octupole strength in doubly magic ^{132}Sn. *Physical Review Lett.*, 121:252501, 2018.

[85] V. Bildstein. *Exploring the Island of Inversion with the d(^{30}Mg,p)^{31}Mg Reaction.* PhD thesis, Technical University of Munich, 2010.

[86] M. Crnac. Neutronski bogate teške jezgre. Master's thesis, University of Zagreb, 2018.

[87] M. Bortolami. Study heavy elements with exotic beams at ISOLDE. Master's thesis, Bachelor degree, University of Padua, 2018.

[88] National Nuclear Data Center. Nuclear Data Sheets. `https://www.nndc.bnl.gov/`.

[89] R. Bock. *Heavy ion collisions, vol. 2.* IINorth-Holland, Amsterdam, 1980.

[90] K. Nowak et al. Spectroscopy of ^{46}Ar by the (t,p) two-neutron transfer reaction. *Physical Review C*, 93:044335, 2016.

[91] M. Rhoades-Brown, M. H. Macfarlane, and S. C. Pieper. Techniques for heavy-ion coupled-channels calculations. I. Long-range coulomb coupling. *Physical Review C*, 21:2417, 1980.

[92] M. Rhoades-Brown, M. H. Macfarlane, and S. C. Pieper. Techniques for heavy-ion coupled-channels calculations. ii. Iterative solution of the coupled radial equations. *Physical Review C*, 21:2436, 1980.

[93] M.H. Macfarlane and S.C. Pieper. PTOLEMY : a Program for Heavy-Ion Direction-Reaction Calculations. *Argonne National Laboratory Report*, 76:11, 1978.

[94] R.A. Broglia, G. Pollarolo, and A. Winther. On the absorptive potential in heavy ion scattering. *Nuclear Physics A*, 361 (1):pg. 307–325, 1981.

[95] G. Pollarolo, R.A. Broglia and A. Winther. Calculation of the imaginary part of the heavy ion potential. *Nuclear Physics A*, 406 (2):369–389, 1983.

[96] I. Tsekhanovich et al. Short-lived isomers in ^{94}Rb. *Physical Review C*, 78:011301, 2008.

[97] R.Broda et al. Two-neutron and core-excited states in ^{210}Pb: Tracing E3 collectivity and evidence for a new beta-decaying isomer in ^{210}Tl. *Physical Review C*, 98:024324, 2018.

[98] J. K. Hwang et al. High-spin states in ^{91,92,93}Rb and ^{155,156}Pm. *Physical Review C*, 80:037304, 2008.

[99] W. Urban et al. Isomeric levels in ^{92}Rb and the structure of neutron-rich ^{92,94}Rb isotopes. *Physical Review C*, 85:014329, 2008.

[100] G. S. Simpson et al. Near-yrast, medium-spin, excited states of ^{91}Rb, ^{93}Rb, and ^{95}Rb. *Physical Review C*, 82:024302, 2010.

[101] S. K. Basu, G. Mukherjee, A. A. Sonzogni. Full evaluation for ^{95}Rb. *Nuclear Data Sheets*, 111:2555, 2009.

[102] C. M. Folden et al. New neutron-rich microsecond isomers observed among fission products of ^{238}U at 80 MeV/nucleon. *Physical Review C*, 79:064318, 2009.

[103] S.A.E. Johansson. Gamma de-excitation of fission fragments (II). delayed radiation. *Nuclear Physics*, 64:147–160, 1965.

[104] C. Sotty et al. $^{97}_{37}$Rb$_{60}$: The cornerstone of the region of deformation around $A \sim 100$. *PhysRevLett*, 115:172501, 2015.

[105] G. Georgiev et al. Study of exotic nuclei through nuclear moment and transition probabilities studies. `https://agenda.infn.it/event/5392/contributions/58435/attachments/42071/49949/GeorgievGeorgi.pdf`.

[106] C. Sotty. *Study of the nuclear structure far from stability : Coulomb excitation of neutron-rich Rb isotopes around N=60; Production of nuclear spin polarized beams using the Tilted Foils technique*. PhD thesis, Paris-Sud University, 2013.

[107] A. Negret, A.A. Sonzogni. Full evaluation for ^{94}Rb. *Nuclear Data Sheets*, 112:, 2011.

[108] C. M. Baglin. Full evaluation for ^{92}Rb. *Nuclear Data Sheets*, 113:2187, 2012.

[109] C. M. Baglin. Full evaluation for ^{93}Rb. *Nuclear Data Sheets*, 112:1163, 2011.

[110] S. K. Basu, G. Mukherjee, A. A. Sonzogni. Full evaluation for ^{95}Sr. *Nuclear Data Sheets*, 111:2555, 2010.

[111] F.G. Kondev, S. Lalkovski. Full evaluation for ^{207}Tl. *Nuclear Data Sheets*, 112: 2555, 2011.

[112] G. J. Igo et al. ^{208}Pb(t,d)^{209}Pb reaction with 20-MeV tritons. *Physical Review*, 177: 1831, 1969.

[113] R. A. Moyer, B. L. Cohen, and R. C. Diehl. Excitation of states in Pb^{207} by Pb$^{208}(d,t)$, Pb$^{206}(d,p)$, and Pb$^{207}(d,d^{'})$ reactions. *Physical Review C*, 2:1898, 1970.

[114] E.R. Flynn et al. An experimental and theoretical investigation of the structure of ^{210}Pb. *Nuclear Physics A*, 195:1, 1972.

[115] M. J. Martin. Full evaluation for ^{208}Pb. *Nuclear Data Sheets*, 108:1583, 2007.

[116] A. Bohr and B. R. Mottelson. *Nuclear structure vol 2.* Singapore: World Scientific, 1998.

[117] R. Julin et al. E0 study of 0^+ states near 5 MeV in ^{208}Pb. *Physical Review C*, 36: 1129, 1987.

[118] M. Yeh et al. Two-phonon octupole excitation in ^{208}Pb. *Physical Review Letters*, 76:1208, 1996.

[119] B. A. Brown. Double-octupole states in ^{208}Pb. *Physical Review Letters*, 85:5300, 2000.

[120] K. Vetter et al. Fragmentation of the two-phonon octupole vibrational states in ^{208}Pb. *Physical Review C*, 58:2631, 1998.

[121] M. Schramm et al. Study of excited states in ^{208}Pb by particle-γ coincidences with the ^{207}Pb(d,p)^{208}Pb and ^{209}Bi(t,a)^{208}Pb reactions. *Physical Review C*, 56:1320, 1997.

[122] M. Shamsuzzoha Basunia. Full evaluation for ^{210}Pb. *Nuclear Data Sheets*, 121:561, 2014.

[123] M. Rejmund et al. High spin states in ^{210}Pb. *Zeitschrift für Physik A Hadrons and Nuclei*, 359:243, 2014.

[124] G.J. Lane et al. Structure of exotic nuclei near and above ^{208}Pb populated via deep-inelastic collisions. *Nuclear Physics A*, 682:71, 2001.

[125] T. P. Sjoreen, U. Garg, and D. B. Fossan. Spectroscopy of ^{213}At, ^{212}Po, and ^{210}Pb following ^{208}Pb+^{7}Li. *Physical Review C*, 21:5, 1980.

[126] D. J. Decman et al. Electromagnetic properties of isomers in ^{210}Pb. *Physical Review C*, 28:3, 1983.

[127] F. G. Kondev, S. Lalkovski. Full evaluation for ^{207}Pb. *Nuclear Data Sheets*, 112: 707, 2010.

[128] M. Matoba et al. Depletion of the $2f_{7/2}$ neutron hole state in ^{207}Pb. *Physical Review C*, 55:3152, 1997.

[129] L.Corradi et. al. Excited states populated via nucleon transfer in the reaction ^{32}S + ^{208}Pb. *Zeitschrift für Physik A Hadrons and Nuclei*, A344:353, 1993.

[130] D. Ralet et al. Evidence of octupole-phonons at high spin in ^{207}Pb. *Physics Letters B*, 797:134797, 2019.

[131] Zs Podolyak et. al. Octupole transitions in the ^{208}Pb region. *Journal of Physics: Conference Series*, 580:012010, 2015.

[132] M. Schramm et al. On the origin of the 2485 keV gamma-ray observed in near-barrier collisions of various heavy ions with ^{208}Pb. *Z. Physik A - Hadrons and Nuclei*, 344:121, 1992.

[133] M. Rejmund et al. Particle octupole-vibration coupling near ^{208}Pb. *European Physical Journal A*, 8:161, 2000.

[134] J. Chen and F.G. Kondev. Full evaluation for ^{209}Pb. *Nuclear Data Sheets*, 126:373, 2015.

[135] C.K.Bockelman D.G. Kovar, N. Stein. Excitation of two-particle-one-hole states by the ^{208}Pb(d,p)^{209}Pb reaction. *Nuclear Physics A*, 231:2, 1974.

[136] M. C. Mermaz et al. One-nucleon stripping reactions to discrete levels induced by a 480 MeV ^{12}C beam on a ^{208}Pb target. *Physical Review C*, 37:5, 1988.

[137] M. Rejmund et al. Gamma spectroscopy of ^{209}Pb with deep inelastic reactions. *European Physical Journal A*, 1:261, 1997.

[138] C. Ellegaard, J. Kantele, P. Vedelsby. Experimental evidence for particle-vibration coupling in ^{209}Pb. *Physics Letters B*, 25:8, 1967.

[139] I. Hamamoto. Particle spectra and particle-vibration coupling in the Pb region. *Physics Reports*, 10:63, 1974.

[140] K. Gorički. To be published. Master's thesis, University of Zagreb.

[141] L. Corradi et al. Nucleon-nucleon pairing correlations probed in the ^{118}Sn+^{206}Pb transfer reactions. *LNL Annual Report 2019*, 259:17, 2020.

[142] Legnaro National Laboratories. Selective Production of Exotic Species project. `https://web.infn.it/spes/`.

[143] G. Prete et al. The SPES project: a second generation ISOL facility. *Physics Procedia*, 26:pg. 274–283, 2012.

[144] K. Nishio A. N. Andreyev and K.-H. Schmidt. Nuclear fission: a review of experimental advances and phenomenology. *Report Prog. Physics*, 016301:016301, 2018.

[145] K.-H. Schmidt et al. Relativistic radioactive beams: a new access to nuclearfssion studies. *Nuclear Physics A*, 665:221–267, 2000.

[146] K.H. Schmidt and B. Jurado. Review on the progress in nuclear fission - experimental methods and theoretical descriptions. *Report Prog. Physics*, 81:106301, 2018.

[147] J. Randrup and P. Moller. Brownian shape motion on five-dimensional potential-energy surfaces: nuclear fission-fragment mass distributions. *Physical Review Letters*, 106:132503, 2011.

[148] G. Scamps and C. Simenel. Impact of pear-shaped fission fragments on mass-asymmetric fission in actinides. *Nature*, 564:382, 2018.

[149] M. Caamano et al. Isotopic yield distributions of transfer- and fusion-induced fission from ^{238}U+^{12}C reactions in inverse kinematics. *Physical Review C*, 88:024605, 2013.

[150] F. Farget et al. Transfer-induced fission in inverse kinematics: Impact on experimental and evaluated nuclear data bases. *The European Physical Journal A*, 51: 175, 2015.

[151] N. Mărginean et al. Evolution of deformation in the neutron-rich krypton isotopes: The ^{96}Kr nucleus. *Physical Review C*, 80:021301, 2009.

[152] D.M. Brink and R.A. Broglia. *Nuclear superfluidity: pairing in finite systems.* Cambridge University Press, UK, 2005.

[153] G. Potel et al. Cooper pair transfer in nuclei. *Reports on Progress in Physics*, 76 (10):106301, 2013.

[154] D. Montanari et al. Neutron pair transfer in ^{60}Ni+^{116}Sn far below the Coulomb barrier. *Physical Review Letters*, 113:052501, 2014.

[155] L. Corradi et al. Single and pair neutron transfers at sub-barrier energies. *Physical Review C*, 84:034603, 2011.

[156] D. Montanari et al. Pair neutron transfer in ^{60}Ni+^{116}Sn probed via γ-particle coincidences. *Physical Review C*, 93:054623, 2016.

[157] A. M. Stefanini et al. The heavy-ion magnetic spectrometer PRISMA. *Nuclear Physics A*, 701:217–221, 2002.

[158] L. Corradi et al. Multinucleon transfer reactions: Present status and perspectives. *Nuclear Instruments and Methods in Physics Research B*, 317:pg. 743–751, 2013.

[159] P. R. John. *Study of shape evolution in the neutron-rich osmium iso- topes with the advanced gamma-tracking array AGATA.* PhD thesis, University of Padua, 2015.

[160] D. Montanari. *Reaction dynamics of neutron rich nuclei in Ca isotopes with heavy ions and gamma spectroscopy.* PhD thesis, University of Milan, 2011.

[161] A. Utepov. Multinucleon transfer reactions in the ^{206}Pb+^{118}Sn system studied with the prisma spectrometer. Master's thesis, University of Padua, 2019.

[162] K. Shima et al. Empirical formula for the average equilibrium charge-state of heavy ions behind various foils. *Nuclear Instruments and Methods in Physics Research*, 200:605–608, 1982.

[163] J. Diklić. *To be published*. PhD thesis, University of Zagreb.

[164] T. Mijatović et al. Neutron-neutron correlations in ^{54}Fe+ ^{92}Mo. *LNL Annual Report 2019*, 259:43, 2020.

[165] S.Akkoyun et al. Agata—advanced gamma tracking array. *Nuclear Instruments And and Methods A*, 668:26–58, 2012.

List of Figures

1.1. The ^{94}Rb+^{208}Pb reaction cross section distribution [mb] calculated by GRAZING for the ^{94}Rb beam energy of 6.2 MeV·A. 2

1.2. Experimentally deduced cross sections for the production of the $N = 126$ isotones as a function of Z. The circles are from MNT [25], while the stars are from fragmentation reactions [29]. 4

1.3. Left: Mass-mass correlation matrix of Te isotopes detected in PRISMA and the heavy partner detected in coincident NOSE detector. From Ref. [6]. Right: experimental total cross sections for neutron stripping channels and different reactions; ^{197}Au+^{130}Te [6], ^{136}Xe+ ^{198}Pt [25], and ^{136}Xe+^{238}U [32] mesaured at the indicated energies (given relatively to the barrier V_{B}). The lines are to guide the eye. From Ref. [30]. 5

1.4. Left: Systematics of the $E_{ex}(2^+)$ energies and $E_{ex}(4^+)/E_{ex}(2^+)$ energy ratios for even-even nuclei around ^{208}Pb. From Ref. [33]. Right: Measured $B(E2)$ values for the isomeric states (black line), compared with the shell-model calculations in the neutron space beyond ^{208}Pb. For more details see Ref. [34]. 6

1.5. Illustration of r-process paths (red squares) and the observed r-process abundances (inset). Blue solid lines indicate proton and neutron magic numbers. From Ref. [39]. 7

1.6. Angle and energy integrated total cross section for ^{58}Ni, ^{40}Ca and ^{40}Ar on the ^{208}Pb target, at energies $E_{\mathrm{LAB}} = 6$, 6.2, and 6.4 MeV·A, respectively. The cross section values of the elastic (+inelastic) channel, with ΔN and $\Delta Z = 0$, are scaled down by a factor 100 to better display the behavior of the transfer channels. From Ref. [12]. 9

1.7. Chart of nuclides. Proton stripping and neutron pick-up are the dominant channels in reactions involving stable projectiles, populating the chart in direction indicated with green arrows. With neutron-rich projectiles, neutron stripping and proton pick-up channels open up, populating the chart in direction indicated with pink arrows. 9

1.8. Contours of Xe+^{208}Pb (E_{CM} = 700 MeV) cross sections as a function of ΔN and ΔZ of projectile, calculated by the model GRAZING. Isotope of Xe is indicated in the spectra. From Ref. [13]. 10

1.9. The ^{90}Zr+^{208}Pb (E_{LAB} = 6.2 MeV·A) Total Kinetic Energy Loss spectra for the indicated MNT channels. The mass distributions associated with the different nuclear charges are shown in the top row (yellow-coloured), with the labels pointing to the pure proton transfer channels (red-coloured TKEL). The centroid of the elastic + inelastic channel corresponds to Q = 0, shifted by 100 MeV. The scale of the Q-value axis is 1 MeV/channel. From Ref. [48]. 11

1.10. Experimental results from ^{90}Zr+^{208}Pb reaction (E_{LAB} = 6.2 MeV·A), obtained with PRISMA coupled to CLARA. Left: total kinetic energy loss distributions (TKEL) for ^{90}Zr. Distributions were extracted without coincidence with γ rays (dotted line), and with at least one γ-ray in coincidence (full line), and by subtracting those two (blue line). Right: experimental (points) and GRAZING calculated (curve) differential cross section for elastic over Rutherford scattering. From Ref. [46]. 12

1.11. Wilczyński plots, kinetic energy E in the laboratory system vs. θ_{LAB}, for selected channels in the ^{40}Ar+^{208}Pb reaction (at E_{LAB} = 6.4 MeV·A). From Ref. [12]. 12

1.12. The ^{64}Ni+^{238}U experimental (points) and calculated (lines) Q-value integrated angular distributions for the indicated transfer channels. Lines are GRAZING calculations. From Ref. [51]. 13

1.13. Illustration of the heavy-ion reactions (in vicinity of the Coulomb barrier), considering the impact parameter b. 14

1.14. Effective interaction potential (Coulomb and nuclear) in a head-on collision (l = 0). Stable projectiles, as given in the inset, have a common ^{208}Pb target. The height of nominal Coulomb barrier E_B at r_B is labeled for the ^{40}Ca+^{208}Pb system. 15

1.15. Adiabatic cut-off functions for one- and two-neutron and proton transfer channels for the ^{58}Ni+^{208}Pb reaction at 330 MeV. Q value is in MeV. The horizontal lines represent the location of all possible transitions (see text for details). From Ref. [3]. 19

1.16. Total experimental cross section (points) for the ^{58}Ni, ^{40}Ca, ^{40}Ar+^{208}Pb reactions, compared to the GRAZING calculations not including (dashed) and including (solid line) neutron evaporation. 21

1.17. Total experimental cross sections in pure neutron-transfer channels obtained with magnetic spectrometer PRISMA. Left: ^{197}Au+^{130}Te experiment (circles) and GRAZING calculations (lines) [6]. Right: ^{136}Xe+^{238}U experiment (lines) and GRAZING (circles) [32]. 21

1.18. Left: energies of the 2^+ and $11/2^-$ states of N = 20-28 argon isotopes. The experimental data are compared with shell-model (full circles). From Ref [64]. Right: Angular distribution of the E_γ = 1630 keV, $11/2^- \rightarrow 7/2^-$, in ^{41}Ar. The result demonstrates the $E2$ character of the transition. From Ref. [65]. 23

2.1. Schematical illustration of the HIE-ISOLDE experimental hall. 1) Proton beamline, 2) General Purpose Separator, 3) REXTRAP, 4) REXEBIS 5) REXLINAC, 6) HIE-ISOLDE, 7) MINIBALL station. The final upgrade involves the installation of six superconducting cryomodules. 28

2.2. Left: the single HPGe capsule assembly and dedicated scheme of the detector's redaout. Right: the photograph of the γ-spectrometer MINIBALL and the spherical target chamber configuration [76]. 29

2.3. Left: schematic view of the front side of the Compact Disk double-sided silicon strip detectors. Right: the photograph of the installed detector. The photograph also shows the tantalum protection ring shielding the innermost strips. 31

2.4. Timing structure of the RIB. X-axis represents the time difference between the particle detected in the CD detector and the proton impinging on the $\mathrm{UC_x}$ target ($T1$). Only the [0,16] s time range is presented. 32

3.1. The ^{152}Eu (red) and ^{133}Ba (blue) γ rays measured with MINIBALL. . . . 36

3.2. The absolute efficiency of MINIBALL as a function of the γ-ray energy, $\epsilon(E_\gamma) = exp(-41.94+28.98ln(E)-6.797ln(E)^2+0.6913ln(E)^3-0.02624ln(E)^4)$ 36

3.3. The d_{CD} vs. E_γ matrix in the selected energy ranges, obtained with the use of 1 mg/cm^2 target. Left: Doppler corrected for light fragment. Right: Doppler corrected for heavy fragment. Notice the difference in the binning. 38

3.4. The θ_{CM} of two fragments detected without a γ-ray in coincidence, at $\phi_{\mathrm{LAB}} = 14°$ and selected d_{CD} (see text). 38

3.5. Energy spectra of the individual ring at $\theta_{\mathrm{LAB}} = 41°$, for each of four CD quadrants. Spectra are obtained from the measurement of ^{20}Ne^{16}O^{12}C^{4}He+^{107}Ag reaction at $E_{\mathrm{LAB}} = 6.2$ MeV·A using the MINIBALL group calibration coefficients. Dotted lines are the energies calculated for the elastic scattering, $E(^{20}\mathrm{Ne}) = 109$ MeV, $E(^{16}\mathrm{O}) = 89$ MeV and $E(^{12}\mathrm{C}) = 69$ MeV. 39

3.6. The measured energy spectrum at the given θ_{LAB} (center of the ring) of each CD detector quadrant. Different quadrants are indicated with different colors. Lines are plotted at $E(\theta_{\mathrm{LAB}} = 41°) = 445$ MeV, $E(47°) = 414$ MeV, $E(51°) = 388$ MeV, $E(55°) = 366$ MeV (see text). 41

3.7. Left: the calculated kinematics of ^{94}Rb and ^{208}Pb at $E_{\mathrm{LAB}} = 6.2$ MeV·A in $E-\theta$ matrix representation. Right: the measured $E-\theta$ matrix of all particles. Black line connects the calibration points (full black circles). . . 42

3.8. The measured energy spectra of the ring at $\theta_{\mathrm{LAB}} = 41°$, before (blue line), and after the single multiplicity gate (red). Left: spectrum obtained with the 136 μm quadrant thickness. Right: spectrum obtained with the 480 μm quadrant thickness. 43

3.9. Gamma energy (E_γ) vs. the time difference between the fragment and γ (Δt) obtained with the use of 1 mg/cm^2 target (left), and of 13 mg/cm^2 target (right). The small offset from 0 ns is hardware related. 44

3.10. Left: γ-ray energy vs. the time difference between the fragment and γ, obtained with the use of 13 mg/cm^2 target and the walk correction. Right: the projection onto the x-axis. Labels are for delayed (Δt_d), prompt (Δt_p) and random (Δt_r, $\Delta t_{r,d}$) timing windows. 44
3.11. Projections of the E_γ-Δt matrix onto the E_γ axis, for the indicated Δt timing gates. Obtained with the use of 13 mg/cm^2 target. 45
3.12. Gamma spectra in coincidence with fragment, obtained by the use of "thick" target. Timing gates are indicated in the inset. 47
3.13. Left: the measured γ-γ time difference. Right: the γ-γ matrix obtained using the $\Delta t_{\gamma\gamma}$ gate. Strongest lines are associated with the β-decay. . . . 48
3.14. The background subtracted γ-γ matrix. Superimposed lines describe the width of the $E_\gamma = 1567$ keV gate, and the background gates (left and right) from it. 49
3.15. Projections of the γ-γ matrix. Top: gate on $E_\gamma = 1567$ keV. Middle: gate on the background. Bottom: gate on $E_\gamma = 1567$ keV, background subtracted. 49
3.16. The measured $E - \theta$ matrix of fragments in coincidence with the γ-ray, background subtracted. The gates are as used in Doppler correction for the light (top), and the heavy binary fragment (bottom). 50
3.17. Background subtracted γ-spectrum in coincidence with Rb-like fragments. Top: non Doppler corrected. Middle: Doppler corrected for the Rb-like. Bottom: Doppler corrected for the Pb-like. Obtained with the use of 1 mg/cm^2 target. 51
3.18. Decay scheme of ^{94}Rb beam [86]. Half-life ($\tau_{1/2}$) of each nuclide is given in parenthesis. 52
3.19. The γ-γ matrix obtained using the sum of the Δt_{rd} and Δt_d fragment-γ gate. Horizontal labels indicate the strongest β-decay associated γ rays, and vertical the γ rays in coincidence with the $E_\gamma = 837$ keV (^{94}Sr). 53

4.1. Wilczyński plots, i.e. the $E - \theta$ matrices, measured with the "thin" target. Left: all the fragments detected in the CD detector (for explanation of gates see the text). Right: the fragments in coincidence with the γ-ray in MINIBALL. Only the reaction γ rays were selected, defined by the Δt_p fragment-γ gate, and background subtracted by the Δt_r gate. 57

4.2. Gamma-ray multiplicity distribution in coincidence with the fragment which is given in the inset. The different θ_{LAB} regions are labeled with different colors, red corresponding to the $\theta_{\mathrm{LAB}} = [41, 54]^{\circ}$, and blue to the $\theta_{\mathrm{LAB}} = [54, 63]^{\circ}$. 59

4.3. Wilczyński plots for different heavy-ion reactions at the indicated energies. From Ref. [89]. 60

4.4. The quasi-elastic angular distribution of the Rb-like fragments (red) and the Pb-like fragments (blue), constructed without a γ-ray in coincidence. The error bars are statistical. 62

4.5. The angular distribution of the 3^- state in ^{208}Pb, from the Rb-like fragments (red) and the Pb-like fragments (blue). The error bars are statistical. 63

4.6. The experimental angular distributions (points) and the DWBA calculations (lines), performed at the beam energy at mid-target, $E_{\mathrm{LAB}} = 575$ MeV. Bottom data and calculations were also normalized to Rutherford. . . 64

4.7. The prompt γ-ray spectra, obtained with the use of 1 mg/cm^2 target. The spectra were Doppler corrected for the Pb-like fragments (top), and for the Rb-like (bottom). The values of E_γ are as tabulated [88], except the E_γ = 405 keV (^{94}Rb) which is as in our work and Ref. [96]. Color code of the γ-transition describes the neutron transfer channel, as given in the inset. Only the relevant parts of the x-axis range are plotted. Labels '*' are for the unattributed γ rays. 67

4.8. The 1 mg/cm^2 target γ-ray spectrum, prompt (top) and delayed (bottom). The values of E_γ are as in Ref. [88], except the E_γ = 297, 405 keV which are as in the our work and Refs. [97] and [96], respectively. Color code of the γ-transition describes the neutron transfer channel, as given in the inset. Only the relevant parts of the x-axis range are plotted. Labels '*' are for the unattributed γ rays. 68

4.9. The "thick" (13 mg/cm^2) target γ-ray spectrum, prompt (top) and delayed (bottom). The values of E_γ are as in Ref. [88], except the $E_\gamma = 297$, 405 keV which are as in the our work and Refs. [97] and [96], respectively. Colour code of the γ-transition describes the neutron transfer channel, as given in the inset. Only the relevant parts of the x-axis range are plotted. Labels '*' are for the unattributed γ rays 70

4.10. Difference in the mean square charge radii in the vicinity of $N = 60$ for Kr, Rb, Sr, Y, Zr, Nb, and Mb isotopes, given relative to their spherical form. Each isotonic chain is set apart by 0.25 fm^2 for clarity. From Ref. [106] . . 73

4.11. Level schemes of ^{97}Rb and ^{99}Rb. Pure $E2$ transitions are given with red arrows, while the mixed ($M1$, $E2$) with blue ones. From Ref. [104]. 73

4.12. Projected γ-γ matrix, obtained with the 217 keV gate (top left), 111 keV gate (top right), and the 405 keV (bottom). 75

4.13. Projected γ-γ matrix, obtained with the 186 keV gate (left) and the 167 keV gate (right). 76

4.14. The experimental level scheme of ^{94}Rb. Relative γ-ray intensities are indicated by the width of the arrows. The energy, spin and parity of levels and the energy of γ transitions, if known, are as in Ref. [107]. $E_\gamma = 405$ keV was attributed to the state at $E_{ex} = 622$ keV in this work. 76

4.15. Projected γ-γ matrix, obtained with the 142 keV gate (left) and the 146 keV gate (right). The inset of the left panel spectrum shows the region in vicinity of $E_\gamma = 142$ and 146 keV, which are labeled with '*'. 77

4.16. The experimental level scheme of ^{92}Rb. Relative γ-ray intensities are indicated by the width of the arrows. The energy, spin and parity of levels and the energy of γ transitions are as in Ref. [108]. 77

4.17. The experimental level scheme of ^{93}Rb. Relative γ-ray intensities are indicated by the width of the arrows. The energy, spin and parity of levels and the energy of γ transitions are as in Ref. [109]. 78

4.18. Delayed γ-ray spectrum in a selected energy range. The values of E_γ are as in Ref. [101]. Obtained with the use of "thick" target. 79

4.19. Projected γ-γ matrix, obtained with the 352 keV gate in ^{95}Sr (see text). . . 80

5.1. A relevant part of the ^{208}Pb shell-model orbitals. Numbers to the right of each orbital label its degeneracy. Blue and red frames indicate $N = 126$ and $Z = 82$ shells, respectively. 83

5.2. Projected γ-γ matrix, obtained with the 2615 keV gate (left) and the 583 keV gate (right). Notice the difference in the x-axis range. 85

5.3. The experimental level scheme of ^{208}Pb. Relative γ-ray intensities are indicated by the width of the arrows. For tentative (dashed-arrow) γ transition intensity is arbitrary. The energy, spin and parity of levels, and the energy of γ transitions are as in Ref. [115]. 86

5.4. The experimental level scheme of ^{208}Pb from: ^{40}Ar+^{208}Pb (left), ^{90}Zr+^{208}Pb (middle), ^{94}Rb+^{208}Pb (right) experiments. Relative γ-ray intensities are indicated by the width of the arrows. For tentative (dashed-arrow) γ-transition intensity is arbitrary. The energy, spin and parity of levels, and the energy of γ transitions are as in Ref. [115]. 87

5.5. Projected γ-γ matrix, obtained with the 298 keV gate (left) and the 800 keV gate (right). 91

5.6. Projected γ-γ delayed matrix, obtained with the 298 keV gate (left) and the 800 keV gate (right). 91

5.7. Projected γ-γ delayed matrix, obtained with the sum of the $E_\gamma = 298$ and 800 keV gate. 92

5.8. The experimental level scheme of ^{210}Pb. Relative γ-ray intensities are indicated by the width of the arrows. For tentative (dashed-arrow) γ transitions intensity is arbitrary. The energy, spin, parity of levels, and the energy of transitions are as in this work and Ref. [97]. 93

5.9. The experimental level scheme of ^{210}Pb from: ^{40}Ar+^{208}Pb (left) and ^{94}Rb+^{208}Pb (right). Relative γ-ray intensities are indicated by the width of the arrows. For tentative (dashed-arrow) γ transitions intensity is arbitrary. The energy, spin and parity of levels, and the energy of γ transitions are as in this work and Ref. [122]. 94

5.10. Spectroscopic factors for the states in ^{207}Pb, from the (d,t) reaction (E_{LAB} = 17 MeV) [113], and (p,d) (E_{LAB} = 35,41 and 65 MeV) [128]. 95

5.11. The experimental level scheme of ^{207}Pb. Relative γ-ray intensities are indicated by the width of the arrows. For tentative (dashed-arrow) γ transitions intensity is arbitrary. The energy, spin and parity of levels, and the energy of γ transitions are as in Refs. [127, 133]. Notice that the $13/2^+$'s half-life is $\tau_{1/2} = 0.8$ s. 98

5.12. The experimental level schemes of ^{207}Pb from: ^{40}Ar+^{208}Pb (left), ^{90}Zr+^{208}Pb (middle) and ^{94}Rb+^{208}Pb (right) reactions. Relative γ-ray intensities are indicated by the width of the arrows. For tentative (dashed-arrow) γ transitions intensity is arbitrary. The energy, spin and parity of levels, and the energy of γ transitions are as in Ref. [127]. 99

5.13. Spectroscopic factors for the states in ^{209}Pb, from the (*d*,*p*) reaction (E_{LAB} = 20 MeV) [135], and the (*t*,*d*) (E_{LAB} = 20 MeV) [112]. 100

5.14. Projected γ-γ coincidence matrix in a selected energy range, obtained with the 1567 keV gate (left) and the 465 keV gate (right). 102

5.15. Projected γ-γ coincidence matrix in a selected energy range, obtained with the 1423 keV gate (left) and the 2419 keV gate (right). 102

5.16. The experimental level scheme of ^{209}Pb. Relative γ-ray intensities are indicated by the width of the arrows. For tentative (dashed-arrow) γ transitions intensity is arbitrary. The energy, spin and parity of levels, and the energy of γ transitions are as in Ref. [134] 104

5.17. The experimental level scheme of ^{209}Pb from: ^{40}Ar+^{208}Pb (left), ^{90}Zr+^{208}Pb (middle), ^{94}Rb+^{208}Pb (right). Relative γ-ray intensities are indicated by the width of the arrows. For tentative (dashed-arrow) γ transitions intensity is arbitrary. The energy, spin and parity of levels, and the energy of transitions are as in Ref. [134]. 105

5.18. The experimental level schemes of ^{207,208,209,210}Pb. Relative γ-ray intensities are indicated by the width of the arrows. Only for tentative (dashed-arrow) γ transitions the intensity is arbitrary. The energy, spin and parity of levels, and the energy of γ transitions are as in our work and as in Ref. [88]. 106

5.19. The experimental strengths of states, obtained from the measurement with the 13 mg/cm^2 target, for ^{207}Pb (top) and ^{209}Pb (bottom). Data was normalized to the largest strength in each isotope. 107

5.20. The experimental level schemes of ^{207,208,209,210}Pb. Only the selected γ transitions of an $E3$ character are plotted (see text). 108

6.1. The experimental level schemes of ^{207,208,209,210}Pb. Relative γ-ray intensities are indicated by the width of the arrows. Only for tentative (dashed-arrow) γ transitions the intensity is arbitrary. The energy, spin and parity of levels, and the energy of γ transitions are as in our work and as in Ref [88]. Obtained with the use of "thin" target. 112

6.2. The ^{94}Rb,^{40}Ar,^{90}Zr+^{208}Pb experimental strengths of states of single-particle character, in ^{207}Pb (top) and ^{209}Pb (bottom). Data were normalized to the largest strengths. The ^{94}Rb+^{208}Pb strengths are from the measurement with the 1 mg/cm^2 target. 113

6.3. The experimental σ_{ex} (blue) and σ_{tot} (red) cross sections in $^{207-210}$Pb (see text). 115

6.4. The experimental cross sections σ_{tot} in $^{207-210}$Pb (green points). The upper error bars are statistical, and the lower are set to σ_{tot}-$\sigma_{\mathrm{g.s.}}$ at each A. Result is compared to the GRAZING code calculations including the effect of evaporation (green histogram), and neglecting it (black dotted histogram).116

6.5. The experimental cross sections compared to the GRAZING calculations. Left: ^{90}Zr+^{208}Pb (E_{LAB} = 6.2 MeV·A) [46]. Middle: ^{40}Ar+^{208}Pb (E_{LAB} = 6.4 MeV·A) [67] Right: ^{197}Au+^{130}Te (E_{LAB} = 5.4 MeV·A) [6]. 117

6.6. The ^{94}Rb+^{208}Pb GRAZING calculations (E_{LAB} = 583 MeV) for total cross sections of Hg isotopes. 119

7.1. Overview of fissioning systems investigated until 2016 in low-energy fission studies taken from Ref. [144]. The multinucleon-transfer induced fission is labeled with purple crosses. Insets show the behaviour of the fission fragments mass distributions. For more details see Ref. [144] and refs. therein. 122

7.2. Selected experimental results from ^{238}U+^{12}C (at E_{LAB} = 6.1 MeV·A). Left: fission mass distribution of ^{240}Pu. Right: neutron excess of pre-evaporation and post-evaporation fission fragments. For more details see text and Refs. [149, 150]. 123

7.3. The experimental results from ^{136}Xe+^{238}U (at $E_{\mathrm{LAB}} \sim 7.4$ MeV×A). Left: matrix of ΔTOF versus Z. Right: the relative contributions of MNT products and fission fragments. Lines are to guide eye. For more details see text and Ref. [32]. 124

7.4. The ^{206}Pb+^{118}Sn experiment (at $E_{\mathrm{LAB}} = 5.8$ MeV·A and $\theta_{\mathrm{LAB}} = 25°$). Top: ΔE versus E matrix. Bottom: E versus *Range* matrix. Sn-like ions and fission fragments (around $Z \sim 40$) are labeled (see text). 126

7.5. Matrix of TKEL versus TOF from the ^{206}Pb+^{118}Sn experiment (at $E_{\mathrm{LAB}} = 5.8$ MeV·A and $\theta_{\mathrm{LAB}} = 25°$). Sn-like ions and fission fragments are labeled. 127

7.6. Schematic layout of the PRISMA spectrometer. 128

7.7. Matrix of the calibrated MCP detector in polar coordinates. The cross-shaped mask and the two probes for calibration purpose are visible. . . . 130

7.8. TOF versus calibrated x_{FP} position matrix, after the time alignment between the different sections. Two main structures correlated with the Pb-like ions (around TOF = 205 ns) and Sn-like ions (around TOF = 155 ns) are visible. 131

7.9. Mass-integrated Z distribution of proton transfer channels. The ΔE was constructed from the first two sections of IC. The multigaussian fits (red lines) describe the absolute yields for the indicated channels. From Ref. [161]. 133

7.10. Sn (top) and Zr (bottom) $\rho\beta$ - E matrices used for charge state selection. 134

7.11. Top: ΔE versus E matrix. Gates illustrate two different ΔE-E regions. Bottom left: charge state distribution for the events inside the left ΔE-E gate (higher energy losses). Bottom right: charge state distribution for the events inside the right ΔE-E gate (lower energy losses). 135

7.12. Matrix of A/q versus x_{FP} position for $Z = 50$. Top: before aberration corrections, botom: after aberration corrections (see text). 137

7.13. Mass spectra for Sn ($Z = 50$), Cd ($Z = 48$), Pd ($Z = 46$). 138

7.14. Mass spectra for selected Z and charge state q (both given in the inset). . 140

A.1. Wilcziński plots, the $E - \theta$ matrix of all fragments. Obtained from the "thick" target measurement. 145

A.2. The Doppler corrected γ spectra of $^{207-209}$Pb. From ^{90}Zr+^{208}Pb at E_{LAB} = 6.2 MeV·A [46, 47, 66]. 146

A.3. The Doppler corrected γ spectra of $^{207-210}$Pb. From ^{40}Ar+^{208}Pb at E_{LAB} = 6.4 MeV·A [12, 67, 140]. 147

List of Tables

3.1. The background associated γ rays in the Δt_p gated γ-spectrum. E_γ is from Ref. [88], and I_γ is the measured intensity. Obtained by the use of "thick" target. 55

4.1. The measured intensity of E_γ attributed to the Pb isotopes, used in the ^{207,208,209,210}Pb cross section evaluation. Top part: I_γ^1 from the prompt γ-spectrum Doppler corrected for the Pb-like, and the non-Doppler corrected for $E_\gamma = 800$ keV. Bottom part: I_γ^1 from the delayed γ-spectrum. E_γ are as in Ref. [88], and I_γ^1 is corrected for the efficiency of MINIBALL. 69

4.2. Gamma rays attributed to ^{94}Rb. The energy, spin, parity of levels, and the energy of γ transitions are as in [107], except for $E_\gamma = 405$ keV (see text). Relative intensities I_γ^{13} are normalized to the strongest γ-ray at $E_\gamma = 217$ keV. 74

4.3. Gamma rays attributed to ^{92}Rb. The energy, spin, parity of levels, and the energy of γ transitions are as in Ref. [108]. Relative intensities I_γ^{13} are normalized to the strongest $E_\gamma = 142$ keV (see text). 77

4.4. Gamma rays attributed to ^{93}Rb. The energy, spin, parity of levels, and the energy of transitions are as in Ref. [109]. Relative intensities are normalized to the strongest $E_\gamma = 324$ keV. 78

4.5. Gamma rays attributed to ^{95}Rb. The energy, spin, parity of levels, and the energy of γ transitions are as in Ref. [101]. Relative intensities I_γ^{13} are given in arbitrary units. 80

5.1. Gamma transitions attributed to ^{208}Pb. The energy, spin and parity of levels, and the energy of γ transitions are as in Ref. [115]. Relative intensities I_γ^{13} are normalized to the strongest $E_\gamma = 2615$ keV. 84

5.2. Gamma transitions attributed to ^{210}Pb. The energy, spin and parity of levels, and the energy of γ transitions are as in Ref. [122]. Relative intensities, I_{γ}^{13} and $I_{\gamma d}^{13}$ correspond to the prompt and delayed fragment-γ coincidence, respectively. They were normalized to the strongest ^{210}Pb transition in the prompt region, $E_{\gamma} = 1234$ keV. 90
5.3. The states and γ rays observed in ^{210}Pb. The energy E_{γ}^{RbPb} and the excitation energies E_{ex}^{RbPb} are as in this experiment. E_{γ}^{PbPb} and E_{ex}^{PbPb} are as in the ^{208}Pb+^{208}Pb experiment [97], and E_{γ}^{ENS} and E_{ex}^{ENS} are as in Ref. [122]. All the values are in keV, with error (if known) given in parenthesis. 92
5.4. Gamma transitions attributed to ^{207}Pb. The energy, spin and parity of levels, and the energy of γ transitions are as in Refs. [127, 131]. Relative intensities I_{γ}^{13} are normalized to the strongest transition, $E_{\gamma} = 570$ keV. . . 96
5.5. Gamma transitions attributed to ^{209}Pb. The energy, spin and parity of levels, and the energy of γ transitions are as in Ref. [134]. Relative intensities I_{γ}^{13} are normalized to the strongest transition in ^{209}Pb, $E_{\gamma} = 1567$ keV. 101
5.6. The states involved in $E3$ transitions and observed in ^{207,209,210}Pb. Given configurations are purely descriptive. 108

6.1. The $I_{J^{\pi}}$ strengths of selected states (i.e. direct populations), used in the ^{94}Rb+^{208}Pb cross section estimation. 114
6.2. The experimental σ_{ex}, $\sigma_{\text{g.s.}}$, σ_{tot} cross sections in $^{207-210}$Pb (see text). . . . 115

7.1. The PRISMA settings for ^{206}Pb+^{118}Sn reaction measurement at $E_{\text{LAB}} =$ 1200 MeV and $\theta_{\text{LAB}} = 25°$. 128
7.2. Main characteristics of the PRISMA spectrometer. 129

Biography

Petra Čolović was born in 1991 in Split, Croatia. She graduated in Physics in 2015 at the Faculty of Science, University of Zagreb and attended one semester at the Univerisity of Padova. Her master thesis, "Experimental determination of the electromagnetic transition multipolarity induced by nucleon transfer reactions", was made within the Laboratory for nuclear physics, at the Ruđer Boškovć Institute, under supervision of Dr. Suzana Szilner. In 2016, Petra got the opportunity to start a research career in the field of Nuclear Physics by joining the project "Nuclear Structure and reactions - experiments towards the neutron drip line", lead by Dr. Szilner and funded by the Croatian Science Foundation (HRZZ). Currently, she is a PhD student at the Faculty of Science, University of Zagreb, and the employee of the Ruđer Bošković Institute.

As an active member of the international scientific collaboration PRISMA, Petra participates in numerous experimental campaigns at the accelerator facilities for stable and radioactive ion beams worldwide. Her main research interests are the multinucleon transfer reactions and the path towards the heavy and neutron-rich nuclei, that she has studied at the MINIBALL experimental station in CERN. She has devoted a great deal of time to the heavy-ion reaction mechanism and the nuclear structure studies at Legnaro National Laboratories, by employing the state-of-art magnetic spectrometer PRISMA, electrostatic deflector PISOLO, and γ-array GALILEO. She has also been very engaged in the experiments that use the assembles of silicon particle detectors, mainly to study the light-ion structure and reactions.

Bibliography of published work:

1. Čolović, Petra; Szilner, S.; Corradi, L.; Mijatović, T.; Pollarolo, G.; Goasduff, A.; Montanari, D.; Chapman, R.; Fioretto, E.; Gadea, A. ; Haas, F. ; Jelavić Malenica, D. ; Marginean, N. ; Mengoni, D. ; Milin, M. ; Montagnoli, G. ; Scarlassara, F. ;

Smith, J.F. ; Soić, N. ; Stefanini, A.M. ; Ur, C.A. ; Valiente-Dobon, J.J.
Stretched configuration of states as inferred from γ*-ray angular distributions in* ^{40}*Ar+*^{208}*Pb neutron transfer reactions*, European Physical Journal A 53 (2017) 166

2. Čolović, Petra; Illana, A. ; Szilner, S.; Valiente-Dobón, J.-J.; Corradi, L.; Mijatović, T.; Benzoni, G.; Borge, M. J. G. ; Boso, A.; Ceruti, S. ; Cubiss, J. ; de Angelis, G. ; Fioretto, E. ; Galtarossa, F. ; Gaffney, L. P. ; Jurado-Gomez, M. ; Kroll, T. ; Marchi, T. ; Menegazzo, R. ; Mengoni, D. ; Napoli, D. R. ; Podolyak, Zs. ; Pollarolo, G. ; Recchia, F. ; Testov, D.
Study of the neutron-rich region in the vicinity of ^{208}*Pb via multinucleon transfer reactions*, EPJ Web of Conferences 223 (2019) 01012
3. Bradbury, J. ; Testov, D. ; Bakes, S. ; Goasduff, A. ; Mengoni, D. ; Valiente-Dobon, J.J. ; de Angelis, G. ; Bazzacco, D. ; Boiano, C. ; Boso, A. ; Cederwall, B. ; Cicerchia, M. ; Colucci, G. ; Čolović, Petra ; Didierjean, F. ; Doncel, M. ; Dueñas, J.A. ; Galtarossa, F. ; Gozzelino, A. ; Hadynska-Klek, K. ; Jaworski, G. ; John, P.R. ; Liu, H. ; Lenzi, S. ; Lunardi, S. ; Menegazzo, R. ; Mentana, A. ; Muller-Gatermann, C. ; Napoli, D.R. ; Pasqualato, G. ; Recchia, F. ; Rocchini, M. ; Riccetto, S. ; Saygi, B. ; Siciliano, M. ; Sobolev, Yu. ; Szilner, S.
Lifetime measurements using a plunger device and the EUCLIDES Si array at the GALILEO γ*-ray spectrometer*, Nuclear Instruments and Methods A 979 (2020) 164345
4. Spitaleri, C. ; Lattuada, M. ; Cvetinović, A. ; Soić, N. ; Milin, M. ; Čolović, Petra ; D'Agata, G. ; Dell'Aquila, D. ; Guardo, G. L. ; Gulino, M. ; Trippella, O. ; La Cognata, M. ; Lamia, L. ; Lattuada, D. ; Li, Chengbo ; Messina, S. ; Nurkić, D. ; Perrotta, S. S. ; Pizzone, R. G. ; Popočovski, R. ; Romano, S. ; Skukan, N. ; Sparta, R. ; Szilner, S. ; Uroić, M. ; Vukman, N.
Study of the quasi-free ^{3}*He+*^{12}*Be*$\rightarrow 3\alpha$ *reaction for the Trojan Horse Method*, European Physical Journal A 56 (2020) 18
5. Montagnoli, G ; Stefanini, A. M. ; Jiang, C. L. ; Colucci, G. ; Bottoni, S. ; Brugnara, D. ; Čolović, Petra ; Corradi, L. ; Fioretto, E. ; Galtarossa, F. ; Goasduff, A. ; Khwairakpam, O. S. ; Heine, M. ; Jaworski, G. ; Mazzocco, M. ; Mijatović, T. ; Siciliano, M. ; Scarlassara, F. ; Szilner, S. ; Van Patten, T. ; Zanon, I.

Fusion of ${}^{12}C+{}^{24}Mg$ far below the barrier: Evidence for the hindrance effect , Physical Review C 101 (2020) 044608

6. Provatas, G. ; Fazinić, S. ; Soić, N. ; Vukman, N. ; Cosic, D. ; Krmpotić, M.; Vukšić, M. ; Crnjac, A.; Popočovski, R.; Palada, L. ; Čolović, Petra ; Dell'Aquila, D. ; Gašparić, I. ; Jelavić Malenica , D. ; Mijatović, T. ; Uroić, M.

   Differential cross section measurements of the ${}^{9}Be({}^{3}He,p){}^{11}B$ reaction for NRA applications, Nuclear Instruments and Methods B 472 (2020) pg.36-45
7. Colucci, G. ; Montagnoli, G. ; Stefanini, A.M. ; Hagino, K.: Caciolli, A. ; Čolović, Petra ; Corradi, L. ; Fioretto, E. ; Galtarossa, F. ; Goasduff, A. ; Grebosz, J. ; Mazzocco, M. ; Montanari, D. ; Parascandolo, C. ; Scarlassara, F. ; Siciliano, M. ; Strano, E. ; Szilner, S. ; Vukman, N.

   Sub-barrier fusion involving odd mass nuclei: the case of ${}^{36}S+{}^{50}Ti$, ${}^{51}V$, European Physical Journal A 55 (2019) 111
8. Montagnoli, G. ; Stefanini, A. M. ; Jiang, C. L. ; Hagino, K. ; Galtarossa, F. ; Colucci, G. ; Bottoni, S. ; Broggini, C. ; Caciolli, A. ; Čolović, Petra ; Corradi, L. ; Courtin, S. ; Depalo, R. ; Fioretto, E. ; Fruet, G. ; Gal, A. ; Goasduff, A. ; Heine, M. ; Hu, S. P. ; Kaur, M. ; Mijatović, T. ; Mazzocco, M. ; Montanari, D. ; Scarlassara, F. ; Strano, E. ; Szilner, S. ; Zhang, G. X.

   Fusion hindrance and Pauli blocking in ${}^{58}Ni+{}^{64}Ni$, Physical Review C 100 (2019) 044619
9. Szilner, S. ; Corradi, L. ; Mijatović, T. ; Montanari, D. ; Galtarossa, F. ; Pollarolo, G. ; Colucci, G. ; Čolović, Petra ; Fioretto, E. ; Goasduff, A. ; Jelavić Malenica, D. ; Montagnoli, G. ; Scarlassara, F. ; Soić, N. ; Stefanini, A.M. ; Valiente-Dobón, J.J. *Probing nucleon-nucleon correlations in heavy-ion transfer reactions*, Il Nuovo Cimento C 41 (2018) 185
10. Colucci, G.; Montagnoli, G.; Stefanini, A. M.; Esbensen, H.; Bourgin, D.; Čolović, Petra; Corradi, L.; Faggian, M.; Fioretto, E.; Galtarossa, F. ; Goasduff, A. ; Grebosz, J. ; Haas, F. ; Mazzocco, M. ; Scarlassara, F. ; Stefanini, C. ; Strano, E. ; Szilner, Suzana ; Urbani, M. ; Zhang, G. L.

    Isotopic effects in sub-barrier fusion of Si + Si system, Physical Review C 97 (2018) 044613
11. Montagnoli, G.; Stefanini, A. M.; Jiang, C. L.; Hagino, K.; Galtarossa, F.; Colucci,

G.; Bottoni, S.; Broggini, C.; Caciolli, A.; Čolović, Petra ; Corradi, L. ; Courtin, S. ; Depalo, R. ; Fioretto, E. ; Fruet, G. ; Gal, A. ; Goasduff, A. ; Heine, M. ; Hu, S.P. ; Kaur, M. ; Mijatović, T. ; Montanari, D. ; Scarlassara, F. ; Strano, E. ; Szilner, Suzana ; Zhang, G.X.
Fusion hindrance for the positive Q-value system $^{12}C+^{30}Si$, Physical Review C 97 (2018) 024610

12. Stefanini, A.M.; Montagnoli, G.; Esbensen, H.; Čolović, Petra; Corradi, L.; Fioretto, E.; Galtarossa, F.; Goasduff, A.; Grebosz, J.; Haas, F. ; Mazzocco, M. ; Soić, N. ; Strano, E. ; Szilner, S.
New results in low-energy fusion of $^{40}Ca+^{90,92}Zr$, Physical Review C 96 (2017) 014603

Acknowledgements

I would like to thank Dr. Suzana Szilner, my research supervisor, for the great effort and care she has been continuously investing in our research work. She has taught and supported me both professionally and personally, that I am deeply thankful for. My thanks are to Dr. Tea Mijatović, who has helped me in numerous ways, especially at the beginning of my career, making it less difficult, and indeed, enlightening. I would also like to thank Prof. Matko Milin, for his unreserved help, kindness, and encouragement. Furthermore, thanks to Dr. Neven Soić, I've had the opportunity to work on many engaging experiments. I feel very grateful to all the members of the Laboratory of nuclear physics at the Ruđer Bošković Institute, where I have met great physicists, and more importantly, great friends.

I wish to thank all our collaborators, for their knowledge and devotion invested in the research and the experimental work. The ^{94}Rb+^{208}Pb experiment at HIE-ISOLDE in CERN has been a memorable experience, realized within the collaborations of MINIBALL and ISOLDE. It has been a great pleasure to work together with Dr. Jose Javier Valiente-Dobón and Dr. Andrés Illana on the results presented in this thesis. Their help and engagement were fundamental for the data analysis and interpretation, that I am genuinely thankful for.

I appreciate the unique opportunity I was given, to profit from the inspiring work environment during my visits to the Laboratori Nazionali di Legnaro. I would like to express my deep gratitude to dr. Lorenzo Corradi, for all of his work and suggestions, and especially for investing his time to read and improve this thesis. Sincere thanks go to Prof. Giovanni Pollarolo who provided us the theoretical calculations necessary to interpret and publish the results. I wish to thank Dr. Franco Galtarossa and Dr. Alain Goasduff, for their patience and effort to teach me ROOT and PRISMA data analysis, and also to Josipa Diklić, who helped me generously. I am deeply grateful to all the

members of the PRISMA group, Dr. Enrico Fioretto, Prof. Fernando Scarlassara, and in particular to Prof. Giovanna Montagnoli, Dr. Alberto Stefanini and Dr. Giulia Colucci, for the very instructive experience at the PISOLO experiments. Working with Legnaro γ-group has broadened my horizons, and I value time spent on shifts with Marco, Giorgia, Irene, Ana, Dmitry, Mariluz, Jose, Grzegorz, Daniele...

I am also very grateful to all my friends and colleagues who have helped me proofreading the thesis, especially Dr. Daniele Dell' Aquila, and my cousins, Sophia and Martina.

Special thanks go to my great friend, Nikola, who had my back these five years. Many thanks to our partners in crime, Deni and Deša, for all the memories we created together when we were abroad. Needless to say, I am very grateful to have profit from our music and sports sections lead by Gašo and Luka.

At last, no words can express my gratitude towards Jure, my family and friends.